

# 1 Mixing of Miscible Fluids

## 1.1 Mixing in Micro Spaces – Drivers, Principles, Designs and Uses

### 1.1.1 'Mixing Fields', a Demand Towards a more Knowledge-based Approach – Room for Micro Mixers?

Many unsolved challenges remain in the field of mixing [1]. The diversity of mixing tasks is large and so is their industrial importance. Mixing is a good example how equipment dominates the type of processing solution chosen (see Figure 1.1) [1]. Mixing has been carried out in stirred tanks over decades and all mixing problems were solved using this assumption as a starting condition.

Meanwhile, there is a slight paradigm shift apart from such equipment design dominance to a more knowledge-based approach (see Figure 1.2), with the mixing objective in the focus, i.e. the so-called 'mixing fields', related to the rate and scales of segregation destruction (for a detailed definition see [1]) [1]. This demands a

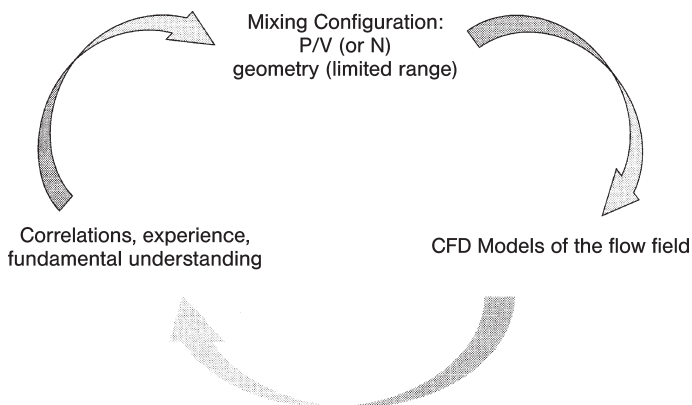


**Figure 1.1** Design and development cycle for equipment-based design: using pre-decided equipment, a mixing configuration is chosen by correlations and experience. For stirred tanks this configuration is given, e.g., by the power-to-volume ratio  $P/V$  and the impeller diameter  $N$ . Then, CFD models are made to describe the flow field [1].

*Chemical Micro Process Engineering.* V. Hessel, H. Löwe, A. Müller, G. Kolb.  
Copyright © 2005 WILEY-VCH Verlag GmbH & Co. KGaA, Weinheim  
ISBN: 3-527-30998-5

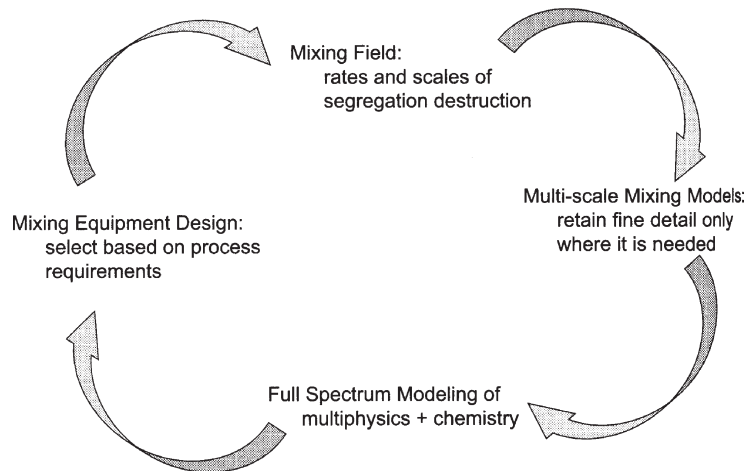


**Figure 1.2** Design and development cycle for mixing-field based design: there is a selection of the mixing equipment based on the process requirements. This leads to the specification of a mixing field. CFD simulations give the flow field reduced to a multi-scale mixing model. The mixing field is integrated with other models of the key process mechanisms, aiming at giving an entire picture of the process [1].

greater variety of equipment solutions and in particular specially equipment, tailor-made for one specific mixing task. Recently, this has led industry to use rotor stators, static mixers, multi-shaft mixers, extruders and pulping machines [1]. It stands to reason that such development may also pave the way for using microstructured mixers for industrial applications.

Experts predict a trend from stirred-vessel mixing to the use of continuous mixing, e.g. by in-line mixers [1]. This again provides a chance for many microstructured mixers.

### 1.1.2

#### Drivers for Mixing in Micro Spaces

Many passive microstructured mixers (see e.g. [2, 3]) follow design principles used at the macro-scale for static mixers with internal packings [4]. It stands to reason that some of the advantages in processing claimed for conventional static mixer also apply or may be even more pronounced when using static mixers [4]:

- compactness and low capital cost
- low energy consumption and other operating expenses
- negligible wear and no moving parts, which minimizes maintenance
- lack of penetrating shafts and seals, which provides closed-system operation
- short mixing time and well-defined mixing behavior
- narrow residence-time distribution
- performance independent of pressure and temperature.

In addition, the following specific chemical engineering drivers may govern the decision to use a micro or microstructured mixer:

- enabling technology for niche mixing, where conventional mixers fail
- enabling technology in particular for mixing under laminar-flow conditions in minute spaces
- fast mixing for even faster reactions in chemical synthesis (see e.g. [5])
- analytical processing of fast reactions, e.g. for quench-flow analysis (< 1 ms) to study rapid biological transformations [6]
- laminar mixing of viscous media [7], as most micro-flow processing is anyway in that regime
- mixing at only small overall internal device volumes, e.g. for
  - handling of rare, precious samples in analysis or synthesis
  - handling and screening of numerous samples on a small format in chemical and biological analysis [8–15])
- mixing below threshold dimensions and at small partial internal volumes to ensure safety [16–19], for both mechanistic and thermal reasons, respectively [16]
- mixing of a flow of high structural regularity [20], e.g. to enhance predictability of modeling and to improve scaling-/numbering-up.

### 1.1.3

#### Mixing Principles

Mixing in minute spaces can basically rely only on two principles which are diffusion and convection. Diffusion between short distances, establishing high concentration gradients (see e.g. [21]), was initially the most frequently applied principle by simply making the channels themselves smaller and smaller. Soon, the limits of that strategy, also in terms of robustness (fouling) and costs (complex microfabrication), became obvious. In recent years, various methods were developed to overcome the limits by diffusion mixing, all of them based on the induction of secondary-flow (convective) patterns which are superposed on the main flow, often in the vertical direction to the flow axis. This includes recirculation patterns, chaotic advection and swirling flows, just to name a few. Convection is effective for mixing, since it serves to enlarge mixing interfaces. Convections of 'gross' mass portions can be used at a much larger scale to 'stir' complete chamber volumes, e.g. by ultrasound, by elektrokinetik instability or acoustic means. At high Reynolds numbers, turbulent mixing can be utilized; however, this is often not practicable, as this implies achievement of unrealistic large flow velocities. The few specially equipment known to use turbulence rely either on free-guided flows or guide through meso-scale channels.

**Means for Mixing of Micro Spaces**

The means of mixing can be classified as either *active* or *passive*. *Passive micro mixers* use part of the flow energy for feeding and thereby generate special flow schemes with ultra-thin flow compartments such as lamellae for diffusion mixing or utilize chaotic advection by secondary flows to enlarge the interfaces. *Active micro mixers* rely on moving parts or externally applied forcing functions such as pressure or electric field.

External energy sources for *active mixing* are, for example, ultrasound [22], acoustic, bubble-induced vibrations [23, 24], electrokinetic instabilities [25], periodic variation of flow rate [26–28], electrowetting induced merging of droplets [29], piezoelectric vibrating membranes [30], magneto-hydrodynamic action [31], small impellers [32], integrated micro valves/pumps [33] and many others, which are listed in detail in Section 1.2.

Devices relying on *passive mixing* utilize the flow energy, e.g. due to pumping action or hydrostatic potential, to restructure a flow in a way which results in faster mixing. For example, thin multi-lamellae can be created in one step in special feed arrangements, termed interdigital [20, 34–42]. A serial way of creating multi-lamellae can be achieved by split-and-recombine (SAR) flow guidance [7, 43, 140]. Chaotic mixing results from superimposed recirculation flow patterns (such as helical flows), with an exponential increase in specific interfaces [27, 28, 44–50]. The injection of many sub-streams, e.g. via an array of nozzles, into one main stream can create micro-plumes with large interfaces [51]. Turbulent mixing can be achieved by collision of jets [52–54]. A number of specially flow guidances are known as well. For example, re-directed flows create eddies which are exploited in Coanda effect mixers [55] and in other recycle-flow mixers [56]. These and more passive principles are described in Section 1.3.

There are more reports about and more different types for passive than for active micro mixers. This is understandable, since for many applications flow energy is given. Also, active micro mixers may be more difficult to fabricate, as they require special additional elements besides the normal fluid pathway as in the case of passive devices. This also demands control of these functions, i.e. further external equipment may be needed. All this implies greater complexity for active devices. On the other hand, these tools are specially designed for mixing tasks which passive mixers cannot accomplish, i.e. mixing at very low flow velocities and/or of large fluid chambers. Sometimes, active mixing devices may consume a much smaller footprint area than passive ones with all their fluid feed channel architecture and large inlet and outlet ports. The complexity of active micro mixers may not be a problem any more for future devices, when microsystem integration is brought to a more advanced level.

## 1.1.5

**Generic Microstructured Elements for Micro-mixer Devices**

The above-mentioned micro-mixer means have to be ‘transformed’ into physical objects, i.e. the microstructures which then perform the mixing (see Figure 1.3). Bi-lamination can be achieved in T- and Y-flow structures [6, 57], which are miniaturized analogues of conventional mixing tees. Multi-lamination is done via structures with alternate feeds. The latter are realized either by interdigital [20, 34–41] or bifurcation [42] structures. To speed up mixing, thinning of the multi-lamellae flow via geometric focusing zones can be utilized [20, 34–39]. Several types of flow dividing and recombining structures were developed for SAR-type mixing, including fork-like, stack-like, Möbius-type and 3-D curved caterpillar designs [7, 43, 125, 126, 140, 141]. Chaotic mixing was first achieved by alternately arranged slanted grooves, so-called herringbone structures, in a micro channel [44, 45]. Barrier-embedded structures may be added and will further improve the mixing efficiency [3, 58]. Later, other structures such as simple curved channels and zig-zag channels were used as well [27, 28, 46–50, 59]. Micro-plume injection is done by multi-hole plates adjacent to a mixing chamber, as simple through-holes with straight injection [51] or complex oblique arrays with tilted injection [54].

These are just a few among other examples of microstructured designs which are discussed in detail in the next two chapters. More information about these micro-mixer designs can be obtained from reviews, e.g. [60–66].

In addition to grouping the mixers according to their mixing principles and their generic microstructure designs, a practically oriented classification refers to the complexity of the fluid network [25]. So-called in-plane mixers rely on streams which are divided and mixed in a fluid network confined to one level (i.e. a pattern that can be projected on to a single plane) [25]. In turn, out-of-plane mixers rely on a

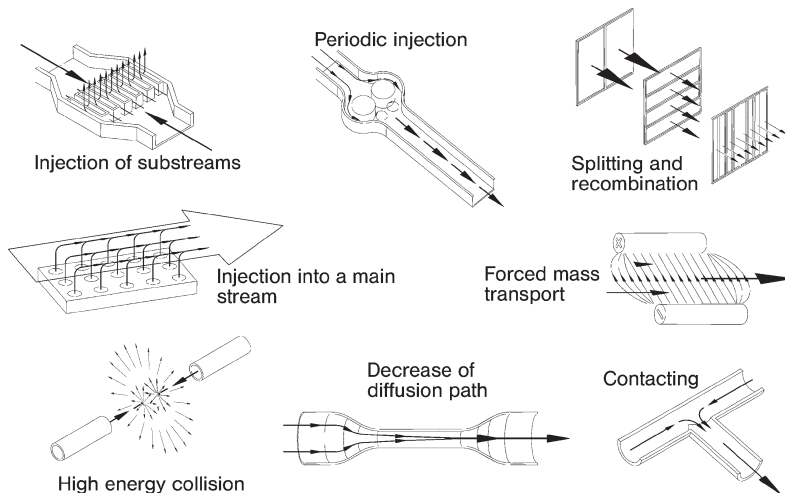


**Figure 1.3** Schematic diagrams of selected passive and active micro mixing principles [66] (source IMM).

more complex, three-dimensional fluid network. Examples of in-plane mixers are bi-laminating, T- and cross-channel mixers as described [57, 67–71]. SAR and most multi-lamination mixers act out-of-plane; examples of these device types are given in [7, 43] and [20, 36, 37, 39], respectively. Another type of out-of-plane mixer is based on micro-plume array injection [51].

It is customary, mainly owing to fabrication needs, that for biological applications chip-like systems with two-layer construction are used, thus being in-plane. Mixers used for the same purposes have to adjust to this fact. Since multi-lamination typically needs several layers to achieve the proper feeding pathways, other mixers with simpler designs such as the electrokinetic instability mixer need to be applied [25]. In contrast, chemical applications, where the mixer is only associated with part of the plant and not integrated in a small, flat device, do not pose such preferences; indeed, multi-layer microfabrication architectures have been used.

#### 1.1.6

##### Experimental Characterization of Mixing in Microstructured Devices

For simulation characterization, the reader should refer to Chapter 2, *Modeling and Simulation of Micro Reactors*, in the first volume of this series [72].

For experimental characterization, flow visualization by colored or fluorescent streams is the most facile method. *Dilution-type experiments* contact dyed and pure water streams (passive mixing) or standing volume portions (active mixing) in a type of photometric experiment. This is usually monitored with the aid of microscopic, photo, video or high-speed camera techniques (see e.g. [20]).

*Reaction-type experiments* underlie mixing with a very fast reaction so that mixed regions spontaneously indicate the result of the reaction (see e.g. [20]). Besides using ‘normal’ fast organic reactions with color formation, change or quenching [20, 73], the usage of acid–base reactions with a pH-sensitive dye or a pH indicator is common. More detailed information is given by *competitive reactions*, i.e. two parallel reactions [74–78]. These reactions develop differently with varying pH, solvent, etc., which is influenced via mixing. Such reactions were first applied for determining mixing efficiency in stirred batch reactors and later adapted to the needs of micro mixer devices [36]. Still later, optimized protocols were developed for micro-mixer testing giving more accurate and more reproducible results [79].

*Concentration profiling* uses on- or in-line measurements of optical properties, typically not done for the whole volume, but along lines such as the channel cross-section (see e.g. [20]). Concentrations are accessible by photometric, electric or fluorescence measurements. Furthermore, vibrational analysis such as IR and Raman spectroscopy can be used for the same task [80, 81]. Concentration profiling can also be achieved simply by gray-scale or comparable image analysis for quantitative data extraction from microscopy images of colored flows [20, 37, 68].

These techniques are the most often used and simplest ways to characterize mixing in microstructured mixers. Certainly, many more were used in the past. Information on such specially techniques given in the next two chapters where the respective mixer is discussed.

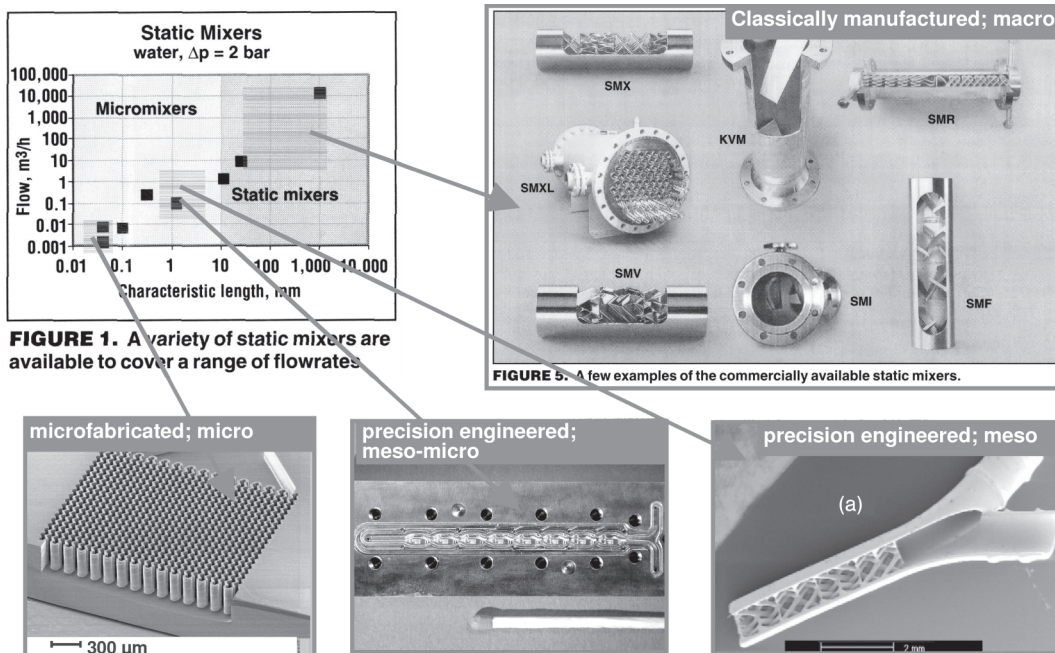


**FIGURE 1.** A variety of static mixers are available to cover a range of flowrates

**FIGURE 5.** A few examples of the commercially available static mixers.

**Figure 1.4** Micro mixers (laboratory scale) and micro structured mixers (pilot scale) close the gap with static mixers, yielding apparatus for a multi-scale concept. Today's microstructured devices achieve mixing at up to about  $1 \text{ m}^3 \text{ h}^{-1}$  liquid throughput [2, 64] (by courtesy of RSC and Chemical Engineering).

### 1.1.7

#### Application Fields and Types of Micro Channel Mixers

Generally, application fields of micro channel based mixers encompass both modern, specialised issues such as sample preparation for analysis and traditional, widespread usable mixing tasks such as reaction, gas absorption, emulsification, foaming and blending [63, 64, 66, 72, 82] (see also [83–90]). For novel and modern chemical and biochemical analysis, typically *micro mixer elements* serve as mixing units within credit card-sized fluidic chips, often being complex integrated systems. Chip-like micro mixer components (*micro mixers*) are employed for the more conventional chemical and chemical engineering applications at the laboratory scale. At pilot or even production scales, much bigger components are applied for the same mixing tasks, typically comprising microstructures in a large housing, therefore being more correctly termed *micro structured mixers*.

Micro mixer elements, micro mixers and micro structured mixers typically have flows in the  $\text{ml h}^{-1}$ ,  $1 \text{ l h}^{-1}$  and  $1000 \text{ l h}^{-1}$  ranges, respectively, thus covering the whole flow range up to the conventional static mixers and being amenable to analysis and chemical production as well (see Figure 1.4). When used at the upper flow limit, microstructured mixers can act as process-intensification (PI) equipment.

## 1.2

### Active Mixing

In the following the state of the art of microstructured mixing devices is presented. Only the mixing of miscible liquids (and gases) is considered; the same micro mixers, however, can usually be used for making liquid/liquid and gas/liquid dispersions, which is outside the scope of this chapter, but certainly is worth consideration in the future. If not otherwise mentioned, liquid mixing is involved. The few examples on gas mixing are explicitly dealt with.

This chapter is on mixing principles, their respective devices and their characterization and is intended to give the reader an idea of how well they already function. This chapter is not really on mixing theory and physics of micro mixers.

The contents are presented in a structured, hierarchical order similar to an encyclopedia style. Hence not one description or work simply follows another, but are intertwined for better comparison. It is aimed at giving a comprehensive picture of the field.

First, the mixing principle is explained in a generic fashion. Then, a device section follows, describing all the different versions of microstructured devices actually realized. Details on the way in which the generic principle is applied are given as well as details on microfabrication and design specifications.

In the *Mixing Characterization Protocols/Simulation* sections, details on the methods of mixing characterization and simulation are provided.

In the *Typical Results* sections, it is pointed out how ready the use of such devices for industry is at present. The reactor and the protocol/simulation are not explained any further, but there is a reference to the respective section. The results are divided according to the special topics they refer to, as indicated by a heading. It is aimed to achieve a logical order of the sequence in which the topics are presented.

#### 1.2.1

### Electrohydrodynamic Translational Mixing

#### Most relevant citations

Peer-reviewed journals: [25, 91, 92]; proceedings contributions: [48, 93, 94].

Mixing can be accomplished by electric forces, when fluids with different electric properties such as conductivity and/or permittivity are exposed [91]. In MEMS devices, electric fields of relatively large amplitude can be generated by means of low voltages so that respective mixing effects should be as pronounced as in theory. Further, MEMS fabrication techniques are fairly advanced concerning the patterning and integration of electrode structures. No moving parts are required for micro mixers of this type, which generally is not easily accomplished at the micro scale.

Electric-force mixing is adequate for mixing flows at very low Reynolds number ( $\sim 1$ ). By lamination of two fluids with different electric conductivity and/or permittivity in a micro mixer, a steep cross-sectional gradient of the respective properties can be established [91]. The electric field may be parallel or perpendicular to the fluid interface, which is also a boundary where electric properties abruptly

change. In the presence of a sufficiently large electric field, a transversal flow secondary flow can be stirred. Direct (DC) and alternating (AC) currents can be applied for this purpose. The latter have oscillating frequency, e.g. of square or sinusoidal type.

Translational motion, i.e. secondary flow lateral to the flow direction, can be achieved by spatially homogeneous or inhomogeneous fields, respectively termed electrophoresis and dielectrophoresis. Rotational motion can be achieved as well, when a dipole is induced and a torque is exerted on that dipole. Then, the rotating entity may be a solid object, e.g. a microsphere, which actively mixes and is not the fluid to be mixed. Such rotating objects generates secondary flow in their vicinity and are described in Section 1.2.2.

Electric fields may interact with flows fed by hydrostatic or pumping action [91]. Flows driven by electroosmotic means may be mixed as well by the action of fluctuating electric fields, which creates oscillating electroosmotic flows and has been termed electrokinetic instability (EKI) [25, 93]. In this way, rapid stretching and folding of material lines are induced, not unlike the effect of stirring. In one realized example, comparatively low frequencies, below  $\sim 100$  Hz, and electric field strengths in excess of  $100 \text{ V mm}^{-1}$  are applied for channels with dimensions of about  $50 \mu\text{m}$  [25].

#### 1.2.1.1 Mixer 1 [M 1]: Electrohydrodynamic Micro Mixer (I)

This micro mixer, named electrohydrodynamic (EHD) microfluidic mixer, comprises a simple T-channel structure (see Figure 1.5) [91]. After passing the T-junction, a bi-laminated stream is realized. Following a downstream zone for such flow establishment, a channel zone with several electrode wires on both sides of the channel is located. In this way, an electric field perpendicular to the fluid interface is generated. Thereafter, an electrode-free zone of the channel is situated for completion of the mixing initiated.

The electrodes face each other with a differential potential between the two sets, one set grounded and the other energized [91].

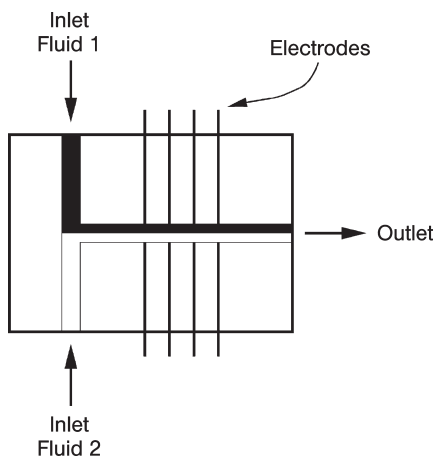


**Figure 1.5** Schematic of the electrohydrodynamic mixer with T-channel and pairs of electrodes adjacent to the channel and perpendicular to the fluid interface generated [91] (by courtesy of RSC).

Device manufacture was made by conventional precision engineering machining [91]. A thin plate was glued on a thick substrate to make it immobile. The slots for the wires were made by saw blading. The electrodes were then press fitted into these slots. A layer of epoxy glue was used for sealing of the electrodes within the slots. The flow channel was milled using a 0.25 mm carbide endmill. A microscope glass cover slip was glued on top of the device to seal the micro channel, but to still allow visual inspection.

Mixer type	Electrohydrodynamic mixer	Wire electrode diameter	250 $\mu\text{m}$
Mixer material	Lexan	Spacing between electrodes	500 $\mu\text{m}$
Plate thickness	3.175 mm	Spacing between electrodes	500 $\mu\text{m}$
Mixing channel width, depth, length	250 $\mu\text{m}$ , 250 $\mu\text{m}$ , 30 mm	Electrode material	Titanium
Slots for wire electrodes	250 $\mu\text{m}$ $\times$ 250 $\mu\text{m}$	Plate dimensions	12 mm $\times$ 15 mm

#### 1.2.1.2 Mixer 2 [M 2]: Electrohydrodynamic Micro Mixer (II)

This electrohydrodynamic (EHD) mixer (Figure 1.6) device provides a simple flow-through chamber which has an upper and lower electrode for generating an electromagnetic field. The chamber channel is given by a sandwich of two plates, one being microstructured [94]. The bottom plate contains a trapezoid channel. Two electrode layers are deposited on parts of the channel bottom and channel top and on the top part of this plate so that they reach the outside for external electrical contact.

By electromagnetic means, surface charges can be induced and accumulated on the boundary of a dielectric material [94]. Liquid samples can be treated the same way. For a non-uniform external electric field, interfacial shear stress in liquids is generated, inducing flow motion which tends to eliminate this stress. In this way, new interfaces are formed and mixing can be achieved.

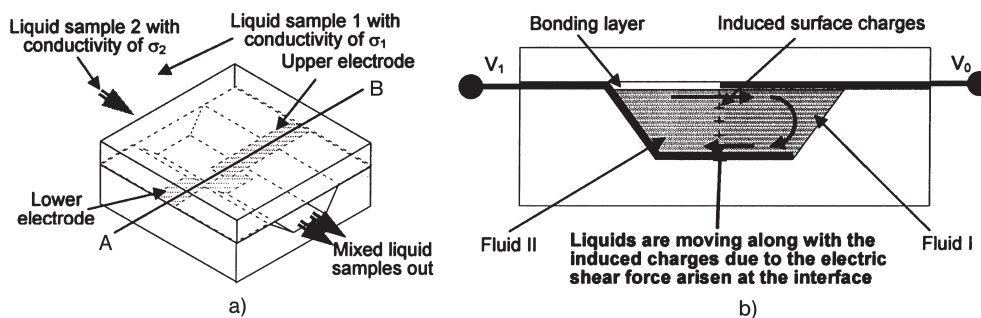


**Figure 1.6** Schematic design of the *electrohydrodynamic (EHD) mixer* (left) and cross-sectional view giving the electrode arrangement and sketching the flow motion induced by interfacial shear (right) [94] (by courtesy of Kluwer Academic Publishers).

So far, only a design study of the EHD mixer has been provided [94], hence no device specifications can be given here.

### 1.2.1.3 Mixer 3 [M 3]: Electrokinetic Instability Electroosmotic Flow Micro Mixer, First-generation Device

This device, named electrokinetic instability (EKI) mixer, is driven by electroosmotic flow (EOF) and thus termed an EKI-EOF micro mixer in the following [25, 93]. It contains two channels which are arranged cross-wise, each having two reservoirs at the ends (see Figure 1.7) The two fluids to be mixed come from the two ends of the shorter channel and merge when entering the longer channel, moving along it. A simple version was cast in polydimethylsiloxane (PDMS) which was considered to be the first-generation device to [M 4] (see below). A high-voltage amplifier coupled with a function generator is connected to one reservoir of the longer channel, generating the electroosmotic flow and causing the whole flow direction to be towards the fourth reservoir at the other end of the longer channel.

The mixer was made by casting, molding and curing [25, 93]. Then, the channels were covered by glass slides. Two ports were placed at the inlet reservoir feeds. The liquids were pumped by hydrostatic pressure. Platinum electrodes were deposited in the upstream and downstream reservoirs by AC excitation. The EKI then occurs along the entire channel.

The frequency and the applied voltage of the AC field were 10 Hz and 1 kV, respectively [25].

Mixer type	Electrokinetic instability electro-osmotic flow mixer, 1 <sup>st</sup> -generation device	EKI micro channel: width, depth, length	1000 $\mu\text{m}$ , 300 $\mu\text{m}$ , 7 mm
Mixer material	PDMS	Plate dimensions	12 mm $\times$ 15 mm
Electrode spacing	9 mm		

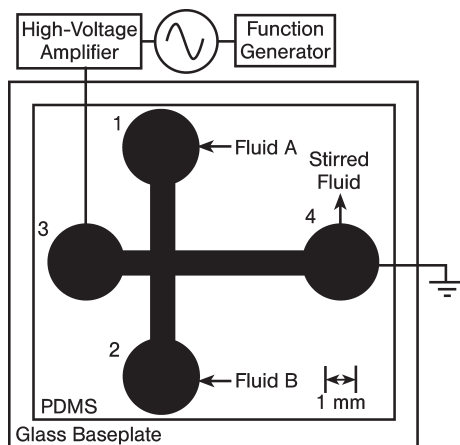


**Figure 1.7** Design of an electrokinetic instability EOF micro mixer, first-generation device [25] (by courtesy of ACS).

#### 1.2.1.4 Mixer 4 [M 4]: Electrokinetic Instability Electroosmotic Flow Micro Mixer, Second-generation Device

This micro mixer was built after first tests with the [M 3] device as a more robust and practical successor device (see Figure 1.8) [25, 93]. Two channels were arranged cross-wise, each having two reservoirs at the ends. Now, the two liquids are pumped into two feed channels which merge in a Y-type configuration. From there, they flow concurrently in one channel and are collected in one reservoir. At the beginning of this channel a quadratic chamber intersects in which the flow is mixed by EKI action. For this purpose, the chamber is connected to two channels with two reservoirs at their ends. These reservoirs are each in contact with electrodes, which equal to [M 3], are connected to a high-voltage amplifier coupled with a function generator.

The mixer is made by standard photolithography and wet etching in glass [25]. The fluidic network was sealed by thermal bonding with another glass plate. Holes were drilled through the cover plate.

The AC field was generated with a sine wave fed into a high-voltage amplifier ( $0 \pm 10$  kV) [25]. The frequency and the applied voltage were 5 Hz and 4 kV, respectively.

Mixer type	Electrokinetic instability (EKI) mixer	Mixing chamber: width, length, depth	1000 $\mu\text{m}$ , 1000 $\mu\text{m}$ ; 100 $\mu\text{m}$
Mixer material	Borofloat glass	Mixing chamber volume	0.1 $\mu\text{l}$
EKI micro channel width, depth	300 $\mu\text{m}$ , 100 $\mu\text{m}$	Plate dimensions	15 mm $\times$ 22 mm

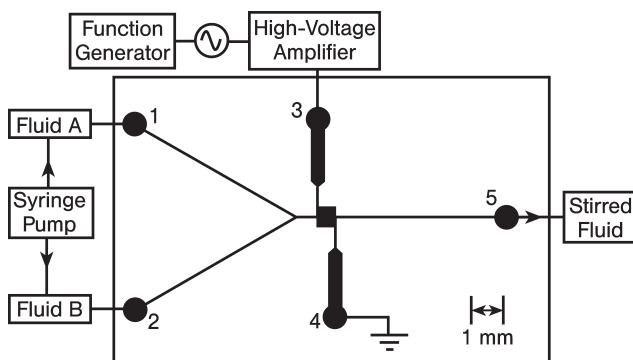


**Figure 1.8** Design of an electrokinetic instability micro mixer, second-generation device, based on the results obtained with the first design given in Figure 1.7. The electrokinetic instability is confined to the square mixing chamber shown in the center of the schematic and, to a small extent, to fluid channel regions attached to it [25] (by courtesy of ACS).

The major improvement of design [M 4] over [M 3] is that now mixing is largely confined to a small mixing space, i.e. the mixing chamber, while before a more extended region was addressed [25]. Actually, the region of EKI instability is confined to the mixing chamber and a small part of the adjacent channels, being no longer than two micro channel widths. Input flow streams can now be either pressure or electric-field driven. Another major improvement was the use of porous, dielectric frits with 0.5  $\mu\text{m}$  pores which serve to separate the external fluid reservoirs from the internal micro channel flows.

#### 1.2.1.5 Mixer 5 [M 5]: Electrokinetic Instability Micro Mixer by Zeta-potential Variation

This electrokinetically driven micro mixer uses localized capacitance effects to induce zeta potential variations along the surface of silica-based micro channels [92]. The zeta potential variations are given near the electrical double layer region of the electroosmotic flow utilized for species transport. Shielded ('buried') electrodes are placed underneath the channel structures for the fluid flow in separate channels, i.e. they are not exposed to the liquid. The potential variations induce flow velocity changes in the fluid and thus promote mixing [92].

The microstructure consists of a cross-shaped feed structure with one longer mixing channel, connecting to the waste [92]. Two of the other three channels serve for feed of the two solutions to be mixed, the third connects to waste. The long channel is placed over nine buried electrodes, having a rectangular shape.

The mixer was made by wet-chemical etching of glass substrates, following a photolithographic step, yielding channels for the fluid flow and for the electrodes. The electrodes (100  $\Omega$  resistors) were made by an electron-beam evaporation process generating thin metallic films in the etched channels [92]. Holes were drilled into the cover plate for inlet and outlet connection. Fusion bonding was used to seal the plates.

Mixer type	Electrokinetic instability micro mixer with zeta potential variation	Shielding electrode channel width, depth	250 $\mu\text{m}$ , 25 $\mu\text{m}$
Mixer material	Glass	Mixing channel width, length	150 $\mu\text{m}$ , 34 mm
Number of electrodes	9	Side channel length of the cross	10 mm
Distance electrodes–mixing channel	130 $\mu\text{m}$	Top channel length of the cross	4.4 mm
Electrode materials and thickness	Cr: 50 nm; Au: 0.4 $\mu\text{m}$	Diameter of reservoirs	1.5 mm

### 1.2.1.6 Mixer 6 [M 6]: Electrokinetic Dielectrophoresis Micro Mixer

This dielectrophoresis (DEP) mixer, specially designed for mixing of dielectric particles was made with a rectangular chamber having one inlet and outlet [48]. Pairs of micromachined electrodes generate the electric field.

Dielectrophoresis is the translational motion of neutral matter owing to polarization effects in a non-uniform electric field. Depending on matter or electric parameters, different particle populations can exhibit different behavior, e.g. following attractive or repulsive forces. DEP can be used for mixing of charged or polarizable particles by electrokinetic forces [48]. In particular, dielectric particles are mixed by dielectrophoretic forces induced by AC electric fields, which are periodically switched on and off.

The mixer was made by using MEMS technology [48]. Inlet and outlet holes were made by anisotropic etching with KOH from the backside (see Figure 1.9) [48]. The electrodes with pads were patterned on the top side and were coated with an insulation layer. The channel walls and the chamber were made by using SU-8 photoresist technology. The cover plate was sealed using a special bonding technique. Electrical connections are placed on the top side, whereas fluidic connections are on the rear.

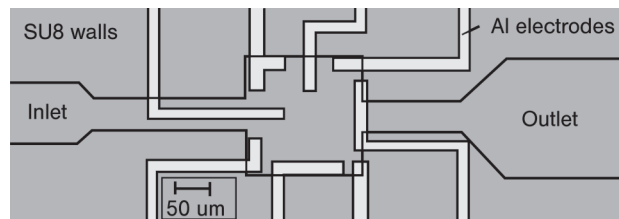


Figure 1.9 Top view of the electrokinetic dielectrophoresis mixer [48] (by courtesy of Springer-Verlag).

Mixer type	Electrokinetic dielectrophoresis mixer	Bonding layer material	SU-8
Mixer material	Silicon	Inlet and outlet channel width	50 μm
Electrode material	Aluminum	Mixing chamber width, depth, length	200 μm, 200 μm, 25 μm
Insulation layer material	SiO <sub>2</sub>		

### 1.2.1.7 Mixing Characterization Protocols/Simulation

Here and throughout, protocols are designated [P 1], [P 2], etc.

[P 1] The electrodes were connected to a signal generator and DC power supply for continuous-voltage operation and an amplifier for alternating-voltage operation [91]. The set-up allowed one to vary the frequency and the potential and to measure their precise values.

The use of pumps was abandoned owing to their pulsation. Instead, hydrostatic pumping was selected and turned out to be sufficient for the flow rates envisaged [91]. The total average velocity was  $4.2 \text{ mm s}^{-1}$ .

One of the fluids was pure Mazola corn oil and the other was the same oil colored with oil-based Teal dye and doped with oil-miscible antistatic Stadis<sup>®</sup> 450 to increase the conductivity and permittivity [91]. The latter values were measured with a broadband dielectric spectrometer in a spatially uniform low electric field for frequencies of 0.5–1 kHz.

The flow was monitored by the use of a microscope and a video camera to detect the color changes [91]. A gray-scale level analysis was performed.

[P 2] Deionized water and KCl aqueous solution (1 mM) containing a dye are mixed in a dilution-type experiment [94].

Simulations were performed using CFD-ACE+ [94].

[P 3] Both dilution and chemical reaction techniques were used for flow visualization in [25] (see also [93]), amenable to optical techniques. In a dilution experiment, a dye dissolved in a medium is mixed with a non-dyed solution, typically the medium of the dyed solution itself. In a reacting experiment, a dye is either created or converted ('quenched') to a non-dye state. In a concrete case, fluorescein was used as dye.

For the reaction experiment, a fast acid–base reaction was applied which affects the fluorescence quantum yield of a dye by changing the pH. Fluorescein again was used [25].

A high-resolution charge-coupled device (CCD) camera records the stirring and diffusion of fluorescein from an initially non-mixed state [25]. The fluorescence intensity is integrated over measurement volumes (voxels), thereby yielding a spatial distribution of the mixing degree. The resolution was  $2.7 \times 2.7 \mu\text{m}^2$ . Ensemble-averaged probability density functions (PDFs) and power spectra of the instantaneous spatial intensity profiles were used to quantify the mixing processes. The use of PDFs was regarded as superior as it takes into account the two-dimensional standard deviation [25]; the latter can have statistical fluctuations of fluorescence intensity. Power spectra display the spectral content of the image intensity fields. Energy at high spatial frequencies equals rapid mixing, while low-frequency components of image-power spectra are associated with both unresolved stirring and well-diffused concentration fields.

[P 4] For details on the simulation, see [92].

The mixing experiments were performed using a mercury lamp-induced fluorescence method [92]. A microscope, a photomultiplier and a CCD camera were used for image monitoring. Sodium borate (10 mM) as buffer and Rhodamine B as sample were used. A gray-scale analysis was performed to obtain data on the concentration distribution.

[P 5] The electric field are generated at 1 MHz and 10 V AC voltage [48]. Different DEP domains for polystyrene particles in aqueous suspensions were investigated.

Kinematic simulations were undertaken to describe the folding of material lines and identify parameter settings which give chaotic mixing [48].

## 1.2.1.8 Typical Results

**Flow perturbation upon continuous (DC) current operation**

[M 1] [P 1] Microscopic observations of the flow were made to detect the changes induced by switching on an electric field for DC operation [91]. Initially a bi-laminated structure resulted owing to the T-junction contact. When the fluids passed the region of the adjacent electrodes, perturbations of the flow became clearly visible, i.e. the interfaces were deformed. The result was a color, i.e. species, distributed in a cross-sectional direction.

**Mixing vs. field strength for DC operation**

[M 1] [P 1] The mixing index, defined via coefficients of the electric field, increased as a function of the field strength for DC operation and then approached a plateau at about  $7 \cdot 10^5 \text{ V m}^{-1}$  [91]. As threshold value for initiation of mixing a field intensity of  $2 \cdot 10^5 \text{ V m}^{-1}$  was detected.

**Flow perturbation upon alternating (AC) current operation**

[M 1] [P 1] For AC operation, frequencies of 0.5, 10, and 100 Hz were applied [91]. As to be expected from the DC experiments and the derived relationship between the electric field and the mixing, the same holds for a non-constant electric field. The maximum action is achieved for maximum electric fields. This becomes evident when looking at the corresponding microscopy images and the deformations of the fluid interface induced (see Figure 1.10).

The dynamic changes actually lead to the formation of a pulse, which is more or less elongated depending on the frequency [91]. This pulse is followed by a hardly deformed zone so that mixed and unmixed zones are created in an alternating

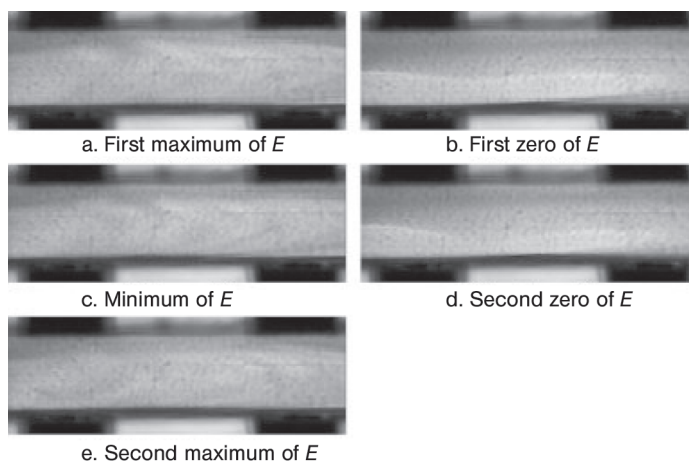


**Figure 1.10** Flow visualization by means of a dilution-type experiment after applying an AC electric field of intensity of  $4.24 \cdot 10^5 \text{ V m}^{-1}$  at a frequency of 0.5 Hz at various times corresponding to (a) first maximum, (b) first zero, (c) first minimum, (d) second zero and (e) second maximum [91] (by courtesy of RSC).

manner. It is important if the flow can fully develop or not between the pulses to achieve axial mixing or to have a more segregated fluid stream. At low frequency the flow can fully develop, whereas at high frequency it cannot.

#### Mixing vs. field strength for AC operation

[M 1] [P 1] The mixing index, defined via coefficients of the electric field, increases as a function of the field strength for AC operation in the range  $0.8\text{--}5.7 \cdot 10^5 \text{ V m}^{-1}$  [91].

#### Mixing vs. frequency for AC operation

[M 1] [P 1] The mixing index, defined via coefficients of the electric field, decreases as a function of the frequency for AC operation in the range 1–5000 Hz (see Figure 1.11) [91].

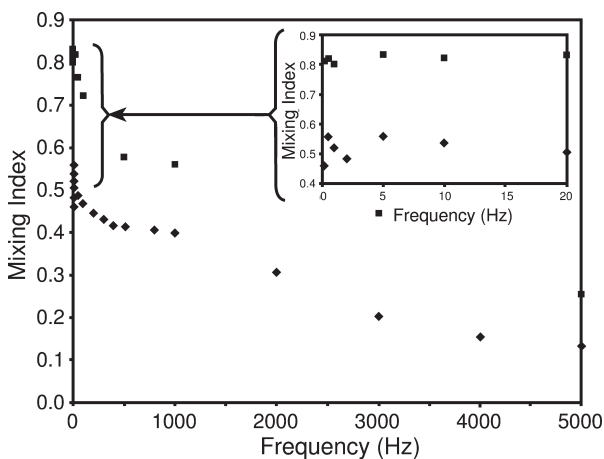


**Figure 1.11** Variation of the mixing index with the frequency for an electric field intensity of  $4.24 \cdot 10^5 \text{ V m}^{-1}$  for an AC sinusoidal (diamonds) and square (squares) electric fields [91] (by courtesy of RSC).

#### Square vs. sinusoidal waves for AC operation

[M 1] [P 1] The analysis of the dependence of the mixing index on the field strength for AC operation clearly shows that high field strengths are favorable for mixing (see *Mixing vs. frequency for AC operation* above); therefore, the use of square waves, i.e. a change between positive and negative maximum values, seems to be advisable [91]. Indeed, it could be shown by microscopy and mixing-index analysis that square waves cause superior deformations of the fluid interface as compared with sinusoidal waves (see Figure 1.11).

#### Multi-electrode operation

[M 1] [P 1] The flow was exposed to three electrode pairs instead of one, as used for all experiments described above [91]. It was shown that a successive progression of the interface deformation and thus of mixing could be achieved in this way. After

passage of the three electrode pairs the mixing seemed to be complete, as indicated by the homogeneous color texture. An advantage of using three instead of one electrode is that the same mixing effect can be achieved at lower field strength. Microscope images of the interface deformation again prove comparable effects for  $2.834 \cdot 10^5 \text{ V m}^{-1}$  applied to each of the three electrode pairs as for  $4.24 \cdot 10^5 \text{ V m}^{-1}$  in the case of one electrode pair only.

#### **Velocity field change upon electric field turning-on**

[M 2] [P 2] A numerical simulation of the velocity field after applying the electric field was made at three times, 1, 10 and 10 ms after the start of the turning-on of the field [94]. The velocity field is considerably changed on this short time scale, which usually is indicative of good mixing.

#### **Electric potential distribution change upon electric field turning-on**

[M 2] [P 2] A numerical simulation of the electrical potential distribution after applying the electric field was made at two times, 1 and 10 ms after the start of the turning-on of the field [94]. The electric potential distribution changes considerably, as does the velocity field (see *Velocity field change upon electric field turning-on* above).

#### **Mixing flow visualization**

[M 2] [P 2] Injecting a dyed and a colorless stream into the EHD mixer yields a visually homogeneous solution after passage through the mixing chamber channel with the electrodes [94].

#### **Feasibility of EKI mixing under EOF conditions**

[M 3] [P 3] Fluorescence images at various times were taken in the main channel, i.e. along the direction of the electric field, of the first-generation micro mixer [25, 93]. After a period of 2 s, the flow becomes unstable and transverse velocities stretch and fold material lines in the flow. The initial seeded/unseeded interface becomes rapidly deformed. Finally after about 13 s, a random distribution of the tracer transverse to the applied AC field is achieved. EKI action is visible throughout the whole channel length of 7 mm. Thus, feasibility of EKI action for micro mixing has been demonstrated.

#### **Improved mixing by confining the EKI region to a small chamber**

[M 4] [P 3] Full-field images of the entire mixing chamber of the improved EKI mixer device with parts of the inlet, outlet and side excitation channels were taken (see Figure 1.12). In the mixing chamber, rapid stretching and folding of the fluorescence tracer were observed [25]. Consequently, a homogeneous fluorescence texture in the outlet channel is found. The full-field images also prove that EKI in all the channels attached to the mixing chamber is small and confined to the vicinity to the chamber; hence no uncontrolled and undesired mixing takes place. The mixing time of 2.5 s is superior to the performance of the prototype device [M 3], needing about 13 s for a similar purpose (see *Feasibility of EKI mixing under EOF conditions* above).

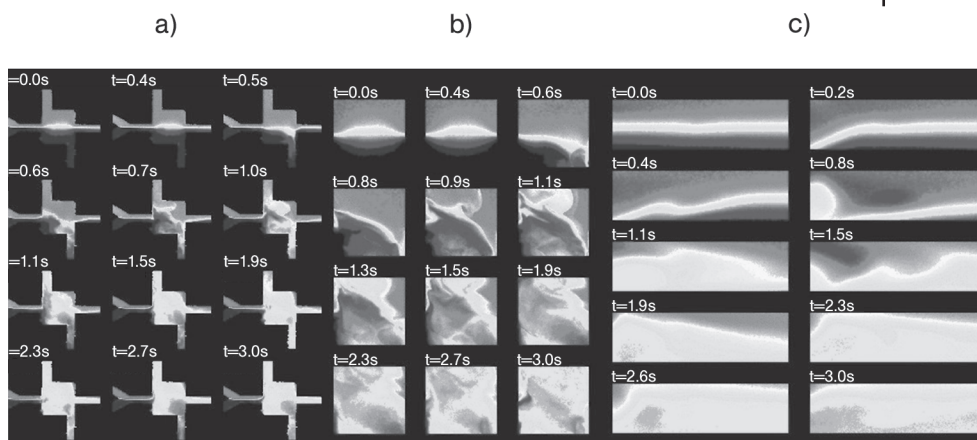


**Figure 1.12** Images obtained by a dilution-type fluorescence mixing experiment for the electrokinetic instability micro mixer, second-generation device. (a) 4× objective images of the mixing chamber with inlet, outlet and side channels. The fluid interface is disturbed when starting the AC field; mixing takes place. (b) 10× objective images of the mixing chamber. Complex fluid motions rapidly distribute the dye throughout the majority of the mixing chamber. (c) 10× objective images of the outlet channel, in close vicinity of the mixing chamber. The near-uniform intensity profile evidences the well-stirred fluid exiting the mixing chamber [25] (by courtesy of ACS).

#### Mixing time for EKI mixing under EOF conditions

[M 4] [P 3] Using the improved EKI mixer device, mixing times of about 2.5 s are obtained [25]. This was deduced from time-resolved images showing the point when a randomly distribution of a fluorescence tracer is achieved (see also *Flow perturbation upon alternating (AC) current operation* above for the lower performance of the first-generation device).

#### Flow velocities and flow range ( $Re$ ) for EKI mixing under EOF conditions

[M 4] [P 3] Using the improved EKI mixer device, bulk-averaged flow velocities in the outlet channel and in the mixing chamber were 0.5 and 0.16 mm s<sup>-1</sup>, respectively [25]. The corresponding Reynolds number ( $Re$ ) is 1.5.

#### Particle tracer experiments for EKI mixing under EOF conditions

[M 4] [P 3] 490 nm particles were used to display the fluid motions in the improved EKI mixer device [25]. Three-dimensional motions were detected. This particle trajectory demonstrates the instability of the electric field and is not expected in a stable electric field.

#### Ensemble-averaged temporal PDF evolution for EKI mixing under EOF conditions

[M 4] [P 3] The ensemble-averaged temporal evolution of voxel-averaged spatial intensity PDFs was followed in the improved EKI mixer device, both in the mixing

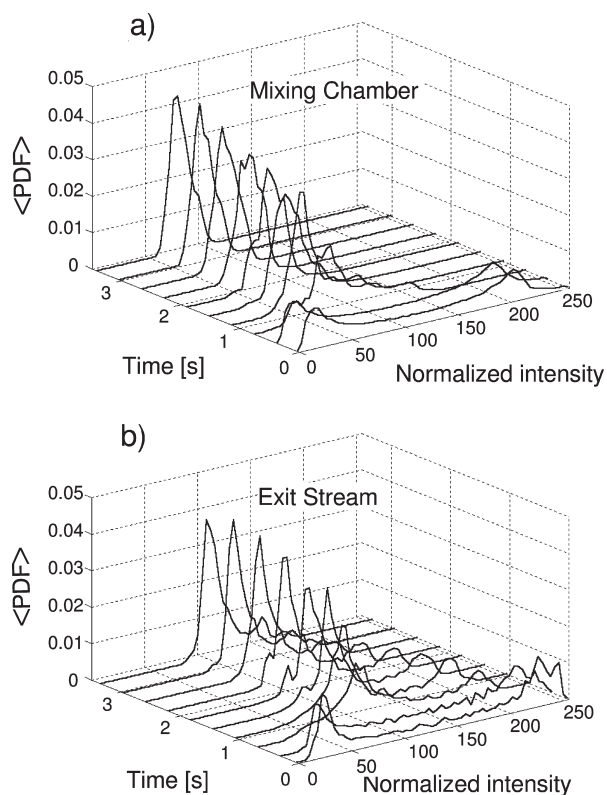


**Figure 1.13** Ensemble-averaged temporal evolution of voxel-averaged spatial intensity PDFs for the electrokinetic instability micro mixer, second-generation device. Each ensemble consists of nine realizations. The dimensions of the fluid voxels correspond to  $100\ \mu\text{m}$  depth and to about  $30\ \text{nm}$  width. (a) Mixing chamber: the initial bimodal distribution becomes unimodal upon application of the AC field; (b) exit stream: a similar behavior is observed, leaving, however, a slight bimodality [25] (by courtesy of ACS).

chamber and in the exit stream (see Figure 1.13) [25, 93]. Each ensemble consisted of nine realizations. The spatial intensity fields were further binned to  $4 \times 4$ , to produce superpixels  $100.7 \times 100.7\ \mu\text{m}^2$  in the image plane. Thus, the dimensions of the fluid voxel correspond to the channel depth of  $100\ \mu\text{m}$  and have an approximate diameter of  $30\ \mu\text{m}$ .

The initial bimodal distribution in the mixing chamber changes to a unimodal distribution after about 2.5 ms of application of the AC field [25, 93]. A similar behavior is found for the outlet channel, downstream of the mixing chamber. A slight bimodality is, however, still present, caused by an unmixed stagnant layer in the corner of the mixing chamber.

The ensemble-averaged temporal evolution of voxel-averaged spatial intensity PDFs was very reproducible from run to run [25, 93].

### Reproducibility of ensemble-averaged temporal PDF evolution, i.e. mixing, for EKI mixing under EOF conditions

[M 4] [P 3] The standard deviation of the voxel-averaged spatial intensity PDFs can be taken as a measure of the level of mixing [25]. The temporal evolution of the above-mentioned figure shows a sharp decrease in the mixing chamber after about 0.5 s of action of the AC field; thus, mixing takes place after a short induction period and being completed in a short time scale. For the flow in the outlet channel downstream of the chamber a more continuous decrease of the standard deviation is found. Error bars of the data reflect the 95% confidence intervals across the realizations and demonstrate the high degree of reproducibility of the PDF development.

### Image power spectra for EKI mixing under EOF conditions

[M 4] [P 3] Image, i.e. non-voxel averaged, power spectra complete the information given by direct imaging (see *Improved mixing by confining the EKI region to a small chamber*) or voxel-averaged spatial intensity PDF evolution (see *Reproducibility of ensemble-averaged temporal PDF evolution, i.e. mixing*) [25]. In the initial unmixed state with no AC field, the image power spectrum is characterized by a frequency band slightly elongated in the vertical direction (see Figure 1.14); this is indicative of higher spatial frequencies transverse to the interface and corresponds well to

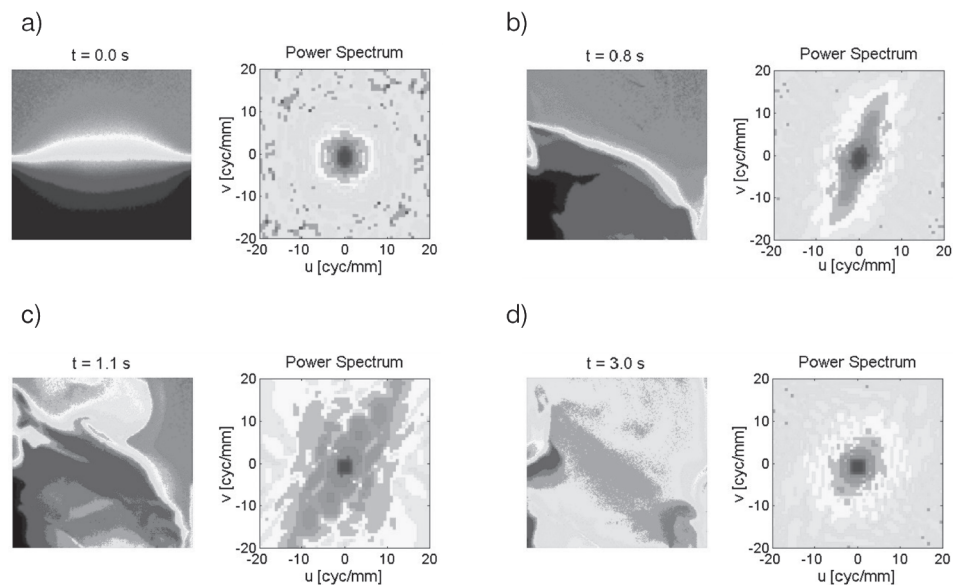


**Figure 1.14** Two-dimensional power spectra of various mixing chamber images for the electrokinetic instability micro mixer, second-generation device. (a) Large frequency components along the vertical direction owing to the initial layered distribution of the dye. (b) Larger spatial frequencies are introduced by the EKI stirring within the chamber. (c) The attenuation of large spatial frequencies corresponds to a nearly homogeneous intensity profile [25] (by courtesy of ACS).

the initial horizontal orientation of the interface, being diffused to a certain extent, however. In the state of mixing development, advective flux arises which creates high spatial frequency gradients in the power spectra. New, undiffused fluid interface lengths are generated in the flow. In the final, mixed state, these high-frequency bands are damped. The corresponding well-stirred power spectra are hence isotropic.

#### Ensemble-averaged power spectra for EKI mixing under EOF conditions

[M 4] [P 3] An analysis of the ensemble-averaged history of the voxel-averaged intensity image bandwidth completes the information given by image power spectra (see Figure 1.15 and *Image power spectra*) [25]. The intensity bandwidth starts at an intermediate value of  $3.1 \text{ cycles min}^{-1}$  (unmixed state), increases to a maximum at  $4.5 \text{ cycles min}^{-1}$ , decreases to a minimum (mixing development) and then levels off at the minimum at less than  $2.7 \text{ cycles min}^{-1}$  (mixed state). The large-magnitude, low-temporal frequency fluctuations are due to the momentary, large-scale displacements of the top and bottom regions of the mixer fluid volume into the side ports. These fluctuations are quickly damped upon increasing stirring in the chamber.

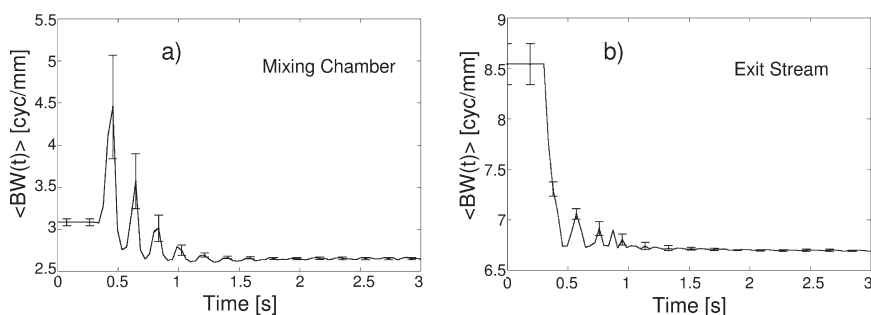


**Figure 1.15** Ensemble-averaged  $-20 \text{ dB}$  bandwidth power spectra for the electrokinetic instability micro mixer, second-generation device. (a) Mixing chamber; (b) exit stream. Error bars are shown with 95% confidence intervals. EKI stirring is immediately observed after application of the AC field at  $t = 0.4 \text{ s}$ . The initial large oscillation is indicative of large-scale fluid displacements. After  $1 \text{ s}$  of actuation, the fluid is sufficiently stirred and the bandwidth remains constant [25] (by courtesy of ACS).

#### Heat generation during EKI for EKI mixing under EOF conditions

[M 4] [P 3] Temperature differences of  $5\text{--}10 \text{ }^\circ\text{C}$  result by the action of the AC field owing to Joule heating for the  $3 \text{ s}$  duration of the pulse [25]. The data were gathered from both thermocouple measurements and capacitance-based heat transfer analysis.

#### Comparison of electrokinetic (EKI) with electrohydrodynamic (EHD) instability

[M 4] [P 3] The EHD instability is usually observed for fluids with electrical conductivities at least  $2\text{--}3$  orders of magnitude lower than for the EKI instability mixing [25].

#### **Applicability of EKI mixing with regard to construction material and media**

[M 4] [P 3] EKI mixing was demonstrated for mixers made of polymer materials such as PDMS or PMMA and of glass [25]. Processing with various electrolytes could be successfully applied, including deionized water and borate and HEPES buffers, with electrical conductivities ranging from 5 to 250  $\mu\text{S cm}^{-1}$ .

#### **Flow patterns and concentration profiles for mixing by zeta potential variation**

[M 5] [P 4] Images of the distribution of a fluorescent species were monitored experimentally and calculated numerically within and behind the mixing section (1/6 Hz, 300 V for electroosmotic flow, 800 V to the electrodes) [92]. Starting from an initial bi-laminating pattern, a transverse movement of the species is detectable and a homogeneous fluorescent texture is observed behind the mixing section.

Concentration profiles were derived by gray-scale analysis from the images mentioned above [92]. Whereas without use of zeta potential variation no difference in concentration profiles between the upstream and downstream positions is visible, a much more flattened, i.e. mixed, profile results under electrokinetically driven conditions in the downstream position.

#### **Impact of control potential, EOF field and frequency for the zeta potential variation**

[M 5] [P 4] With increasing applied control voltage increased mixing efficiency is achieved (0–700 V) [92]. At about 600 V, a plateau is achieved.

Mixing performance is decreased with higher EOF driven field shows decreasing as a consequence of the shorter residence times [92]. The higher the frequency, the lower is the mixing performance [92]. A threshold value at about 1/8 Hz is found.

#### **Simulation of material line folding**

[M 6] [P 5] The folding and stretching of material lines when entering a cavity with electrodes and thus exposure to a non-uniform electric field were investigated [48]. At small amplitude only weak oscillations of the material lines along the channel are found. In contrast, all particles are trapped around the electrodes at large amplitude. At medium amplitude, the desired folding and stretching occur, resulting in enhancement of mixing.

#### **Particle motion owing to the electric field**

[M 6] [P 5] The particles are trapped at the edges of the electrodes, align with field lines and form pearl chains at a frequency of 100 kHz [48]. At a frequency of 10 MHz, particles are repelled from the edges of the electrodes towards the field gradient minima.

#### **Imaging of particle motion**

[M 6] [P 5] At zero electric field, a bi-laminated system with straight interface can be seen for contacting deionized water and a particle solution (see Figure 1.16) [48]. After switching on of the electric field, folding and stretching takes place.

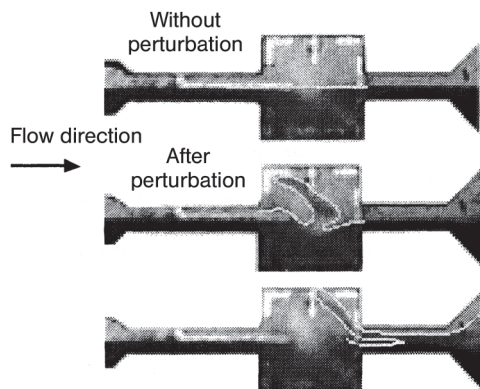


**Figure 1.16** Imaging of the folding and stretching of particle lines when an electrokinetic perturbation is applied. The bright line indicates the interface between the particle solution and pure water [48] (by courtesy of Springer-Verlag).

### 1.2.2

#### Electro Rotational Mixing

##### Most Relevant Citations

Peer-reviewed journals: [95].

Objects having a dipole can be set into rotational motion by applying a torque by means of an electric field [95]. Electrorotation is the rotation of particles as a consequence of the induction of dipole moments and torque exertion by a rotating electric field. Coupled electrorotation (CER) uses static external fields which are spatially fixed to induce dipoles in two or more adjacent particles. This creates oscillating components of the electric field, finally resulting in a rotating electric field (for more details, refer to the original literature [95]).

If one of the objects cannot rotate, e.g. because it is fixed in space, CER still can induce rotation of the other object [95]. That is the basis for the mixing principle presented here. A microsphere is positioned nearby a (fixed) microstructure, typically of the same or similar material. By application of an electric field, the above-mentioned interaction takes place and the microsphere rotates.

##### 1.2.2.1 Mixer 7 [M 7]: Coupled Electrorotation Micro Mixer

This coupled electrorotation mixer was actually not built as a complete device, but realized as a prototype version with simple microstructures, which were made by sputtering on to glass cover slips [95]. By photolithography a small gap was etched in the middle of the coated slip to separate it into two equal halves. The latter are used as two electrodes of equal size. A wedge, freshly cut from the corner of a raw material piece, is placed on the gap as a kind of fixed microstructure to perform as the static ‘dipole object’ so that an adjacent microsphere can be set into rotation.

Mixer type	Coupled electro-rotation micro mixer	Electrode layer thickness	~100 nm
Mixer base material	Glass cover slip	Gap separating the electrodes	10 $\mu\text{m}$
Cover slip size	24 mm $\times$ 60 mm	Wedge material	PDMS
Sputtered electrode material	Gold	Microsphere material	Polybead carboxylate microspheres

### 1.2.2.2 Mixing Characterization Protocols/Simulation

[P 6] A ~50  $\mu\text{l}$  droplet with 2  $\mu\text{m}$  latex spheres suspended in water was spread over both electrodes on to the chip. The mixing was followed by a microscope with an oil immersion objective [95]. Evaporation of the droplet solution has to be minimized, as this notably affects the electroration.

The radiofrequency output from a function generator was coupled directly to the electrodes on the chip [95]. Wires are attached to electrodes using a conductive epoxy. A 500 kHz electric field sine wave (60  $\text{kV cm}^{-1}$ ) was applied.

Mixing was visualized by additional fluorescent 500 nm tracer particles (yellow-green carboxylate FluoSpheres), marking by their tracer trajectories the flow pattern [95].

### 1.2.2.3 Typical Results

#### Tracer trajectories giving the flow field around a rotating microsphere

[M 7] [P 6] By coupled electroration of a microsphere local circulation of the surrounding liquid can be induced, as proven by the trajectories of fluorescent particle tracers around the (larger) rotating microsphere [95]. Hence the mixing effect was shown qualitatively. No details on quantitative results such as mixing time were given.

#### Some thoughts on future applications of rotating microspheres

[M 7] [P 6] The fact that probably efficient mixing in the close vicinity of the sphere can be induced (see *Tracer trajectories giving the flow field around a rotating microsphere* above) suggests its use for mixing in real miniature fluid compartments, e.g. with characteristic diameter below 1  $\mu\text{m}$ , which hardly can be mixed by other means [95]. No physical contact is then required, unlike other types of miniature rotating actors. The mixer itself, i.e. the microsphere, does not need to be microfabricated, but can be purchased commercially. Mixing can be switched on and off, unlike for static fluid mixing. Positioning of the microsphere is easily achieved to have control over the region which is exposed to mixing.

### 1.2.3

#### Chaotic Electroosmotic Stirring Mixing

#### Most Relevant Citations

Peer-reviewed journals: [28].

When electroosmotic flows in micro channels are superimposed by temporal modulation of non-uniform  $\zeta$  potentials along the conduits' walls, it is possible to induce chaotic advection which can lead to mixing by stirring-analogue material transport [28]. Non-uniform  $\zeta$  potentials can be obtained by coating the channel's walls with different materials or by using different buffer solutions. Both spatial and temporal control of the  $\zeta$  potential can be achieved by imposing an electric field perpendicular to the solid-liquid interface. In practice, the generation of such normal electric fields can be accomplished by placing electrodes beneath the solid-liquid interface, provided that these electrodes are insulated from the liquid. Alternatively, photosensitive surfaces can be surface charged with light.

In the following, the use of periodical  $\zeta$  potentials will be described; the periodicity will be denoted  $T$  [28]. Switching between two or more flow patterns is performed inducing chaotic advection. One flow field is maintained in one time interval and another flow field in a second interval. This is repeated with the period  $T$ . The switching of the flow fields is accomplished by controlling the distribution of the  $\zeta$  potential created by the electrodes. By flow field alternation, particles virtually expose a zig-zag path, thereby distributing material all over the channel's cross-section. Such transport is similar to efficient stirring.

#### 1.2.3.1 Mixer 8 [M 8]: Chaotic Electroosmotic Micro Mixer

This chaotic electroosmotic micro mixer has not been realized so far; only a theoretical study on the principle of the device was made [28]. A schematic was given which can serve as base for the future realization of such a device (see Figure 1.17).

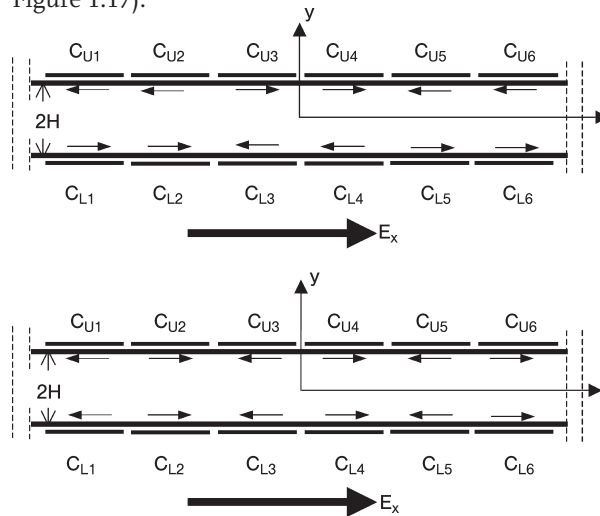


**Figure 1.17** Schematic of a micro channel equipped with many electrodes at the upper ( $U_i$ ) and lower ( $L_i$ ) walls for control of the  $\zeta$  potential. The arrows in the channel denote the directions of the electroosmotic velocities creating one type of flow pattern, here a counter-current arrangement of top and bottom flows (top); alternating-flow arrangement, demonstrating another type of control over the  $\zeta$  potential (bottom) [28] (by courtesy of ACS).

A micro channel of height  $2H$  is equipped with electrodes at the upper ( $U_i$ ) and lower ( $L_i$ ) walls [28]. These electrodes are used to control the  $\zeta$  potential at the solid–liquid interface. In this way, the direction of the electroosmotic flow near the interface can be changed locally. The external electric field is given as  $E_x$ .

### 1.2.3.2 Mixing Characterization Protocols/Simulation

[P 7] The topic has only been treated theoretically so far [28]. A mathematical model was set up; slip boundary conditions were used and the Navier–Stokes equation was solved to obtain two-dimensional electroosmotic flows for various distributions of the  $\zeta$  potential. The flow field was determined analytically using a Fourier series to allow one tracking of passive tracer particles for flow visualization. It was chosen to study the asymptotic behavior of the series' components to overcome the limits of Fourier series with regard to slow convergence. In this way, with only a few terms highly accurate solutions are yielded. Then, alternation between two flow fields is used to induce chaotic advection. This is achieved by periodic alteration of the electrodes' potentials.

### 1.2.3.3 Typical Results

#### Time-independent electroosmotic flows

[M 8] [P 7] Flow fields were analyzed for time-independent electroosmotic flows at a variety of  $\zeta$  potential distributions (see Figure 1.18) [28]. The four basic flow structures  $\Psi_{EO}$ ,  $\Psi_{EE}$ ,  $\Psi_{OO}$  and  $\Psi_{OE}$  are given in [28].  $\Psi$  denotes a stream function and the subscripts  $EO$ ,  $EE$ ,  $OO$ , and  $OE$  denote, respectively, even in  $X$  and odd in  $Y$ , even in  $X$  and even in  $Y$ , odd in  $X$  and odd in  $Y$ , and odd in  $X$  and even in  $Y$ .  $U^+$ ,  $U^-$ , and  $U^\pm$  are dimensionless slip velocities and provide the following boundary conditions:

- (a)  $U^\pm(X) = -U^\mp(X) = 1$ ;
- (b)  $U^+(X) = -U^-(X) = 1$ ;
- (c)  $U^\pm(X) = -U^\pm(-X)$ ,  $U^+(X) = -U^-(X) = 1$ ;
- (d)  $U^+(X) = -U^+(-X) = 1$ ;  $U^\pm(X) = -U^\pm(-X)$ ,  $U^+(X) = U^-(-X)$  and  $U^-(X) = -U^+(-X) = 1$ .

where  $X$  and  $Y$  are the longitudinal and transverse dimensions in the channel.

For case (a), the flow field consists of a single convective cell which circulates around an elliptic point (center) located at  $X = Y = 0$  [28]. For case (b) the flow field consists of two counter-rotating cells with centers at  $X = 0$  and  $Y = \pm 0.58$ . The cells are separated by the surface  $Y = 0$ . For case (c), the flow field is similar to (b) in the sense that the flow field consists of two counter-rotating cells separated by the surface at  $X = 0$ . The centers of rotation are at  $X = \pm 1$  and  $Y = 0$ . For case (d), the flow field consists of four counter-rotating cells separated by two surfaces at  $X = 0$  and  $Y = 0$ .

Thus, complex flow patterns can be generated for non-uniform distributions of the  $\zeta$  potential in a time-independent manner [28]. However, the flow is highly regular and no transport transverse to the streamlines is given. Particles will only follow the streamlines which does not give as good mixing as the action of stirring.

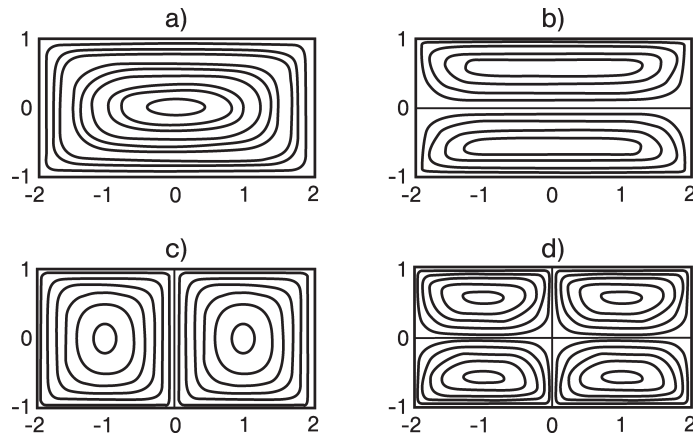


**Figure 1.18** Streamline patterns for various electroosmotic flows when  $h = 2$  ( $h$  being the periodicity of arranging the electrodes). (a)  $U^{\pm}(X) = -U^{\mp}(X) = 1$ ; (b)  $U^+(X) = -U^-(X) = 1$ ; (c)  $U^{\pm}(X) = -U^{\pm}(-X)$ ,  $U^+(X) = -U^-(X) = 1$ , (d)  $U^+(X) = -U^+(-X) = 1$ ;  $U^{\pm}(X) = -U^{\pm}(-X)$ ,  $U^+(X) = U^+(-X)$  and  $U^+(X) = -U^+(-X) = 1$  [28] (by courtesy of ACS).

#### Time-dependent electroosmotic flows – chaotic advection

[M 8] [P 7] The effect of switching between the flow fields (a) and (d) given in Figure 1.18 at various periods  $T$  was analyzed (see Figure 1.19) [28]. For very high alterations, a simple superposition of the flow fields is achieved. Elliptic fixed points surrounded by closed orbits (tori) of various periods are found.

For larger  $T$  ( $T = 1.6$ ), chaotic behavior arises, the hyperbolic fixed point is disrupted and the tori are perturbed (see Figure 1.20) [28]. A chaotic region appears with homoclinic tangle and formation of new hyperbolic and elliptic points.

On further increasing  $T$  to 2, 4 and 6, the complexity of the flow becomes more pronounced (see Figure 1.21) [28]. First, the particles wander around the superimposed image. Then, particles stray further away from the ‘regular path’ and sample most of the cell’s area. Chaotic advection is now present.

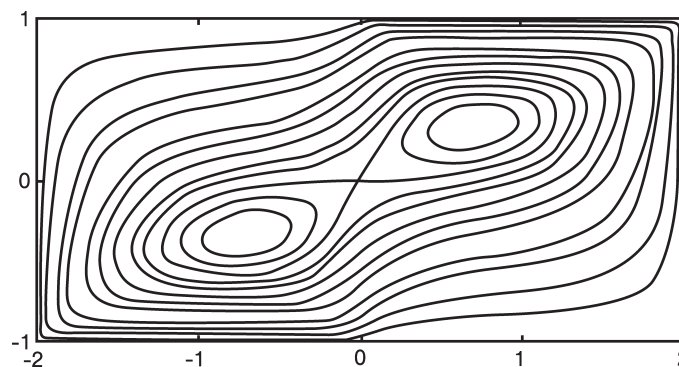


**Figure 1.19** Streamline pattern for the superimposed flow structure, by switching between the flows (a) and (d) given in Figure 1.18, for  $h = 2$  [28] (by courtesy of ACS).

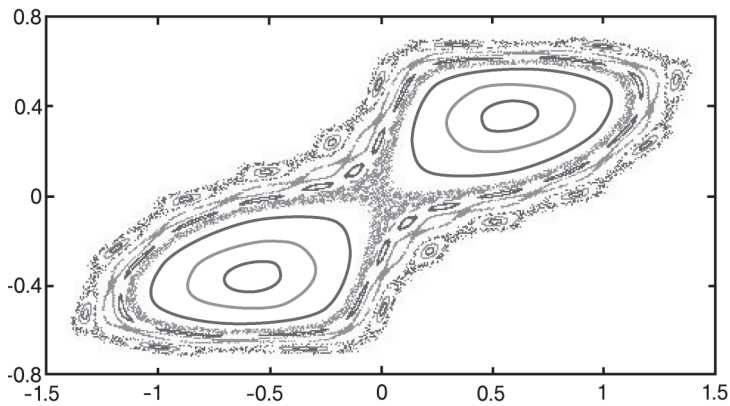


**Figure 1.20** Pointcaré section when  $T = 1.6$  and  $h = 2$ . Passive tracer particles were placed at selected places, given in [28] (by courtesy of ACS).

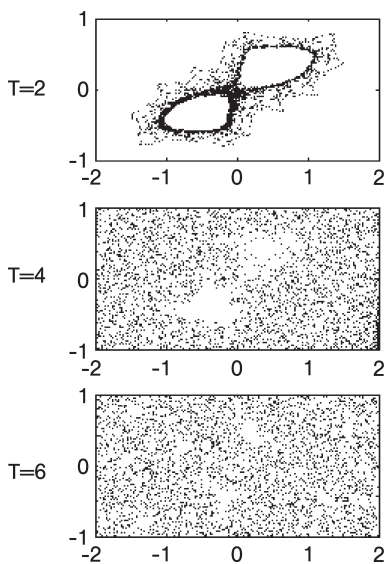


**Figure 1.21** Pointcaré sections for various periods  $T = 2, 4$  and  $6$  and  $h = 2$ . A passive tracer particle was initially inserted at  $(x_0, y_0) = (0, 0.01)$ , and its motions were followed by 3000 periods [28] (by courtesy of ACS).

#### Deformation of a blob by chaotic advection – simulation of a stirring process

[M 8] [P 7] In order to simulate a stirring process, a square material blob is placed in the center of the channel (see Figure 1.22) [28]. This is equivalent to inserting a drop of a dye in the channel. Rapid stretching and folding processes, characteristic of chaotic advection, arise on periodically switching between flow fields. Eventually, the blob is spread over the entire cell's area. Hence efficient stirring is given.

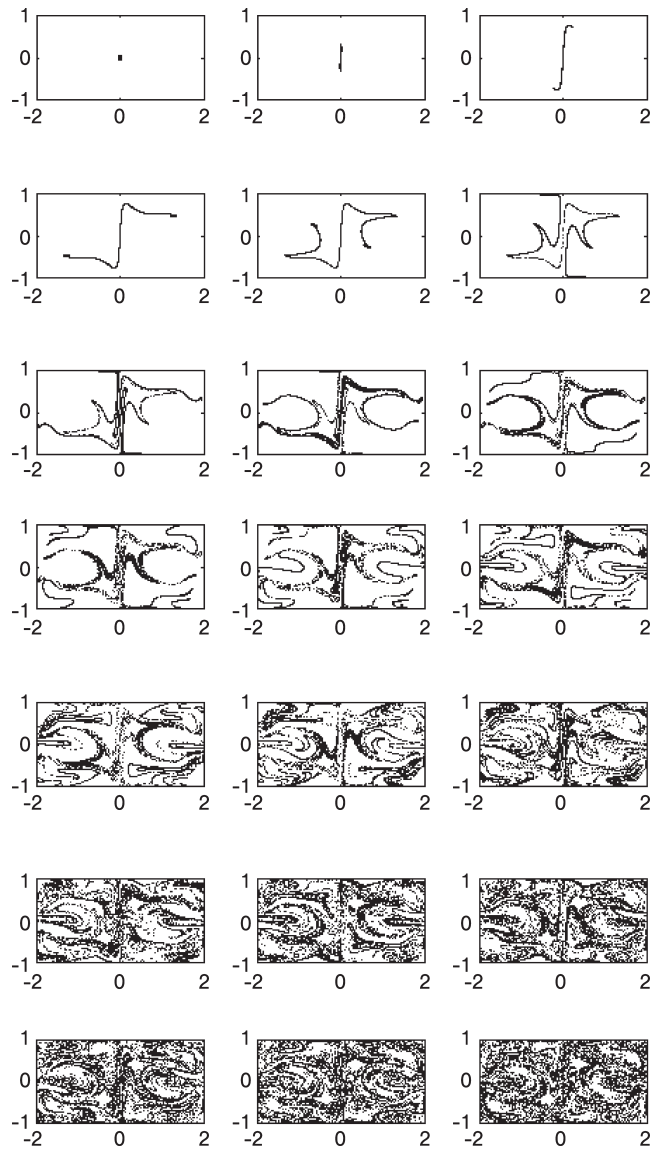


**Figure 1.22** Deformation of a blob with an initial edge of 0.1. Initially ( $t = 0$ ) centered at  $(0,0)$ .  $T = 4$ .  $t/T = 0, 1, \dots, 17$  [28] (by courtesy of ACS).

#### Variation of the number of electrodes

[M 8] [P 7] The above-mentioned simulations were made with two electrodes each on the top and bottom of the walls [28]. When using four embedded electrodes, even more complex flow fields are achieved, which are in parts similar to those generated by switching with two electrodes. Superimposed fields are found and also chaotic patterns.

## 1.2.4

**Magnetohydrodynamic Mixing****Most Relevant Citations**

Peer-reviewed journals: [96].

The above-mentioned examples have proven the suitability of using electric fields generated by electrode arrays for mixing of liquids. In the following example, a micro channel is also equipped with an array of electrodes which can generate a complex electric field [96]. By alternate potential differences, currents are induced in various directions. This electric field can be coupled to a magnetic field yielding Lorentz body forces for fluid mixing. In this way, cellular motion is achieved which stretches and deforms material lines.

**1.2.4.1 Mixer 9 [M 9]: Magnetohydrodynamic Micro Mixer**

This device consists of a rectangular channel which contains uniformly spaced electrodes, transversely oriented to the flow direction (see Figure 1.23) [96]. The electrodes are connected to the positive and negative poles of a DC power supply. The direction of the electric current varies from one location to another. A uniform magnetic field normal to the channel bottom is applied. By coupling of the electric and the magnetic forces, a Lorentz body force is yielded which is perpendicular to the electric and magnetic fields and directed towards the side walls. The direction of this force also alternates. As a result, the fluid is moved up- and downwards. The net effect is eddy-type convection.

The device was built from a bottom plate with a five-electrode structure, five plates which altogether form a rectangular mixing chamber, and a cover plate [96]. All plates contain vertical vias for electrical connection. The plates were realized as ceramic green tapes which a fired to a solid stack in the following way.

Thin green tapes are cast and microstructured by milling. Alternatively, laser machining or photolithography may be applied [96]. Rectangles of the desired size were blanked from these tapes. According to the information given above,

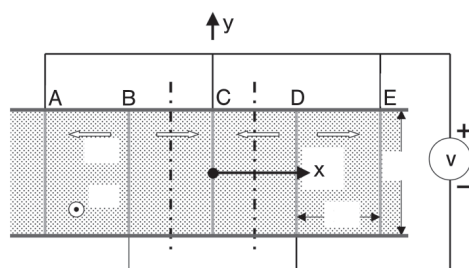


**Figure 1.23** Schematic of the top view of the magnetohydrodynamic mixer. The electrodes are denoted A–E. The electrodes are connected to positive and negative poles of a power supply in an alternate manner. The x-direction corresponds to the long axis of the mixing chamber. The magnetic field is normal to the figure's plane [96] (by courtesy of Elsevier Ltd.).

seven tapes were fired. By firing, the organic material was removed and sintering took place, leaving a solid body. If needed, many more tapes (> 80) can be stacked together and co-fired to yield even more complex assemblies with channels and electrodes. Transparent windows can also be attached to allow inspection of the flow. Metal paths were hand-printed to form electrodes. Three electrodes were connected to a single conductor and two to a second conductor.

A permanent magnet was placed below the mixer [96]. The size of the magnet was chosen to be much larger than the mixer internals to result in a homogeneous magnetic field.

Mixer type	Magneto-hydrodynamic micro mixer	Gold electrode paste material	DuPont 5734
Mixer material	LTCC 951AT	Paste filler for vias	DuPont 6141
Tape thickness	~250 $\mu\text{m}$	Soldering pad material	DuPont 6146
Mixing chamber width, length, depth	4.7 mm, 22.3 mm, 1 mm	Magnet material	Neodymium
Electrode depth, width, distance	20 $\mu\text{m}$ , 700 $\mu\text{m}$ , 3.3 mm	Magnet load capacity	12–15 lb

#### 1.2.4.2 Mixing Characterization Protocols/Simulation

[P 8] The resistance between the electrodes was measured in situ. The power supply was operated in constant-voltage mode [96]. A low-volume tracer was injected with a syringe and then applied a voltage of 4 V across the channel. The current was of the order of  $\mu\text{A}$  and was below the resolution level of the power supply (10 mA).

Details on the simulations based on the Navier–Stokes equation with a body force are given in [96].

#### 1.2.4.3 Typical Results

##### Simulation of circular motions

[M 9] [P 8] Simulations show that magnetic forces induce circular motion within the liquid [96]. This is shown by several findings, e.g. by a streamline analysis, a plot of the velocity versus dimensions of the channel, constant pressure contour lines and the pressure distribution.

##### Simulation of interface stretching

[M 9] [P 8] Simulations predict the extent to which and by which pattern the interfaces are stretched, which is a qualitative measure of mixing efficiency (see Figure 1.24) [96]. The evolution of the interface is given as a function of the dimensionless time. An initial bi-layered system forms a vortex-type structure with increasing spiral winding upon time.

A quantitative analysis shows that the interface increases slightly faster than a linear function of time [96]. This is better than for having diffusion only, but is behind the performance of chaotic advection.

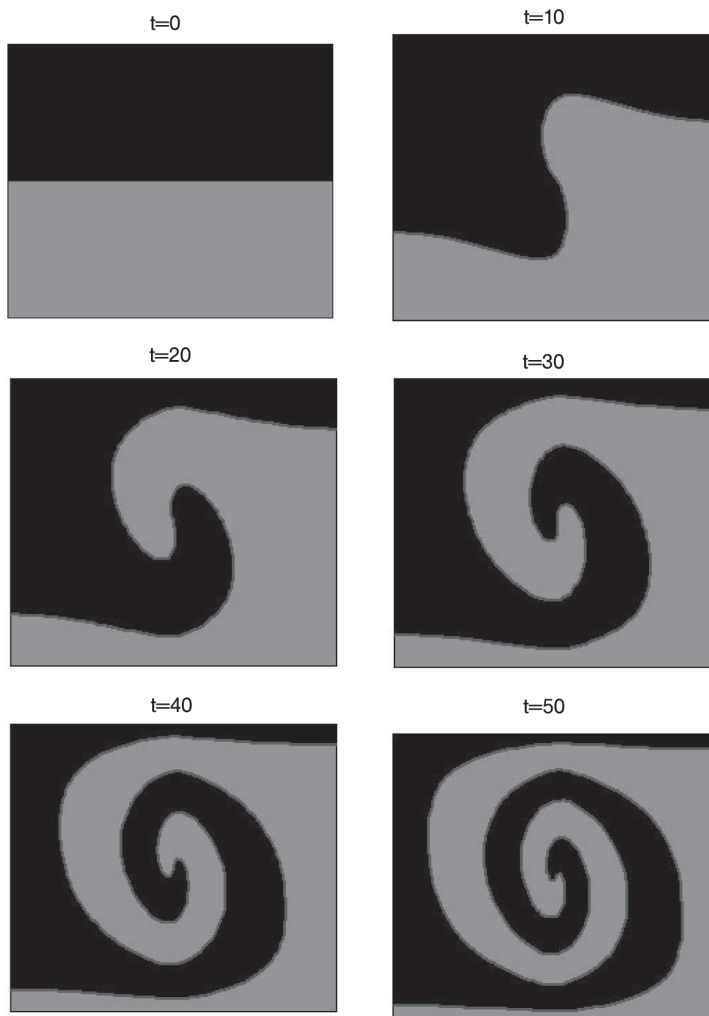


**Figure 1.24** Evolution of the flow pattern and corresponding interface stretching as a function of dimensionless time [96] (by courtesy of Elsevier Ltd.).

#### Experimental flow observation

[M 9] [P 8] Owing to the DC potential difference, visible flow was clearly induced for a water-filled chamber with a central dyed line by magnetohydrodynamic action [96]. Upwards and downwards fluid motion in a rotating fashion was observed.

#### Reversal of electrode polarity

[M 9] [P 8] After reversal of the polarity of the electrodes, a formerly deformed dyed line remains to the original state, a straight line and finally reaches a mirror-imaged deformed dyed line (see Figure 1.25) [96]. After some time, the dye is fairly homogeneously distributed over the mixing chamber.

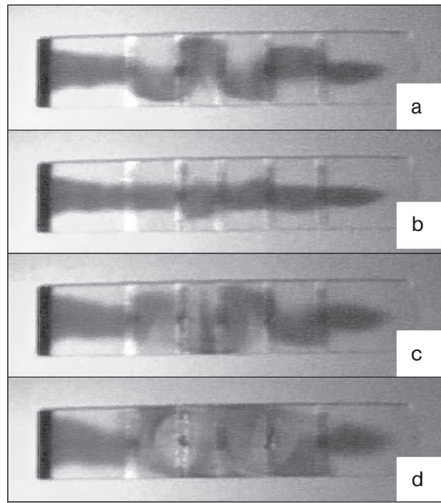


**Figure 1.25** Dye mixing visualization experiments starting from a water-filled mixing chamber with a central dyed line. (a) Initial deformation of the dyed line by action of the Lorentz force; (b) change of electrode polarity leads to deformation of the dyed line which returns to the original state, the straight dyed line; (c) deformation mirror-imaged to (a) by continuing action of the Lorentz force after change of electrode polarity; (d) eddy formation becomes apparent on continuing the Lorentz-force action given in (d) [96] (by courtesy of Elsevier Ltd.).

#### Experimental and computed mixing time

[M 9] [P 8] Experimental and simulated times were compared for the movement of a tracer from one location to another [96]. Only dimensionless times were given. The computed times were smaller than the experimentally found values. This may be due, for example, to incorrect estimation of the magnetic field strength.

#### 1.2.5

##### Air-bubble Induced Acoustic Mixing

#### Most Relevant Citations

Peer-reviewed journals: [23, 24].

An air bubble in a liquid medium can act as actuator, i.e. the bubble surface behaves like a vibrating membrane, when it is energized by an acoustic field [23, 24]. This bubble actuation is largely determined by the bubble resonance characteristics (for more details hitherto, see [23, 24]). Bubble vibration due to a sound field induces friction forces at the air/liquid interface which cause a bulk fluid flow around the air bubble, termed *cavitation microstreaming* or *acoustic microstreaming*. Circulatory flows lead to global convection flows with a ‘tornado’-type pattern which enhances mixing. At low driving amplitudes, the insonation frequency has to meet the resonance frequency for pulsation. The bubble then has to be fixed at a solid boundary. The frequency of acoustic microstreaming is, as expected, strongly dependent on the bubble radius and vice versa.

Acoustic microstreaming is a method of mixing fluids in micro chambers having a certain, relatively large internal volume [23, 24]. Typically, mixing in such volumes solely by the aid of diffusion would require several hours' mixing time. A special design with micromachined air pockets was made to entrap air bubbles. By use of a commercially available piezoelectric (PZT) disk, fluid motion can be generated which leads to mixing. In this way, the mixing time can be reduced from hours to a few seconds.

#### 1.2.5.1 Mixer 10 [M 10]: Acoustic Microstreaming Micro Mixer, Version 1

This micro device consists of a round or square micro chamber machined in a bottom plate sealed by a cover slip with double-sided adhesive tape [23]. Sound irradiation was achieved by a PZT disk below. The PZT disk was bonded by super glue to the surface of the micro chamber. The PZT disk was driven by an HP functional generator

The micro chamber was fabricated using a milling machine [23].

The device [M 10] was fabricated in three versions, differing in the number of air pockets [23].

- Version (a): one bubble only held in a conduit, situated at the chamber boundary, adjacent to the inlets; round micro chamber.
- Version (b): four bubbles, or air pockets, placed symmetrically at the arc of the circle; round micro chamber.
- Version (c): multiple ( $4 \times 4$  array) bubbles, or air pockets, placed as a symmetric matrix all above the micro chamber; square micro chamber.

Mixer type	Acoustic micro-streaming micro mixer, version 1	Mixing chamber, version (c): width, length, depth	12 mm, 15 mm, 125 $\mu$ m
Base plate material	Polycarbonate	Air pockets version (b): depth, diameter	2 mm, 300 $\mu$ m
Cover slip	Polycarbonate	Air pockets version (c): depth, diameter	500 $\mu$ m, 500 $\mu$ m
Thickness of adhesive tape	125 $\mu$ m	PZT disk: diameter	15 mm
Mixing chambers, version (a) + (b): diameter, depth	15 mm, 300 $\mu$ m		

#### 1.2.5.2 Mixer 11 [M 11]: Acoustic Microstreaming Micro Mixer, Version 2

This micro device consists of a square micro chamber which has as a bottom plate a conventional DNA micro-array chip sealed by a cover slip with double-sided adhesive tape (see Figure 1.26) [24]. The adhesive tape serves as a spacing gasket to define the shape and dimensions of the chamber. The cover slip contains the air pockets with a uniform, pitched distribution. The air pockets trap the air bubbles

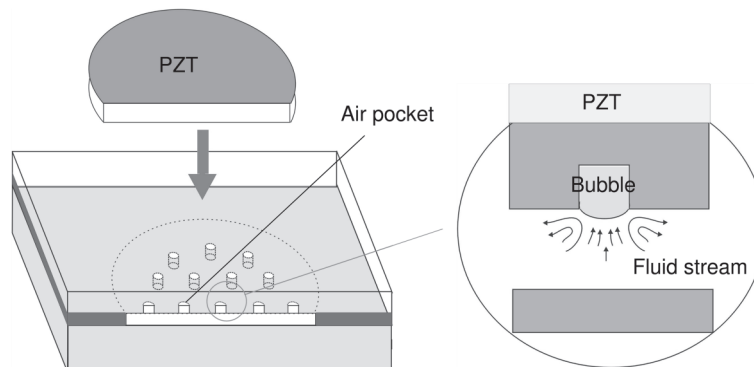


**Figure 1.26** Schematic of a cover slip with an array of air pockets sealed to a DNA biochip chamber by adhesive tape. (a) Overview; (b) detail with side view of one air pocket [23] (by courtesy of RSC).

in the reaction solution. A PZT disk was bonded on the cover slip using super glue.

The air pockets were fabricated using a milling machine [24].

The sound was generated by the PZT disk driven by an HP functional generator [24].

Mixer type	Acoustic micro-streaming micro mixer, version 2	Mixing chamber: width, length, depth	16 mm, 16 mm, 200 $\mu\text{m}$
Microarray material	Glass	Air pockets: depth, diameter	500 $\mu\text{m}$ , 500 $\mu\text{m}$
Cover slip	Polycarbonate	PZT disk: diameter	15 mm
Thickness of adhesive tape	200 $\mu\text{m}$		

### 1.2.5.3 Mixer 12 [M 12]: Design Case Studies for Micro Chambers of Acoustic Microstreaming Micro Mixer, Version 2

Three artificial micro chambers were proposed for the simulations, described under [P 11] [23]. They comprised mixing chambers with one bubble pocket in the center (a), four bubble pockets at the corners (b), and five air pockets with four at the corners and one in the center (c).

#### 1.2.5.3 Mixing Characterization Protocols/Simulation

[P 9] Visual observations were made using a stereoscope [23]. Half of the chamber was filled with deionized water and the other with an aqueous solution composed of the dye phenolphthalein and sodium hydroxide, giving a red color. A sinusoidal wave of 2 kHz frequency with a peak-to-peak amplitude of 5 V was used for device types [M 10] (a) and (b). A sinusoidal wave of 5 kHz frequency with a peak-to-peak amplitude of 5 V was used for device type [M 10] (b).

[P 10] All conditions being the same as for [P 9]; only a square wave with 5 kHz frequency with a peak-to-peak amplitude of 40 V was used [24].

[P 11] Simulations were carried with a simplified chamber and air-bubble pocket geometry. Details on this geometry and the several assumptions taken for describing the fluid dynamics can be found in [23] and are not described further here. Generally, the experimental known fluid dynamic features were taken into account, e.g. the convective motion based on vortices was assumed also in the model.

#### 1.2.5.4 Typical Results

##### Sonic irradiation without air bubbles

[M 11] [P 9] Sonic irradiation without the use of air bubbles causes only little fluid motion [23, 24].

##### Induction time

[M 12] [P 11] A certain induction time was found for artificial bubble configurations in a micro chamber [23]. This period was 10 wall motion cycles or 100 time steps.

##### Flow visualization for acoustic microstreaming

[M 10] [M 11] [P 9] [P 10] Sonic irradiation with the use of air bubbles caused considerable gross fluid motion for a dye solution [23, 24]. Owing to the uniform distribution of the air pockets, mixing is induced in the complete micro chamber and not localized to one part only.

When starting the PZT, single microstreaming fields around the bubbles are generated and interact with each other [23, 24]. At the gas/liquid interface churning motion was observed, inducing a convection streaming with a ‘tornado’-like pattern. A narrow stream occurs which moves rapidly towards the bubble surface (see Figure 1.27). In the close vicinity of the bubble, the stream velocity is decreased and the stream spreads into the liquid bulk.

[M 10a] [P 9] In a round micro chamber with one bubble only held at a small conduit, the streaming field is composed of orderly patterns with a symmetry about an axis perpendicular to the solid wall through the center of the bubble [23]. Fluidic

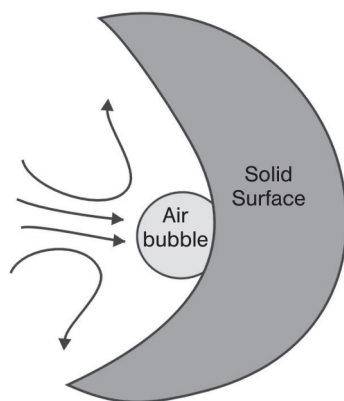


**Figure 1.27** Schematic of flow patterns, being part of acoustic microstreaming, induced by an air bubble resting on a solid wall and actuated by a piezoelectric disk [23] (by courtesy of RSC).

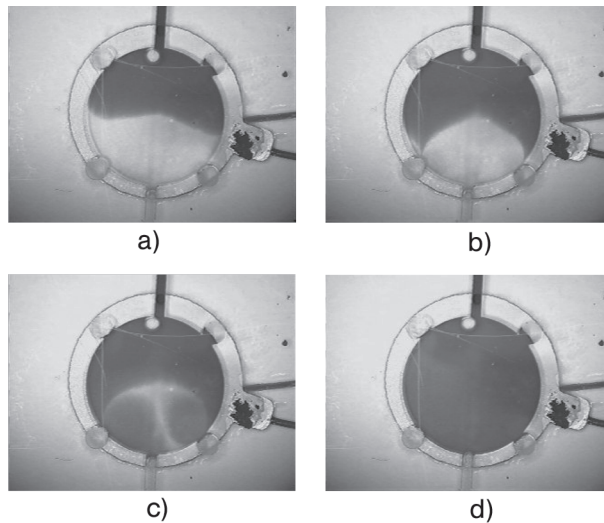


**Figure 1.28** Photographs showing acoustic microstreaming in a micro chamber (with  $300\ \mu\text{m}$  depth and  $15\ \text{mm}$  diameter) which has four air pockets ( $300\ \mu\text{m}$  depth and  $2\ \text{mm}$  diameter) at time (a) 0, (b) 10, (c) 25 and (d) 45 s [23] (by courtesy of RSC).

elements move towards the center of the bubble towards this axis. Here, also the above-mentioned spreading of the stream is observed, when approaching the bubble. The maximum speed of these streams was estimated to be  $\sim 5\ \text{mm s}^{-1}$ .

[M 10b][P 9] In a round micro chamber with four bubbles held in four air pockets, notable gross liquid motion and orderly vortex-like patterns near the bubbles were seen (see Figure 1.28) [23]. Churning motion was also present.

[M 10c][P 11][P 9][P 10] In multiple-bubble micro chambers, even tighter control of fluid motion and mixing is feasible [23, 24]. The microstreaming fields around each bubble interfere with the other. The dye is moved from one side of the chamber to the other.

#### Mixing time

[M 10a][P 9] By one-bubble microstreaming mixing, the dye completely fills the micro chamber within about 110 s [23].

[M 10b][P 9] By four-bubble microstreaming mixing, the dye completely fills the micro chamber within about 45 s [23]. This is an improvement in mixing time of about 40% compared with the [M 10a] device with one bubble only.

[M 10c][P 9] By multiple-bubble microstreaming mixing, the dye completely fills the micro chamber within about 105 s (5 kHz; 5 V) [23]. Mixing based on pure diffusion in the same volume would have taken about 6 h.

[M 11][P 9] Increasing the peak-to-peak amplitude further enhances mixing. By multiple-bubble microstreaming mixing at 5 kHz and 40 V, the dye completely fills the micro chamber within about 6 s (see Figure 1.29) [24]. Mixing based on pure diffusion in the same volume would have taken about 8 h.

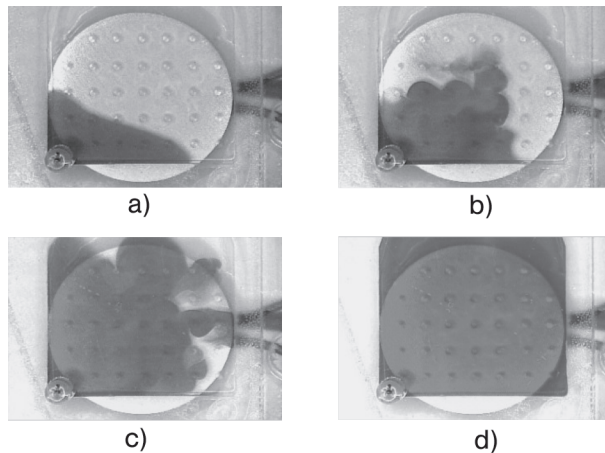


**Figure 1.29** Photographs of the mixing of an aqueous dye solution with de-ionized water by acoustic microstreaming ( $7 \times 5$  top bubbles; 5 kHz; 40 V) in a  $16 \times 16$  micro chamber ( $0.2 \text{ mm}^3$  volume). (a) 0, (b) 2, (c) 4 and (d) 6 s [24] (by courtesy of ACS).

#### Type of wave

[M 10] [M 11] [P 9] [P 10] Square waves give faster mixing than sinusoidal waves [23, 24].

#### Height of amplitude

[M 10] [M 11] [P 9] [P 10] The higher the amplitude, the more improved is the mixing [23, 24]. At 5 kHz and 5 V, multiple-bubble microstreaming mixing is completed within about 105 s [23]. Increasing the peak-to-peak amplitude further to 40 V enhances mixing. By multiple-bubble microstreaming mixing at 5 kHz and 40 V, mixing is completed within about 6 s (see Figure 1.29) [24].

#### Critical stirred volume/critical micro chamber dimensions

[M 10] [M 11] [P 9] [P 10] Bubbles with radii of 0.5 mm can stir fluid volumes in a distance with a radius smaller than 2 mm [23, 24]. Thus, any micro chamber is suitable for acoustic microstreaming with a depth  $< 2$  mm and with an air pocket pitch  $< 4$  mm.

#### Enhancement of immunomagnetic cell capture experiments – shear strain field

[M 10c] [P 9] Immunomagnetic cell capture experiments need mixing of the bacterial cell (*Escherichia coli* K12) matrix suspended in blood with magnetic capture beads, which results in highly effective immunomagnetic cell capture. Bacterial viability assay experiments demonstrated that acoustic microstreaming mixing has a relatively low shear strain field [23]. The capture efficiencies of acoustic mixing (90%, at best) were as high as for conventional vortex mixing (91%, at best). They were much larger than for non-mixed samples (4%, at best). Double staining tests with SYTO 9 green fluorescence and propidium iodide red fluorescence showed that the blood cells and bacteria remained intact after mixing.

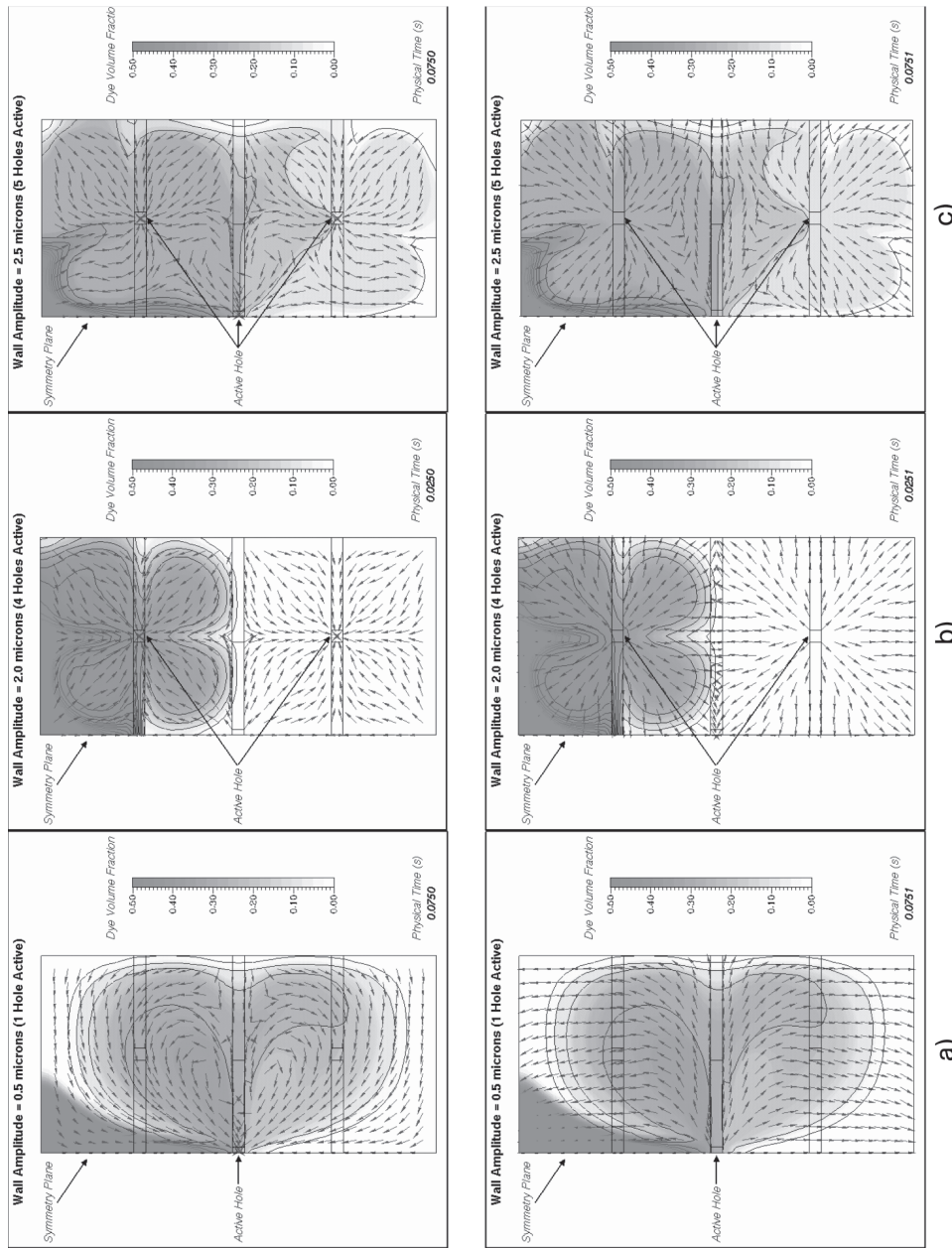


**Figure 1.30** Dye penetration results for acoustic mixing by (a) one hole, one bubble, (b) four holes, four bubbles, and (c) five holes, five bubbles. Also shown is the flow-field geometry given by the velocity vectors at the inflow and outflow portions of the wall oscillation cycle [23] (by courtesy of RSC).

### Enhancement of hybridization performance – interplay mixing–reaction

[M 11] [P 10] Since the acoustic microstreaming micro mixer was part of a DNA microarray chip, the enhancement of the hybridization performance by the micro mixing was investigated [24]. By acoustic microstreaming, the hybridization signal was increased by a factor of five. The signal uniformity was also improved compared with diffusion-based (2 h) chips. In addition, the kinetics were accelerated by a factor of five when acoustic microstreaming was applied. Further advantages of the use of acoustic microstreaming as the mixing mechanism are the simplicity of the apparatus, the ease of implementation, the low power consumption (~2 mW) and the low cost.

### Simulation of the effect of the number of holes and their positions

[M 12] [P 11] To analyze the effect of the number of holes and their positions on the acoustic mixing, three artificial mixing micro chambers were proposed, the first with one bubble pocket in the center (a), the second with four bubble pockets at the corners and the third with five air pockets with four at the corners and one in the center [23]. It was found that acoustic mixing depends largely on the number of holes and their positions (see Figure 1.30).

The holes act as sources and sinks for fluid motion [23]. They draw the dye from in the surrounding region and expel it in a jet-like action into other parts of the liquid. These jet-like structures are mainly responsible for mixing. Where flow symmetries delineated by the formation of internal stagnation zones exist, mixing is retarded. Best mixing results are obtained for the five-bubble arrangement.

An analysis of the flow patterns created on the basis of velocity vectors shows that the dye spread along with velocity vectors twice during the wall motion cycle: with its suction and blowing stages [23].

A certain induction time was found for all three configurations [23]. This period was 10 wall motion cycles or 100 time steps.

#### 1.2.6

### Ultrasonic Mixing

#### Most Relevant Citations

Peer-reviewed journals: [22].

Mixing can be achieved by ultrasound using lead zirconate titanate (PZT), a piezoelectric ceramic, operated in the kHz region [22]. In this way, liquid streams can be moved and even turbulent-like eddies are induced. Favorably, ultrasonic action is coupled into a closed volume, a micro chamber. Here, the creation of standing waves has been reported.

Compared with other means of creating turbulence in closed chambers, such as mixing by valves, ultrasonic mixing is said to have advantages with regard to sensitivity towards the presence of bubbles and can freely choose the flow ratio between the two liquids to be mixed (which is not given for valve mixing) [22].

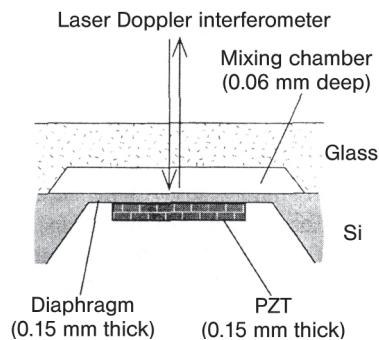


**Figure 1.31** Schematic of the cross-section of the mixing chamber. An etched glass substrate is joined to a silicon wafer by anodic bonding. The silicon plate is etched from the backside to yield a diaphragm, and a PZT is attached to the oscillating diaphragm [22] (by courtesy of Elsevier Ltd.).

#### 1.2.6.1 Mixer 13 [M 13]: Ultrasonic Micro Mixer

This micro device for ultrasonic mixing was made from two plates, one of which has a shallow open volume to give a micro chamber after assembly (see Figure 1.31) [22]. The area that actually covers the micro chamber is considerably thinned compared with the remaining thickness of the top plate. On this diaphragm, a thin PZT membrane is deposited, which acts as ultrasonic wave generator. The micro chamber is connected to two inlet channels and one outlet channel.

The excitation frequency was up to 60 kHz [22]. A function generator connected to a power amplifier was used to generate a square wave (50 V peak-to-peak at 60 kHz) for the PZT excitation.

The micro chamber was made by standard photolithographic methods and HF isotropic etching in the framework of bulk silicon micromachining [22]. Anodic bonding of silicon to glass was used for sealing the device. For fabrication of the diaphragm anisotropic silicon etching was used. A piece of bulk piezoelectric PZT ceramic was attached directly on the diaphragm by using an epoxy resin.

Mixer type	Ultrasonic micro mixer	PZT ceramic: width, length, thickness	5 mm, 4 mm, 150 $\mu\text{m}$
Base plate material (with mixing chamber)	Glass	Excitation frequency	60 kHz
Cover plate material (with diaphragm)	Silicon	Wave type	square; 50 V peak-to-peak
Mixing chamber: width, length, depth	6 mm, 6 mm, 60 $\mu\text{m}$		

#### 1.2.6.2 Mixing Characterization Protocols/Simulation

[P 12] The mixing performance was analyzed by a dilution-type experiment. Here, water and the fluorescent dye uranine, sodium fluorescein [22]. The latter is water-soluble. External pressure was applied to the liquids using a fluid dispenser. The flow rates of both water and the aqueous uranine solution were  $5 \mu\text{l min}^{-1}$ . A fluorescent microscope with a digital CCD camera with a  $1.25\times$  objective was used for optical mixing analysis. Fluorescent filters at 460–490 and 515–550 nm

for excitation and absorption, respectively, were used. The images were inverted, thereby changing the fluorescent bright zones to dark ones and vice versa with the non-fluorescent zones. The temperature was monitored with a thermo-inspector. Temperature measurements were done in a non-flow mode. A water-filled chamber was exposed for 5 min to ultrasonic action at room temperature. Diaphragm displacements were measured by using a laser Doppler interferometer.

### 1.2.6.3 Typical Results

#### Flow patterns by ultrasonic mixing

[M 13] [P 12] In the absence of ultrasonic mixing, two stable fluid regions with the separated water liquid and the uranine solution were found in the mixing chamber [22]. A straight interface was given; only a low degree of mixing was observed, being limited to the interface by slow molecular diffusion.

Upon ultrasonic action, turbulence occurred, moving material throughout the whole mixing chamber [22]. After termination of ultrasonic mixing, the initial pattern rapidly developed, the two zones being separated by a straight interface.

#### Mixing time

[M 13] [P 12] From video observation, a mixing time of about 2 s was judged [22]. A more exact determination was not possible, as images could be taken only every 7 s; hence it had to rely on direct microscope observation.

#### Fluorescence intensity monitoring

[M 13] [P 12] Fluorescence intensity measurements were made using data from the CCD camera, although these figures are not proportional to the uranine concentration, as no calibration could be performed with the existing equipment [22]. The intensities were taken along a cross-sectional line in the (left) feed side of the mixing chamber. Accordingly, the intensity plot without ultrasonic action shows two zones, one with maximal and one with zero uranine intensity signal, i.e. unmixed zones (see Figure 1.32). In between, a steep rise of concentration is

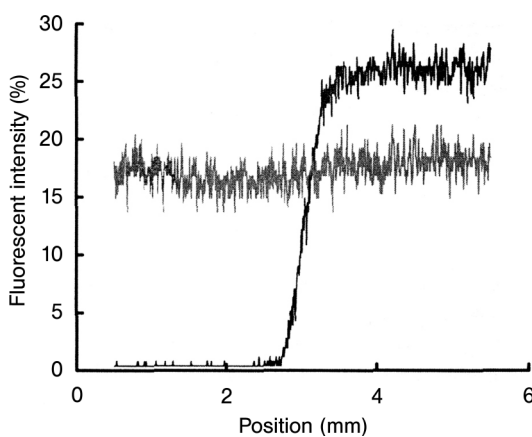


**Figure 1.32** Qualitative mixing performance by plotting the non-calibrated fluorescence intensity measured near the outlet of the mixing chamber along a cross-sectional line as a function of the position on this line. The mixing performances are shown before (gray curve) and after (black curve) the ultrasonic action. Position 0 refers to the top of the mixing [22] (by courtesy of Elsevier Ltd.).

observed, giving rise to an interface, diffused over about 0.4 mm. After onset of ultrasonic mixing, a medium intensity at all positions of the measurements, i.e. also in the edges of the mixing chamber, is achieved, thus complete mixing has taken place. The average intensity now, however, is not exactly half of the former maximum intensity signal, which is explainable owing to the missing calibration.

#### **Relationship between PZT excitation frequency and ultrasonic mixing**

[M 13] [P 12] A comparison of the frequency plots of the mixing performance and the diaphragm displacement displays no similarities [22]. The relationship between mixing performance, roughly measured by the extent of the mixed area, and frequency was complex. No mixing could be observed until a frequency of 8 kHz. The mixed area became larger until about 15 kHz. From then on, the mixed area remained at the same size until ~90 kHz, then decreased. At ~130 kHz, an increase was observed again.

The mixing performance–frequency plot does not resemble the diaphragm displacement–frequency characteristics of the PZT piezoelectric ceramic [22].

#### **Relationship between mixing performance and input power**

[M 13] [P 12] The mixed area increased on increasing the input power, as evidenced by the mixing of red ink in ethanol under 50, 60, 70, and 90 V [22]. However, the mixing speed was not altered by changing the input power.

#### **Role of diaphragm oscillation**

[M 13] [P 12] The oscillation of the diaphragm has no obvious effect on the mixing and is not essential for performing ultrasonic mixing [22]. The oscillating diaphragm, however, is useful to prevent the ultrasonic irradiation escaping into other parts of the micro device and to focus it into the mixing chamber. In a control experiment without a diaphragm, no mixing could be achieved when operating the PZT piezoelectric ceramic.

### 1.2.7

#### **Moving- and Oscillating-droplet Mixing by Electrowetting**

##### **Most Relevant Citations**

Peer-reviewed journals: [29, 97] (see also [98] for the basic microfluidics).

Some modern microfluidic approaches rely on the movement of discrete droplets rather than handling continuously flowing streams (see e.g. [97, 98]). In this way, flexible chemical protocols can be carried out, not unlike the traditional processing of batch systems. Especially with regard to  $\mu$ TAS applications, the footprint area the sample volume for fluidic handling are notably decreased.

The movement of droplets is based on an electrostatic method which changes the interfacial tension of the droplets by voltage, which is known as electrowetting (see Figure 1.33) [97, 98]. The nature of the liquid to be moved has to be polarizable and/or conductive. Application of an electric field on only one side of the droplet creates an imbalance of interfacial tension which can drive bulk flow of the droplet.

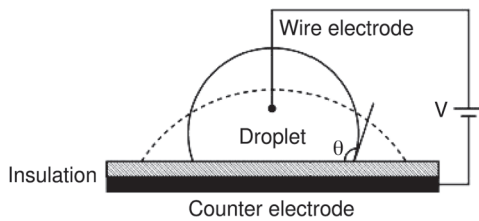


**Figure 1.33** The electrowetting effect. A droplet of conducting liquid has a contact angle  $\theta$  with a solid hydrophobic insulator (solid contour). The solid/liquid interfacial energy is reduced on applying a voltage  $V$  between the droplet and a counter-electrode below the insulator. This decreases  $\theta$  and leads to improved wetting of the solid by the droplet (dashed contour) [98] (by courtesy of RSC).

Passive ('moving') droplet mixing uses simple droplet merging and the merged droplet rests on the electrode, relying on diffusion as the mixing mechanism [97, 98]. Active ('oscillating') bubble mixing relies on the fast movement of the merged droplet between many electrodes. In this way, convections are induced that further promote mixing [97].

#### 1.2.7.1 Mixer 14 [M 14]: Moving- and Oscillating-droplet Micro Mixer

This device consists of two glass plates, held at a fixed distance by a spacer, which sandwich the droplets (see Figures 1.34 and 1.35) [97, 98]. The bottom glass plate carries an array of independently addressable control electrodes patterned in a thin layer of chromium. The electrodes are interdigitated for better contact with the droplets, albeit non-interdigitated electrodes were also applied. The electrodes were coated with an insulating material. The top plate was coated with a conducting, optically transparent layer to form the ground electrode. Both top and bottom glass plate were coated with hydrophobic layers.

The height of the gap between the two glass plates, i.e. the droplet height, has a considerable influence on droplet motion and mixing, as is to be expected [97].

Referring to Figure 1.34, several electrode configurations are possible owing to different arrangements of the ground and control electrodes and their combinations

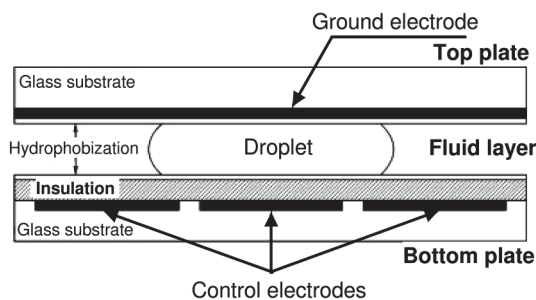


**Figure 1.34** Schematic of the cross-section of the electrowetting chip. A droplet is sandwiched between two glass plates carrying electrodes [98] (by courtesy of RSC).

[98]. The ground electrode may be placed in the top glass part and an array of control electrodes in the bottom glass part. The ground electrode may be either insulated or directly in contact with the fluid, which affects its capacitance per area and thus the amount of electrostatic energy at the interface. Even configurations with no ground electrode are possible. Here, the pitch of the control electrodes may be enhanced. The ground and control electrodes may be arranged coplanar, i.e. in the same bottom plate. The ground electrode has a larger pitch than the control electrode and is positioned underneath the latter within the bottom plate, whereas the control electrode is on the surface. Finally, control and ground electrodes may be arranged as areas in the top and bottom plates.

Mixer type	Moving- and oscillating-droplet mixer	Insulator material	Parylene C
Mixer base material	Glass	Insulator layer thickness	800 nm
Electrode material	Chromium	Conducting top material	Indium tin oxide (ITO)
Electrode layer thickness	200 nm	Hydrophobic layer material	Teflon AF
Gap between electrodes (passive mixing)	800 $\mu\text{m}$	Hydrophobic layer thickness	50 nm
Gap between electrodes (active mixing)	600 $\mu\text{m}$	Spacer material	Glass

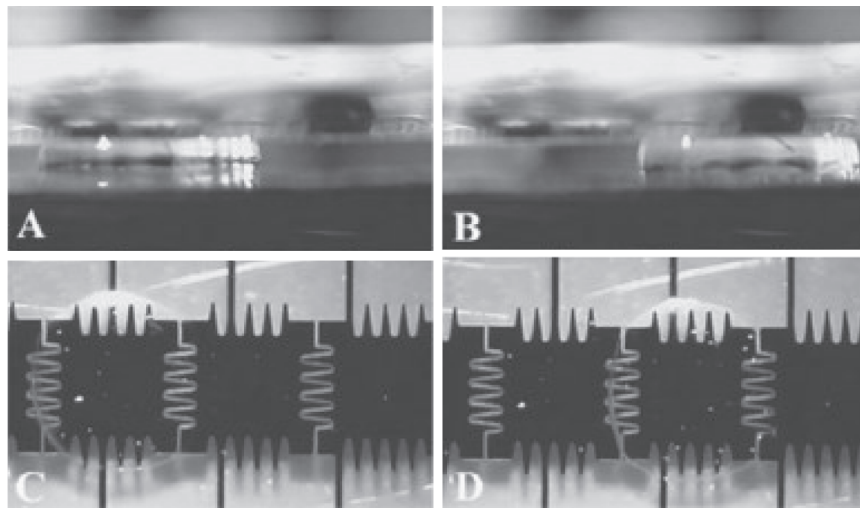


**Figure 1.35** Photographs of droplet transfer. Moving droplets from the side (A), (B) and top (C), (D) at 66 ms intervals. Side-view experiments: droplet in air; top-view experiments: droplet in silicone oil [98] (by courtesy of RSC).

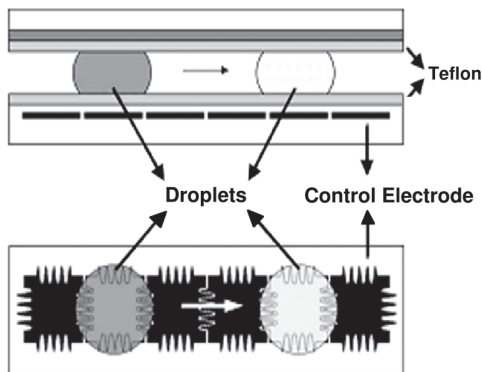


**Figure 1.36** Schematic of top and side views of a central part of the electro-wetting-based mixer [97] (by courtesy of RSC).

#### 1.2.7.2 Mixing Characterization Protocols/Simulation

[P 13] The volume of the droplets is set slightly larger than the pitch of the electrodes (see Figure 1.36) [97]. Thereby, an overlap to adjacent electrodes is achieved. An immiscible filler fluid, 1 cSt silicone oil, surrounds the droplets to prevent evaporation and to reduce the voltage needed. The electrodes were individually switched by using a custom controller.

Flow and mixing visualization were achieved by means of fluorescence dilution imaging [97]. A fluorescent droplet (1 mM fluorescein, 0.125 M KCl, 0.125 M sodium hydroxide) was merged with a non-fluorescent droplet (0.125 M KCl, 0.125 M sodium hydroxide). The volume of the droplet in passive mixing was 1.75  $\mu\text{l}$ , while 1.32  $\mu\text{l}$  droplets were applied for active mixing. The actuation voltage was 30 V. The fluidic properties of the filler and droplet fluids were closely matched. The interfacial tension between the two liquids was 36 and 37  $\text{dyn cm}^{-1}$  for the non-fluorescent and the fluorescent droplets, respectively.

Droplet visualization was achieved both from top and side views [97]. The latter is essential, since erroneous conclusions can be drawn when only inspecting from the top view owing to integration of intensity profiles along the optical axis (see Figure 1.37). In this way, non-mixed liquids can have a homogeneous fluorescence texture which could suggest mixing, but indeed only resembles a segregated structure. Details on the fluorescence set-up can be found in [97]. An image-processing toolkit in MATLAB was applied to judge mixing times and a calibration based on the intensity of the mixed state was performed.

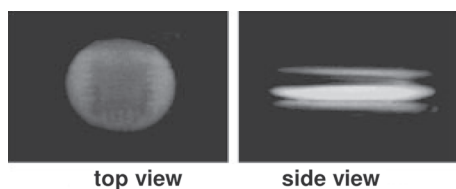


**Figure 1.37** Top and side views taken 15 s after merging of two droplets, one being fluorescent and the other transparent. Having only the top view can lead to the erroneous conclusion that mixing is completed, while the side view shows that actually a segregated, layered fluid system exists [97] (by courtesy of RSC).

[P 14] Measurements of droplet displacement were made by video imaging techniques, by which the droplet velocity could also be determined. Further information concerning the experiments is given in [98].

### 1.2.7.3 Typical Results

#### Velocity profile upon droplet displacement

[M 14] [P 14] Video-image analysis of the droplet displacement shows that an S-shaped dependence over time is yielded, i.e. the initial and final velocities are low, having the highest velocity after an induction period for the moving droplet [98].

#### Threshold voltages for droplet displacement in air and silicone oil

[M 14] [P 14] A certain threshold voltage has to be passed before the droplet is moved [98]. This threshold is dependent on the medium surrounding the droplet. The voltage needed is higher in air than in silicone oil (air 48 V, silicone oil 13 V for a 900 nl droplet of 0.1 M aq. KCl (see Figure 1.38); further details can be found in [98]).

#### Scaling properties of threshold voltage

[M 14] [P 14] For electrode arrays of different pitches with fixed geometric ratios the threshold voltage and the droplet transport, i.e. the velocity-voltage function, did not change [98].

#### Droplet dispensing

[M 14] [P 14] Dispensing of unit-sized droplets can be achieved from a larger initial droplet or from an external source through a series of binary splitting operations [98]. Asymmetric dispensing is also possible.

#### Passive mixing of fluidically matched droplets

[M 14] [P 13] The fluorescent droplet is moved towards the non-fluorescent droplet and the coalesced droplet is held in place [97] (see also an initial experiment in [98]). By this action, the fluorescent droplet moves underneath the non-fluorescent one. From a top view, a homogeneous texture is yielded; however, a vertically segregated fluidic system exists (see Figure 1.37). Mixing takes then place by diffusion and needs about 90 s to be completed.

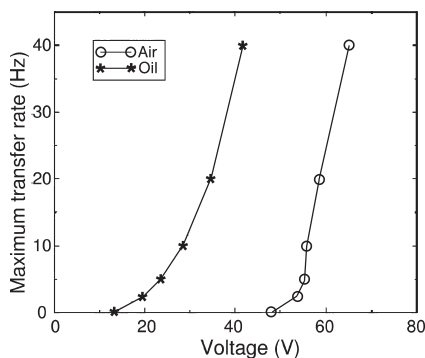


**Figure 1.38** Effect of the medium on droplet transport. The threshold value for droplet movement (900 nl; 0.1 M aq. KCl) is given by the x-axis intercept. [97] (by courtesy of RSC).

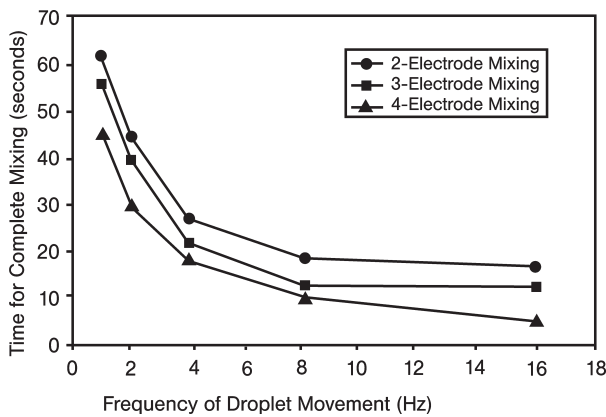


**Figure 1.39** Liquid mixing time as a function of the droplet oscillation frequency, given for two-, three- and four-electrode structures [97] (by courtesy of RSC).

#### Passive mixing of droplets with different fluidic properties

[M 14] [P 13] On changing the fluidic properties by giving the non-fluorescent droplet a different composition (KCl solution only) than the fluorescent droplet, a donut shape is evident from the top view [97]. Now, the side view gives a homogeneous texture. The fluorescent droplet engulfs the non-fluorescent KCl droplet. A mixing time of 90 s was determined, which is equal to the matched-droplet mixing, basically because the diffusion distances are the same in both cases.

#### Active mixing of droplets – droplet frequency and number of electrodes

[M 14] [P 13] Mixing times were determined as a function of the frequency (1–16 Hz) of droplet movement and the number of electrodes (2, 3, 4) [97]. The mixing times decrease on increasing either the frequency or the electrode number. This is due to improve oscillation ('shaking') of the droplets inducing secondary flows (see Figure 1.39). For example, at 1 Hz and using one electrode a mixing time of about 60 s is found, whereas only 4.6 s are needed for 16 Hz and four-electrode mixing. Frequencies larger than 16 Hz give no further gain.

#### Active mixing of droplets – two-electrode flow imaging

[M 14] [P 13] Starting from one engulfed coalesced droplet, two-electrode active mixing leads to protrusions of fluorescent and non-fluorescent fluid compartments [97]. In this way, new interfacial areas are created and mixing is promoted. However, owing to the laminar regime, flow reversibility is observed, that is, achievements in protrusion are (partly) undone on moving the droplet back to the prior electrode position.

#### Active mixing of droplets – three-electrode flow imaging

[M 14] [P 13] Three-electrode active mixing creates in a similar way protrusions (see Figure 1.40) [97]. Despite the flow reversibility also observed, a better mixing performance than for the two-electrode mixing is given. This can be explained by the higher number of configurations of the droplet movement yielding more complex patterns and generating larger interfaces.

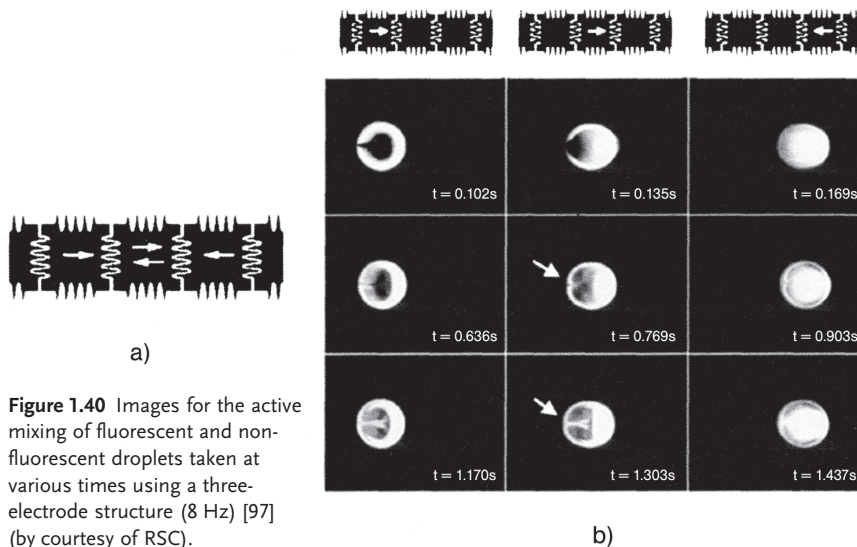


**Figure 1.40** Images for the active mixing of fluorescent and non-fluorescent droplets taken at various times using a three-electrode structure (8 Hz) [97] (by courtesy of RSC).

#### Active mixing of droplets – four-electrode flow imaging

[M 14] [P 13] Four-electrode active mixing gives more droplet configurations and achieves better mixing than two- and three-electrode mixing [97]. Flow reversibility is still present but to a reduced extent.

#### Effect of aspect ratio

[M 14] [P 14] The mixing in the droplets was investigated as a function of the aspect ratio, i.e. the ratio of the gap height to the electrode pitch size [29]. It was known before that this aspect ratio has a large influence on droplet formation and splitting; hence it could be anticipated that the same holds for the mixing of a merged droplet.

The flow patterns and the mixing times differ remarkably depending on the aspect ratio (see Figure 1.41) [29]. It is found that mixing times decrease from 15 to 6 s on raising the aspect ratio from 0.1 to 0.5. Thereafter, a slight increase in mixing

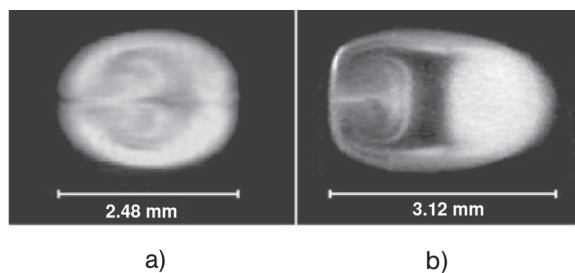


**Figure 1.41** Top view of droplets mixed by a linear four-electrode array with aspect ratio (gap height to the electrode pitch size) of (a) 0.4 and (b) 0.2 after 1.2 s (16 Hz switching frequency) [29] (by courtesy of RSC).

time is observed again. This is due to the formation of complex flow patterns at aspect ratios of 0.4–0.5, whereas only bi-layered structures are found for small aspect ratios. The latter results in smaller interfacial areas, and hence leads to longer mixing times. The increase in mixing time for aspect ratios  $> 0.5$  is to the larger volume, i.e. the slightly less efficient generation of interfaces under such conditions.

#### **Mixing strategies for droplets formed at low aspect ratio/split and merge mixing**

[M 14] [P 14] Splitting of droplets can only occur at aspect ratios  $< 0.2$  (for definition see *Effect of aspect ratio*) [29]. Since this is an important microfluidic action, it was worth finding suitable novel mixing strategies to overcome this limitation.

The simplest solution is to use droplet splitting and then oscillation ('shaking') followed by re-merging and second splitting [29]. This is named split-and-merge mixing. A three-electrode structure is the simplest engineering solution to achieve such multiple splitting and merging actions.

#### **Avoidance of flow reversibility at high aspect ratio – $2 \times 2$ electrode array**

[M 14] [P 14] It was shown above that mixing of droplets is fairly fast at an aspect ratio of about 0.4, in the order of 4–5 s [29]. It was assumed that a further reduction of mixing time is not possible, as the flow reversibility poses limits here, which is the 'relaxation' of a new flow pattern, with increased or fresh interface, to the original state.

For a such case, linear arrays of electrodes may be used; however, this will lead to extended structures when using, e.g., more than four electrodes. Instead of using such unidirectional motion, the droplet may be moved in circular fashion by a square-like  $2 \times 2$  array of electrodes. Indeed, faster mixing times compared with simple droplet merging can be achieved, albeit not faster than for the respective four-electrode linear structure. Actually, a small portion of the droplet remains unmixed. This was explained as due to the droplet pivoting around the array center. For this reason, a non-symmetric array ( $2 \times 3$ ) was developed as mentioned below.

#### **Avoidance of flow reversibility at high aspect ratio – $2 \times 3$ electrode array**

[M 14] [P 14] In order to have the droplet turning about a moving pivot point, a  $2 \times 3$  array of electrodes was developed [29]. An average mixing time of 6.1 s was thus achieved, which is a better performance as compared with the  $2 \times 2$  array with a 9.95 s mixing time. The better mixing was related to additional translation between the pivot points. Indeed, the flow patterns exhibit different forms during one loop passage (see Figure 1.42). An unmixed part, as for the  $2 \times 2$  array, is given no longer. However, the mixing performance is still worse compared with the four-electrode linear array.

#### **Combining the positive aspects of linear and circular arrays – $2 \times 4$ electrode array**

[M 14] [P 14] In order to combine the effect of efficient oscillation of the extended linear arrays and the avoidance of flow reversibility of the circular arrays, an extended circular array ( $2 \times 4$ ) of electrodes was developed [29]. This has three possible pivot points with up to two translations. This enhances the number of possible paths for the droplet which may result in enhanced mixing.

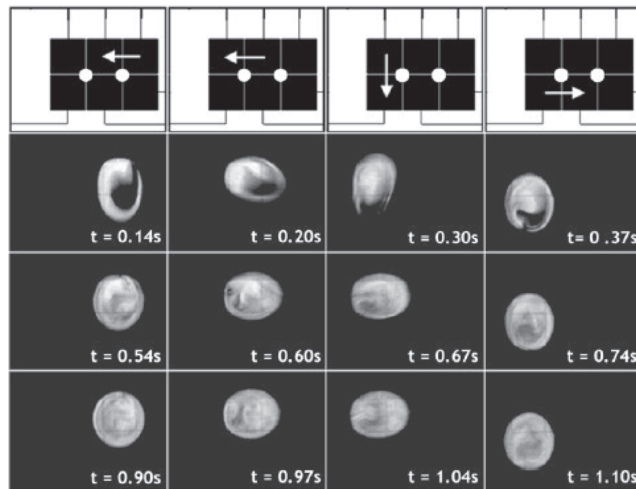


**Figure 1.42** Schematic of the pivot point around which the droplet moves in a  $2 \times 3$  mixer array (top row). Images of droplet mixing in a  $2 \times 3$  array taken at various times (16 Hz switching frequency) [29] (by courtesy of RSC).

A mixing time of only 2.9 s was derived [29]. More complex flow patterns were determined than for all the arrays investigated so far.

#### Pseudo $3 \times 3$ electrode array

[M 14] [P 14] In order to complete the possible design variations of circular arrays, a pseudo  $3 \times 3$  array of electrodes was developed [29]. This allows quasi-unidirectional movement of droplets. Each movement occurs about a different pivot point. The mixing time was slower as compared with the  $2 \times 4$  array, having the same total number of electrodes.

#### Overall comparison of all electrode arrays

[M 14] [P 14] To have an overall comparison of the results given in all the subsections above, a comparison of the mixing time for moving droplets on the different arrays were made (see Table 1.1). The mixing times are roughly halved on adding a second dimension, i.e. additional pivot points (e.g. on going from a  $1 \times 2$  to a  $2 \times 2$  array) [29]. The mixing times are also reduced by having more electrodes, i.e. additional translation steps (e.g. on going from a  $1 \times 2$  to a  $1 \times 3$  array). The best result, i.e. the lowest mixing time, is given by the  $2 \times 4$  array mixer.

**Table 1.1** Mixing times for liquid droplet mixing in various  $1 \times N$  and  $2 \times N$  array mixers at 16 Hz [29].

Mixer array	$1 \times 2$	$2 \times 2$	$1 \times 3$	$2 \times 3$	$1 \times 4$	$2 \times 4$
Mixing time (s)	16.8	10.0	12.1	6.1	4.6	2.9

## 1.2.8

**Moving- and Oscillating-droplet Mixing by Dielectrophoresis****Most Relevant Citations**

Peer-reviewed journals: [99–101]; proceedings contributions: [101].

In addition to using electrowetting (see Figure 1.42), electrophoretic and dielectrophoretic forces can be used for moving droplets [99]. Electrophoretic droplet movement depends on the application of large DC fields, which may pose problems for fluid systems such as suspensions. For dielectrophoretic operation, however, AC fields are sufficient, as for electrowetting.

Electrowetting forces depend largely on the cleanness of the substrates, since even small traces of impurities may notably change the wetting behavior [99]. This certainly can be controlled under laboratory conditions, but may experience limitations under ‘dirty’ real-world applications. Further limitations on the droplet volume are given by the geometric constraints of the electrode chamber which needs to be wetted at the floor and ceiling.

Dielectrophoretic forces act as body forces on the droplet, rather than being surface forces as in the case of electrowetting [99]. By proper design of electric field geometries and using non-wetting surfaces, the dielectrophoretic forces can be set into action. This allows two-dimensional translation of the droplets and droplet injection over a large range of volume scales for reagent titration.

Dielectrophoretic forces depend on the polarizability of species, rather than on movement of charges [99]. This allows the movement of any type of droplet being immersed by a dielectrically distinct immiscible carrier medium. Since dielectric forces are generated by spatially inhomogeneous fields, no mechanical actuation is required. In addition to this, dielectrophoretic droplet movement benefits from the general advantages given by droplet microfluidic, i.e. discrete, well-known very small volumes, no need for channels, avoidance of dead volumes and more.

**1.2.8.1 Mixer 15 [M 15]: Dielectrophoretic Droplet Micro Mixer**

This dielectrophoretic droplet mixer, called a programmable fluidic processor, contains two rows of 32 pads for the electrodes; these rows being at the upper and lower edges of the substrate and connected to the  $8 \times 8$  electrode array in the center of the chip [99]. The electrodes form a square matrix with an upper and lower half owing to the connectivity to the pads. The electrodes have a square shape.

Mixer type	Dielectrophoretic droplet micro mixer	Array format	$8 \times 8$
Substrate material	Glass	Electrode width, length	30 $\mu\text{m}$ , 30 $\mu\text{m}$ ; 100 $\mu\text{m}$ , 100 $\mu\text{m}$ ; 300 $\mu\text{m}$ , 300 $\mu\text{m}$
Electrode material	Gold on titanium	Passivation layer material and thickness	Fluoro-Pel <sup>®</sup> , ~0.5 $\mu\text{m}$
Total chip size	40 mm $\times$ 40 mm		

A two-dimensional array was patterned by standard photolithographic techniques on a substrate [99]. An open fluid reservoir was achieved simply by sealing the internal part of the device, including the array, with an O-ring. This open-face arrangement was for laboratory experiments, while the device has to be sealed for later practical uses. A hydrophobic coating served for electrical insulation. The device was connected to a computer-controlled switching circuit.

#### 1.2.8.2 Mixer 16 [M 16]: Electrical Phase-array Panel Micro Mixer

From this device, several sub-versions were made. These so-called electrical panel devices were realized as three- and six-phase array devices and a nine ( $3 \times 3$ ) electrode dot device [100, 101]. The three- and six-phase array devices consist of a substrate with electrode arrays of a paste printed on using a silkscreen printmaking process. This substrate is covered with an insulating covering film.

Mixer type	Electrical phase-array panel device	Multi pitch length	0.5 mm, 0.75 mm, 1.0 mm, 2.0 mm
Substrate material	Polyester	Multi pitch width	0.2 mm
Substrate thickness	300 $\mu\text{m}$	Insulating covering film material	Teflon or polypropylene
Electrode material	Silver	Insulating covering film thickness	90 $\mu\text{m}$

#### 1.2.8.3 Mixer 17 [M 17]: Electrical Dot-array Micro Mixer

This nine ( $3 \times 3$ ) electrode dot device comprises a four-layer printed circuit board [100, 101]. The first layer has a nine-phase electrode dot matrix. The entire electrode dot matrix consists of multiple  $3 \times 3$  units. Each electrode has a hole in its center for connection to the electric circuits of the layers below. These layers were connected to external terminals. Sequential voltages were applied to the three-phase electrode columns and lines.

Mixer type	Electrical dot-array panel device	Electrode unit in the array	$3 \times 3$
Layer material	Glass reinforced epoxy	Total electrode area	$150 \times 150 \text{ mm}$
Average pitch and width of first layer	1.0 mm, 0.5 mm	Insulating covering film thickness	90 $\mu\text{m}$

#### 1.2.8.4 Mixing Characterization Protocols/Simulation

[P 15] The reservoir of the dielectrophoretic droplet mixer was filled with 1-bromododecane, a low-permittivity, low-viscosity, water-immiscible hydrocarbon [99]. AC signals of up to 180 V<sub>p-p</sub> and frequencies between 5 and 500 kHz were formed using a programmable function generator and amplified by variable gain amplifiers.

The AC signal was distributed to an array of solid-state switches, operating under a microcontroller that was driven by a Lab software program. Images of the moved droplets were taken using a microscope and a CCD camera. A trans-illuminating quartz–halogen lamp was used for most viewing and a xenon lamp for fluorescence studies.

In addition to point-to-point movement of droplets, the dielectrophoretic droplet mixer could form droplets at pressurized orifices near electrodes [99]. In the latter, the fluid is normally kept by a ‘hydrostatic holdoff’, which is then overcome by the dielectrophoretic action.

The droplets were moved by switching electrodes on and off, creating a minimum of the electric field energy and exerting a lateral force on the droplet [99].

[P 16] Sequential voltages with six-phase rectangular profiles were applied [100, 101]. Following some first evaluations, it turned out that the sequence [+++ –] was the most efficient means for droplet transport. Most smooth droplet transports were found for voltages > 350 V. The upper limit was, however, fixed at 400 V, since otherwise cross-electrode discharge may lead to damage.

As surrounding liquids oils or a specially liquid, fluorinert, can be used [100]. For the actual experiments, a vegetable oil was chosen. It has a density lower than most aqueous solutions so that such droplets sink in the oil medium towards the panel surface. The droplets were applied using a normal pipet. Such prepared droplets are almost spherical on the polypropylene film. Often superhydrophobic materials were used as substrates.

### 1.2.8.5 Typical Results

#### Controlled droplet motion

[M 15] [P 15] In order to demonstrate the basic functionality of the dielectrophoretic fluid processor, some complex droplet motions were made (see Figure 1.43) [99]. As an example, one 0.18 nl and two 0.065 nl droplets were guided over an  $8 \times 8$  array (30  $\mu\text{m}$  electrodes) and one after the other combined with a 0.38 nl droplet. Spontaneous fusion was observed. In this way, a 0.69 nl droplet resulted, containing all the initial volumes. This droplet was finally moved over the array. A speed of  $> 1.8 \text{ mm s}^{-1}$  was achieved.

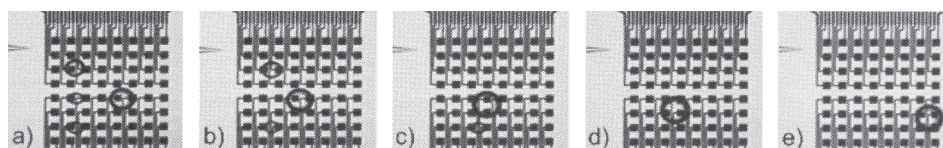


**Figure 1.43** Multiple droplet motion and fusion on an  $8 \times 8$  array fluid processor with 30  $\mu\text{m}$  electrodes. (a) Four droplets of varying size, three on one line and one separate large droplet; (b) spontaneous fusion of the middle droplet on the line with the large droplet; (c) spontaneous fusion of the upper droplet on the line with the large droplet; (d) spontaneous fusion of the lower droplet on the line with the large droplet; (e) movement of the remaining large droplet to the edge of the array [99] (by courtesy of RSC).

**Non-mechanical droplet metering**

[M 15] [P 15] Discrete aliquots of the liquid were injected onto a reaction surface by means of dielectrophoretic forces generated by a fluid processor [99]. Micropipet injectors were immersed in the fluid reservoir and placed close to the electrodes. A vertical distance of 10–20  $\mu\text{m}$  was maintained. By means of a micromanipulator, the lateral distance was adjusted. The pressure was controlled by a syringe pump.

The droplet injection was initiated by energizing the electrode nearest the injector [99]. By dielectrophoretic forces, fluid is drawn out of the pipet and forms a droplet, which then moves to the edge of the electrode. The dielectrophoretic forces have to be balanced properly with the interfacial tension forces to give uniformly sized droplets. 18  $\mu\text{m}$  (3 pl) sized droplets; for example, were made in that way.

**Droplet fusion and reaction**

[M 15] [P 15] Two aqueous droplets in a liquid hydrocarbon were placed on two adjacent electrodes (30  $\mu\text{m}$ ) with a 30  $\mu\text{m}$  distance [99]. By activation of intervening electrodes the droplets were brought together and gave spontaneous fusion. Fast mixing of the droplet contents followed this merging; using the reaction between fluorescein in dilute HCl solution and NaOH solution, the change in fluorescence intensity could be taken as rough measure of the mixing speed. In this way, the speed of the diffusion front was estimated to be about 170  $\mu\text{m s}^{-1}$ .

**Droplet-based fluorescence assay**

[M 15] [P 15] As some sort of feasibility test for biochemical analysis, nine droplets of *o*-phthalaldehyde were placed using a micropipet on an electrode of an  $8 \times 8$  array [99]. Varying quantities of a 0.5  $\text{g l}^{-1}$  solution of bovine serum albumin were metered towards these droplets from a second injector, the newly introduced droplets being 0.18 nl in volume ( $\sim 70 \mu\text{m}$ ). Such produced fused droplets had protein concentrations in the range 0.266–232  $\mu\text{g ml}^{-1}$ . This corresponded well with the varying fluorescence intensities of the droplet observed at the maximum wavelength of the fluorescence spectra of the protein-bound *o*-phthalaldehyde, i.e. demonstrating that the reaction was achieved.

**Droplet motion in electrode array devices with sequential voltage**

[M 16] [P 16] Droplet transport could be achieved for frequencies of the sequential voltages in the range 0.5–3.0 Hz [100, 101]. An increase in the ratio of electrode width to pitch facilitated the droplet transport. Since only perpendicular transport can also be achieved, fluid guiding is necessary. This can be accomplished, e.g., by use of thin polymer films.

**Droplet motion in electrode dot devices with sequential voltage**

[M 17] [P 16] Using electrode dot devices, each droplet can be moved independently [100, 101]. This was evidenced by two droplets next to each other, where only one electrode was activated. Only the respective droplet moved and the other stayed where it was.

**Chemical reaction in electrode dot devices with sequential voltage**

[M 17] [P 16] A pH-indicator reaction was performed by merging droplets containing phenolphthalein and aqueous NaOH solution on an electrode dot device [100, 101]. The reaction immediately followed the merging and mixing of the droplet, as evidenced by the respective color change.

**Biochemical reaction in six-phase electrode array devices with sequential voltage**

[M 16] [P 16] The same findings as for the chemical reaction (see *Chemical reaction in electrode dot devices with sequential voltage*) were made for the luciferin–luciferase enzyme reaction with adenosine triphosphate on the six-phase electrode array device [100, 101]. The reaction rapidly followed the mixing, as evident from the luciferin luminescence of the droplet after merging.

**Problems during chemical reaction in electrode array devices with sequential voltage**

[M 16] [P 16] For reasons of depletion of reactants during a chemical reaction, as given, e.g., for the phenolphthalein pH change (see above), the surface tension of the respective droplets may change considerably [100, 101]. In the case of large voltages, this may lead to deformation of the droplets and finally to break-up of the droplet. Many small droplets were generated.

## 1.2.9

**Bulge Mixing on Structured Surface Microchip****Most Relevant Citations**

Peer-reviewed journals: [102].

In addition to using electrowetting effects for droplet movement and merging, surface-guided flow due to selective wettability can do a similar job [102]. Structured surfaces can form so-called ‘liquid micro channels’ without having any wall, besides the surface structure. These continuous, cylinder-like liquids can undergo fragmentation above a certain critical liquid load to bulges, structures similar to extended droplets. By having a proper geometry of the surface structures, the position of the bulges can be fixed and by approaching such structures close together, mixing between selected solutions can be performed at a selected place.

**1.2.9.1 Mixer 18 [M 18]: Structured Surface Bulge Micro Mixer**

Mixer type	Structured surface bulge micro mixer	MgF <sub>2</sub> layer thickness	20 nm
Substrate material	Hydrophobic silicone rubber or thiolated gold substrate	Surface structure width	About 30–40 μm *
Wettable surface structure	MgF <sub>2</sub>	Surface structure length	Several hundred μm *

\* Parameters are not specified in [102]; data are judged from scanning electron micrographs presented.

This device comprises a hydrophobic surface using the wettability pattern of hydrophilic stripes for a surface-guided flow, ‘micro channels’ [102]. As substrates, hydrophobic materials were employed. The hydrophilic stripes were generated by mask-through thermal vapor deposition of  $\text{MgF}_2$  on a silicone rubber or thiolated gold substrate.

### 1.2.9.2 Mixing Characterization Protocols/Simulation

[P 17] The substrate was exposed to an atmosphere with 40% humidity at room temperature. By cooling to 5 °C the dew point was reached and water condensed on the wetting hydrophilic stripes. Such covered hydrophilic stripes can be interpreted as liquid micro channels with a channel wall in only one dimension [102].

### 1.2.9.3 Typical Results

#### Filling of the stripes/fluid instability and droplet break-up at large coverage

[M 18] [P 17] By depositing a small amount of water on the hydrophilic stripes the channels are shaped homogeneously as cylinder segments. The real shape of the cylinders depends on the contact angle. If subsequently more and more water is deposited on the stripes, the volume of the cylinders increases until suddenly a single bulge with a characteristic shape is formed (see Figure 1.44).

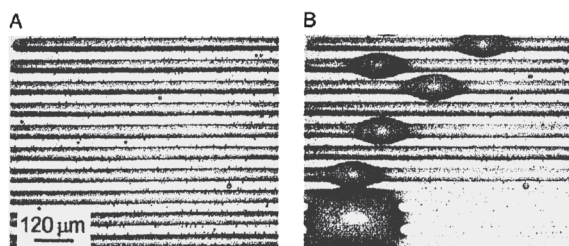


**Figure 1.44** Stripes covered with water. (A) Low water coverage with constant cross section and small contact angle; (B) high water coverage with partially bulge formation and merging of two bulges of two neighboring channels [102] (by courtesy of AAAS).

#### Theoretical analysis of the fluid instability

[M 18] [P 17] In theoretical work, the surface channel instability was investigated [102]. It could be shown that the surface channel instability is different from the Rayleigh-plateau instability (compare [72], Chapter 3), which describes the decay of a fluid cylinder into a periodically droplet array. In contrast to the Rayleigh-plateau instability, the fluid cylinders attached to a surface form a single bulge instead of decaying into droplets. A detailed theoretical description of the experimental findings is given [102].

#### Bulge mixing at corners

[M 18] [P 17] The wettable pattern can be used as micro-fluidic chips or micro reactors. Pairs or multiples of different hydrophobic stripes can be filled, e.g., with

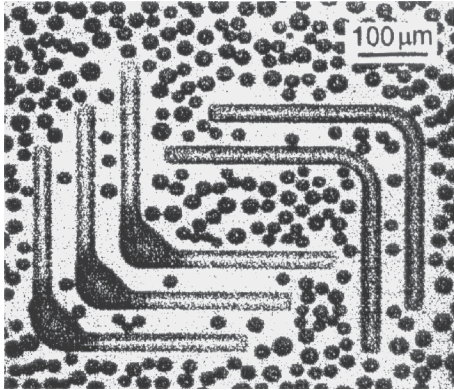


**Figure 1.45** Surface micro channel domains with corners. The bulge prefers to sit at the corner because of maximum contact with the hydrophilic stripe. If the corners are close enough, two or more adjacent bulges will coalesce and form a fluidic bridge [102] (by courtesy of AAAS).

different reactants. By overloading with liquids, the bulges formed can coalesce and form bridges between two or more of these surface channels. By merging the bulges, mixing of the fluids is easily performed. This bridging position happens by chance, so to control the bridging position on a chip, the shape of the stripes used either changing the width or forming corners into the otherwise straight surface channels (see Figure 1.45) [102].

#### **Solidification of the fluidic network**

[M 18] [P 17] If the filled liquid channels and bridges can be fixed by, e.g., freezing, polymerization or sol–gel reactions, a mold insert could be formed which would allow one to transfer the fluidic network structure as ‘real’ channels into plastic or other materials [102].

#### 1.2.10

#### **Valveless Micropumping Mixing**

##### **Most Relevant Citations**

Peer-reviewed journals: [103].

A powerful pumping principle is represented by PZT (Pb–Zr–Ti)-driven valveless micropumps which by operation at high frequency (kHz range) is said to be able to induce turbulence locally [103]. When using two feed inlets into a pumping chamber and one outlet, the pumping action can be transferred into mixing action owing to the turbulence achieved by the heavy flow motion.

##### 1.2.10.1 Mixer 19 [M 19]: Valveless Micropumping Micro Mixer

This valveless micropump comprises a pair of diffuser elements and a chamber with oscillating diaphragm (see Figure 1.46) [103]. The two diffusers are located at the side of the chamber. By variation of the chamber volume owing to diaphragm displacement, fluid motion is generated. Flow resistance of the diffusers is directionally varying so that directed flow guidance is given. During pumping, work turbulence is induced.

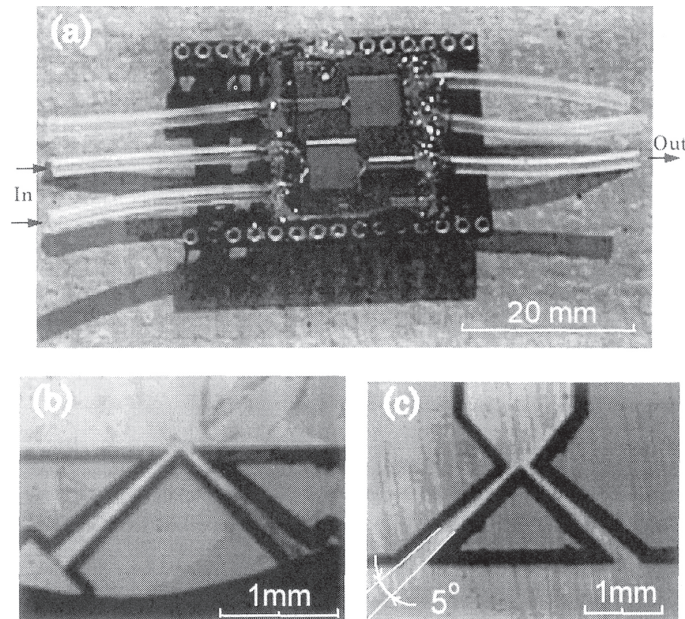


**Figure 1.46** Valveless micropumping mixer with two mixing chambers. (a) Photograph of the total device; (b) details of the diffusers at the inlet; (c) details of the diffusers at the outlet [103] (by courtesy of Kluwer Academic Publishers).

HF isotropic etching of glass was used for making the diffuser and mixing-chamber structures [103]. The diaphragm was etched into silicon by standard silicon micromachining. Anodic bonding was used for sealing of these two structured plates. A PZT piece was glued on the diaphragm.

Mixer type	Valveless micropumping micro mixer	Diaphragm length, width, thickness	6 mm, 6 mm, 0.15 mm
Mixing chamber and diffuser material	Pyrex glass	Mixing chamber length, width, depth	6 mm, 6 mm, 0.04 mm
Diaphragm material	Silicon	Mixing chamber length, width, thickness	6 mm, 6 mm, 0.2 mm
Diffuser length, angle	1.5 mm, 5°	Total device size	20 mm × 20 mm

#### 1.2.10.2 Mixing Characterization Protocols/Simulation

[P 18] A square-wave voltage (120 V peak-to-peak) was applied for excitation of the diaphragm to change the volume of the mixing chamber [103]. The pumping mixer was operated with water, methanol and ethanol. The flow rates were measured with a 70  $\mu\text{m}$  glass micropipet and the pressures were determined using a miniature pressure meter.

### 1.2.10.3 Typical Results

#### Pumping performance

[M 19] [P 18] Pumping action up to 10 kHz was achieved for excitation by square-wave voltage [103]. Pumping ethanol,  $15.6 \mu\text{l min}^{-1}$  as the maximum flow rate at a zero flow pressure of 2.16 kPa was achieved (870 Hz square wave). Operation was also achieved with sinusoidal and triangular excitation.

#### Mixing performance

[M 19] [P 18] For characterization of mixing performance, colored solutions were generated by dissolving various pigments in water, methanol and ethanol [103]. The formation of a homogeneous color was followed on mixing each of these solutions with the corresponding pure uncolored liquids. It was concluded that mixing is efficient, although no details on the mixing time and flow patterns created are given.

### 1.2.11

#### Membrane-actuated Micropumping Mixing

##### Most Relevant Citations

Proceedings contributions: [30].

##### 1.2.11.1 Mixer 20 [M 20]: Membrane-actuated Micropumping Micro Mixer

This device (see Figure 1.47) achieves active mixing by fast periodical changes of a mixing-chamber volume via actuation of a thin membrane by a piezo disk [30]. Similar to the pumping action of membrane pumps, based on the same principle, fluid motion is achieved in this way. The design thus comprises two layers with the bottom part containing the inlet and outlet ports and with the top part forming the mixing chamber. The top side of the mixing chamber is the thin membrane, above which the piezo disk is located. The outlet port is placed in the center of the mixing chamber, while the two inlet ports are on opposite sides close to the channel wall.

The chip carrier contains electrical contacts for wire bonding of the piezo disk [30].

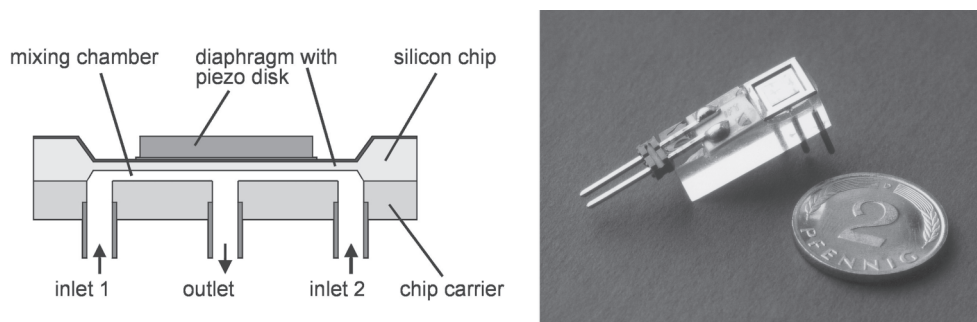


**Figure 1.47** Schematic design of the membrane-actuated micropumping mixer (left) and photograph of the device (right) [30] (by courtesy of Kluwer Academic Publishers).

Standard silicon micromachining was applied for device manufacture using wet-chemical etching by KOH [30].

Mixer type	Membrane-actuated micropumping micro mixer	Membrane thickness	40 $\mu\text{m}$
Membrane and mixer material	Silicon	Mixing chamber length, width, depth	5.1 mm, 5.1 mm, 15 $\mu\text{m}$
Mixer top side layer material	Alumina	Chip carrier material	PPMA; PEEK
Total membrane area	5.1 mm $\times$ 5.1 mm	Total device size	7 mm $\times$ 7 mm

#### 1.2.11.2 Mixing Characterization Protocols/Simulation

[P 19] Dilution-type mixing monitoring of a blue-dyed aqueous solution and water was carried out using video taping [30].

For testing the  $\mu\text{TAS}$  module, colorimetric pH detection with bromothymol blue indicator was used [30]. A stock solution was prepared at a concentration of 3 mg ml<sup>-1</sup> in ethanol. Thereafter, this stock solution was diluted with water to 40  $\mu\text{g ml}^{-1}$ . Later a water-soluble salt was employed. Detection was carried out at 610 nm, close to the maximum absorption of the dye.

#### 1.2.11.3 Typical Results

##### Passive mode of the mixer

[M 20] [P 19] An investigation of the flow patterns in the mixer outlet was made by dilution-type dye imaging [30]. On contacting the two streams only in the mixer devices without any membrane actuation (static or passive case), a bi-layered system results with no obvious degree of mixing, as is to be expected.

##### Active mode with single downward stroke

[M 20] [P 19] An active single downward stroke yields a parabolic shock wave traveling along the mixer outlet and disturbing the laminar pattern, thus promoting mixing [30]. Maximal action is achieved when placing the outlet in the center of the mixing chamber, thus being below the maximal deflection of the membrane.

##### Active mode with many oscillating strokes

[M 20] [P 19] Setting multiple downward strokes yields superposition of many parabolic shock waves traveling along the mixer outlet [30]. In this way, a much more effective disturbance of the laminar pattern is given than for a single stroke only. Using a dilution-type mixing experiment, high dispersion of the dye is evident, which is indicative of a high mixing efficiency.

##### Amplitude and frequency

[M 20] [P 19] By colorimetric measurement the impact of the frequency and amplitude of actuation on the mixing efficiency was characterized (100 Hz;

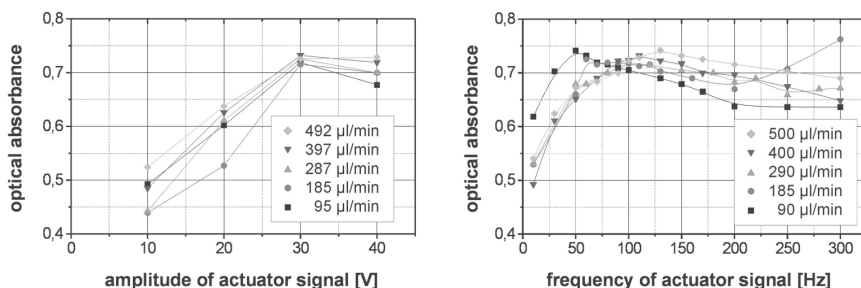


**Figure 1.48** Mixing efficiency, determined by photometry, as a function of the amplitude (left) and frequency (right) of the actuating membrane [30] (by courtesy of Kluwer Academic Publishers).

95–492  $\mu\text{l min}^{-1}$ ) (see Figure 1.48) [30]. An optimum signal amplitude between 30 and 40 V was found corresponding to a total membrane stroke of 6–7  $\mu\text{m}$ . For lower voltages, mixing was incomplete. At higher amplitude, no further improvement was noted. This is probably due to a too large deflection of the membrane touching the bottom of the mixing chamber and actually closing the outlet channel, hence massively disrupting the mixing process.

At most measured flow rates, mixing performance is nearby constant over the frequency of the actuator signal, actually giving a slight maximum (30 V) [30]. The differences between curves taken at various flow rates are due to flow-dependent variation of the perturbation zone distances in the mixer outlet.

#### Functioning within a $\mu\text{TAS}$ module for colorimetric analysis

[M 20] [P 19] The  $\mu\text{TAS}$  module is made for performing colorimetric analyses as typically applied in cuvette tests, e.g. for on-site water analysis [30]. A continuous test replaces copious manual pipetting of the sampling volumes. The module consists of a micro flow restrictor, a micro mixer and an optical microcuvette for colorimetric analysis. The sample is injected by a conventional FIA (flow injection analysis) system. By close connection, a dead volume of only 2.2  $\mu\text{l}$  is given.

Owing to the very small mixing chamber, fast changes by mixing can be induced, resulting in a fast response of the  $\mu\text{TAS}$  module, i.e. a large test-throughput frequency may potentially be achieved [30]. Several cycles were reported between baseline and active mixing measurements. The original state was reached perfectly after each measurement, which means, e.g., that no sample cross-contamination occurred. The results also prove that complete mixing is ascertained. In this way, a full pH calibration curve was repeatedly obtained.

#### 1.2.12

##### Micro Impeller Mixing

##### Most Relevant Citations

Proceedings contributions: [32].

Impellers of all types dominate conventional mixing; numerous textbooks are available in this field (see e.g. [104, 105]). This is typically carried out in a batchwise

manner. Since in many  $\mu$ TAS applications liquids in mixing chambers of comparatively extended volumes have to be mixed, it is not too far-fetched to develop miniaturized stirrers [32]. Claimed advantages of micro impellers are the possibility of matching the impeller diameter to the mixing volume, of performing large-area mixing, of effecting mixing on-demand (switch on/off) and the flexibility of the mixing approach, e.g. concerning the choice of liquids.

#### 1.2.12.1 Mixer 21 [M 21]: Impeller Micro Mixer

This device contains micro impellers several tens of microns in diameter consisting of a cap, hub and two rotary blades which were made by electroplating and thin-film technology from the ferromagnetic material Permalloy (see Figure 1.49) [32]. These mixers are built in molded PDMS structures containing recesses as mixing chambers. Upon actuation with a standard magnetic stirrer, rotational speeds up to 600 rpm can be reached.

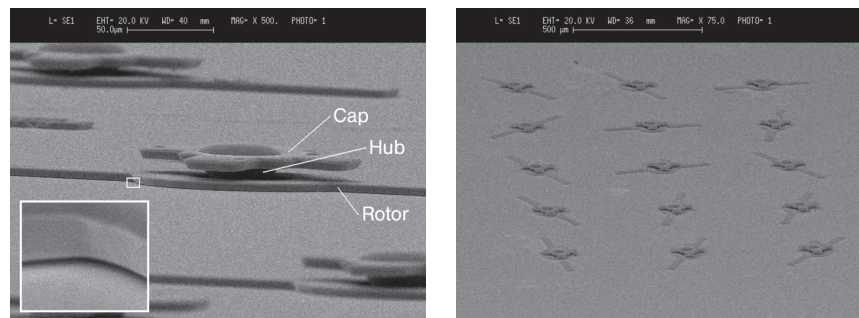


**Figure 1.49** Scanning electron micrograph of a  $5 \times 3$  micro-impeller array [32] (by courtesy of Kluwer Academic Publishers).

Mixer type	Impeller micro mixer	Rotational impeller speed	Up to 600 rpm
Mixer material	Permalloy	Exemplary chamber diameter, depth	2.5 mm, 40 $\mu$ m
Impeller diameter	About 100 $\mu$ m		

#### 1.2.12.2 Mixer 22 [M 22]: Ferromagnetic Sphere-chain Micro Mixer

This device forms impeller-like structures by the assembly of several small objects such as spheres, instead of making an artificial micro impeller by micromachining [104, 105]. This has the advantage that comparatively cheap items can be used for building up the impeller. One way to do so is to use ferromagnetic spheres which rest in a mixing chamber. In the presence of a magnetic field, the spheres attract each other and form a chain. If a rotating magnetic field is applied the chain rotates, essentially like an impeller, and stirs the liquid in the chamber. The diameter of the spheres is chosen so that it is slightly smaller than the depth of the mixing chamber; the number of spheres is given by the simple geometric constraint that the length

of the chain has to be slightly shorter than the chamber diameter (for circular chambers) or width (when being rectangular or square). The spheres are retained by a kind of frit structure at the chamber end. The spheres can be introduced before sealing of the mixing chamber or after by suspending them via the feed channels.

#### 1.2.12.3 Mixing Characterization Protocols/Simulation

[P 20] Flow visualization was achieved by a dilution-type experiment [32].

A simulation model was used based on CFD-ACE [32].

#### 1.2.12.4 Typical Results

##### Scanometric color index profiles at T-junction

[M 21] [P 20] Mixing near a T-junction (channel 750  $\mu\text{m}$  wide and 40  $\mu\text{m}$  deep) is complete at a 0.17  $\mu\text{l min}^{-1}$  flow rate when using a micro impeller at 120 rpm, as demonstrated by scanometric color index profiles providing line concentration profiles [32].

##### Flow visualization in mixing chamber

[M 21] [P 20] Mixing of an extended circular mixing chamber (diameter 2.5 mm, depth 40  $\mu\text{m}$ ) is complete after 55 s when using a  $3 \times 3$  array of micro impellers at 600 rpm, as demonstrated by dye flow visualization and color histograms [32].

##### Simulation of mixing compared to experimental results in an impeller array

[M 21] [P 20] CFD simulation results for micro impeller mixing in an extended circular mixing chamber (width 2 mm, length 2 mm, depth 50  $\mu\text{m}$ ) is in line with experimental results yielded under similar condition. Mixing is complete within less than 1 min when using a  $3 \times 3$  array of micro impellers at 600 rpm [32].

##### Liquid mixing time

[M 21] [P 20] A liquid mixing time of 55 s was determined for mixing a volume of an extended circular mixing chamber (diameter 2.5 mm and depth 40  $\mu\text{m}$ ; impeller at 600 rpm) (see Figure 1.50) [32].

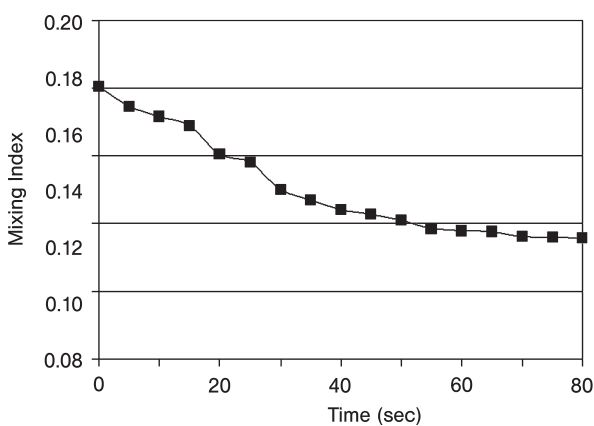


**Figure 1.50** Liquid mixing time of micro-impeller mixing in a mixing chamber derived by plotting a mixing index yield by photometry versus time [32] (by courtesy of Kluwer Academic Publishers).

## 1.2.13

**Magnetic Micro-bead Mixing****Most Relevant Citations**

Proceedings contributions: [106]; patents: [107].

An integrated micro device containing a mixer was developed for biochemical experiments [106, 107]. For amplification reactions the handling of very small volumes ( $< 10 \mu\text{l}$ ) of DNA and RNA under non-batch conditions was required. Thus, the key issue for design of the mixer was to minimize the volume of the components of the micro device, thereby, among other things, stimulating the development of a micro mixer with reduced dead volume.

**1.2.13.1 Mixer 23 [M 23]: Magnetic Micro-bead Micro Mixer**

This magnetic micro-bead mixer relies on a dynamic mixing principle, based on stirring of externally driven small particles in a small mixing chamber [106, 107]. Magnetic beads made of nickel were enclosed in this chamber. The externally stimulated bead motion resulted in rapid homogenization of the solutions to be mixed.

## 1.2.14

**Rotating-blade Dynamic Micro Mixer****Most Relevant Citations**

Proceedings contributions: [108].

A dynamic micro mixer has been proposed using curved blades mounted on a rotating shaft [108]. The system can be operated with and without a stator system. Advantages are seen in a more uniform flow distribution, since no feed splitting such as in interdigital micro mixers is necessary and the energy demand is said to be lower than in T-mixers. In this way, lamellae are generated in a very thin and narrow helical pattern. The mixer was characterized for its macro and micro mixing using a reaction sensitive to back-mixing. The power demand was also tested.

The above-mentioned results were presented in the framework of an oral presentation [108]. In the open literature there is no further information known to the authors.

**1.3****Passive Mixing**

## 1.3.1

**Vertical Y- and T-type Configuration Diffusive Mixing****Most Relevant Citations**

Peer-reviewed journals: [68]; proceedings contributions: [57, 69, 70].

Y- and T-type micro mixers resemble mixing tees which are used for simple, undemanding mixing tasks conventionally. Whereas the latter are typically operated

under turbulent-flow conditions, their microstructured analogues use solely diffusion in laminar regimes for mixing, by virtue of decreasing the distances and enlarging the specific interfaces, respectively.

When mixing is done exclusively by diffusion, bi-layered flow typically is given. This bi-layer can be arranged vertically (with respect to the plane of mixer plate or the ground level of the mixing channel) or horizontally. In the first case, a two-level feed section is required which is placed on top of each other at the injection zone into the mixing channel. Horizontal injection can be realized more simply with regard to microfabrication; two branches of a T or a Y merge within one plane and are followed by the mixing channel.

In a simulation study, generic investigations on the impact of design details of Y- and T-type micro mixers of the mixing efficiency for gaseous mixing were made [57]. Similar findings were reported for liquid mixing in cross- and T-type micro mixers [57, 68–70].

#### 1.3.1.1 Mixer 24 [M 24]: T-type Micro Mixer

A design of a T-type micro mixer was proposed with the same cross-sections in the feed branches and the mixing channel attached [57]. The T-shape was exactly matched, i.e. the branches are at a 90° angle to the mixing channel.

Mixer type	T-type micro mixer	Mixing channel width, depth, length	500 μm, 300 μm, 5 mm
Mixer material	Artificial design	Angle between branch and mixing channel	90°
Feed branch channel width, depth, length	500 μm, 300 μm, 5.5 mm		

#### 1.3.1.2 Mixer 25 [M 25]: Y-type Micro Mixer

A design of a Y-type micro mixer was proposed with the same cross-sections in the feed branches and the mixing channel attached [57]. The Y-shape was matched, i.e. the branches are at 45° angle. An inverse Y-shape design with a –45° angle was also proposed.

Mixer type	Y-type micro mixer	Mixing channel width, depth, length	500 μm, 300 μm, 5 mm
Mixer material	Artificial design	Angle between branch and mixing channel	45°
Feed branch channel width, depth, length	500 μm, 300 μm, 5.5 mm		

#### 1.3.1.3 Mixer 26 [M 26]: Y-type Micro Mixer with Venturi Throttle

A design of a Y-type micro mixer with a Venturi-type throttle (a tiny orifice which opens like a diffuser to the mixing channel) at the connection of feed branches and

mixing channel was proposed [57]. The same cross-sections were assumed for the feed branches and the mixing channel attached.

Mixer type	Y-type micro mixer with Venturi throttle	Mixing channel width, depth, length	500 $\mu\text{m}$ , 300 $\mu\text{m}$ , 5 mm
Mixer material	Artificial design	Angle between branch and mixing channel	45°
Feed branch channel width, depth, length	500 $\mu\text{m}$ , 300 $\mu\text{m}$ , 5.5 mm	Venturi throttle diameter	160 $\mu\text{m}$

#### 1.3.1.4 Mixer 27 [M 27]: Y-type Micro Mixer with Extended Serpentine Path

An Y-junction feeds a long serpentine channel with 18 bends, arranged on a square format [69]. A top plate was thermally bonded under pressure.

Milling was applied for device manufacture [69].

Mixer type	Y-type micro mixer with extended serpentine path	Mixing channel width, depth, length	200 $\mu\text{m}$ , 200 $\mu\text{m}$ , 40 mm
Mixer material	PMMA	Total plate dimensions	30 mm, 30 mm, 50 mm

#### 1.3.1.5 Mixer 28 [M 28]: T-type Micro Mixer with Straight Path

For means of liquid mixing, a mixer device was designed with a simple T-structure with a straight mixing channel [68]. The width of the mixing channel is twice the width of the inlet channels to ensure undisturbed vertical bi-lamination. At the three ends of the mixing channel structure small square ports are formed which are connected to larger square inlet ports for flow guidance to the macro world.

Mixer type	T-type micro mixer with straight path	End port at channels	500 $\mu\text{m}$ $\times$ 500 $\mu\text{m}$
Mixer material	Silicon/Pyrex glass	Inlet ports with end ports in the center	2000 $\mu\text{m}$ $\times$ 2000 $\mu\text{m}$
Mixing channel widths	20, 40, 60, 100, 200 $\mu\text{m}$	Thickness of Pyrex top plate	500 $\mu\text{m}$
Inlet channel widths	10, 20, 30, 50, 100 $\mu\text{m}$	Material of bottom plate	Polystyrene
Mixing channel length	5.65 mm	Thickness of bottom plate	2 mm
Channel length of both inlets	3.0 mm	Hole diameter in bottom plate	1.58 mm
Channel depth	Various depths, all < 100 $\mu\text{m}$	Tubing material	PEEK

A silicon wafer was manufactured using three photolithographic and etch steps [68]. Etching was performed from both sides of the wafer so that conduits were produced. Vertical walls were achieved by applying a silicon dry etching technique. Thus, the channels had a rectangular cross-section. The etched silicon structure was anodically bonded to a Pyrex glass wafer. The array of micro mixers produced was then diced into pieces. Using an adhesive, the mixers were bonded to a polymer plate with fluid connectors.

#### 1.3.1.6 Mixing Characterization Protocols/Simulation

[P 21] The mixing of gaseous methanol and oxygen was simulated. The equations applied for the calculation were based on the Navier–Stokes (pressure and velocity) and the species convection–diffusion equation [57]. As the diffusivity value for the binary gas mixture  $2.8 \times 10^{-5} \text{ m}^2 \text{ s}^{-1}$  was taken. The flow was laminar in all cases; adiabatic conditions were applied at the domain boundaries. Compressibility and slip effects were taken into account. The inlet temperature was set to 400 K. The total number of cells was  $\sim 17\,000$  in all cases.

As base case, the following scenario was considered [57]. The velocities of both fluids were set to  $0.3 \text{ m s}^{-1}$ , corresponding to a Peclet number of 8.08 in the mixing channel (see Figure 1.51). The mixing length of the base case amounts to 2.83 mm and the pressure drop is 14.6 Pa.

[P 22] Red and green pen inks were diluted and contacted in a Y-type flow configuration at  $20 \mu\text{l min}^{-1}$  [69]. The colored flows were visualized by a color CCD

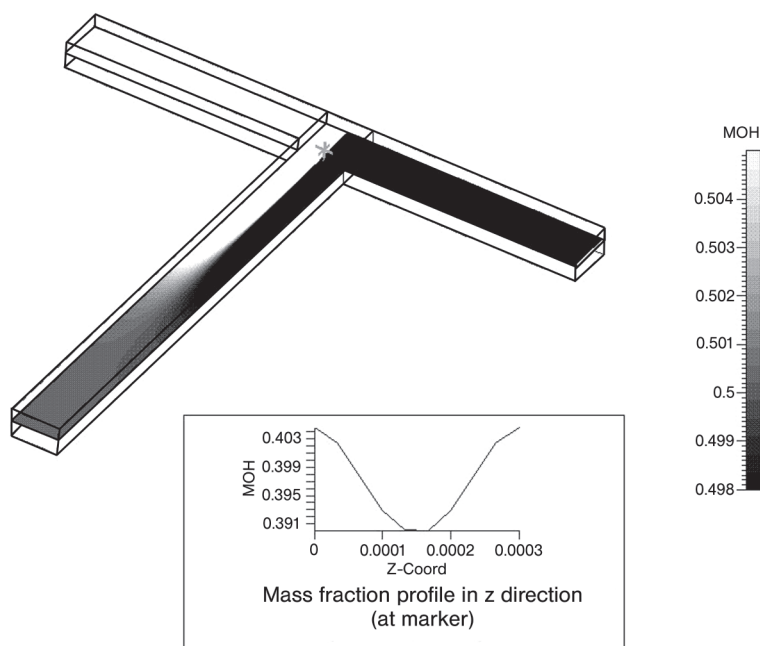


**Figure 1.51** Methanol mass fraction for mixing in the T-micro mixer design with base case geometry and parameters [57].

camera with a magnifying lens using direct illumination of the micro chip from the camera. Color data were extracted from the images.

[P 23] Pumping was achieved by raising the pressure in stainless-steel liquid reservoirs through gas flow from a nitrogen gas cylinder [68]. Albeit maybe involving more technical expenditure than simply using pumps, this has the advantage of notably reduced pulsations. The pressure of the liquid just before entering the micro mixer was measured by a pressure transducer.

A commercial blue dye solution was mixed with colorless deionized water [68]. Images were taken by an optical microscope fitted with a video camera. The color images were converted to gray-scale images and the combined effect of red, green and blue (RGB) elements in a pixel of an image were analyzed. A computer program was written for automated RGB analysis. Using premixed solutions, some sort of calibration curve was obtained.

In analogy with this dilution-type mixing experiment, reaction-type experiments were undertaken so as to have complementary information, that is to get a more 3-D image of the mixing process [68]. The hydrolysis of dichloroacetyl phenol red by sodium hydroxide solution was studied, a reaction known to be completed within about 100  $\mu\text{s}$ . The same RGB analysis and calibration curves as mentioned above were used.

[P 24] Computer simulations were carried out using the software Fluent 6 [68]. A 3-D solid model of the T-channel micro mixer was built and named in Gambit. The simulations were made solely for the zone of the T-junction, since for all other zones, including the downstream section of the mixing channel, laminar flow was assumed. Thus, a fine mesh of 173 000 brick elements could be used for the solid model.

[P 25] Confocal fluorescence microscopy was applied to generate 3-D profiles of the species concentration in a Y mixer [70]. A commercial non-fluorescent compound, Fluo-3 (5 mmol l<sup>-1</sup>), forms a strong fluorescent complex with calcium ions; actually calcium chloride solution (1 mmol l<sup>-1</sup>) was used.

A numerical analysis using FlumeCAD was made, solving the incompressible Navier–Stokes equation for the velocity and pressure fields [70]. The steady-state velocity field was then used in the coupled solution of three species transport equations (two reagents and one product). Further details are given in [70].

### 1.3.1.7 Typical Results

#### Fluid velocity variation – gas mixing

[M 24] [P 21] The inlet gas velocities of gaseous methanol and oxygen were varied from  $1.0 \cdot 10^{-3}$  to  $0.5 \text{ m s}^{-1}$  (Pe range from 0.027 to 13.49) [57]. Mixing lengths in the range of 1–3 mm were determined. At small Pe, mixing occurs at the interface between the fluids in the T-junction. At larger Pe, mixing is completed in the mixing channel and requires the above-mentioned length scale.

#### Aspect ratio variation at constant width – gas mixing

[M 24] [P 21] The base case aspect ratio is 0.6. Applying the parameter set defined for the base case (see [P 21] above), it was found that an increase of the aspect ratio

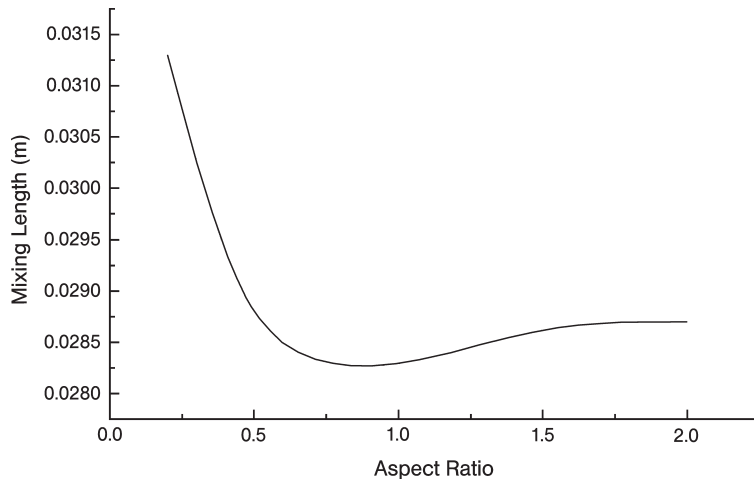


**Figure 1.52** Mixing length as a function of the aspect ratio for a T-type micro mixer with a mixing channel width of 500  $\mu\text{m}$  [57] (by courtesy of IOP Publishing Ltd.).

initially decreases steeply the mixing length, which is attributed to the effect of horizontal wall shear due to different viscosities and hence different velocity profiles (see Figure 1.52) [57]. Thereafter, a minimum exists at an aspect ratio of 0.8. At larger ratios the mixing length increases slightly and becomes invariant of the aspect ratio at a value of 1.5. At increasing aspect ratio, the effect of horizontal wall shear decreases, which leads to a symmetrical velocity profile and hence improved mixing. Diffusion becomes the dominant mixing mechanism at aspect ratios  $> 0.45$ . Mixing is further influenced by the different residence times of the two species and their longitudinal velocities, giving rise the minimum curve observed.

#### Aspect ratio variation at constant hydraulic diameter – gas mixing

[M 24] [P 21] The hydraulic diameter of the base case channel is 375  $\mu\text{m}$  [57]. On increasing the aspect ratio at this constant hydraulic diameter, a monotonically decreasing mixing length is found. This is due to a decrease in the diffusion distances in the vertical to the flow. However, some of this mixing improving effect is counterbalanced by velocity gradients in the longitudinal direction, reducing to an extent the mixing efficiency.

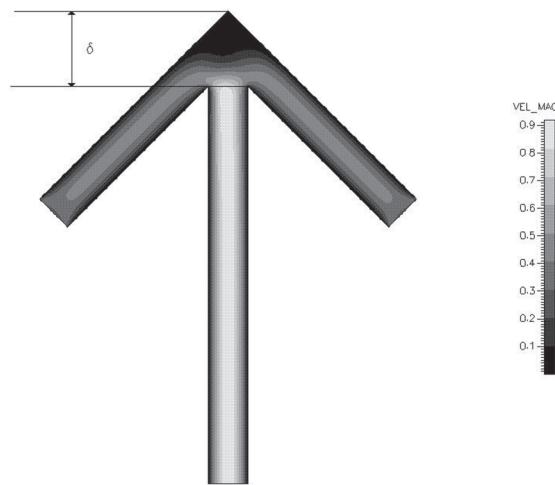
#### Mixing angle variation – gas mixing

[M 25] [P 21] The impact of the mixing angle on the mixing efficiency and the pressure drop was investigated [57]. Physically speaking this is equivalent to transferring the T design into a Y or inverse Y design. The angle values are defined with respect to the horizontal, i.e. the feed branch axis of the T-mixer. Thus, the angle of the latter device is  $0^\circ$ , whereas the normal Y design has a value of  $45^\circ$ .

The variation of the mixing length, from 1.93 to 2.25 mm, is fairly small compared with the changes in the feed angle, from  $+45^\circ$  to  $-65^\circ$  (see Table 1.2) [57]. Therefore,

**Table 1.2** Calculated mixing lengths and pressure drop for Y-type micro mixers with different mixing angles of the two feed branches [57].

Mixing angle (°)	Mixing length (mm)	Pressure drop (Pa)
+45°	2.03	3.54
+30°	1.93	3.57
+20°	1.93	3.59
+0°	1.96	3.64
-20°	1.97	3.68
-45°	2.12	3.71
-65°	2.25	3.76

**Figure 1.53** Velocity magnitude contours of gas flows in an inverse Y-type micro mixer with a  $-45^\circ$  mixing angle at 0.3 m inlet velocities [57] (by courtesy of IOP Publishing Ltd.).

it can be concluded that the angle variation has only a minor impact and, vice versa, this parameter can be chosen rather freely, if other demands make this necessary, e.g. to reduce the footprint area of the mixing element via negative-angle feeds. In contrast, the latter devices have stagnant zones (see Figure 1.53), whereas positive-angle devices have not.

In addition, the angle variation has only a minor impact on the pressure loss, ranging from 3.57 to 3.76 Pa [57].

#### **Venturi-type mixing: impact of throttle diameter – gas mixing**

[M 26] [P 21] One means of speeding up mixing is based on putting an orifice directly after the T-junction [57]. Since this involves built-up of a large pressure drop, special designs for pressure recovery such as Venturi-type designs were introduced. It was aimed to exploit this effect also on the micro-scale. Using a throttle diameter of 160  $\mu\text{m}$  (and otherwise the base-case parameters), differences in the results between 2-D and 3-D simulations were pointed out.

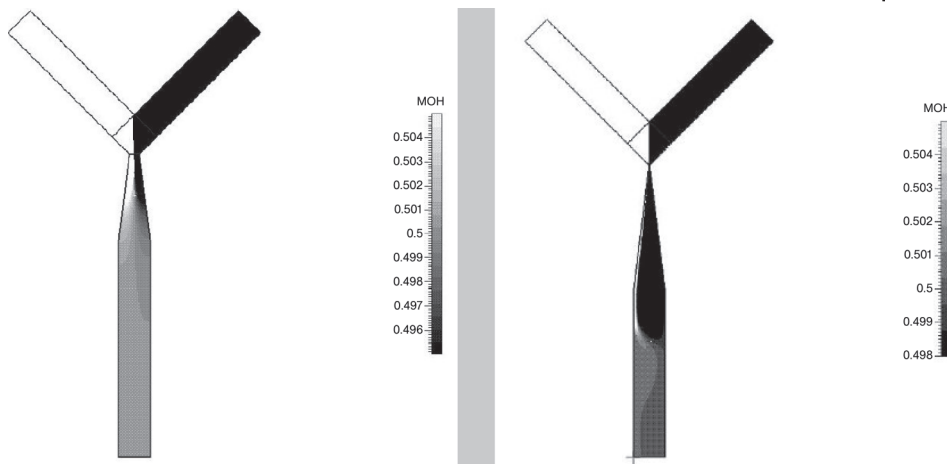


**Figure 1.54** Methanol mass fraction contours in a 160  $\mu\text{m}$  throttle at an inlet velocity of 0.3  $\text{m s}^{-1}$  (left); methanol mass fraction contours in a 10  $\mu\text{m}$  throttle at an inlet velocity of 5  $\text{m s}^{-1}$  (right) [57] (by courtesy of IOP Publishing Ltd.).

Varying the throttle diameter from 10 to 500  $\mu\text{m}$  has a considerable effect on the mixing length, as is to be expected (see Figure 1.54 left) [57]. In this way, the mixing length can be reduced from about 2 mm to < 0.1 mm. The actual shape of the corresponding curve is slightly sigmoidal with points of inflection owing to changes in velocity profiles. Below 10  $\mu\text{m}$  the flow is in the slip regime.

The corresponding pressure drops ranged from 3.54 to 1631 Pa for the largest and smallest throttle sizes [57].

#### **Venturi-type mixing: impact of inlet velocity – gas mixing**

[M 26] [P 21] Only the 10  $\mu\text{m}$  throttle is capable of completing gas mixing within the length of the mixing channel attached even at high gas inlet velocities [57]. Thus, for this design the inlet velocities were varied up to 5  $\text{m s}^{-1}$ . For the latter velocity, a mixing length of 3.5 mm results. The corresponding pressure drops range from 1632 to  $125 \cdot 10^3$  Pa [57].

An increase of the mixing length with increasing inlet velocity is found, displaying two points of inflection [57]. The first point at low velocity is associated with a core fluid moving at higher velocity within the throttle. The second, high-velocity inflection relates to the appearance of recirculations just behind the throttle (see Figure 1.54 right).

#### **Use of color data – liquid mixing**

[M 27] [P 22] The applicability of using red, green and blue color data to imagine bi-laminated flows from red and green solutions is discussed in [69]. Finally, the red color data were chosen for further investigations.

In this way, cross-sectional concentration profiles could be determined with fairly high accuracy [69].

**Impact of surface roughness and bend shape – liquid mixing**

[M 27] [P 22] The impact of surface roughness in micro channels and of bends on the mixing of a bi-laminated fluid was investigated [69]. The surface roughness of the mixing channel was varied from 0.66 to 38.5  $\mu\text{m}$  by changing the milling speed. Cross-sectional concentration profiles were measured before and after passing a rough/right angle, smooth/right angle and smooth/round corner angle bends. A kind of mixing degree was defined from the ratio of the areas of the concentration profiles.

The highest mixing degree was found for the rough/right angle design, probably owing to secondary flows [69]. The two other designs behaved similarly.

**Detailed visualization of flow patterns at the start and end of a T-channel – liquid mixing**

[M 28] [P 23] The mixing times were compared for four T-channel micro mixers of different dimensions and thus hydraulic diameter at constant Reynolds number [68]. By means of a dilution-type experiment, completeness of mixing was judged from the positions along the mixing channel where a homogeneous color texture was achieved, after having confirmed that the same holds for a reaction-type experiment. The expected sequence of mixing times was found, i.e. the smaller the hydraulic diameter, the shorter is the mixing time. The quantitative data are given in Table 1.3.

**Table 1.3** Liquid mixing times for T-channel micro mixers of varying hydraulic diameter [68].

Channel width, depth ( $\mu\text{m}$ )	Hydraulic diameter of the micro mixer ( $\mu\text{m}$ )	Reynolds number	Mixing time (ms)
200, 82	116	442	1.48
200, 51	81	467	0.97
100, 51	67	489	0.77
60, 51	55	–	–

The millisecond-mixing times are orders of magnitude faster than calculated times for diffusion based on Fick's law [68].

**Detailed visualization of flow patterns at the start and end of a T-channel – liquid mixing**

[M 28] [P 23] The liquid mixing process in the T-shaped micro mixer was investigated using both dilution-type and reactive-type imaging approaches [68]. In order to provide fine details, images were taken at the inlet T-junction and outlet region, both containing roughly half of the mixing channel separately.

Very distinct patterns were found depending on the flow regime [68]. For Reynolds numbers below 150, bi-laminated streams were found, displaying a low degree of color interpenetration and thus mixing. This is in line with the reaction experiments, showing virtually colorless solutions. For  $Re = 150\text{--}400$ , striations are found both in the dilution- and reaction-type experiments, i.e. layer-like fluidic compartments with either predominant dark or light color. This is due to cross-flow of the lamellae starting already at the T-junction. Here, new interfaces are created and mixing is

intensified. The formation of striations is more pronounced in the dilution-type than the reaction-type experiments. This is indicative of segregation of the lamellae into compartments of still comparatively large volume. For  $Re > 400$  (up to 500 being investigated), fairly homogeneous color textures result for both types of imaging.

#### Simulation of liquid flow at the T-junction – liquid mixing

[M 28] [P 23] The liquid flow was simulated for six different scenarios, involving symmetrical and asymmetric flow rates, equal and different viscosities and presence or absence of vertical velocity components [68]. A mixer device with a 100  $\mu\text{m}$  channel was taken.

*Scenario 1:* For the symmetrical case (equal flow rates and viscosities), almost no penetration of the liquid layers into each other is achieved [68]. Symmetrical fluid trajectories along the two symmetry planes of the mixing channel result (see Figure 1.55).

*Scenario 2:* For the case with a vertical ( $z$ -) flow velocity component, one layer went slightly upwards, the other slightly downwards (actually the  $z$ -component was only 1% of the  $y$ -velocity along the channel axis) [68]. Upon collision, a swirling flow is formed and a transverse motion of species is induced, strongly enhancing mixing (see Figure 1.56).

*Scenario 3:* This effect is only given at high Reynolds number (489) and is not observed at low Reynolds number (121).

*Scenario 4:* For the asymmetric case, i.e. different flow rates (at the same viscosity), also penetration of species from one layer to the other was observed [68].

*Scenario 5:* For dissimilar viscosities, one having twice the value of the other, also penetration of the lower-viscosity species into the high-viscosity layer was observed [68].

*Scenario 6:* When the  $z$ -component was more intense, 10% of the  $y$ -velocity component instead of 1%, the highest degree of penetration from all six scenarios was reached [68].

The mixing efficiency was characterized by a dimensionless parameter, called the intensity of segregation, for the six scenarios [68]. This parameter is based on the distribution of the mass fractions of the species. The results given in Table 1.4 show the importance of the  $z$ -component of the flow velocity to induce penetration of species and thus to promote mixing.

**Table 1.4** Dimensionless values for the intensity of mixing at the outlet face of the T-channel micro mixer for the six scenarios simulated [68].

Scenario	1	2	3	4	5	6
Intensity of mixing	0.36	0.71	0.34	0.35	0.55	0.83

The results show that small undulations such as inaccurate surface profiling of the micro channels, possibly inducing a  $z$ -component or leading to asymmetric flow rates, may considerably change mixing [68]. The same holds when asymmetric flow pumping is given for external reasons, e.g. improper action of pumping such as pulsations.

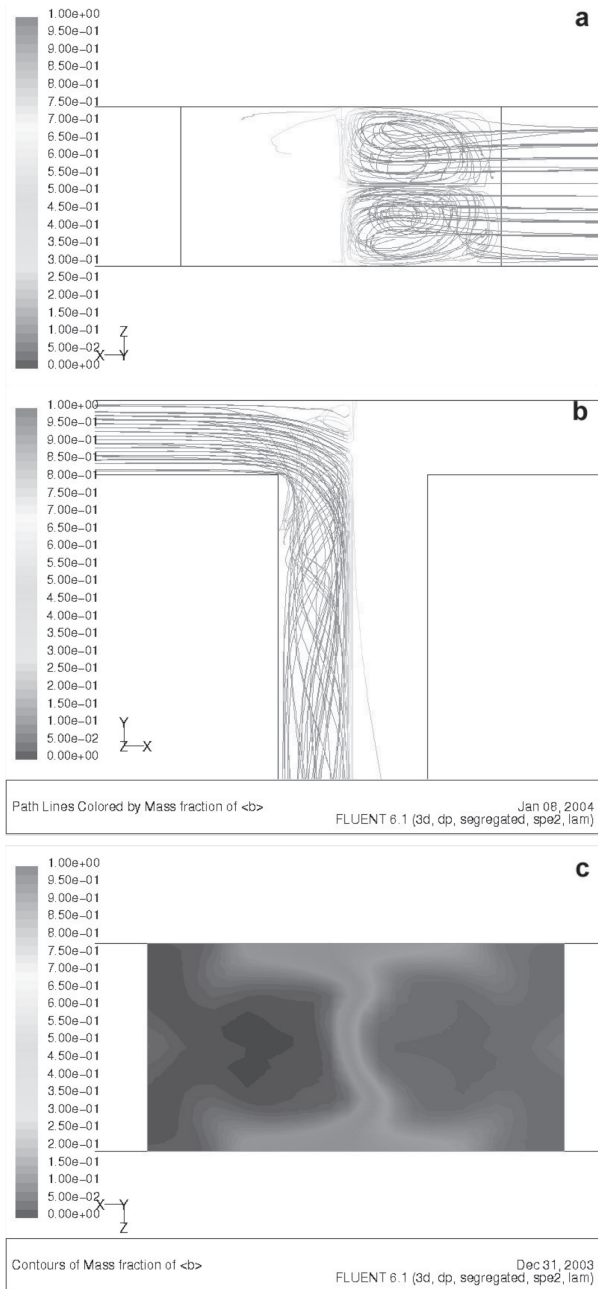


**Figure 1.55** Scenario 1: symmetric flow rates lead to symmetric flow fields giving an overall two-layered fluid structure with hardly any species penetration and a low degree of mixing. (a) and (b) show fluid trajectories of one species for the cross-sectional area at the mixing channel front and the whole T-channel design; (c) gives a mass-fraction contour plot of the other species at the outlet face [68] (by courtesy of Elsevier Ltd.).

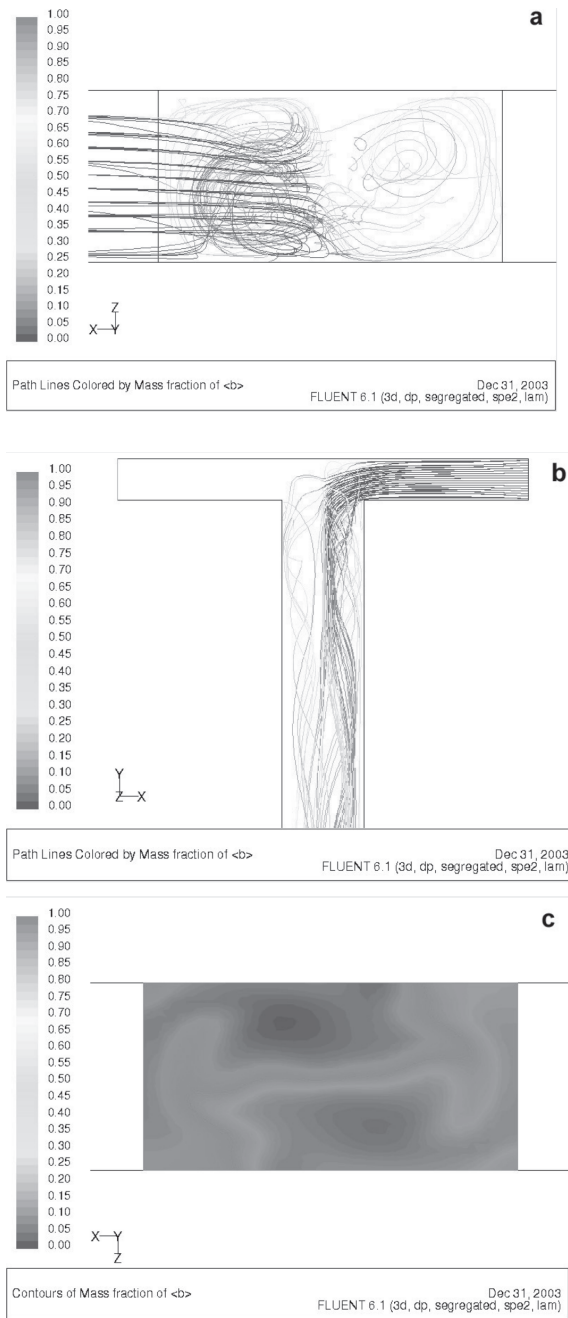


**Figure 1.56** Scenario 2: vertical z-components of the flow lead to species penetration and induce secondary flows. (a) and (b) show fluid trajectories of one species for the cross-sectional area at the mixing channel front and the whole T-channel design; (c) gives a mass-fraction contour plot of the other species at the outlet face [68] (by courtesy of Elsevier Ltd.).

**Relationship of pressure drop and Reynolds number – liquid mixing**

[M 28] [P 23] According to laminar flow theory, the Reynolds number of the flow varies linearly with the pressure gradient [68]. This is only given for one T-channel mixer device presented above, whereas all others show progressively less increase in Reynolds number with increasing pressure gradient. This is due to the recirculations of the crossing flows mentioned above. While at low Reynolds number the viscous forces dominate, the inertia forces for the reasons given above come into play. This consumes part of the energy of the flow, which is used for mixing and decreases the flow velocity.

Based on these considerations, a schematic was proposed showing regions of vortices and of secondary cross flow in the T-junction by which the findings given above can be explained (see Figure 1.57) [68]. This is said to resemble secondary flow of Prandtl's first kind as a result of centrifugal force when fluid flows in curved path.

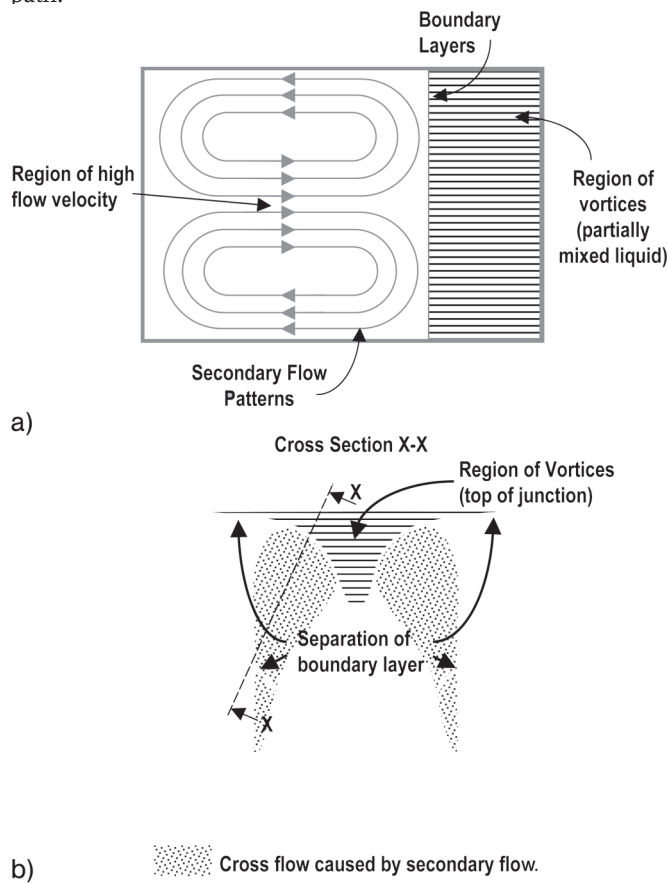


**Figure 1.57** (a) Cross-sectional view of the image (b) at X–X showing the separation of a partially mixed zone and a recirculation zone, inducing cross flow for mixing. (b) Top view of the T-junction showing the respective distribution of the same zones [68] (by courtesy of Elsevier Ltd.).

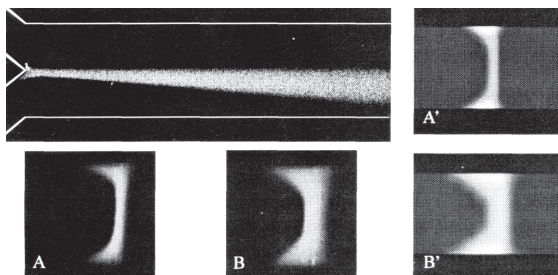


**Figure 1.58** Experimental images of the lateral and cross-sectional profiles of a fluorescent species formed by mixing and subsequent immediate reaction. Left, experimental images; right, simulated images [70] (by courtesy of Kluwer Academic Publishers).

#### Cross-sectional concentration profiles in a Y micro mixer

(No details on mixer in [109]) [P 25] By use of confocal microscopy, cross-sectional concentration profiles were derived in a Y micro mixer (see Figure 1.58) [70]. At the top and bottom of the channel large fluorescent areas were found, while this region thinned in the channel center. The experimental images perfectly match the simulated concentration profiles.

Similar very good agreement was found for a quantitative mixing analysis when determining the diffusive widths at various locations along the mixing channel and for various flow rates [70]. Thus, the use of the confocal fluorescence technique for complex mixing analysis was demonstrated and compared with the potential of standard microscopy set-ups.

#### 1.3.2

##### Horizontally Bi-laminating Y-feed Mixing

###### Most Relevant Citations

Peer-reviewed journals: [110].

The usually slow mixing characteristics of unfocused bi-lamination can be exploited for a purpose. It allows one the sensing of a reaction in a rather unmixed state and, by stopping the flow, to have short mixing reaching the reaction state [110]. Thus, by pulsing the flow rate, rapid switching between reactant and product flows can be achieved, e.g. to investigate the kinetics of a reaction. In one realized example (see below), only two streams were layered (bi-lamination), albeit fed by multi-channel feeds.

##### 1.3.2.1 Mixer 29 [M 29]: Unfocused Horizontally Bi-laminating Y-feed Micro Mixer

An interdigital micro mixer with two multi-parallel feed lines and a rectangular mixing chamber was realized for pulsed/stopped-flow operation of reacting flows [110]. The feed lines are mirror-imaged inclined to the longitudinal axis of the mixing chamber and 'merge' to an alternate pattern just in front of the latter. Actually, only a bi-lamination is achieved since in each multi-channel feed, i.e. on one device level, only one fluid is guided. The parallel splitting serves to achieve a homogeneous distribution of the flow in the axial direction.

The material choice and hence the microfabrication was based on the specific needs of Fourier transform infrared (FTIR) spectroscopy, to have IR-transparent materials [110]. For this reason,  $\text{CaF}_2$  disks are an essential part of the device. The main part of the device consists of two polymer layers sandwiching one metal layer which are encased by the two disks, acting as a kind of end plates.

In a first step, the negative working photoresist SU-8 is spin-coated on to the disk and soft baked [110]. The disk is then UV-exposed to pattern the bottom layer. A silver thin metal layer is thereafter evaporated. The metal layer is spin-coated with an AZ-type photoresist, dried, exposed and developed. In this way, the metal layer can be developed independently from the patterning of the SU-8 layer underneath. The metal layer is patterned by wet-chemical etching. As a next step, a second SU-8 layer is deposited, soft-baked and exposed. Top and bottom layers are now developed. After a hard bake, a second  $\text{CaF}_2$  disk is attached to the stack and sealed by a light-curing epoxy resin.

Mixer type	Unfocused bi-lamination micro mixer	Metal layer material	Silver (evaporated)
Mixer material	Polymer SU-8	Metal layer thickness	2 $\mu\text{m}$
Polymer layer thickness	$\sim 10 \mu\text{m}$	Number of feed channels	7
Inspection window material	$\text{CaF}_2$	Feed channel width, depth	100 $\mu\text{m}$ , $\sim 10 \mu\text{m}$
Inspection window thickness, diameter	1 mm, 20 mm	Mixing channel width, depth	1 mm, $\sim 22 \mu\text{m}$

### 1.3.2.2 Mixing Characterization Protocols/Simulation

[P 26] Time-resolved FTIR spectroscopy was performed by operation of an infrared spectrometer in the rapid scan acquisition mode (see Figure 1.59) [110]. The effective time span between subsequent spectra was 65 ms. Further gains in time resolution can be achieved when setting the spectral resolution lower (here  $8 \text{ cm}^{-1}$ ) or by using the step-scan instead of rapid-scan mode.

For liquid feed, a double-channel syringe pump with two 500  $\mu\text{l}$  syringes, a high-speed pneumatic switching valve and PTFE tubing with an inner diameter of 254  $\mu\text{m}$  was used [110]; 0.5  $\mu\text{m}$  PTFE microfilters were set in front of the micro mixer to remove particles. The flow rate was set to  $6 \text{ ml h}^{-1}$ .

For repetition of stopped-flow shots, the control software of the spectrometer and the software for pump and valve operation were coupled [110]. A typical FTIR measurement section was as follows. After start of the pumping with opened valve, the FTIR spectrometer recorded five interferograms for the unmixed state, prior to reaction. Following a signal by the spectrometer, the valve switched to the stopped-flow mode. Now the liquid was standing in the mixing channel and mixing took place via diffusion. By continued FTIR scanning the course of reaction could then be followed. Now the valve was opened again and the sequence could be repeated as often as desired to obtain a sufficient signal-to-noise ratio.

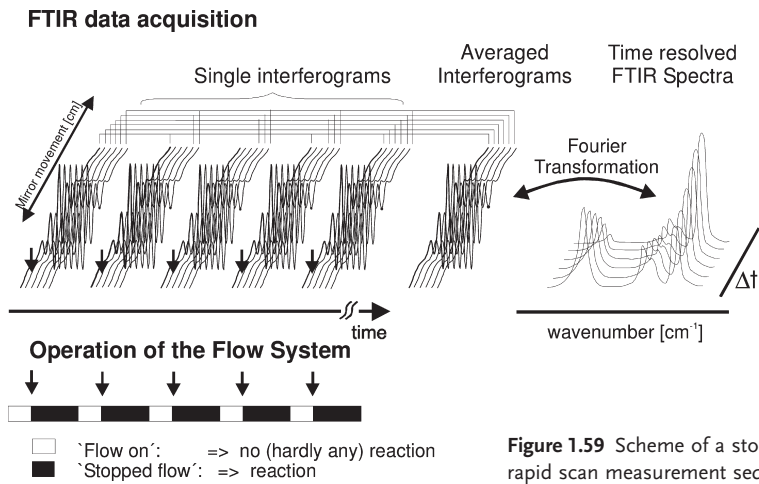


**Figure 1.59** Scheme of a stopped-flow rapid scan measurement sequence [110] (by courtesy of RSC).

### 1.3.2.3 Typical Results

#### Velocity and pressure profiles by CFD simulations

[M 29] [P 26] Even velocity profiles are found throughout the whole rectangular mixing channel at a pressure drop of 0.8 bar [110]. This pressure drop is considerably lower than for a former, similar design with more complex feed.

#### Contour plot of mass fractions/mixing time/pre-mixing

[M 29] [P 26] A calculated contour plot of the mass fraction of one component with a diffusion coefficient of  $1 \cdot 10^{-9} \text{ m}^2 \text{ s}^{-1}$  is indicative of diffusive mixing [110]. It can be seen that completion of mixing is only expected at larger distances from

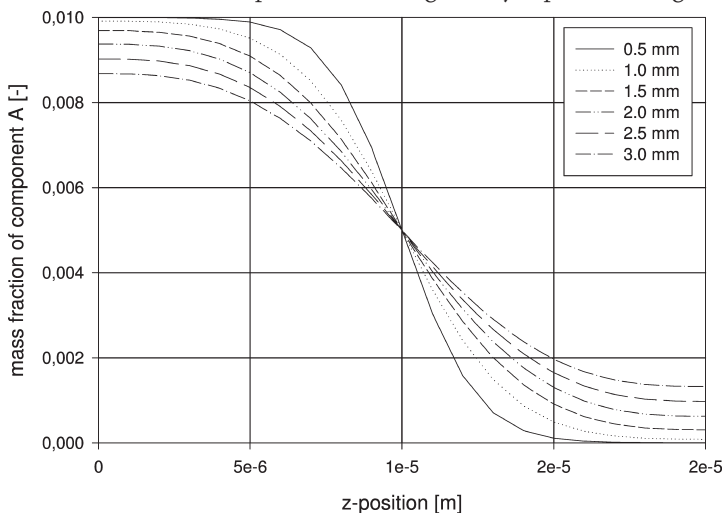


**Figure 1.60** Contour plot of the mass fraction of one component with a diffusion coefficient of  $1 \cdot 10^{-9} \text{ m}^2 \text{ s}^{-1}$  across the longitudinal axis of the mixing channel at various distance from the feed section [110] (by courtesy of RSC).

the inlet. Pre-mixing takes place to a certain extent, which depends on the distance from the feed section (see Figure 1.60).

At a distance of 1.0 mm from the inlet, which corresponds to the center of the IR beam, a mixing time of about 100 ms is calculated for the stopped-flow mode (see *Neutralization model reaction*, below) [110]. This mixing time is < 50% compared with a previous, similar design with more complex feed.

#### Neutralization model reaction

[M 29][P 26] The neutralization of acetic acid with sodium hydroxide is an extremely fast reaction which can be monitored by FTIR spectroscopy [110]. The speed of the reaction allows one to monitor mixing directly, since the reaction will always immediately follow the mixing course. It can be seen that the time for completion of mixing is about 100 ms, in good accord with the simulation results (see Figure 1.61 and *Contour plot of mass fractions/mixing time/pre-mixing*, above).

It also evident from the FTIR spectra that a certain degree of pre-mixing, due to diffusion in the continuous-flow mode, occurred, leading to a correspondingly large pre-reaction [110].

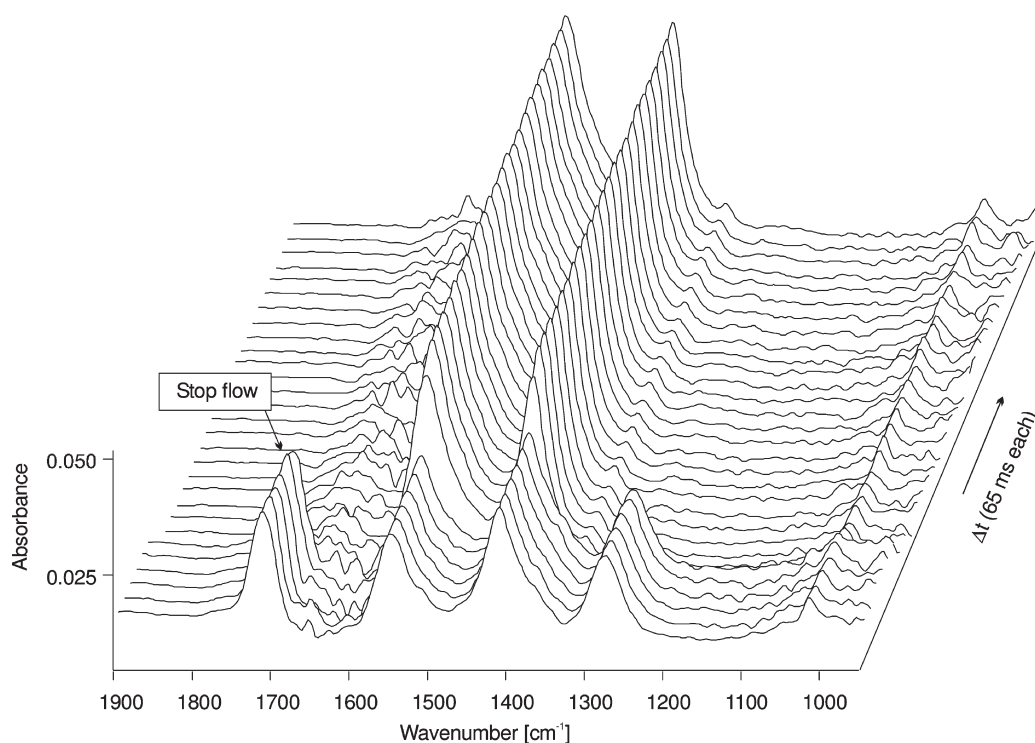


**Figure 1.61** Stack plot of FTIR spectra at various time spans (each 65 ms) for the neutralization reaction between acetic acid and sodium hydroxide [110] (by courtesy of RSC).

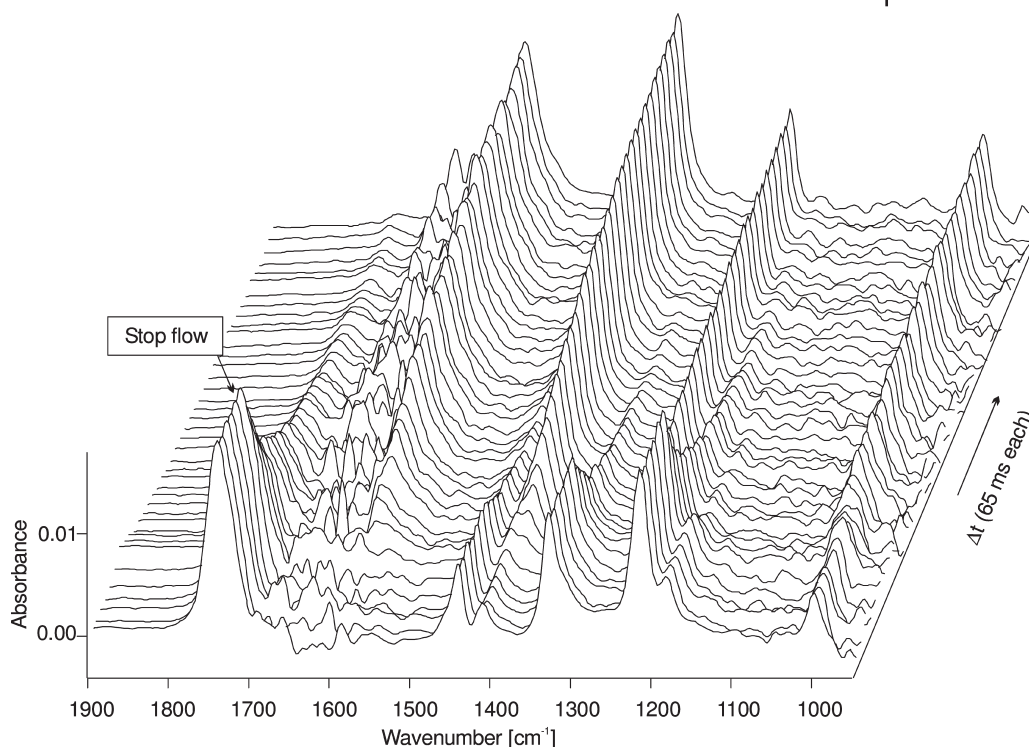


**Figure 1.62** Stack plot of FTIR spectra at various time spans (each 65 ms) for the saponification reaction between methyl monochloroacetate and sodium hydroxide [110] (by courtesy of RSC).

#### Saponification model reaction

[M 29] [P 26] The saponification of methyl monochloroacetate with sodium hydroxide is a slow reaction which can be monitored by FTIR spectroscopy [110]. Owing to the slow reaction, despite pre-mixing no detectable reaction could be monitored by FTIR (compare with *Neutralization model reaction*). On stopping the flow, the reaction products chloroacetate and methanol appear (see Figure 1.62). After a few hundred milliseconds of reaction time, the reaction is completed.

#### Accessible FTIR spectral region

[M 29] [P 26] When using water as liquid (see description of the two reactions, above), the accessible spectral region to follow chemical reactions was determined as 950–1600 and 1700–3000  $\text{cm}^{-1}$  [110]. Owing to the strong absorption of the bending vibration of the solvent water, the 1600–1700  $\text{cm}^{-1}$  region cannot be used. This poses a limit for monitoring biological samples having amide bonds which absorb in the same spectral region.

## 1.3.3

**Capillary-force, Self-filling Bi-laminating Mixing****Most Relevant Citations**

Proceedings contributions: [111].

The development of this mixing concept orients on generating a portable tool for medical and environmental analysis, preferably done in field experiments on-site [111]. This means first of all eliminating pumps for feeding of the solutions to be mixed, since these are usually costly and heavy parts. In addition, ruggedness was a major desire, since many field samples contain particles or are contaminated, different from 'clean' laboratory probes. Hence the target was to find a simple self-filling principle which in turn more or less automatically is followed by reasonably fast mixing.

Capillary forces are a suitable means for manual self-filling of samples into minute channel cavities [111]. However, this usually allows one to fill in only one liquid. Therefore, a specially technique had to be developed which allows the filling of two liquids, based on a self-closing and self-re-opening mechanism.

**1.3.3.1 Mixer 30 [M 30]: Capillary-force, Self-filling Bi-laminating Micro Mixer**

Two adjacent micro channels of trapezoid shape are separated by a type of cantilever structure leaving a small gap which can permit fluid contact (see Figure 1.63) [111]. The left channel has a smaller cross-sectional area and is placed at a higher position than the other more voluminous channel.

The first solution, the sample taken in the field, is filled in the upper channel by using the capillary-force self-filling mechanism (see Figure 1.64) [111]. By capillary forces the cantilever is slightly bent and automatically closes the sample volume, leaving the second channel still unfilled. The second solution to perform the analysis is filled into the second channel, directly on-site or later, in the latter case still manually or also by using pumps.

The device actually made contained seven pairs of such adjacent channels with a small gap, placed in parallel in a quadratic format [111].

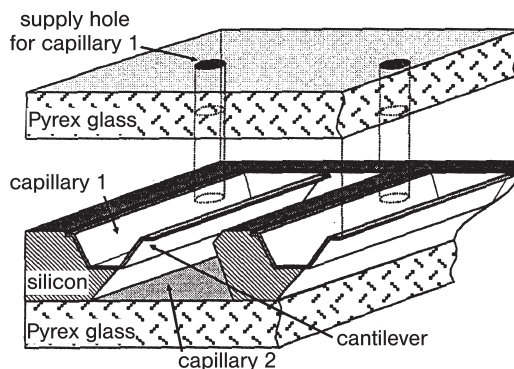


**Figure 1.63** Schematic of the capillary-force, self-filling device [111] (by courtesy of Springer-Verlag).

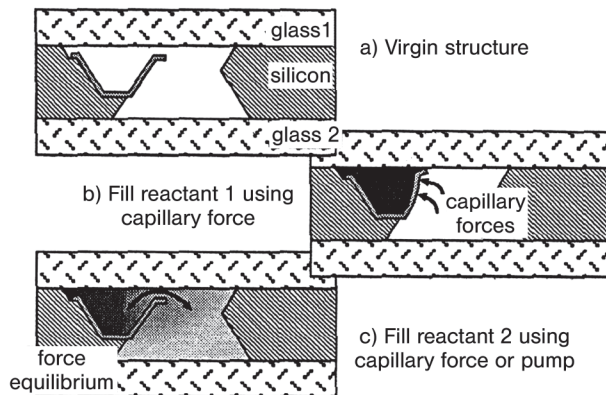


**Figure 1.64** Schematic of the capillary-force, self-filling and self-closing mechanism, followed by re-opening, again owing to capillary forces. Thereafter, an interface is provided for mixing of the solutions, being previously encased [111] (by courtesy of Springer-Verlag).

It can be envisaged that, facing the target application in environmental and medical analysis, cleaning can be done by solvents or hot vapor [111]. Alternatively, disposable materials may be employed so that the device can be used as once-only tool. For medical analysis, the integration of a needle may be advisable.

The channels are anisotropically etched into silicon and are separated by a thin  $\text{SiO}_2$  layer, the cantilever [111]. This microstructure, open to both sides, is closed by anodic bonding to Pyrex glass wafers.

Mixer type	Capillary-force, self-filling bi-laminating micro mixer	Gap for diffusion	20 $\mu\text{m}$
Mixer material	Silicon	Volume channel 1	0.22 $\mu\text{l}$
Cover material	Pyrex	Volume channel 1	0.86 $\mu\text{l}$
Channel width, depth, length for liquid 1	300 $\mu\text{m}$ , 200 $\mu\text{m}$ , 10 mm	Total size of the mixing chip	20 $\times$ 20 mm
Channel width, depth, length for liquid 2	500 $\mu\text{m}$ , 300 $\mu\text{m}$ , 10 mm	Pairs of adjacent channels	7
Cantilever plate thickness, length, height	2 $\mu\text{m}$ , 10 mm, 245 $\mu\text{m}$		

### 1.3.3.2 Mixing Characterization Protocols/Simulation

[P 27] Red and blue comestible colors were chosen as test liquids [111].

Analysis was done using light microscopy [111]. Owing to the transparent glass cover, other spectroscopic techniques such as UV-Vis can also be applied.

### 1.3.3.3 Typical Results

#### Confirmation of self-filling and automixing principles

[M 30] [P 27] The self-filling principle was confirmed by introducing two colored solutions serially into the channels [111]. This also proved the self-closing mechanism of the cantilever, because no cross-over of liquids was observed. A gross change of color in the larger channel could be observed as the end result of diffusion of two colored solution into each other. Details of the diffusion process itself could not be observed owing to the limited contrast of the light microscopy observation.

#### Mixing Time

[M 30] [P 27] Based on general assumptions of diffusion in aqueous solutions, the mixing in the self-filling device is assumed to be of the order of seconds and minutes [111]. This is slow compared with other micro mixers, but having a fast mixing time is not a requirement for the target applications of the device, namely field analysis and medical applications. The time needed for mixing is more than given during sampling and transfer to the measuring equipment.

### 1.3.4

#### Cross-injection Mixing with Square Static Mixing Elements

##### Most Relevant Citations

Proceedings contributions: [71].

The insertion of small static mixing elements (SME) is common to achieve swirls and eddies in pipe flow, albeit usually not being turbulent [71]. The flow obstacles are fairly small compared with the pipe diameter, unlike typical packings of static mixers which fully cover the diameter of the channel. Such mixing elements provide abrupt changes in surface orientation to result in flow separation and subsequent eddy production.

#### 1.3.4.1 Mixer 31 [M 31]: Cross-shaped Micro Mixer with Static Mixing Elements

The channel structure of the mixer is a simple cross, i.e. four channels which all merge at one junction [71]. A cross was preferred over a T-channel mixer since two interfaces instead of only one are initially created when the fluids are contacted. The top channel feeds one fluid, while the other fluid is injected via the left and right channels. The last, bottom channel functions as mixing and outlet zone. Squares, much smaller than the channel width, are positioned at the walls of this mixing channel and function as static mixing elements. The squares are positioned on alternate sides of the channels and at a distance corresponding to multiple square widths.

Three versions of the cross-shaped mixer were designed for simulation [71]. One version contained no SMEs, one was equipped with two SMEs on alternate sides of the mixing channel, and one with five SMEs, two of them in the inlet side channels directly at the cross and three on alternate sides of the mixing channel.

A micro fabrication of the designs mentioned above has not been realized so far; the designs were only taken for simulation [71].

Mixer type	Cross-shaped micro mixer with static mixing elements	Outlet channel width, depth	30 $\mu\text{m}$ , 40 $\mu\text{m}$
Mixer material		Side channel width, depth	25 $\mu\text{m}$ , 40 $\mu\text{m}$
Inlet channel width, depth	40 $\mu\text{m}$ , 40 $\mu\text{m}$	Static mixing element width, length, depth	10 $\mu\text{m}$ , 10 $\mu\text{m}$ , 40 $\mu\text{m}$
Distance cross-second SME (Two-SME design)	75 $\mu\text{m}$	Distance cross-first SME (Two-SME design)	45 $\mu\text{m}$

#### 1.3.4.2 Mixing Characterization Protocols/Simulation

[P 28] A 3-D solid model of the cross-shaped micro mixer is meshed to a sufficiently fine scale with brick elements of 2  $\mu\text{m}$  for the simulations [71]. Simulation results were intended at very short time scales, e.g. in intervals of 50  $\mu\text{s}$ , to verify the mixing patterns at the initial state after application of pressure. The numerical values of the mass fraction are taken to give quantitative measures of the mixing efficiency. The pre-processor fluidics solver and post-processor of ConventorWare<sup>TM</sup> were used for the simulations. The software FLUENT 5 was used for verification of these results, since the former software is so far not a widely established tool for fluid dynamic simulation.

A pressure of 2 bar was set at the inlets and of  $2 \cdot 10^{-4}$  bar at the outlet of the micro mixer [71].

#### 1.3.4.3 Typical Results

##### Comparison of cross-injection mixing without and with static mixing elements

[M 31] [P 28] Flow simulations revealed that swirled flow generating eddies can be achieved in a cross-shaped micro mixer with SME [71]. Comparing the distribution of the mass fractions at the mixing channel's outlet, it is evident that complete mixing can be achieved for the cross-shaped mixer with two SMEs, whereas the same overall channel structure without any SMEs, a simple straight channel, is still largely segregated, exhibiting a coiled three-layered fluid (see Figure 1.65).

##### Time evolution of the flow patterns in the cross-injection SME mixing at the initial stage

[M 31] [P 28] The time evolution of the flow patterns in the cross-shaped micro mixer with two static mixing elements was monitored by simulation at time intervals of 50, 150, 500  $\mu\text{s}$  and 1 ms after application of pressure [71]. In addition to seeing the evolution of the swirling patterns, it was concluded from this analysis that at 500  $\mu\text{s}$  a nearly homogeneous distribution of the mass fractions is given and at 1 ms this is indeed completed. Hence the theoretical mixing time of the mixer may be below 1 ms.

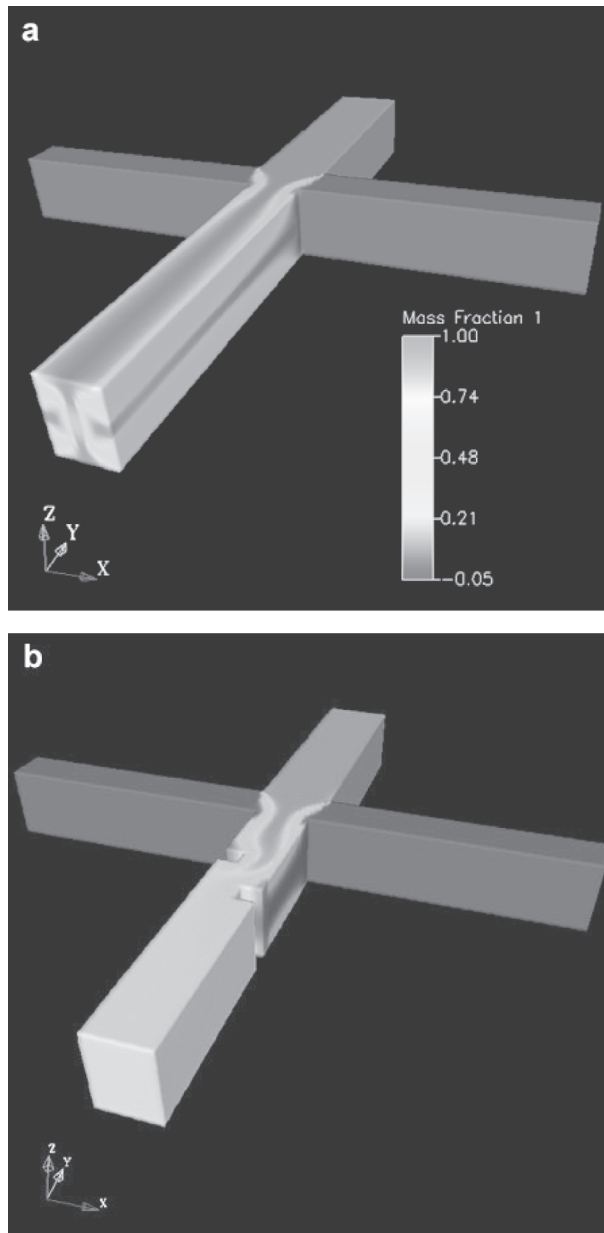


**Figure 1.65** CFD simulations giving 3-D mass contour plots in the cross-channel structure for a design without and one with two static mixing elements. The completeness of mixing can be judged from the cross-sectional mass distribution at the outlet [71] (by courtesy of Elsevier Ltd.).

#### Verification of the ConventorWare™ software

[M 31] [P 28] The flow patterns simulated by the ConventorWare™ and FLUENT 5 software concerning the flow in the cross-shaped micro mixer with two static mixing elements the same; hence the predictability of the ConventorWare™ software was demonstrated [71].

#### Velocity vector and contour plots

[M 31] [P 28] Velocity vector plots show the separation of the boundary layer before and after approaching the static mixing element [71]. Backflow occurs in the separation region. By this unsteady reattachment of the flow, new interfaces are constantly generated, when the flow has to pass a series of such mixing elements.

The velocity contour plots show a higher velocity, a higher velocity gradient and rapid change of the direction of the velocity components in the proximity of the static mixing elements compared with the rest of the flow in the channel (see Figure 1.66) [71].

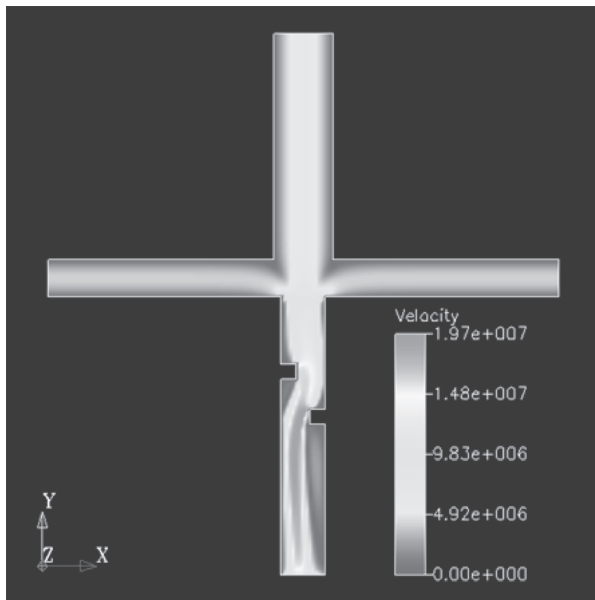


**Figure 1.66** Velocity contour plots of the flow in the cross-channel mixer [71] (by courtesy of Elsevier Ltd.).

#### Pressure drop plots – intensity of segregation and velocity vector plots

[M 31] [P 28] Pressure drop plots show that the bulk of the pressure drop occurs in the mixing channel due to the action of the static mixing elements [71]. This means that the additional pressure drop has to be paid for by speeding up mixing, e.g. at the cost of reducing the overall flow rate. The decrease in flow rate is estimated to be 30–37% compared with flow through a straight channel of the same size. However, this loss in capacity is more than counterbalanced by the increased mixing

performance, as the calculated intensities of segregation and variation coefficient show. The latter are measures for the mixing efficiency. Here, the cross-shaped micro mixers with SMEs are much better than the same channel structure without static elements (see Table 1.5). The incorporation of five elements is still better than a two-SME cross-shaped mixer, having completion of mixing already after flow passage through the SME zone (without the need to further pass the residual open channel).

**Table 1.5** Measures for mixing efficiency calculated from mass contour plots yielded by CFD simulation – benchmarking cross-shaped mixers with and without static mixing elements (SME) [71].

<b>Flow configuration</b>	<b>Intensity of segregation</b>	<b>Coefficient of variation</b>	<b>Flow rate (<math>\mu\text{l s}^{-1}</math>)</b>	<b>Mean flow velocity (<math>\text{m s}^{-1}</math>)</b>
No SME	0.3115	0.5343	11.9	9.92
2 SMEs	0.0211	0.1349	8.55	7.13
5 SMEs	0.0006	0.0210	7.45	6.21

### 1.3.5

#### Hydrodynamic Focusing Cross-Injection Mixing

##### Most Relevant Citations

Peer-reviewed journals: [112]; proceedings contributions: [113].

Ultra-fast diffusive mixing can only be achieved by an extreme reduction of the fluid layer thickness, being not more than several tens of nanometers [112]. Microfabricated devices alone are not adequate to generate such thin lamellae. Therefore, further compression of the micrometer thin lamellae, generated in a microstructure, has to be performed by hydrodynamic means. This is achievable by contacting two fluids of extremely different volume flows. Owing to volume conservation, the fluid of higher flow tends to form a thick lamella, while an ultrathin lamella of the other fluid results. Since the final thin lamella thickness is achieved after only a short entrance flow region, the whole process is termed ‘hydrodynamic focusing’.

##### 1.3.5.1 Mixer 32 [M 32]: Hydrodynamic Focusing Cross-injection Micro Mixer

In a cross-flow configuration, one stream with one fluid enters from the left and two streams carrying the same other fluid are fed from above and below [112]. The latter have much larger flow rates as the first stream so that this layer is hydrodynamically compressed when all three streams enter the outlet channel on the right side of the cross. The channel which carries the stream to be focused narrows to a kind of nozzle when approaching the T-junction

In order to analyze mixing phenomena occurring very close to the first fluid contact, i.e. directly behind the mixing element, a planar design completely covered by a transparent plate was chosen (see Figure 1.67) [112]. This permits characterization without any dead times, hence permitting observation of the entire mixing process.

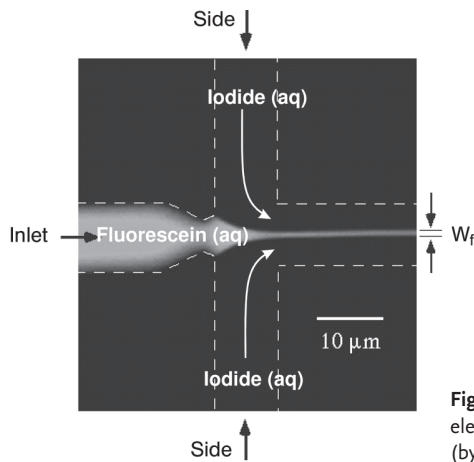


**Figure 1.67** Hydrodynamic focusing mixing element with cross-like structure [112] (by courtesy of APS).

The mixers were realized by means of silicon micromachining using standard photolithographic techniques and a chlorine reactive ion etching process [112]. The structured silicon wafers were sealed with a thin coating of cured silicone rubber. This silicone layer could be withdrawn after use, allowing cleaning of the mixer. After repetition of coating, experiments could be continued using the cleaned structure. Four holes, for fluid connection of inlet and side flows and of the mixture to external sample reservoirs, were drilled into the backside of the wafer.

Mixer type	Hydrodynamic focusing cross-injection micro mixer	Channel width	10 $\mu\text{m}$
Mixer material	Silicon	Nozzle width	2 $\mu\text{m}$
Cover material	Glass		

#### 1.3.5.2 Mixing Characterization Protocols/Simulation

[P 29] No details on the experimental results were given in [113].

[P 30] Sample dosing was achieved without using any pump. Instead, the liquids were fed by applying pressure, controlled by regulating the incoming flow of nitrogen gas, on the head of each reservoir [112]. The finite precision of pressure control directly influenced the minimum thickness of lamellae achievable.

Fluorescence monitoring was used for depicting the concentration changes due to the mixing process [112].

#### 1.3.5.3 Typical Results

##### Thickness of compressed lamellae

[M 32] [P 30] The focusing width was controlled by varying the volume flows of the side and inlet flows [112]. Widths as small as 50 nm were measured, yielding a nearly instantaneous interdiffusion of the side flow into the inlet flow. However, it

should be mentioned that this is not true for the dispersion of the inlet flow within the overall mixing volume, i.e. the fluid of the side flow has to serve as an excess reagent.

After mixing, the time evolution of a subsequent reaction can be spatially separated, and the resolution is only determined by the flow velocity [112]. A resolution better than  $1 \mu\text{s} \mu\text{m}^{-1}$  was achieved since laminar flow was even maintained at high velocities, owing to the small size of the channels.

#### Sample consumption

[M 32] [P 30] Owing to the small mixer dimensions, the sample consumption is low [112]. The volume flows of the focused reactant stream are typically of the order of nanoliters per second, which is more than three orders of magnitude lower than the typical rates needed for turbulent mixers. This is important, in particular, for applications in biochemistry, usually demanding the consumption of expensive samples.

#### Variation of jet width and mixing time by adjustment of feed pressures

[M 32] [P 29] Based on an analogy of the fluid flow with the current flow in a resistive circuit, the jet width was calculated for various pressures [113]. In the range of pressures investigated, jets from 1 down to  $0.02 \mu\text{m}$ , i.e. 20 nm, width resulted. These calculated values are in excellent agreement with experimental data. Thus, mixing can be performed within microseconds with only nanoliter sample consumption.

[M 32] [P 30] It was found that hydrodynamic focusing was achievable in the mixer over a wide range of volume flow ratios, expressed as the ratio  $\alpha$  of the corresponding pressures, defined as follows:

$$\alpha = \frac{P_s}{P_i} \quad (1.1)$$

where  $P_s$  is the pressure of the side flow channel and  $P_i$  refers to that of the inlet flow channel [112]. The minimum and maximum values of  $\alpha$ , limiting the range of focusing, were determined as  $\alpha_{\min} = 0.48$  and  $\alpha_{\max} = 1.28$  [112]. Increasing  $\alpha$  results in a narrowing of the focused stream. Below the lower limit, the inlet flow enters the side channels, instead being directed to the outlet channel. Above the upper limit, the same phenomena occur for the side flow, hence streaming into the inlet flow channel. Both flow reversals were independent of the overall pressures  $P_s$  and  $P_i$ .

The experimental data for  $\alpha$  were compared with theoretical values calculated by means of analogy considerations to electric flow (Ohm's law) [112]. Simple circuit models based on a network of resistors were applied to simulate the cross-type configuration chosen. It could be shown that the calculated values for  $\alpha_{\min}$  and  $\alpha_{\max}$  were in excellent agreement with the experimental data.

#### Visualization of the hydrodynamically focused lamellae by fluorescence

[M 32] [P 30] The mixing process was visualized by epifluorescence and confocal microscopy images (see Figure 1.68) [112]. A bright inlet flow, labeled with a

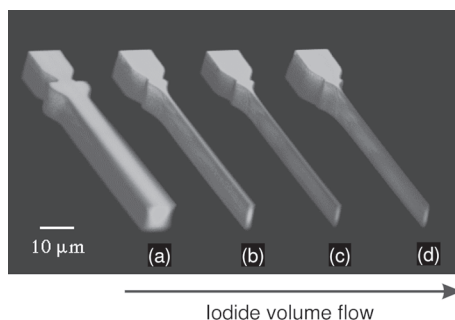


**Figure 1.68** Visualization of hydrodynamic focusing of a fluid layer by means of fluorescence imaging [112] (by courtesy of APS).

fluorescent dye, was mixed with non-fluorescent buffer side flows. The light emission of excited molecules of a focused fluorescein solution was quenched by a solution containing iodide ions. Thus, the time evolution of iodide diffusion into the fluorescein solution was revealed as a change in the fluorescence intensity.

Lamellae of the fluorescein solution larger than  $1\ \mu\text{m}$  could be directly imaged [112]. In addition, a non-imaging approach, based on a fluorescence technique, was applied to analyze even smaller lamellae. This technique allowed one to determine widths as small as  $50\ \text{nm}$ . Data obtained at a flow of  $5\ \text{nl s}^{-1}$  showed that the mixing process was completed at best after  $10\ \mu\text{s}$ . The experiments consumed extremely small sample volumes, needing only  $25\ \text{nl}$  of fluorescein solution and  $1\ \mu\text{l}$  of the buffer solution per measurement.

### 1.3.6

#### Geometric Focusing Bi-laminating Mixing

##### Most Relevant Citations

Peer-reviewed journals: [114]; proceedings contributions: [115, 116].

The focusing bi-laminating micro mixer was realized in the framework of the development of a flow injection analysis (FIA) system [114, 115]. The mixer is placed downstream of the two-fold injection of sample and reagent streams into the carrier. Thereafter, the mixed stream enters a reaction chamber and finally passes a detector. An easy integration is required, as the mixing element is part of an integrated system which has the minimization of size as one issue.

FIA is a chemical analysis method based plug-wise injection into a carrier stream [114–116]. These plug samples can be further manipulated, e.g. by reaction to compounds better detectable by a detector. The sample consumption can be reduced via miniaturization; however, then usually laminar-flow conditions are given so that micro mixers are needed which are efficient in that regime.

The analysis target was the detection of ammonia in aqueous solutions, e.g. in surface water [114–116]. The Berthelot reaction scheme was employed to monitor ammonia, by chemical conversion to indophenol blue, using a chlorination step first followed by coupling of two phenol moieties. The absorption of the dye was measured by a photometric-type experiment. Full conversion by efficient mixing is mandatory for a good analysis.

Design targets for the application were to have a total system volume  $< 1 \text{ cm}^3$  and to achieve one sample throughput per minute [115]. The reaction time for the Berthelot reaction is about 40 s so that only 20 s are left for all other process steps. This involves the injection of the sample, mixing and an optical absorption measurement. Therefore, mixing has to be fast, requiring only a few seconds.

### 1.3.6.1 Mixer 33 [M 33]: Geometric Focusing Bi-laminating Micro Mixer

This micro mixer is based on a bi-laminated stream which has to pass a considerably narrowed flow passage having the function of reducing the diffusion distance and thereby speeding up liquid mixing [114–116].

A central demand for the mixer is the very accurate setting of the channel width. For this reason, a microfabrication technique was chosen that is known to achieve very smooth and ideally-vertical channel walls, namely the reactive ion etching (RIE) technique [114–116]. The fluidic connections are made from the bottom by RIE. Anodic bonding serves for interconnection.

Mixer type	Geometric focusing bi-laminating micro mixer	Initial bi-laminating channel width, depth, length	300 $\mu\text{m}$ , 200 $\mu\text{m}$ , 1.65 mm
Mixer material	Silicon/Pyrex	Focusing channel width, depth, length	100 $\mu\text{m}$ , 200 $\mu\text{m}$ , 1.65 mm

### 1.3.6.2 Mixing Characterization Protocols/Simulation

[P 31] Liquid mixing times were calculated based on assuming diffusion as the only mixing mechanism and considering Fick's law which takes into account the diffusion constant and the diffusion distance [114].

For judging completion of mixing experimentally, a flow guidance with two injection inlets and two outlets was used [114]. A phenol solution was injected via one inlet port; the completion of mixing was indicated when both outlets gave the same phenol concentration. The concentration was determined by conductivity measurement. Mixing efficiency was defined as the ratio of the concentrations in the outlets. Thus, this parameter ranges from 0 to 1 for no to complete mixing if one stream is charged with the target species and the other not at all.

The experimental set-up used Hamilton syringes for liquid feed [114]. Two syringes pump and another two extract solution from the mixer. The pressure drop was measured differentially, by determining the pressure at one inlet and outlet, respectively.

### 1.3.6.3 Typical Results

#### Calculated liquid mixing time

[M 33] [P 31] The liquid mixing time was calculated for phenol ( $D = 0.89 \cdot 10^{-9} \text{ m}^2 \text{ s}^{-1}$ ) in an aqueous solution using the bi-laminating focusing mixer [114, 116]. For example, with a reduction in the channel width from 300 to 100  $\mu\text{m}$  the time can be reduced from 35 to 4 s.

**Calculated focusing channel length**

[M 33] [P 31] For the bi-laminating focusing mixer, the length required for liquid mixing was calculated [114, 116]. For a flow of  $6 \mu\text{l min}^{-1}$  and a channel height of  $200 \mu\text{m}$ , a mixing length of  $1.65 \text{ mm}$  results.

**Calculated pressure drop**

[M 33] [P 31] The pressure drop was calculated for a flow of  $6 \mu\text{l min}^{-1}$  at various micro channel widths [114]. For channel widths in the range  $50\text{--}300 \mu\text{m}$ , the pressure drop decreases from about  $1000$  to  $300 \text{ Pa}$ .

**Experimental liquid mixing time**

[M 33] [P 31] The liquid mixing time was measured for phenol ( $D = 0.89 \cdot 10^{-9} \text{ m}^2 \text{ s}^{-1}$ ) in an aqueous solution using the bi-laminating focusing mixer [114]. At flow rates exceeding  $60 \mu\text{l min}^{-1}$  virtually no mixing occurred, whereas nearly complete mixing was achieved below  $1 \mu\text{l min}^{-1}$ .

## 1.3.7

**Bi-laminating Microfluidic Networks for Generation of Gradients****Most Relevant Citations**

Peer-reviewed journals: [117].

Gradients of diffusible substances having chemo-attractant or chemo-repellent properties play an important role in, e.g., biological pattern formation, morphogenesis, angiogenesis and axon path finding. The generation of such gradients in solution, even with a complex shape, divergent from the normal parabolic-shaped concentration profiles, is possible by using networks of micro channels designed to control diffusive mixing of substances [117].

**1.3.7.1 Mixer 34 [M 34]: Bi-laminating Microfluidic Network**

Several fluid manipulation steps occur within the 'Christmas tree', including splitting, combining and mixing of the different fluids. While keeping the number of inlets low, the splitting increases the number of streams with different concentration of the fluids forming a concentration profile in the broad outlet channel. One fluidic device described is a three-input/nine-output network, i.e. the three input fluid streams are split into four sub-streams which are mixed in the serpentine channel array (shown as a zigzag line in Figure 1.69). The used flow rates ensure a complete diffusive mixing. Subsequently, after flow through the four serpentine channels, the fluids form again inputs which are split into five sub-streams entering a second array of serpentine channels. Downstream of the microfluidic network all sub-streams are merged forming concentration profiles of different shape in the outlet channel [117].

The microfluidic devices, often called 'Christmas tree' owing to the pattern of the channels, were fabricated from polydimethylsiloxane (PMDS) using common micro technologies (see Figure 1.69). A mask is formed by using a high-resolution  $3300 \text{ dpi}$  printer to transfer the CAD pattern to a transparent mask substrate.

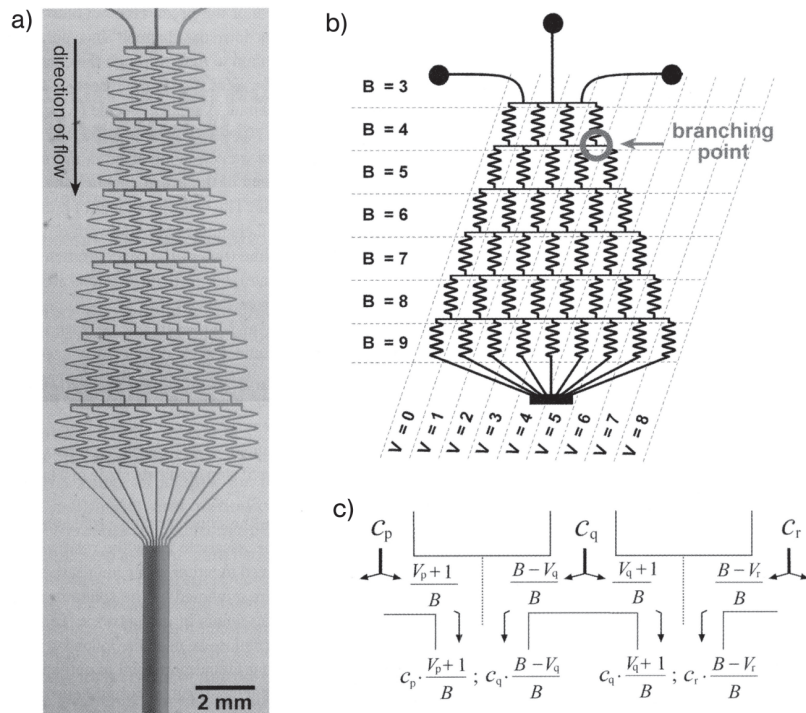


**Figure 1.69** (a) Schematic of a 3-input/9-output ‘Christmas tree’ microfluidic network ([117]). (b) Schematic for explanation of the mathematical solution of the microfluidic network. (c) Schematic demonstration of the derivation of equations governing the splitting ratios at the branching points. The dotted lines indicate the boundary between the two combined streams. The concentrations at the end of the serpentine channels can be calculated by multiplying the concentration of the incoming streams ( $c_p$ ,  $c_q$ ,  $c_r$ ) with the corresponding splitting ratio  $[(V_p + 1)/B, (B - V_q)/B, (V_q + 1)/B$  and  $(B - V_r)/B]$  [117] (by courtesy of APS).

A minimum feature size of  $\sim 20 \mu\text{m}$  is achievable with this method. The mask pattern is transferred into SU-8 photoresist coated on a silicon wafer using 1 : 1 contact photolithography and, after some subsequent process steps, a negative master of the channel network is achieved. Positive replicas can be achieved by molding the master with PMDS again. After punching the inlet and outlet holes, the PMDS surface and the glass cover plate are treated in air plasma. Putting both parts together, an irreversible tight seal is formed.

### 1.3.7.2 Experimental Characterization Protocols/Simulation

[P 32] The concentration profiles are generated by permuting the order at the inlets of fluorescein solutions (fluorescein in 100 mM  $\text{NaHCO}_3$  buffer, pH 8.3, green) with different concentrations (100, 50 and 0%) and a solution of tetramethylrhodamine ethyl ester in ethanol. The overall flow velocity ranges from  $800 \mu\text{m s}^{-1}$  to  $1.2 \text{ mm s}^{-1}$  [117].

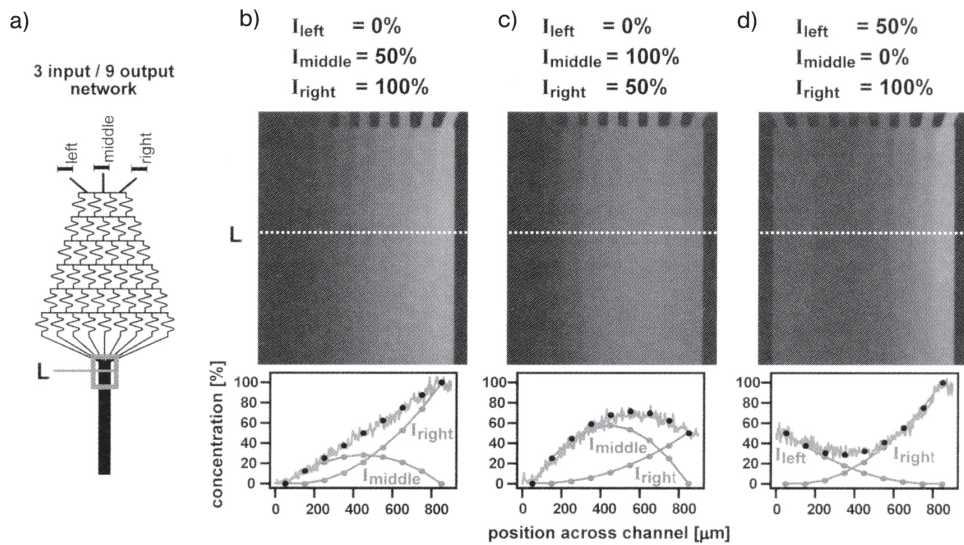


**Figure 1.70** (a) Schematic of a 3-inlet/9-outlet microfluidic network. (b) Linear and (c, d) parabolic gradients of fluorescein in solution. The inlet concentrations are indicated by  $I_i$ . The plots show the fluorescence intensity profile across the broad outlet channel. The theoretically calculated concentration profiles and the contributions of the individual inlets are marked • [117] (by courtesy of ACS).

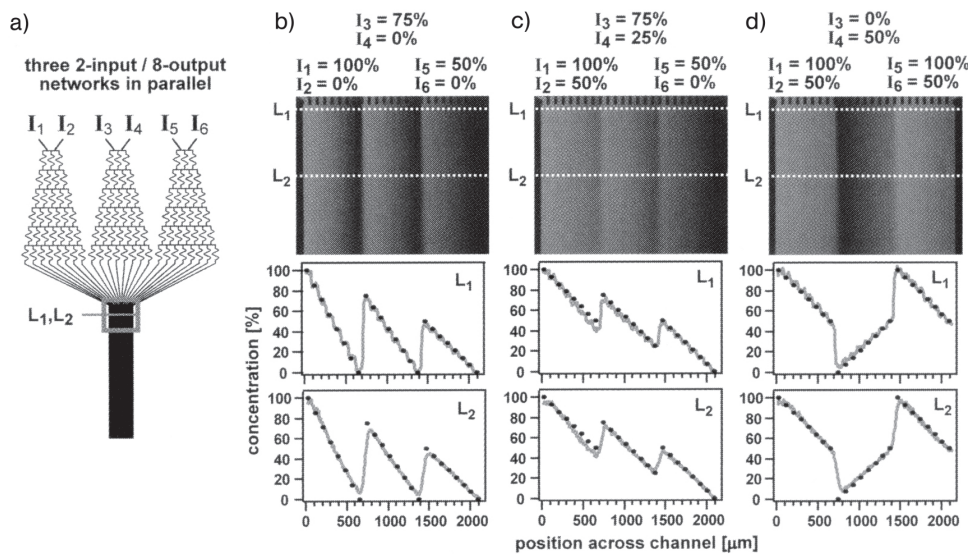


**Figure 1.71** (a) Schematic of a 2-inlet/8-outlet microfluidic network in parallel. (b) Linear and (c, d) parabolic gradients of fluorescein in solution. The inlet concentrations are  $I_i$ . The plots show the fluorescence intensity profile across the broad outlet channel at the beginning of the channel and 800  $\mu\text{m}$  downstream. The theoretically calculated concentration profiles are marked • [117] (by courtesy of ACS).

### 1.3.7.3 Typical Results

#### Linear and parabolic gradients

[M 34] [P 32] Linear and parabolic gradients can be generated at the outlet of the microfluidic network. In all cases, calculated concentrations [see Figure 1.70 (•)] are in a good agreement with the experimentally observed concentration profiles.

#### Periodic gradients

[M 34] [P 32] Periodic gradients can be formed by combining, in parallel, three networks each having two inlets. Since in each of these networks independently different linear concentration profiles can be generated, a variety of saw-tooth gradients can be established when the individual linear profiles are brought together in the broad outlet channel (see Figure 1.71) [117].

Increasing the number of inlets from two to three at the individual networks extends the accessible range of profiles. It is possible to form symmetric gradients of three parabolic parts or, by using preformed linear gradients, mixed profiles consisting of linear and parabolic parts are accessible [117].

#### Superpositioned gradients

[M 34] [P 32] Superposition of gradients can be generated by feeding the inlets of a two two-inlet/eight-outlet parallel network with different substances, e.g. of fluorescein (green) and tetramethylrhodamine ethyl ester (red). In both branches of the network an individual saw-tooth profile is generated. When both saw-tooth profiles merge in the outlet channel, superimposed periodic profiles are formed. Overlapping gradients can be used for comparing and quantifying the role of competing gradients in chemotaxis [117].

### 1.3.8

#### Bifurcation Multi-laminating Diffusive Mixing

##### Most Relevant Citations

Peer-reviewed journals: [42]; micro machining: [118]; analytical application/kinetic studies: [119].

Multi-lamination mixing relies on the generation of an alternating arrangement of thin fluid compartments, multi-lamellae, which are then mixed by diffusion. Multi-lamination is realized by alternating feed arrangements (type  $A-B-A-B- \dots$ ), the outlets of which direct into a flow-through mixing chamber and thus create the multi-lamellae pattern. The aim is to generate sufficiently small fluid compartments so that steep concentration gradients result which give fast mixing by diffusion. Most common feed schemes for interdigital mixing are bifurcation branching (see below) and interdigital branching (see Section 1.3.9).

Bifurcation branching achieves equidistribution by flow symmetry (see Figure 1.72). The outlet arrangement is basically identical with the interdigital feed concept. While the bifurcation concept does not demand the build-up of an additional pressure barrier (see the interdigital structures in Section 1.3.9), besides the pressure drop for the flow passage itself, it poses much higher demands on the structural

precision and the absence of fouling or deposits within the channels, as both will break the ideal splitting geometry of bifurcation.

Bifurcation structures are self-replicating patterns which serially branch channels until a multitude is reached. In this way, a main stream can be split into many sub-streams just relying on flow symmetry. These sub-streams can be contacted in an interdigital-type arrangement with the sub-streams of a second feed and then be guided into a main channel or into an inverse bifurcation structure.

#### 1.3.8.1 Mixer 35 [M 35]: Bifurcation Multi-laminating Micro Mixer

One inlet channel is split by a bifurcation structure into 16 sub-channels. On the backside of the same wafer, an identical bifurcation structure is made (see Figure 1.72) [42]. These sub-streams are redirected via wafer-through nozzles close to the end of the bifurcation structure on the other side. Here, the sub-streams are guided through short channels which lie next to the ends of the bifurcation structure. Two such alternate channels merge repeatedly to yield finally an inverse bifurcation structure which ends in a broad channel. Different from the first bifurcation structure having the same width all along the flow path, in the inverse structure the width increases constantly owing to the increasing number of streams. In this way, the lamellae thickness of the fluid is kept constant. The broad outlet channel is very long to ensure completion of mixing by diffusion.

Microfabrication is effected by etching a wafer from both sides which contains through-holes for the fluid connectors [42]. Two transparent cover plates close the open structures and also have through-holes. A glass capillary was attached to the three-plate chip. The holes in the cover plate were made by sandblasting.

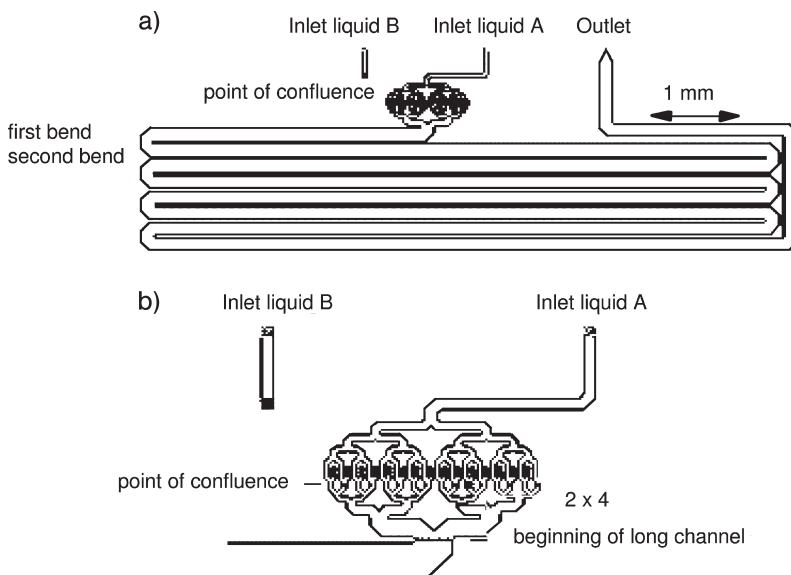


**Figure 1.72** Schematic of the mixing element of the bifurcation laminating micro mixer [42] (by courtesy of RSC).

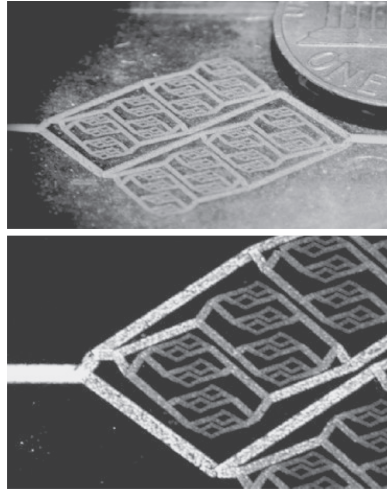


**Figure 1.73** Biomimetic vasculatures [118] (by courtesy of RSC).

Mixer type	Bifurcation multi-laminating micro mixer	Channel width	49–58 $\mu\text{m}$
Mixer material	Silicon	Capillary material	Fused silica
Cover material	Glass	Capillary outer diameter, inner diameter	375 $\mu\text{m}$ , 50–150 $\mu\text{m}$
Number of bifurcation branches	16	Outer size of the chip	5 mm $\times$ 10 mm
Nozzle (lamellae) width	20 $\mu\text{m}$	Total internal volume	600 nl

The fabrication of bifurcation structures was also achieved by a high-brightness diode-pumped Nd:YAG laser direct write method [118]. A PDMS structure was realized in one step and tested for mixing function by fluorescence imaging. The method provides rapid prototyping of master structures and is said to have high flexibility. Furthermore, it allows one to realize a bifurcation structure with multi-width multi-depth micro channels, i.e. a 3-D object. Such structures are similar to biomimetic vasculatures whose channel diameters change according to Murray's law, which states that the cube of the radius of a parent vessel equals the sum of the cubes of the radii of the daughters (see Figure 1.73). In this way, micro channel networks similar to physiological vascular systems may be fabricated, having all the favorable properties of the latter. First steps in this direction are described in [118].

#### 1.3.8.2 Mixing Characterization Protocols/Simulation

[P 33] Reactive imaging was used for mixing and flow-pattern analysis [42]. Fluorescence quenching (using a photomultiplier tube) offers a very sensitive method to determine the completion of mixing.

Syringe pumps (25  $\mu\text{l}$  syringes) were used for feeding the streams [42]. The flow is visualized via a microscope using a video camera. For quantitative measurements, the set-up is further modified.

For flow visualization, fluorescence solutions contained 40  $\mu\text{mol l}^{-1}$  fluorescein and 100  $\mu\text{mol l}^{-1}$  rhodamine B [42]. For the quenching experiments, 20  $\mu\text{mol l}^{-1}$  fluorescein and 2  $\text{mol l}^{-1}$  potassium iodide in borate buffer were used.

### 1.3.8.3 Typical Results

#### Ratio of dead volumes

[M 35] [P 33] The calculated dead volume referred to the inlet volumes (about 36 nl), which is small compared with the total internal mixer volume (600 nl) [42].

#### Liquid mixing time

[M 35] [P 33] The liquid mixing time for 95% mixing is about 15 ms [42]. Further mixing requires more time, also because the lamellae close to the wall are thicker than the internal ones.

#### Flow asymmetry

[M 35] [P 33] The lamellae close to the channel walls are larger than those in the interior [42]. In addition, a velocity profile exists, the lamellae at the walls moving much slower than the internal ones. Thus, the mixing of these different lamellae is for two reasons completed at a very different length. For high degrees of mixing, therefore, the diffusion of the boundary layers becomes dominant.

#### Quantitative mixing judgement

[M 35] [P 33] By fluorescence quenching, the degree of mixing at various stages of the flow path could be determined (see Figure 1.74) [42]. The data in the long outlet channel are in good agreement. In contrast, mixing in the flow passages beforehand is slower than expected. This is explained by the greater striation thickness at the point of confluence. From there, thinning of the lamellae occurs rapidly, consequently promoting mixing. At the point of confluence of the inverse bifurcation structure, the slower mixing is explained by the many layers being close to the channel walls. Owing to passing a curved flow passage (bend), the lamellae are, in addition, compressed in an asymmetric way, again slowing the mixing.

#### Time-resolved FTIR spectrometry for protein conformation kinetic study

[M 35] [protocol see [119]] A protein conformation kinetic study of the small protein ubiquitin was performed both in the continuous and in a stopped-flow mode at low reactant consumption [119]. The bifurcation mixer was used prior to an IR flow cell for data monitoring. The change of conformation from native to the A-state was followed when adding methanol under low pH conditions to the protein solution. In the continuous mode, long data acquisition could be made and the reaction time was determined by the flow rate and the volume interconnecting zone between the mixer and IR flow cell, which was small, but not negligible. In the stopped-flow mode, the reaction time resolved was dependent on the time resolution of the FTIR instrument.

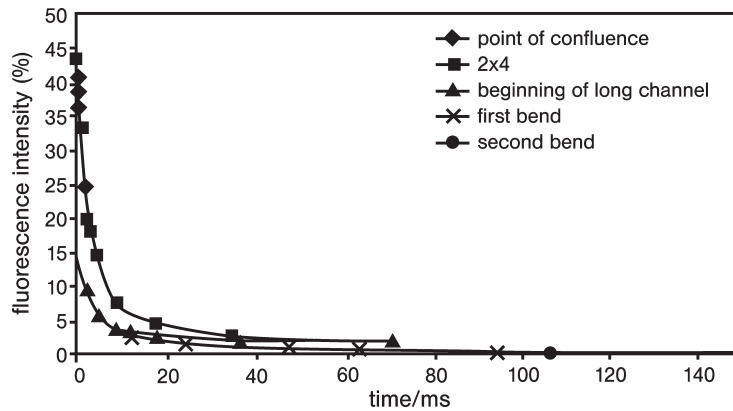


**Figure 1.74** Decay of fluorescence intensity at selected points in the bifurcation laminating mixing element. These data are taken as a measure for spatially judging the mixing efficiency [42] (by courtesy of RSC).

### 1.3.9

#### Interdigital Multi-laminating Diffusive Mixing (Normal and Focusing)

##### Most Relevant Citations

Peer-reviewed journals: [20, 36–39, 41, 67]; proceedings contributions: [34, 40, 120, 121]; patents: [122, 123].

Interdigital feeds, termed in analogy with the respectively arranged electrode structures, provide multiple outlet ports with alternately arranged fluids (type  $A-B-A-B$ , etc.) [34, 67]. The typical architecture of interdigital feeds comprises a large reservoir from which many equal sub-stream channels branch ending in nozzle-type outlets, for each fluid. The equidistribution to these is given by applying a pressure barrier, i.e. making the hydraulic diameter of the sub-stream channel much smaller than that of the reservoir.

When the multi-lamellae pattern is vertical to the feed reservoir layers, this is named vertical multi-laminating. When both are oriented in the same way, this is the horizontal variant.

In a vertically multi-laminating variant of the interdigital principle, the two arrays of the multiple sub-streams, belonging to two fluids, are overlaid in such a way that the above-mentioned alternate arrangement results (see Figure 1.75) [34, 67]. This usually requires the reservoirs to be placed in two different layers of the microstructured device. The sub-stream channels typically start in the two different layers and merge in a common layer.

The direction of the feed flows before approaching the mixing chamber in the vertical multi-laminating variant can be counter-, cross-flow or co-flow, the selection of which is mainly governed by microfabrication needs (see Figure 1.75). In the case of counter-flows, the streams have to be re-directed before entering the mixing channels. In this way, co-flow entering is achieved.

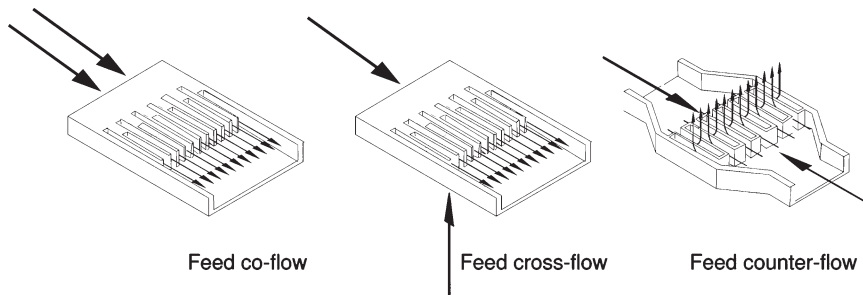


**Figure 1.75** Vertically multi-laminated interdigital feeds. For the horizontal variant, counter-, cross- and co-flow injection schemes are given (large arrows). The alternating streams enter the mixing channel in all cases as co-flows (small arrows) [39].

In a horizontally multi-laminating variant, plates, typically with multi-channel arrays, are stacked on *A–B–A–B*-type manner (see Figure 1.75) [40, 41]. Here, the complete multi-channels feed one lamellae, while in the vertical variant this is done by a single channel. In this way, fairly large throughputs can be achieved. The outlets of the multi-channel arrays of the vertical variant may have straight or oblique directions (see Figure 1.81) [40, 65]. In the latter case, it is thought that the fluids keep this direction for a distance so that swirling flow patterns may be generated.

Considering the width of typical interdigital outlets, which are of the order of several tens of microns, it stands to reason that multi-lamination on its own is a rather slow mixing process, typically needing liquid mixing times of the order of seconds (see Figure 1.76 and, e.g., [34]).

This may be adequate for  $\mu$ TAS applications, where stream velocities are low and hence residence times are large. For most chemical and chemical engineering applications, however, faster mixing times are required. Though today's micro-

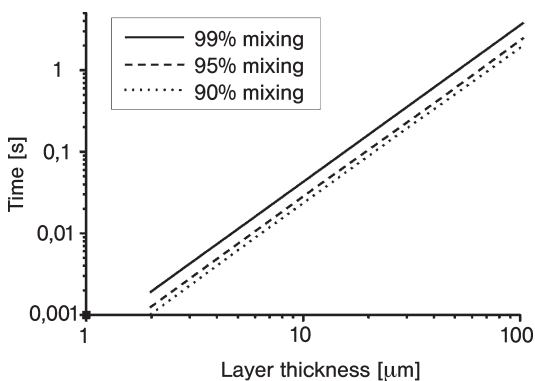


**Figure 1.76** Typical mixing times calculated for a range of diffusion distances, physically corresponding to the lamellae width, assuming diffusion to be the only mixing mechanism [34] (by courtesy of AMI).

fabrication potentially allows one to manufacture outlet widths at the micron level (and below), this is neither cost-efficient nor practical facing throughput or fouling–stability issues. An alternative concept for mixing speed-up utilizes the well-known hydrodynamic focusing concept [112] (see Section 1.3.5). In this way, fluid lamellae are compressed by external forces, e.g. stream constraints. Favorably, this can be achieved by posing geometric constraints [114–116]. This principle, performed first for bi-laminated streams [114–116] (see Section 1.3.6), has been transferred to interdigital multi-laminated devices [20, 35, 37, 124]. The result of geometric focusing is the generation thinner lamellae which mix faster.

Although the compression of lamellae follows a hydrodynamic principle, it was decided to term this approach ‘geometric focusing’ throughout this chapter, to distinguish this design-based method better from the processing-based hydrodynamic focusing relying on setting very different pressures for the inlet streams.

Geometric focusing via triangular-shaped focusing chambers using horizontal co-flow injection schemes has become state-of-the-art for interdigital mixers (see Figure 1.77) [20, 35, 37, 124].

Initially, geometries other than triangles, such as sections of an arc, were employed, mainly for fabrication reasons [36]. These had a too extreme focusing ratio resulting in inhomogeneous lamellae formation and lamellae tilting and winding at high  $Re$  [20]. Thereafter, triangular focusing chambers were introduced, with focusing ratios of the order of several tens [20, 35, 37, 124]. Based on these first achievements and a semi-analytical optimization study, a novel focusing design of much larger focusing ratio was developed with the targets to have regular focusing with equally spaced lamellae at a liquid mixing time of only a few milliseconds [20, 37]. In addition, it was demanded that the mixing should be completed within

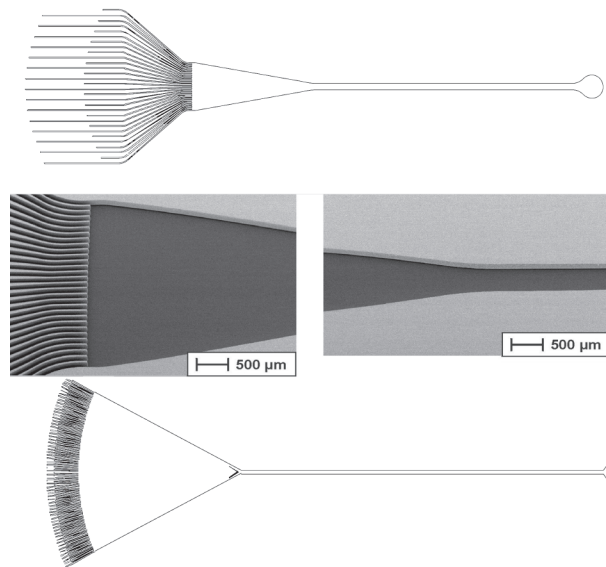


**Figure 1.77** A triangular focusing geometry for multi-lamellae flows (source IMM).

the micro device, and not in the attached tubing [20, 37]. The novel, optimized design was termed *SuperFocus* (see [M 44]). A second-generation version of the *SuperFocus* mixer was developed with the issue of throughput enhancement into the range of several hundred liters per hour, considering an aqueous system [39].

The focusing–interdigital approach is comparatively simple to scale up, as this means only increasing the number of lamellae within one plane (equalling-up or internal numbering-up). In addition, the flow rate can be further increased simply by enlarging the height of the fluid compartments in the vertical direction, i.e. having a larger structural depth of the flow-through mixing chamber.

The interdigital feed with flow compression (geometric focusing) can have additional flow expansion which introduces a jet in a flow-through chamber [20, 36, 37].

#### 1.3.9.1 Mixer 36 [M 36]: Unfocused Interdigital Multi-laminating Micro Mixer with Co-flow Injection Scheme (I), ‘Rectangular Mixer’

This micro mixer simply creates multi-laminated streams via an interdigital feed arrangement, but does not rely on geometric focusing of these streams by geometric constraints as triangular mixers [M 43] do [20] (see also [39]). Mixing is performed in a mixing chamber, which has a rectangular format from top view, giving the name of the device, ‘rectangular mixer’.

The rectangular mixer is composed of four plates (see Figure 1.78) [20, 39, 124]. The second plate contains the complete interdigital feed for one fluid (reservoir + multi-channel feed), the multi-channel feed of the other fluid (without reservoir), the focusing section and the mixing channel. The third plate comprises two rows of multiple holes serving as conduits to the underlying fluid reservoir. Fluid distribution is achieved via these holes. A first plate serves as cover.

The microstructures are fabricated by photoetching of a specially glass (see Figure 1.79) [20, 124]. Such microstructured plates are joined by soldering. The joint plate stack is held in a frame.

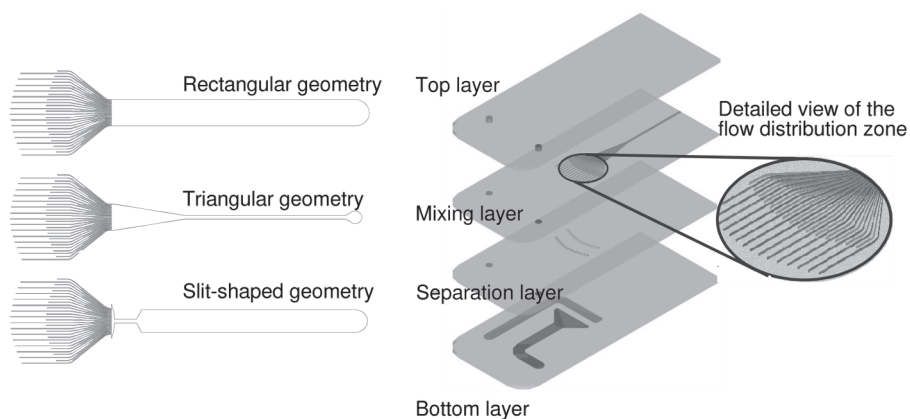


**Figure 1.78** Exploded view of a glass micro mixer (right) and design variations of the mixing zone (left) [124] (source IMM).

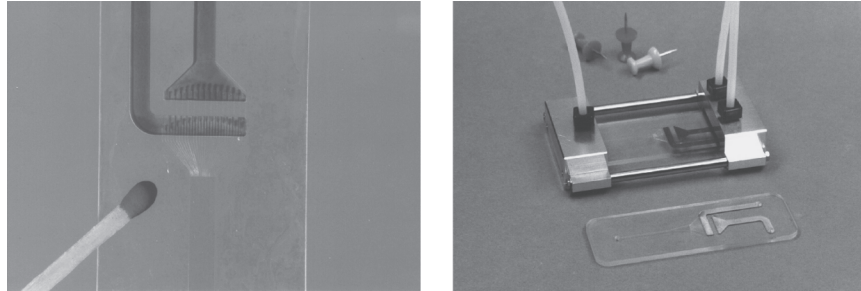


**Figure 1.79** Microstructured four-plate glass stack of the interdigital micro mixer (left) and assembled device with steel frame (right) [124] (source IMM).

Mixer type	Interdigital rectangular micro mixer with co-flow injection scheme	Feed channel width and depth, width of separating walls	60 $\mu\text{m}$ , 150 $\mu\text{m}$ , 50 $\mu\text{m}$
Mixer material	Specially glass (Foturan <sup>®</sup> )	Number of micro channels	2 $\times$ 15
Mixer frame material	Stainless steel/ aluminum	Mixing chamber length, width, height	27.4 mm, 3.25 mm, 150 $\mu\text{m}$
Device outer dimensions: length, width, thickness	76 mm, 26 mm, 2.3 mm		

### 1.3.9.2 Mixer 37 [M 37]: Interdigital Vertically Multi-laminating Micro Mixer with Co-flow Injection Scheme (II)

This device uses an alternate arrangement of streams (see Figure 1.80) which are much thinner compared with their width, i.e. the diffusion distances were set deliberately large [67]. The corresponding diffusion-based mixing was named lateral mixing. For comparison, a so-called vertical mixing device was made (see Figure 1.80). Here, the thin layers are overlaid so that the diffusion distances are kept small, rather than placing them side by side.

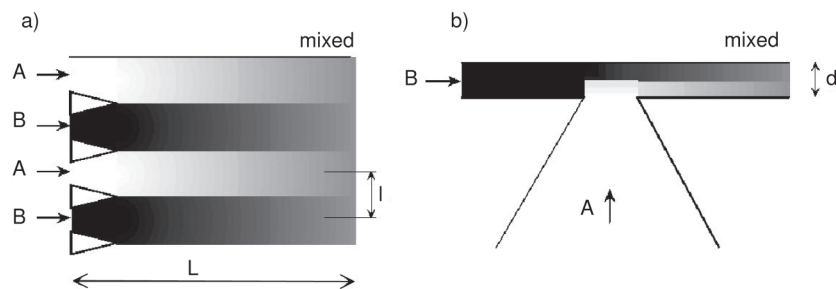


**Figure 1.80** Schematic of the flow guidance and the mixing principle of micro mixers for (a) lateral view of lamination and (b) vertical view of lamination [67] (by courtesy of IOP Publishing Limited).

In practice, the above-mentioned design issues are realized by having a large reservoir within a multi-plate rig on which the mixing device is mounted and screwed using seals [67]. At the top of this reservoir several orifices form through-holes to an interdigital structure for each liquid. The orifices of one liquid are arranged in-line, perpendicular to the liquid flow. From each orifice a separate feed channel originates and guides to a rectangular flow-through chamber. The orifices of the other liquid are placed in-line, at a distance to the first line of orifices. The position of each orifice is chosen so that it is placed in between two feed channels carrying the other liquid, yielding an *A-B-A-B*-type pattern. Behind this second row of orifices, multiple, parallel channels lead to a large rectangular flow-through chamber where multi-lamellae mixing takes place.

Micro fabrication was made by conventional silicon wet etching. Sealing was achieved by anodic bonding to Pyrex glass [67].

Mixer type	Interdigital vertically multi-laminating micro mixer with co-flow injection scheme	Feed channel width, depth, length for liquid 2	10 $\mu\text{m}$ , 5 $\mu\text{m}$ , 0.335 mm
Mixer material	Silicon	Mixing chamber width	2.21 mm
Cover material	Pyrex	Total chip size	7.5 $\times$ 4 mm
Number of micro channels liquids 1 and 2	14, 13	Rig material	PVC
Feed channel width, depth, length for liquid 1	40 $\mu\text{m}$ , 5 $\mu\text{m}$ , 2.335 mm	Rig sealing material	Silicone rubber
Fin distance between the feed channels	70 $\mu\text{m}$		

#### 1.3.9.3 Mixer 38 [M 38]: Interdigital Horizontally Bi-laminating Micro Mixer with Cross-flow Injection Scheme, Reference Case to [M 37]

This device performs a bi-lamination using two fluid layers of basically the same dimensions as the device reported above, [M 37] (see Figure 1.80) [67]. In contrast, however, these layers are not laterally oriented, but are superposed in the vertical direction. The device serves mainly as a benchmark for the performance of [M 37].

Fluid feed is realized by feeding one liquid through one rectangular through-inlet, [67]. This flow is entering a flow-through chamber and fills this volume. At a distance to the first inlet, the second inlet is introduced from below via 42 rectangular orifices so that the lower half of the channel depth is filled with the other liquid stream, the upper half being composed of the first liquid. The orifices are grouped into four rows, two with 10 orifices and two with 11 orifices. From there, a bi-laminated flow is passed through the chamber, which now serves for diffusion mixing. The whole flow-through chamber has a lower depth as compared with its width.

The device is mounted and screwed using seals on a multi-plate rig on which the mixing device is located [67].

Micro fabrication was effected by conventional silicon wet etching. Sealing was achieved by anodic bonding to Pyrex glass [67].

Mixer type	Interdigital horizontally bi-laminating micro mixer with cross-flow injection scheme, reference case to [M 37]	Mixing chamber depth, width	5 $\mu\text{m}$ , 2.21 mm
Mixer material	Silicon	Total chip size	7.5 $\times$ 4 mm
Cover material	Pyrex	Rig material	PVC
Number of micro channels liquids 1 and 2	1 : 1	Rig sealing material	Silicone rubber

#### 1.3.9.4 Mixer 39 [M 39]: Interdigital Horizontally Multi-laminating Micro Mixer with Co-flow Injection Scheme

This device achieves a horizontal orientation of the lamellae by alternate vertical stacking of plates, which carry one fluid each. This is different from the interdigital micro mixers described above having a vertical *A–B*-type orientation [40, 41].

Vertical orientation is preferably achieved by placing multi-channel plates as a stack in such a way that the plates carry the fluids alternately [41]. For this purpose, two sets of plates have to be manufactured which typically have a mirror-imaged design to be fed from two oppositely placed fluidic ports. The stack-like design is amenable to numbering-up to operate even many thousands of channels in parallel and large throughputs [65].

Such multi-platelet stacks were realized with tilted, straight (V-type) and curved (P-type) multi-channel arrays (see Figure 1.81) [41]. The V-type device has slanted outlets so that neighboring jets may collide; the P-type has parallel streams.

The microstructures were realized by a special, advanced turning technique [41]. The platelet stacks were diffusion bonded for sealing and encased in a housing by

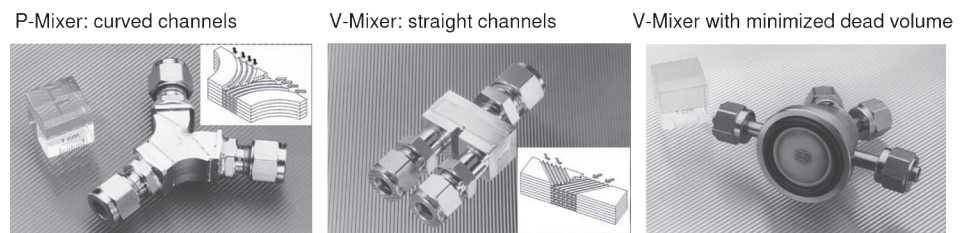


**Figure 1.81** Two different horizontally multi-laminating mixers with different co-flow schemes; curved-channel design (P-type, left), straight-channel design (middle). In addition, a part of a V-type mixer with minimized dead volume is shown [Pfeifer et al., Chem. Ing. Tech. 76, 5 (2004) 607].

electron beam welding. The housing also contains a mixing chamber typically of the same cross-section as the stack.

The flow in the feed channels is laminar, as is to be expected [41]. Owing to the size of the mixing chamber and the high fluid velocities, liquid mixing is expected to have a fast transition from laminar to turbulent. Evidence for this is given below. Different from conventional micro mixers, the primary vortices are in the range of about 100  $\mu\text{m}$ , hence smaller than usual. Thus, mixing is different and should be faster.

(a) Version described in [41].

Mixer type	Interdigital horizontally multi-laminating micro mixer (I)	Feed channel depth, width	70 $\mu\text{m}$ , 100 $\mu\text{m}$
Mixer material	Stainless steel	Wall width	30 $\mu\text{m}$
Housing material	Stainless steel	Number of micro channels	2500

(b) Version described in [40] (see Figure 1.82).

Mixer type	Interdigital horizontally multi-laminating micro mixer (II)	Number of channels per passage	480
Mixer material	Stainless steel	Platelet thickness	200 $\mu\text{m}$
Housing material	Stainless steel	Width of micro-structured stack	7.9 mm
Feed channel depth, width, length	100 $\mu\text{m}$ , 100 $\mu\text{m}$ , 20 mm	Width of mixer chamber	11.2 mm
Number of channels per platelet	40	Height of mixer device	4.8 mm
Number of platelets per passage	12		

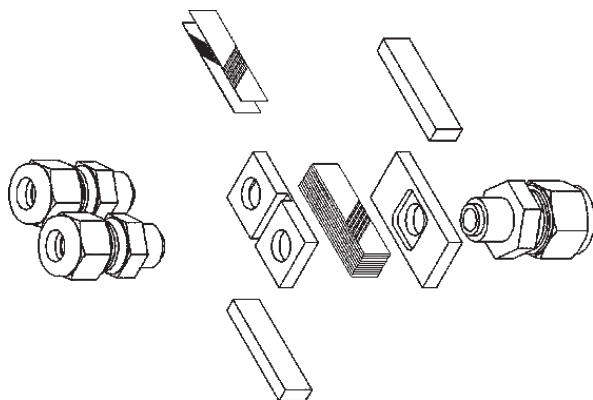


**Figure 1.82** Exploded view of a horizontally multi-laminating mixer with a multiple-plate stack as central feed element, having multiple parallel channels on each plate [Pfeifer et al., Chem. Ing. Tech. 76, 5 (2004) 607].

### 1.3.9.5 Mixer 40 [M 40]: Interdigital Vertically Multi-laminating Micro Mixer with Counter-flow Injection Scheme – ‘3-D Slit Mixer’

This device is made from a microstructured inlay with an interdigital element which is inserted in a recess of a two-piece housing (see Figure 1.83) [36].

The inlay has a counter-flow configuration consisting of many parallel channels fed by one reservoir each (see Figure 1.84). The parallel channels branch in an interdigital structure. The shape of the channels was not straight, but was of meandering nature, mainly for fabrication reasons to allow the realization of high-aspect-ratio structures. From there the sub-streams are redirected at 90° into a flow restriction zone, called ‘slit’, owing to its initial cross-sectional shape. This area is rapidly decreased, since the vertical extension resembles the shape of a small section of an arc [20]. Thereby, hydrodynamic focusing takes place, yielding lamellae compression to speed up diffusion. The slit conduit is connected to tubing. This tubing itself can consist of two cylinders with expanding flow cross-section or simply one cylinder, roughly of the same hydraulic diameter as the end of the slit. In the case of expanded tubing, it is known that a jet forms at sufficiently high flow velocities and possibly jet mixing could assist diffusion mixing. The extent of the jet mixing so far has not been quantified. The fluid connectors are all set side-by-side on the top part of the housing. The bottom part contains the recess.

The inlay is typically made by the LIGA technique, a combination of deep X-ray lithography, electroforming and molding, which gives very precise and steep microstructures [36]. Here, the electroformed structure made in metal was taken as the end product; no molding step was applied. Alternatively, advanced silicon etching (ASE) can be applied to achieve structures of virtually the same quality in silicon. Specially inlays were made in stainless steels including high-alloyed

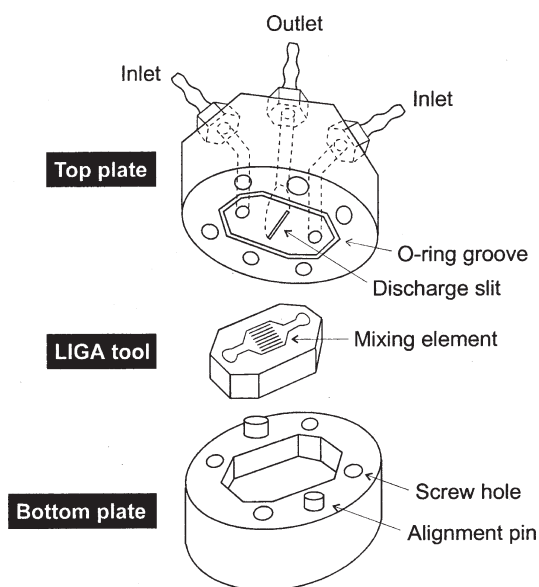


**Figure 1.83** Exploded view of the interdigital mixer device [36] (by courtesy of ACS).

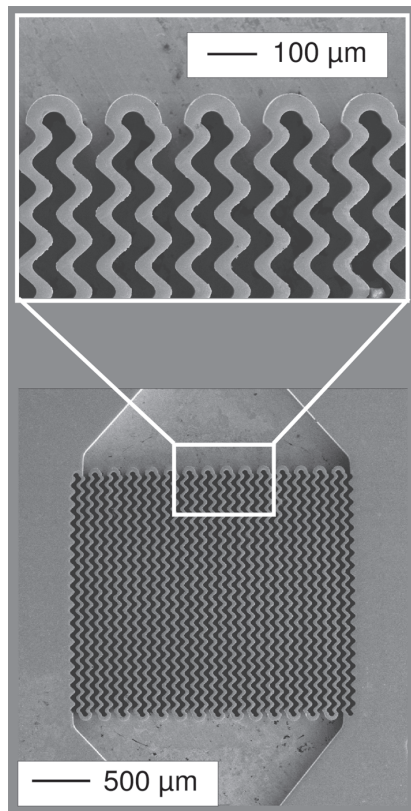


**Figure 1.84** SEM image of the interdigital mixer element [36] (by courtesy of ACS).

modifications such as Hastelloy by using  $\mu$ EDM. To save machining time, linear channels of reduced aspect ratio were made instead of the periodically curved ones. By means of laser ablation, similar structures were made in polymers.

The housing was fabricated by precision engineering, including drilling, milling and  $\mu$ EDM.

In a very early version, the interdigital elements presented above were made in glass by photoetching and joined by a thermal bonding process [125, 126]. In this way, transparent structures were achieved. The mixer was part of an integrated microfluidic system composed of many photoetched glass plates which were thermally bonded [126]. Heating and cooling channels and delay loops were placed besides two mixing elements connected in series. Instead of having tiny slits, larger square openings were put above the interdigital elements, probably at the price of reduced mixing. Characterization of such system has not been reported in the open literature.

Later, the same fabrication and interconnection process was used with an interdigital design, being more adapted to the basic elements, flat plates [20, 124]. Instead of having a complex 3-D channel guidance, the flows always follow the plate horizontally and only change from one plate to another at certain location.

Mixer type	Interdigital vertically multi-laminating micro mixer with counter-flow injection scheme	Slit width	60 $\mu\text{m}$
Mixer inlay material	Metals such as nickel or silver; to a lesser extent: silicon, stainless steels, polymers	Tubing diameter	50 $\mu\text{m}$
Mixer housing material	Stainless steel	Second tubing diameter (specially version)	500 $\mu\text{m}$
Feed channel width, depth, length (two versions)	40 $\mu\text{m}$ , 300 $\mu\text{m}$ , 1 mm 25 $\mu\text{m}$ , 300 $\mu\text{m}$ , 1 mm	Sealing material	O-ring polymer seals
Number of micro channels for one feed (two versions)	15, 18	Total size (diameter, height)	20 mm, 16 mm

#### 1.3.9.6 Mixer 41 [M 41]: Interdigital Vertically Multi-laminating Micro Mixer with Counter-flow Injection Scheme, 10-fold Array

This device is based on a numbered-up design of the cross-flow interdigital elements of [M 40] [36]. The basic parts of this device are essentially the same, a micro-structured inlay and a two-piece housing (see Figure 1.85, bottom). Ten interdigital mixing elements are operated in parallel in a star-like arrangement (see Figure 1.85, top). The feed distribution of one fluid is achieved from tubing to a ring-like channel structure in the top housing part. The other fluid is fed to the center of the inlay and spread in a star-like manner. The laminated streams are guided through a dodecagon-shaped slit and collected via a through-hole in the slit channel.

Fabrication is carried out in the same way as reported for [M 40].



**Figure 1.85** Single and 10-fold array interdigital mixer inlays (left) and assembled and disassembled 10-fold array micro mixer device (right) [36] (by courtesy of ACS).

Mixer type	Interdigital vertically multi-laminating micro mixer with counter-flow injection scheme, 10-fold array	Number of micro channels for one feed and one element (two versions)	15, 18
Mixer inlay material	Metals such as nickel or silver	Slit width	350 $\mu\text{m}$
Mixer housing material	Stainless steel	Second tubing diameter (one version only)	500 $\mu\text{m}$
Feed channel width, depth, length (two versions)	40 $\mu\text{m}$ , 300 $\mu\text{m}$ , 1 mm 25 $\mu\text{m}$ , 300 $\mu\text{m}$ , 1 mm	Sealing material	O-ring polymer seals

#### 1.3.9.7 Mixer 42 [M 42]: Interdigital Vertically Multi-laminating Micro Mixer with 'Slit-type' Focusing – 'Plane Slit Mixer'

This slit-type interdigital micro mixer is a planar version of the device [M 40] (see also [M 41]) mentioned above, because it comprises an identical focusing zone [20, 37, 124]. In slit-type focusing zone use, the multi-laminated streams are compressed at large focusing ratio by geometric constraints [20]. Then, the mixing channel with the multi-laminated streams is connected to a mixing chamber of much larger cross-section where a jet is formed surrounded by two eddies at sufficiently large flow velocity.

The construction and microfabrication are identical with those of the rectangular micro mixer [M 36] (see above) [20, 37, 124].

Mixer type	Interdigital vertically multi-laminating micro mixer with 'slit-type' focusing	Number of micro channels	$2 \times 15$
Mixer material	Specially glass (Foturan®)	Slit depth in steel housing	60 $\mu\text{m}$
Mixer frame material	Stainless steel/ aluminum	Mixing channel: length, width, height	19.4 mm, 500 $\mu\text{m}$ , 150 $\mu\text{m}$
Device outer dimensions: length, width, thickness	76 mm, 26 mm, 2.3 mm	Focusing factor	6.5
Slit-type chamber: initial width, focused width, depth, focusing length, expansion width, expansion length, expansion angle	4.30 mm, 500 $\mu\text{m}$ , 150 $\mu\text{m}$ , 300 $\mu\text{m}$ , 2.8 mm, 24 mm, 126.7°		

### 1.3.9.8 Mixer 43 [M 43]: Interdigital Vertically Multi-laminating Micro Mixer with Triangular Focusing (I)

Triangular micro mixers use hydrodynamic focusing of multi-laminated streams by geometric constraints [20, 39, 124]. The multi-channel feed section with the two reservoirs and pressure barriers is initially set on two plate levels. The feed channels are combined to the interdigital structure on one plate level in a co-flow injection scheme. In a triangularly shaped focusing section, a linear decrease in the cross-section is achieved. In standard triangular mixers, focusing ratios, i.e. the amount of the lamellae compression, are small (about 2–10); a specially version, the so-called SuperFocus, is designed to have very high focusing ratios up to 200 [20, 37, 39, 121].

The construction and microfabrication are identical with those of the rectangular micro mixer [M 36] (see above) [20, 124].

Mixer type	Interdigital vertically multi-laminating micro mixer with triangular focusing	Number of micro channels	$2 \times 15$
Mixer material	Specially glass (Foturan®)	Mixing chamber: length, initial width, height, opening angle	8 mm, 3.2 mm, 150 $\mu\text{m}$ , 20°
Mixer frame material	Stainless steel/aluminum	Mixing channel length, width, height	19.4 mm, 50 $\mu\text{m}$ , 150 $\mu\text{m}$
Device outer dimensions: length, width, thickness	76 mm, 26 mm, 2.3 mm	Focusing factor	6.5
Feed channel width and depth, width of separating walls	60 $\mu\text{m}$ , 150 $\mu\text{m}$ , 50 $\mu\text{m}$		

### 1.3.9.9 Mixer 44 [M 44]: Interdigital Vertically Multi-laminating Micro Mixer with Optimized Triangular Focusing – ‘SuperFocus’

The SuperFocus micro mixer is a specially version of the triangular mixer [M 43] with a very high focusing ratio (see Figure 1.86) [20, 37, 39, 121]. High ratios  $a/b$  ( $a$  = arc of inlet channel ends;  $b$  = mixing channel width) are achieved by increasing both the inlet ( $a$ ) and outlet ( $b$ ) diameter of the focusing zone. Owing to this fact, the number of inlet channels of the SuperFocus mixer is notably increased compared with the triangular device [M 43]. The inlet channels are made larger to diminish fouling effects, when SuperFocus mixers are designed for large liquid throughputs. The focusing length  $c$  should be kept small, in order to have a small residence time in the focusing zone, but not too small, since otherwise lamellae tilting and twisting may occur (see *Lamellae twisting in multi-lamination patterns*).

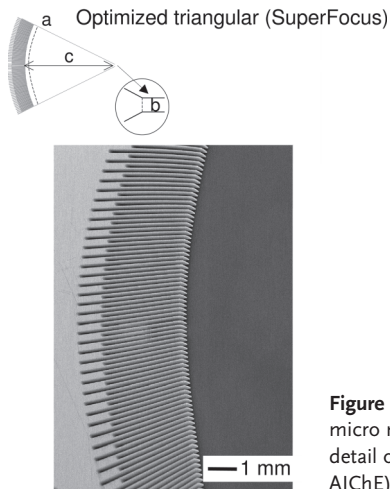


**Figure 1.86** Design of an optimized triangular interdigital micro mixer, termed SuperFocus, and SEM image showing detail of the corresponding feeding zone [20] (by courtesy of AIChE).

**(a) Glass version [20, 37, 39, 121]**

The glass version of the SuperFocus mixer is composed of three layers containing similar structures to the standard triangular mixer [M 43] (see above) [20, 37, 39, 121]. Photoetching of a specially glass is used for manufacture.

Mixer type	Interdigital vertically multi-laminating micro mixer with optimized triangular focusing – SuperFocus	Number of micro channels	$2 \times 62$
Mixer material	Specially glass (Foturan®)	Mixing chamber: length, initial width, height, opening angle	22 mm, 19.84 mm, 500 $\mu\text{m}$ , 50°
Mixer frame material	Stainless steel/ aluminum	Mixing channel: length, width, height	50 mm, 500 $\mu\text{m}$ , 500 $\mu\text{m}$
Device outer dimensions: length, width, thickness	100 mm, 26 mm, 5.2 mm	Focusing factor	39.7
Feed channel width and depth, width of separating walls	100 $\mu\text{m}$ , 500 $\mu\text{m}$ , 60 $\mu\text{m}$		

**(b) Steel version [39]**

The steel version comprises a two-piece housing, on request with an inspection window. Thin-wire erosion is used for microfabrication of the tiny cogs which served as inlet structures to achieve the multi-lamination (see Figure 1.87). High-speed

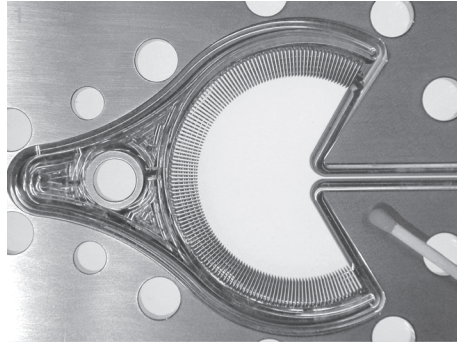


**Figure 1.87** Central part of the steel SuperFocus mixer, a plate with the interdigital cogs, machined by  $\mu$ EDM (source IMM).

milling is used for manufacture of the fluid distribution structures which are large reservoirs. These feeds are arranged on opposite sides of a plate, comprising in its center the focusing and mixing zones (see Figure 1.87). This plate is inserted in a two-piece housing and sealed with graphite gaskets. The feeds are open to every second cog, which forms a channel after assembly within the housing. In this way an interdigital feed channel arrangement is created.

Mixer type	Interdigital vertically multi-laminating micro mixer with triangular optimized focusing – SuperFocus	Number of micro channels	$2 \times 69$
Mixer and housing material	Stainless steel	Mixing chamber: length, initial width, height, opening angle	20 mm, 82.96 mm, 5 mm, $240^\circ$
Device outer dimensions: diameter, thickness	140 mm, 35 mm	Mixing channel: length, width, height	38 mm, 500 $\mu$ m, 5 mm
Feed channel width and depth, width of separating walls	360 $\mu$ m, 5 mm, 250 $\mu$ m	Focusing factor	165.9

#### 1.3.9.10 Mixer 45 [M 45]: Interdigital Vertically Multi-laminating Micro Mixer with Triangular Focusing Zone (II)

This interdigital micro mixer with a triangular focusing zone was realized consisting of a main channel and five feed channels for each fluid [120]. The two sets of feed channels are interdigitated, end at the beginning of the main channel and have the shape of half a star. At the end of the channels, ports are arranged on the section of an arc. There is an inner arc for one fluid and an outer arc for the other. The sets of ports are fed by one connector each. The main mixing channel has a short focusing region at the beginning, albeit of low focusing ratio.

Microfabrication was made using the SU-8 technique [120]. In particular, a two-layer manufacture without intermediate resist development was chosen to create two-levelled channel structures. SU-8 was brought on to a silicon substrate and UV irradiated twice, then dissolution of part of the resist was performed. For sealing, a special technique was developed. An SU-8 layer coated on a quartz or Pyrex substrate was pressed against the exposed resist structure. By baking and UV light exposure through the transparent top plate, both SU-8 layers are merged to one body, yielding a capped micro channel. If desired, the silicon substrate can be removed by wet-chemical etching.

Mixer type	Interdigital vertical multi-laminating micro mixer with triangular focusing zone	Feed channel width	50 $\mu\text{m}$
Mixer material	SU-8 Polymer	Mixing channel width	1 mm

#### 1.3.9.11 Mixer 46 [M 46]: Interdigital Vertically Multi-laminating Micro Mixer with Flow-re-directed Focusing Zone

In this version of a focusing interdigital mixer, one feed is realized via through-holes in the top plate of a device [34]. The reservoir is placed below the top plate; contacting with the other fluid is achieved on the same level. The holes are framed by a U-type wall so that the flow is allowed to pass via the opening of this 'U' structure (see Figure 1.88). The other fluid is passed through a conduit outside the frame. The frames are arranged in arrays with a short distance to each other, so shaping this conduit. The groups of such linear arrays form a V-like superstructure.

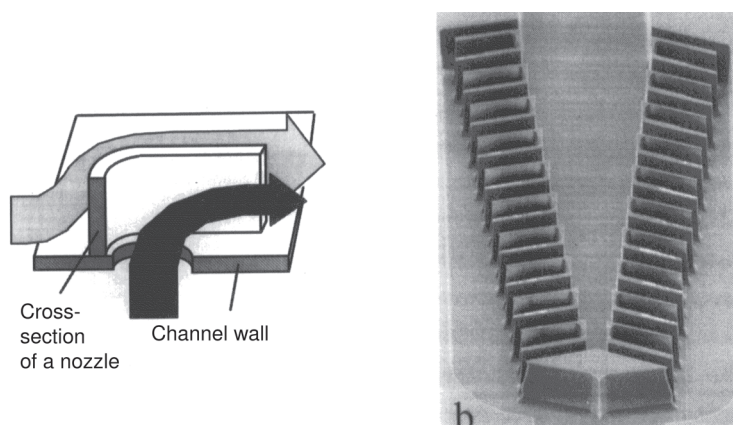


**Figure 1.88** 'U'-type frame with hole and opening forming an injection-nozzle structure (left) for an interdigital multi-laminating feed of V-like superstructure (right) [34] (by courtesy of AMI).

In the interior of the 'V' the reservoir of the one fluid is given (the other being below as mentioned above). Outside the 'V', two triangular-shaped mixing chambers are formed with a cross-sectional expansion in the flow direction in such a way that the lamellae thickness is kept constant. The flow is re-directed within these mixing chambers nearly perpendicular to the injection via the 'U'-type openings. In this way, geometric focusing of the flow is achieved, decreasing the lamellae width and promoting mixing. The two flow-through chambers merge, as do the corresponding multi-lamellae streams.

Microfabrication was effected by anisotropic reactive ion etching (RIE) using a plasma [34]. Back-side structures were realized by wet-chemical etching. A transparent plate is bonded on top of the microstructures.

Mixer type	Interdigital multi-laminating micro mixer with flow-re-directed focusing zone	Channel depth	50 $\mu\text{m}$
Mixer material	Silicon	'U' frame width, length	$\sim 40 \mu\text{m}$ , $\sim 80 \mu\text{m}$
Cover material	Glass	Lamella initial thickness	$\sim 30 \mu\text{m}$

No further details on geometries are given in [34].

#### 1.3.9.12 Mixing Characterization Protocols/Simulation

[P 34] Dilution-type dye imaging with phenol red indicator and dilute hydrochloric acid solution was applied and monitored by video taping [34]. Details on flow rates were not given.

[P 35] A reaction system with two competitive parallel reactions was used for mixing characterization [36]. The Dushman reaction involves the mixing of iodate, iodide and sodium acetate in one solution and a strong acid such as sulfuric acid or hydrochloric acid in another solution. If mixing is fast, the neutralization of the acid and the base dominates as the faster reaction. The redox reaction of iodide and iodate then is a slow process; nearly no iodine is formed as the redox product.

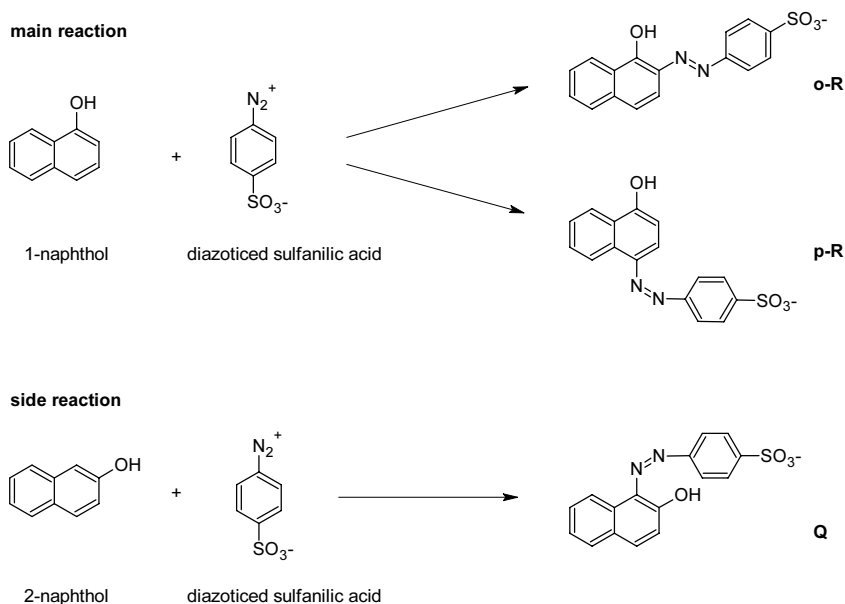
For slow, bad mixing there will be local acid and base excesses [36]. The excess of the acid can promote the redox reaction mentioned above. This acid-catalyzed reaction is much faster than the redox reaction without acid. Thus measurable contents of iodine are formed. These quantities can be detected photometrically using a UV-Vis spectrometer.

The reaction was originally used for characterizing batch mixing [78]. Here, highly concentrated drops were added to large volume in a vessel having a lower concentration [36]. For a micro-reactor operation using typically 1 : 1 ratios of the solutions to be mixed, the concentration had to be increased relative to the batch-mixing protocol to achieve comparable sensitivity. Later, an optimized micro-reactor protocol was developed using a boronic acid buffer to avoid post-reaction of the

mixed volume to iodine which was present for the original protocol [79]. Thereby, the prior existing flow-dependent error of the determination of the mixing efficiency was eliminated.

[P 36] Reactive-type dye imaging with a 10% ammonia solution in water and a solution of phenolphthalein in ethanol–water (5 g in 500 ml/500 ml) were contacted to yield an intense, pink color after mixing [67]. Transparent tubing was used for estimating the volume flow by measuring the flow speed of moving bubbles, inserted deliberately. The pressure was set hydrostatically in the range 3.5–9 kPa.

[P 37] A competitive parallel reaction was used for analyzing mixing efficiency in azo-type reaction between 1- and 2-naphthol and diazotized sulfanilic acid was chosen (see Scheme 1.1) [41]. This was mainly done owing to the speed of the reaction. Large differences are given for the rate constants, as long as complete mixing is achieved. Thus the ratio of the isomers is indicative of the mixing efficiency.



**Scheme 1.1** Reaction scheme for the azo reaction with 1- and 2-naphthol with diazotized sulfanilic acid.

A mathematical correlation between the selectivity of the azo reaction and the scale of mixing by laminar and turbulent flow is described in [41].

A modified azo reaction protocol is given in [122, 123].

Computational fluid dynamics were used to describe the flow which undergoes a fast transition from laminar (at the fluid outlets) to turbulent (in the large mixing chamber) [41]. Using the commercial tool FLUENT, the following different turbulence models were applied: a  $k\varepsilon$  model, an RNG- $k\varepsilon$  model and a Reynolds-stress model. For the last model, each stream is solved by a separate equation; for the two first models, two-equation models are applied. To have the simulations at

practical times, the computing was done for part of the design using symmetry correlations.

[P 38] Gas mixing in a flow-through mixing chamber was followed by sampling at defined places in the front of the mixer feed outlets [40]. This was achieved by a motor-driven capillary, with an outer diameter of 30  $\mu\text{m}$  and an inner diameter of 20  $\mu\text{m}$ , which automatically scans a pre-defined path. Larger capillaries may disturb the flow and give false results. The position of the camera was checked with a CCD camera. A typical scan was a lateral movement over the full extension of the mixing chamber followed by a slight change in the vertical direction and scanning laterally in the reverse way and so on. The velocity of the capillary was restricted to 2.5  $\mu\text{m s}^{-1}$ , basically owing to have a sufficient response time of the analysis system, using a mass spectrometer.

The fluid temperature was kept at 25 °C. Argon–nitrogen and helium–nitrogen mixing was investigated at throughputs from 1.25 to 5.0  $\text{l min}^{-1}$ , corresponding to 4.34 to 17.36  $\text{m s}^{-1}$  [40].

[P 39] Dilution-type mixing uses blue-colored water and pure water solutions as two feeds [20, 39]. The flow pattern is visualized and mixing is indicated by giving intermediate blue colors. Photographic imaging was applied.

Aqueous solutions with high concentrations of the commercial dye ‘water blue’ (5  $\text{g l}^{-1}$ ,  $6.25 \cdot 10^{-3}$  M) and pure water were fed through the interdigital micro mixers [7, 20]. These blue-colored solutions provide excellent contrast owing to the high solubility and large extinction coefficient of the dye. They are, in particular, suitable to image multi-laminated systems arranged parallel to the direction of observation and multi-phase systems such as gas/liquid and liquid/liquid (results not shown here; see for instance [127]). However, when assuming a layer structure horizontal or tilted with respect to the observer, it stands to reason that one cannot distinguish between a real mixed system and a layered fluid structure.

One disadvantage of using the dye ‘water blue’ imaging has to be mentioned [7, 20]. Owing to the high molecular weight of this dye, diffusion is certainly different from low-molecular weight species such as the iron ions. However, when using organic dyes, this feature is inherent to most molecules thereof, belonging to condensed extended aromatic systems.

[P 40] A reaction-type mixing uses iron trichloride and sodium rhodanide solutions as two feeds [20, 39]. A brownish solution results with the product iron rhodanide. Photographic imaging was applied.

Mixing of uncolored iron ion ( $\text{Fe}^{3+}$ ) and rhodanide ( $\text{SCN}^-$ ) solutions (81.3  $\text{g l}^{-1}$ , 0.5 M  $\text{FeCl}_3$ , and 40.5  $\text{g l}^{-1}$ , 0.5 M  $\text{NaSCN}$ ), resulting in the formation of the respective brownish complex, turned out to provide reasonable contrast and is free from any plugging phenomena [20]. Different from the ‘water blue’ solutions (see [P 39]), potentially providing information both on the fluid layer formation at the very beginning and on the course of mixing, the iron rhodanide system only displays the completion of mixing, linked to the color reaction. Thereby, mixing even in complex fluid systems, e.g. tilted lamellae, can be visualized.

[P 41] Semi-analytical calculations were performed for determining mixing quality [39]. Assuming uniform lamella formation and the absence of lamellae tilting, and

neglecting the velocity distribution in the channel, the convection-diffusion problem of mixing can be translated into a pure diffusion problem. Assuming periodic boundary conditions, the problem can be solved by modeling the diffusion process over the domain of a single lamella. A diffusion coefficient of  $10^{-9} \text{ m}^2 \text{ s}^{-1}$  was assumed.

The numerical results are based on the solution of the incompressible Navier–Stokes equation:

$$\frac{\partial v_i}{\partial t} + (v_j \cdot \nabla_j) v_i = -\frac{1}{\rho} \nabla_i p + \frac{\eta}{\rho} \nabla^2 v_i, \quad \nabla_i v_i = 0 \quad (1.2)$$

and a convection–diffusion equation for the concentration field:

$$\frac{\partial c}{\partial t} + (v_i \cdot \nabla_i) c = D \nabla^2 c \quad (1.3)$$

by means of the finite-volume method.  $V_i$  is the fluid velocity,  $\rho$  and  $\eta$  its density and viscosity,  $D$  the binary diffusion constant and  $c$  denotes concentration, respectively. For pressure–velocity coupling, the SIMPLEC algorithm was used. The simulations were done with the commercial flow solver CFX4 from AEA Technology.

A mixing residual was defined as given in [37] (see [39]):

$$r = \frac{1}{A} \int_S \left| c(x, t) - \frac{1}{2} \right| da \quad (1.4)$$

The initial value is 0.5 for concentration values of 0 and 1.

[P 42] A further extension of the above-mentioned approach [P 41] for design optimization is described in [38]. Here, the convection–diffusion problem was also reduced to a pure diffusion problem. Further details can be found in [38].

The CPU times needed for these calculations were  $< 1 \text{ min}$  [38].

[P 43] A defined illumination was established by using a light-guide system with two goose necks for quantitative in-line monitoring of concentration profiles through transparent micro mixers [20]. Owing to problems with achieving a constant fixed illumination with the existing equipment, a new calibration was made for each experimental run (typically lasting a day) with each mixer by using standard solutions of the dye with known concentration. The images of both calibration and experimental solutions were converted to gray-scale format. Thereby, the concentration distribution was gathered when analyzing the images taken under fixed illumination with images of the calibration solutions. Using imaging software, concentration profiles along the channel cross-section were obtained.

### 1.3.9.13 Typical Results

[M 36] [P 39] A regular multi-lamination pattern composed of 30 lamellae is found for a rectangular interdigital mixer [20, 39, 124]. Within the limits of a photographic image, no notable deviations are observed. No mixing is observed for residence times ranging from 4.3 to 1140 ms.

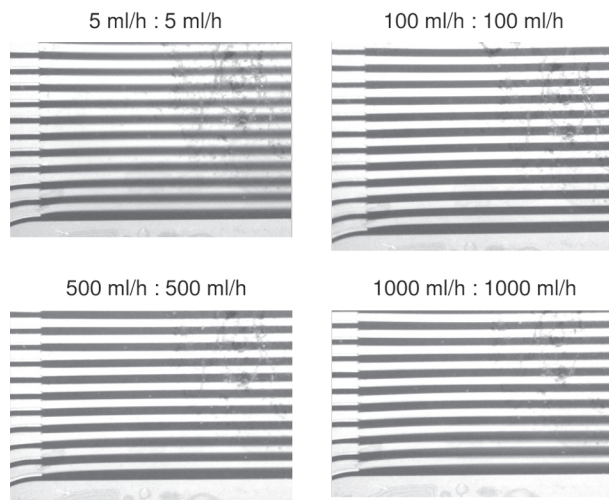


**Figure 1.89** Multi-lamination flow patterns in the rectangular interdigital micro mixer for various flow rates [20] (by courtesy of AIChE).

The flow pattern remains the same for total flow rates from 10 to 2000 ml h<sup>-1</sup>, corresponding to residence times of 4.3–1140 ms (see Figure 1.89). [20]. Thus ‘pure’ laminar flow without any secondary flow patterns applies.

[M 43]/[P 39] A regular multi-lamination pattern composed of 30 lamellae is found for a triangular interdigital mixer [20, 39]. Within the limits of a photographic image no notable deviations are observed.

At a low volume flow rate of 20 ml h<sup>-1</sup>, separated light and dark sections become increasingly smaller when passing through the triangular zone and reveal a more homogeneous color profile after entering the rectangular outlet zone. This is confirmed by detailed analysis of the concentration profile (see Figure 1.90).

Moreover, Figure 1.90 shows that not all lamellae have absolutely equal thickness, as opposed to the observations in Figure 1.89. The thickness decreases from the interior towards the exterior. An analysis of the lamellae thickness at various cross-sectional positions was derived by precise measurement of the respective high-

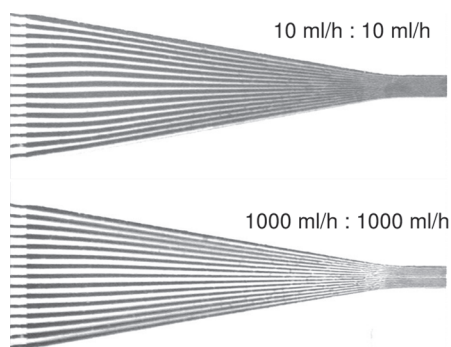


**Figure 1.90** Multi-lamination flow patterns superposed by geometric focusing in the triangular interdigital micro mixer at two flow rates [20] (by courtesy of AIChE).

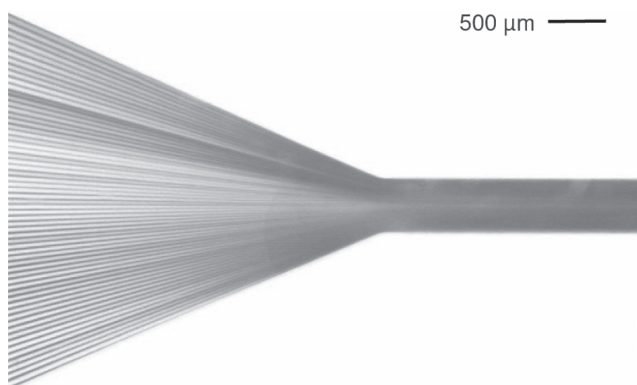


**Figure 1.91** Multi-lamination flow pattern superposed by focusing in the SuperFocus interdigital micro mixer, visualized by rhodanide reactive imaging ( $4 : 1 \text{ l h}^{-1}$ ) [20] (by courtesy of AIChE).

contrast image at high magnification. The interior lamellae are up to 50% larger than those near the wall. This deviation is probably caused by the parallel orientation of the inlets, i.e. the various lamellae flows have different angles with respect to the channels' direction, rather than being guided in the same direction. Thereby, the lamellae width becomes slightly dependent on the channel position.

[M 44a] [P 40] A fairly regular multi-lamination pattern composed of 124 lamellae (see Figure 1.91) is found for a SuperFocus interdigital mixer (glass version; small arc of interdigital feeds) [20, 39, 121]. Small deviations in lamellae thickness obviously lead to the different share of mixing observed visually, i.e. parts of the lamellae are darker than the rest. It seems that the interior lamellae have less mixing, i.e. are lighter in color.

The fairly uniform color formation in the mixing channel demonstrates that mixing is close to completion [20]. A total flow of  $8 \text{ l h}^{-1}$  at a pressure drop of 2.5 bar can be achieved owing to the parallel feed of many inlet channels.

[M 44a] [P 40] A regular multi-lamination pattern composed of 138 lamellae is found for a SuperFocus interdigital mixer (glass version; large arc of interdigital feeds) [39, 121]. Deviations are found only for some outer lamellae leading to the different share of mixing. Owing to the dilution-type experiment, these areas have more diffuse colors. The reason is unclear at present; it may be due to lamellae tilting (albeit this is not in line with simulations) or may reflect the velocity profile.

When using an asymmetric flow ratio ( $5 : 1$ ) for still better flow visualization, the regularity of the multi-laminated pattern is the most striking feature (see Figure 1.92) [39].

#### Multi-lamination patterns for focused, re-directed streams

[M 46] [P 34] A multi-lamination pattern was evident in the central and inner parts of the flow when entering a triangular focusing section with re-directed flow ( $\sim 90^\circ$ ) [34]. The outer part, i.e. close to the channel walls, was disordered, probably owing to flow maldistribution.

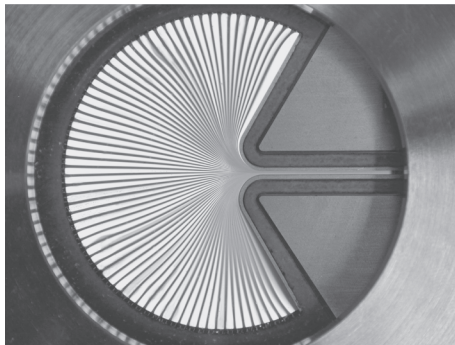


**Figure 1.92** Regular arrangement of liquid lamellae in the focusing chamber of the SuperFocus micro mixer (steel version; large arc of interdigital feeds). For better flow visualization, an asymmetric flow ratio (5 : 1) was chosen, setting the dyed water solution at a lower flow rate [39].

#### Multi-lamination patterns for lateral multi-lamination

[M 37] [P 36] The onset of mixing for a lateral multi-lamellae flow was demonstrated by pH-driven color formation using an indicator solution (7 kPa;  $1.2 \mu\text{l min}^{-1}$ ) [67]. Two channels of the multi-lamellae flow were blocked so that also non-dyed zones were visible. Applying higher flow rates led to incomplete mixing. The fact that complete mixing could be only achieved at comparatively long residence times in the order of one second or so can be explained by the rather large diffusion distances, about  $100 \mu\text{m}$ , provided by the first-generation device.

Simulations predict a high degree of mixing for the conditions of the experiment [67]; however, the visual inspections so far only vaguely confirm this.

#### Multi-lamination patterns for vertical bi-lamination – reference case

[M 38] [P 36] Using a reactive visualization experiment based on pH-driven color formation, the homogeneous texture of the color of the mixed flow at the end of the mixing chamber suggests that mixing was not far from completion for a vertical multi-lamellae flow (3.5 kPa;  $0.9 \mu\text{l min}^{-1}$ ) [67].

Some deviations from ideal are also arise. Directly next to some outer orifices color formation is much more intense, probably owing to the longer residence time of the flow next to the walls. The same is applies to nearly all orifices in the fourth row. However, both color formations vanish shortly after a rising so that a colorless flow follows in each case, yielding color only at considerable distance at the end of the mixing chamber.

Simulations predict a high degree of mixing for the conditions of the experiment [67]; however, only the visual inspections so far can vaguely confirm this.

#### In-line concentration monitoring of multi-laminated streams

[M 36] [P 39] The concentration profiles of a multi-laminated (unfocused) stream along the cross-sectional axis of a rectangular interdigital micro mixer were determined by a special illumination technique (see Figure 1.93) [20]. These profiles were taken at a distance to the interdigital outlets within the rectangular mixing chamber attached. Within one plot, which was taken at one flow rate and one residence time, minor differences can be seen, e.g. small statistical variations in dye intensity and lamellae thickness or systematic differences such as thicker

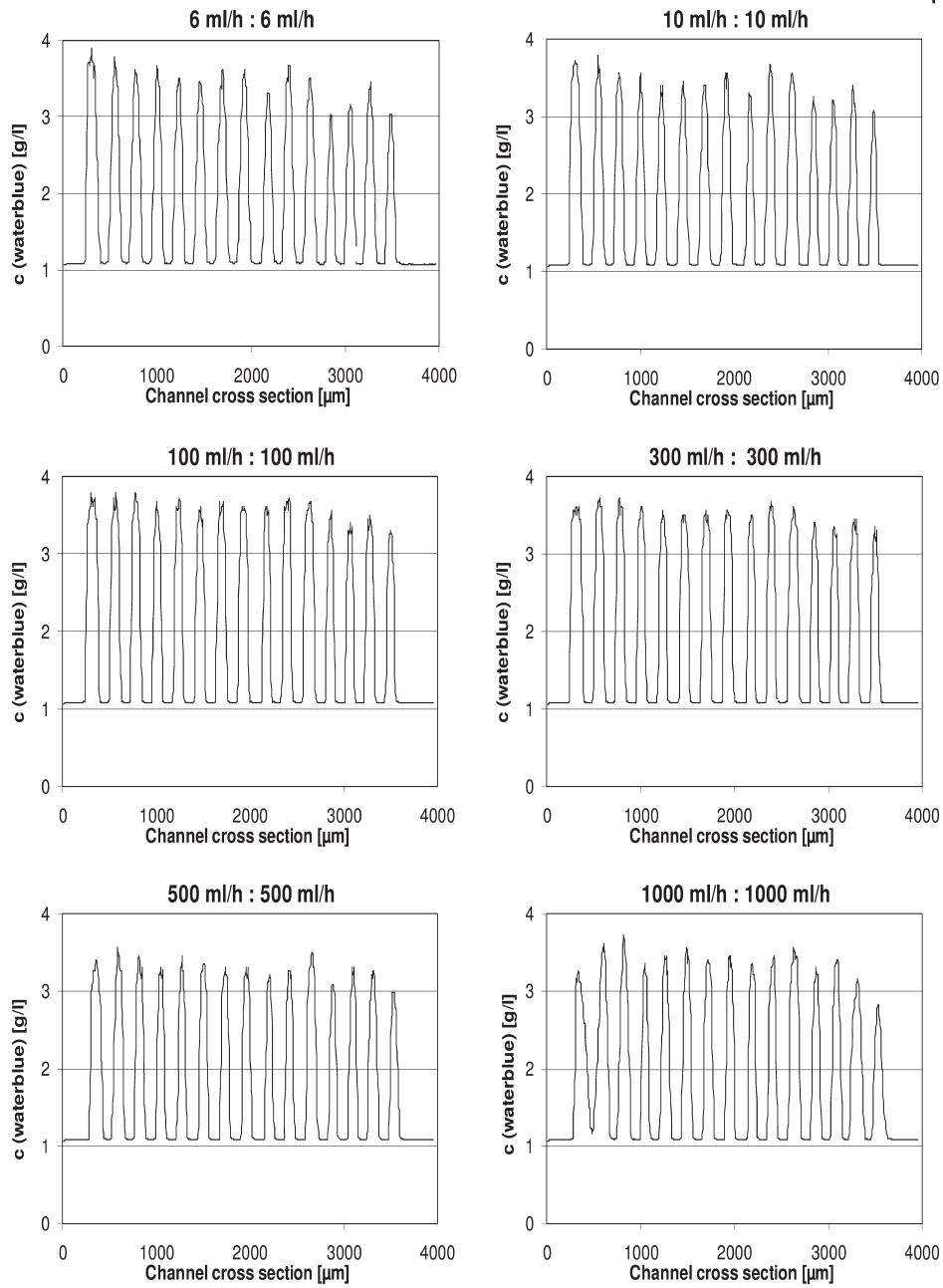


**Figure 1.93** Cross-sectional concentration profiles for multi-lamination flow patterns in the rectangular interdigital micro mixer for various flow rates [20] (by courtesy of AIChE).

lamellae at the channel walls. The different plots are virtually the same, apart from minor deviations. The latter may result from statistical fluctuations, e.g. pulsating pumps (see the inner lamellae), or systematic deviations, e.g. by surface or flow distribution effects.

Hence, the main information is that the in-line concentration profiles confirm the uniform multi-lamellae formation over a favorable large range of flow rates given already by photographic flow-pattern imaging (see *Multi-lamination patterns*) [20].

[M 43] [P 39] The concentration profiles of the triangular interdigital mixer differ from those of the rectangular mixer for two reasons [20]. First, the degree of mixing is higher owing to the geometric focusing effect. At total volume flows of 12 and 20 ml h<sup>-1</sup>, long residence times and more flattened profiles are obtained compared with those of the rectangular mixer. The profile at 12 ml h<sup>-1</sup> indicates a higher degree of mixing than that at 20 ml h<sup>-1</sup> due to the longer mixing time. Moreover, both profiles show strong deviations in concentration between outer and inner lamellae (curved profile), in particular for one of the outer lamellae next to the mixing chamber wall. The origin for the curved profile is not totally clear but may be correlated with small bending of the cover of the mixing chamber, thereby slightly changing the optical path over the cross-section.

The second major difference of the flow patterns of the triangular to the rectangular mixers that more complex concentration profiles are found which have more peaks than the number of generated lamellae [20]. This becomes evident at volume flows  $\geq 200$  ml h<sup>-1</sup>.

#### Combined hydrodynamic and geometric focusing of multi-laminated streams

[M 36] [P 39] Hydrodynamic focusing was achieved in a rectangular interdigital mixer by setting the two flow rates of the liquids at different levels [20]. In this way, one set of lamellae can be thinned considerably. The corresponding flow pattern are described as a function for the ratio of the individual flow rates of the two liquids.

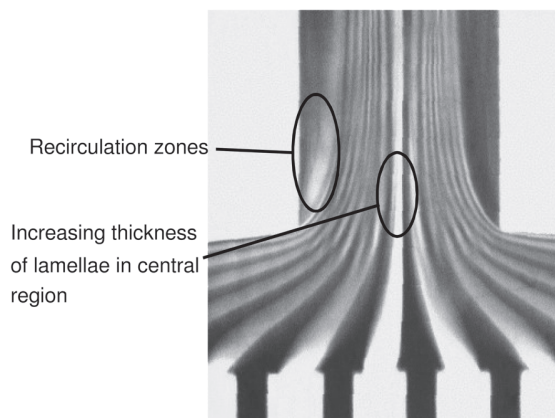


**Figure 1.94** Multi-lamination flow pattern superposed by focusing in the slit-shaped interdigital micro mixer. Blurred zones indicate lamellae tilting and winding within the entire focusing zone [20] (by courtesy of AIChE).

[M 43] [P 39] For a triangular interdigital mixer, the possibility of exerting hydrodynamic focusing was demonstrated, i.e. the enlarging of lamellae thickness for one liquid at the expense of thinning the other by having a higher flow rate for the first liquid [20, 124]. Since a triangular device is applied, the hydrodynamic effect is combined with geometric focusing in this way.

[M 42] [P 39] For a slit-type interdigital mixer the focusing performance was also characterized [20]. Owing to the moderately high focusing ratio in combination with the short focusing length, the thickness of the lamellae was considerably different. The interior lamellae are much thicker than the exterior ones. Dead zones are situated on both sides of the multi-laminated stream in the adjacent mixing channel. These dead zones are enriched with one fluid, thus are far from the final mixture.

The most striking feature, however, is that blurred zones are found in the entire focusing region with the exception of the central part (see Figure 1.94). Here, simulation results show that lamellae tilting and winding occurs.

#### Mixing time and mixing length of non-focusing and focusing interdigital mixers

[M 42] [M 43] [M 44] [M 36] [P 41] The mixing performances of several types of interdigital mixers were compared at a fixed flow rate ( $100 \text{ ml h}^{-1}$ ) – the non-focusing rectangular and the focusing triangular, slit-type and SuperFocus mixers (see Figure 1.95) [37] (see also [121]). The mixers were compared using semi-analytical calculations under certain simplified assumptions (see [37] and [P 41]). As expected, the performance of the rectangular device is worse than those of all focusing mixers. The difference is smaller when comparing mixing length than mixing time owing to the increase in flow velocity for the focusing mixers (which increases the mixing length). The SuperFocus mixer is still considerably better than the triangular mixer owing to the higher focusing ratio. For the slit-shaped mixer, only diffusion within the interior smaller lamellae was taken into account in the semi-analytical calculations. Thus, the performance is close to that of the SuperFocus mixer. However, other regions in the slit-shaped mixer will give slower mixing characteristics.

A mixing time of about 5 ms for 95% mixing is determined for the SuperFocus mixer [37] (see also [121]). This corresponds to a mixing length of about 0.6 mm at a volume flow rate of  $100 \text{ ml h}^{-1}$ . This means that complete mixing can be achieved even for flow rates of several  $\text{l h}^{-1}$  in SuperFocus mixers, needing not more than a 20 mm mixing channel length for flow rates up to  $4 \text{ l h}^{-1}$ .

[M 44a] [P 40] In order to demonstrate that fast mixing at high flow rates can be achieved in the SuperFocus mixer, experimental and theoretical derived mixing residuals were compared (see Figure 1.96) [37] (see also [121]). The experimental data were collected from on-line concentration monitoring by a spectrometric analysis of calibrated photographic images using a gray-scale analysis of the originally colored images. Albeit the experimental and theoretical data sets do not match perfectly, there is reasonable agreement, proving the assumption that SuperFocus mixers can achieve fast mixing also at  $\text{l h}^{-1}$ -flow rates. The experimental mixing length needed for 95% mixing ( $\sim 5 \text{ ms}$ ) at  $4 \text{ l h}^{-1}$  amounts to about 35 mm.

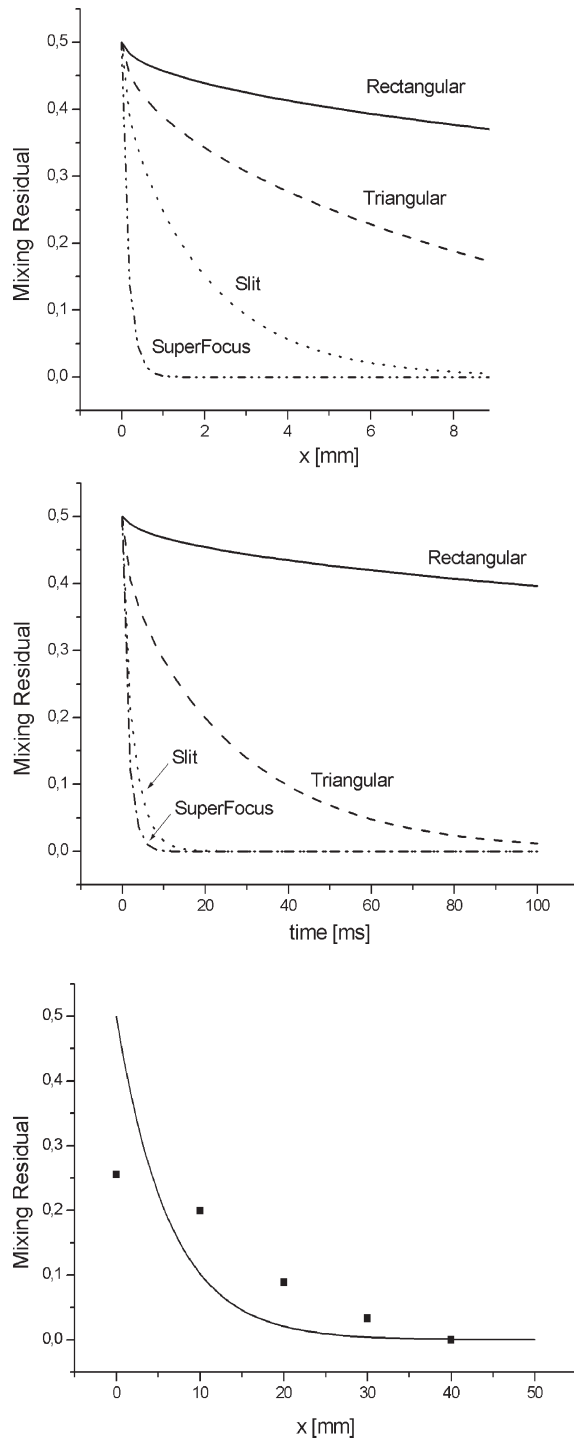


**Figure 1.95** Mixing residual as a function of distance (top) and time (bottom) [37] (by courtesy of AIChE).

**Figure 1.96** Comparison of experimental (squares) and theoretical (solid line) mixing residuals as a function of the length of the channel flow passage [37] (by courtesy of AIChE).

#### Optimization of focusing interdigital mixers by analytical modeling

[M 44a] [P 42] An intrinsic problem with the focusing concept is that a share of the flow passage has to be taken for the focusing zone in addition to the mixing zone [38] (see also [37]). Accordingly, additional residence time is required and part of the mixing sets in already in the mixing zone. Thus, the mixing performance as specified in *Liquid mixing time – benchmarking*, deliberately ignoring the focusing zone effects to circumvent a too complex analysis, is actually worse, to an extent which has to be specified.

In [38], an optimization strategy is shown for reducing the focusing zone effects with regard to residence time and mixing. The main measure for optimization is to change the depth of the focusing zone (in conjunction with changing the depth of the mixing channel attached). Therefore, the residence time was plotted as a function of the chamber depth in the focusing zone for various pressures. The quantity pressure was chosen, since it reflects other parameters of the SuperFocus mixers as a sum, regarding the focusing and mixing channel zones. Depending on the parameters chosen, residence times of the order of several tens of milliseconds are predicted. With increasing chamber depth, the residence time within the focusing chamber has a smaller relative share, which is counter-intuitive at first sight; however, this relates to the assumption of a constant pressure which is required for structural changes of the mixing channel which overcompensate the effect of changing the chamber depth. Above a chamber height of 500  $\mu\text{m}$ , the residence times become constant. At higher pressures, shorter residence times are yielded over the whole range of chamber depths investigated.

Similar behavior was observed when calculating the mixing residual [38]. The percentage of mixing can be reduced to about 10% with a sufficiently deep focusing chamber. At small depths, the amount of mixing before entering the mixing channel increases drastically. This relates directly to the residence time, enhancing diffusion.

The focusing angle also has a considerable impact on the share of the residence time in the focusing zone and the respective share of mixing [38]. Larger focusing angles decrease the residence time and mixing, e.g. down to 20 ms at 100°.

The CPU times needed for these calculations were < 1 min [38].

#### Jet flow patterns created from multi-lamination patterns

[M 42] [P 39] In a slit-type interdigital micro mixer, first multi-lamination patterns are created [20, 124]. Then, the multi-laminated stream is introduced into a chamber of larger cross-section. A jet is formed and induces two eddies in the dead zones adjacent to the initial channel (see Figure 1.97). Mixing is not completed within the chamber, as evidenced by the non-uniform color distribution. The contribution of the jet mixing to the total mixing is unclear.

The jet formation is only observed above a certain threshold flow rate [20]. At flow rates of 500  $\text{ml h}^{-1}$  jet formation takes place, whereas a multi-laminated pattern is found at 10  $\text{ml h}^{-1}$  (see Figure 1.98). In the latter case, thus a simple defocusing of the stream occurs. At still higher flow rates (2  $\text{l h}^{-1}$ ), the texture of the liquid in the large mixing chamber is homogeneous, i.e. the jet cannot be seen visually any longer. Already at the beginning of the channel attached to the chamber, the multi-

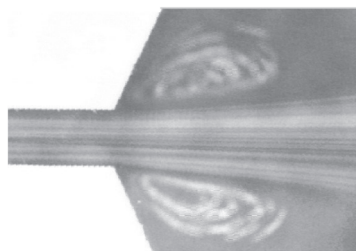
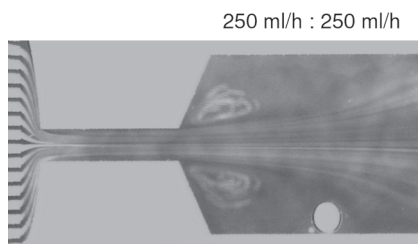


**Figure 1.97** Jet formation by reopening of the cross-sectional flow area for a multi-lamination stream which was before focused in the slit-shaped interdigital micro mixer [20] (by courtesy of AIChE).

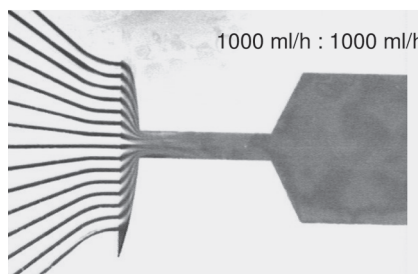
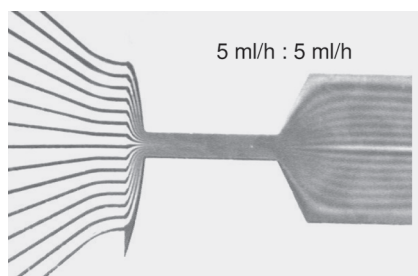
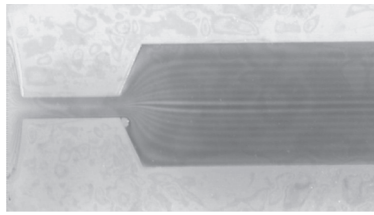


**Figure 1.98** Pure multi-lamination flow pattern (top,  $10 \text{ ml h}^{-1}$ ) and superposed by focusing and reopening/jet formation (bottom,  $2 \text{ l h}^{-1}$ ) in the slit-shaped interdigital micro mixer visualized by blue-colored water dilution imaging [20] (by courtesy of AIChE).

lamination pattern of the focusing zone breaks up and after some distance the color of the solution is fairly homogeneous. This may be due to mixing; however, it could also be caused by tilting of lamellae. In any case, this demonstrates that the degree of dispersion of the two liquids is increased.

In a decisive experiment it was judged whether mixing or only dispersion by tilting has taken place (see Figure 1.99) [20]. By reactive rhodanide imaging it was found that at  $2 \text{ l h}^{-1}$  no mixing occurred, as demonstrated by the absence of color formation due to reaction within the jet area. In the dead zones nearby, having much longer residence times, color formation was intense. The validity of this analysis is finally



50 ml/h : 50 ml/h



1000 ml/h : 1000 ml/h

**Figure 1.99** Pure multi-lamination flow pattern (top,  $10 \text{ ml h}^{-1}$ ) and superposed by focusing and reopening/jet formation (bottom,  $2 \text{ l h}^{-1}$ ) in the slit-shaped interdigital micro mixer visualized by rhodanide reactive imaging [20] (by courtesy of AIChE).

demonstrated by the fact that dilution and reactive images gave equal information at a low flow rate of  $10 \text{ ml h}^{-1}$ . Here, indeed, mixing took place and lamellae tilting was absent. Hence, the results also show that there is a need for the two mixing characterizations (dilution and reactive) in order to obtain complementary information to have information at a 3-D level on the mixing process.

#### Applicability of CFD simulation to diffusion mass transfer – numerical diffusion

[M 44a] [P 40] Numerical errors which are due to discretization of the convective terms in the transport equation of the concentration fields introduce an additional, unphysical diffusion mechanism [37]. Especially for liquid–liquid mixing with characteristic diffusion constants of the order of  $10^{-9} \text{ m}^2 \text{ s}^{-1}$  this so-called numerical diffusion (ND) is likely to dominate diffusive mass transfer on computational grids.

There are couple of measures that can taken in order to minimize ND [37]. Higher order discretization schemes such as the QUICK scheme reduce the numerical errors. Furthermore, ND depends strongly on the relative orientation of flow velocity and grid cells. ND can be minimized by choosing grid cells with edges parallel to the local flow velocity.

For the example of the slit-type interdigital micro mixer, it was shown that the higher order differencing scheme (QUICK scheme) better describe the flow pattern of the multi-lamellae than a first-order upwind scheme [37]. In the latter case, gray areas between the black and white encoded lamellae are found in the focusing zone and are due to numerical diffusion, but not correlated with a physical diffusive mixing process. However, the QUICK scheme also shows gray areas due to numerical diffusion in the mixing channel. Hence, such CFD simulations cannot properly give a quantitative description of the mixing process, but can only be used for a qualitative judgement. For quantitative analysis, semi-analytical calculations were applied instead.

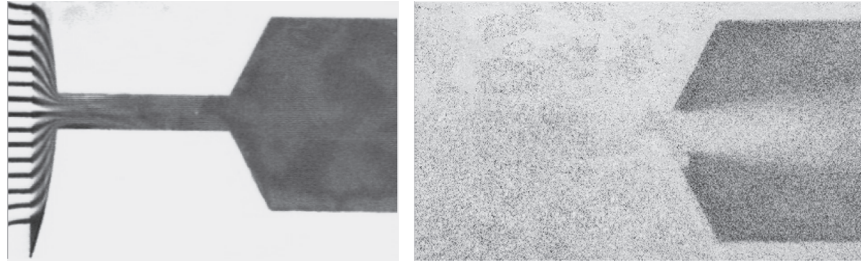


**Figure 1.100** Characterizing mixing by diffusion of a dye in an aqueous solution (left) and by a chemical reaction yielding a colored product (right) in the slit-shaped interdigital micro mixer; viewing direction is the flow direction [37] (by courtesy of AIChE).

#### Lamellae twisting in multi-lamination patterns

[M 42] [P 39] [P 40] In the focusing zone of the slit-type interdigital micro mixer, having an extreme focusing ratio, lamellae twisting and winding are observed [37] (a first hint is given in [124]). This is evidenced by having diffuse colors up to uniform color formation for dilution-type experiments, while finding no color formation for reaction experiments (see Figure 1.100). Both results seem to be contradictory at first sight. However, the latter definitely means that mixing is absent. Thus, for the first result, often indicative of mixing, a new explanation needs to be given. The dilution–color formation can be explained by having both colored and uncolored zones in the optical axis under investigation (see Figure 1.101). The result is a ‘mixed’ optical spectrum, but not relying on a mixed fluid system, but rather characterizing a dispersed one.

The underlying process was described by CFD simulations, taking into account the experiences made for reducing the numerical diffusion (see *Applicability of CFD simulation to diffusion – numerical diffusion*). Owing to inertial forces stemming from the velocity distribution in the channel, tilting occurs at low  $Re$  and transforms to lamellae winding at  $Re$  larger than about 50. Details on the lamellae winding are given in Figure 1.101.

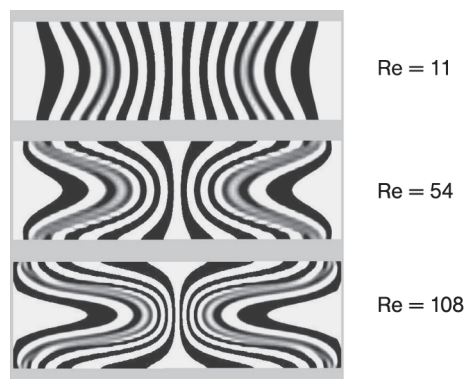


**Figure 1.101** Orientation of liquid lamellae in the mixing channel of the slit-shaped interdigital micro mixer; viewing direction is the flow direction [37] (by courtesy of AIChE).

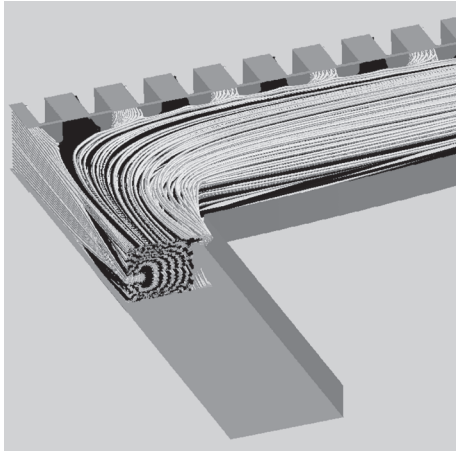


**Figure 1.102** Streamline pattern in the slit-shaped interdigital micro mixer at  $Re = 2160$  [37] (by courtesy of AIChE).

At still higher  $Re$  (2160), the lamellae become highly intertwined, as evidenced by the streamline pattern (see Figure 1.102) [37].

#### Liquid mixing time – benchmarking

[M 44a] [P 41] The liquid mixing time was calculated to 3.5 ms for a SuperFocus mixer creating lamellae about  $4\ \mu\text{m}$  thick (see Table 1.6) [39] (see also [121]). This calculation neglects the premixing in the focusing region and the respective residence time.

For an experimental validation of the mixing time, see *Liquid mixing length – benchmarking*, below. For calculation of the share on mixing of the focusing zone, see *Share of mixing of focusing zone relative to mixing zone*, below.

[M 43] [M 36] [P 41] The liquid mixing time was calculated to be 59 ms for a standard triangular mixer creating lamellae about  $110\ \mu\text{m}$  thick (see Table 1.6) [39]. For comparison, the liquid mixing time of the rectangular mixer having  $100\ \mu\text{m}$  thin lamellae is 2.48 s.

[M 43] [M 36] [P 39] The liquid mixing time was measured to be about 100 ms for a standard triangular mixer and about 3 s for the rectangular mixer [124]. The differences from the calculated liquid mixing times given above may be due to inaccuracies of judging the completion of mixing by visual inspection of dyed solutions.

**Table 1.6** Comparison of mixing performance of three interdigital micro mixers with  $8\ \text{l h}^{-1}$  aqueous streams.

Type of mixer	Mixing length for mixing residual of 0.05* (m)	Mixing time for mixing residual of 0.05* (s)
Rectangular	11.30	2480
Triangular	1.74	59
SuperFocus	0.031	3.5

\* For the definition of the mixing residual, see [39].

**Liquid mixing length – benchmarking**

[M 44a] [P 41] At a total flow rate of  $8 \text{ l h}^{-1}$ , the liquid mixing length was calculated to be 3.1 cm for a SuperFocus mixer creating lamellae about  $4 \mu\text{m}$  thick (see Table 1.6) [39] (see also [121]). This calculation neglects the premixing in the focusing region and the respective mixing length.

[M 44a] [P 40] At a total flow rate of  $4 \text{ l h}^{-1}$ , a liquid mixing length of about 3 cm was measured for a SuperFocus mixer creating lamellae about  $4 \mu\text{m}$  thick (mixing residual of 0.05) [39]. These experimental results correspond reasonably to calculation results (see *Liquid mixing time – benchmarking*, above) and generally confirm the fast, millisecond mixing properties of the device.

[M 43] [M 36] [P 41] At a total flow rate of  $8 \text{ l h}^{-1}$ , the liquid mixing length was calculated to be 1.74 m for a standard triangular mixer creating lamellae about  $110 \mu\text{m}$  thick (see Table 1.6) [39]. For comparison, the liquid mixing length of the rectangular mixer having  $100 \mu\text{m}$  thin lamellae is 11.30 m.

**Share of mixing of focusing zone relative to mixing zone**

[M 44a] [P 42] For focusing interdigital mixers, part of the residence time after lamellae contacting is needed to pass the focusing chamber. Here, mixing starts under changing conditions which is not desired and actually prolongs the real mixing time. Therefore, a reduction of the time needed for flowing through the focusing chamber is an important optimization function of the SuperFocus mixer [38]. This can be achieved by setting a different geometry, i.e. chamber depth, in the focusing zone as compared with the mixing zone.

Whereas the share of mixing in the focusing zone can be as high as 60% for a depth of 0.3 mm, it can be reduced to about 12% for a 0.5 mm depth at a certain flow rate, equivalent to a pressure drop of 4.5 bar (see Figure 1.103) [38]. Above 0.5 mm the share remains constant. The pressure drop, i.e. the flow rate, also has an influence on the mixing share, e.g. a decrease in pressure from 4.5 to 0.5 bar increases the mixing share from about 12 to 30%.

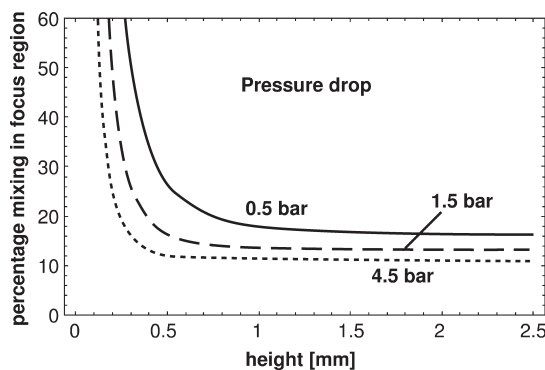


**Figure 1.103** Share of mixing in the focusing zone relative to the mixing zone as a function of the focusing zone depth. The impact of the design details, expressed as pressure drop, is also given (full line, 0.5 bar; long dashed line, 1.5 bar; short dashed line, 4.5 bar) [38] (by courtesy of Elsevier Ltd.).

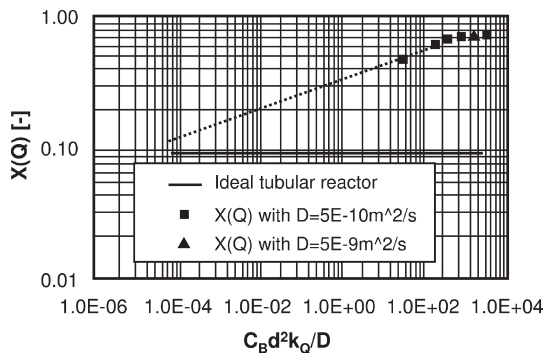


**Figure 1.104** Selectivity of an azo-type parallel reaction for testing mixing efficiency as a function of the dimensionless number  $\Pi$  [41] (by courtesy of Elsevier Ltd.).

#### Competitive parallel reactions – mixing process under laminar flow

[M 39] [P 37] Using an azo-type competitive reaction, the mixing efficiency could be determined via the selectivity [41]. Using a P-type micro mixer, laminar flow mixing could be investigated (see Figure 1.104). The selectivities measured are far from the ideal behavior of a tubular reactor.

The diffusion length was varied from 10 to 100  $\mu\text{m}$ ; for the whole range the selectivities did not indicate good mixing [41]. This shows that pure laminar diffusion cannot compare with the ideal tubular reactor. Hence, such mixers may not be adequate for fast to very fast reactions, when side reaction selectivities are considered.

[M 39] [P 37] Using an azo-type competitive reaction, the selectivities were compared for the P- and V-type micro mixers having straight and oblique fluid injection, respectively [41]. In this way, laminar- and turbulent-flow mixing achieved by vertical interdigital microstructured mixers can be compared. The selectivities of the turbulent V-type mixer are better to some extent as compared with the P-type device; however, neither approaches the characteristics of the ideal tubular reactor. The micro devices, however, are better than a conventional jet mixer.

The difference between the microstructured mixers can be understood when considering the fact that the crossing of the streams yields additional shearing which provides new interfaces for mixing [41]. Concentration differences are reduced much faster in this way.

The latter is confirmed by CFD; perpendicular-oriented velocity components are quickly compensated downstream [41]. After about 800  $\mu\text{m}$ , parallel flow of the streams is attained as for the P-type mixer.

#### V-mixer – comparison with conventional nozzle mixer

[M 39] [P 37] Using an azo-type competitive reaction, the selectivities were compared for the V-type micro mixers and conventional nozzle mixers with and without internals as a function of a specific power parameter [122, 123]. Considerably lower amounts of consecutive products, indicative of good mixing, are formed. All mixers show increasing mixing efficiency on enhancing the power.

### Turbulent energy for P-mixer and V-mixer

[M 39] [P 37] As is to be expected from the above-mentioned results, the turbulent energy is higher for the V-mixer than for the P-mixer, as CFD simulations prove [41]. These findings correlate with the analysis of the velocity components, also given above.

### Applicability of turbulent models

[M 39] [P 37] The Reynolds–stress model describes best the experimental findings out of three turbulent models investigated (see Figure 1.105) [41]. Then, the model was used for predictions of the mixing efficiency as determined by an azo-type parallel reaction. It was found that the wall thickness has no major influence, whereas the channel depth, as expected, has an influence, affecting the shearing.

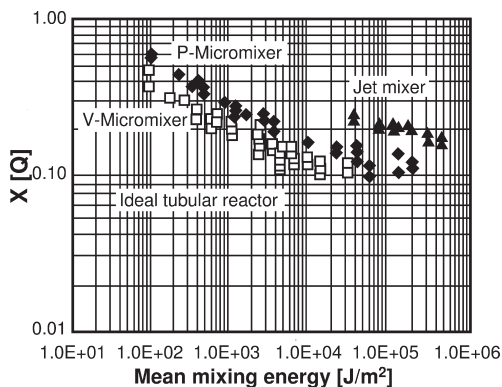


**Figure 1.105** Experimental (azo-type parallel reaction) and calculated selectivities by the Reynolds–stress model [41] (by courtesy of Elsevier Ltd.).

### Gas mixing by vertical interdigital feeds

[M 39] [P 38] Mixing argon and nitrogen in a vertical interdigital feed arrangement yields periodical, alternating (multi-lamination) concentration patterns, when analyzed at a short distance of 50  $\mu\text{m}$  to the feed outlet [40]. The concentration profile matches the feed outlet architecture. At a larger distance of 550  $\mu\text{m}$ , mixing has taken place to a large extent, i.e. the amplitude of the periodical concentration profile is decreased. For the lamellae close to the outlet, mixing is slightly less advanced as compared with the interior. After a mixing length of 800  $\mu\text{m}$ , complete mixing was attained.

### Mixing degree of gas mixing

[M 39] [P 38] The degree of mixing of argon–nitrogen was determined as a function of the mixing length [40]. As expected, an increase in mixing is found. On enhancing the volume flow from 1.25 to 5.0  $\text{l min}^{-1}$ , the degree of mixing at a given mixing length is smaller. Using species of faster diffusion such as He yields higher degrees of mixing at a given mixing length (see Figure 1.106). In most cases, complete mixing is achieved after an 800  $\mu\text{m}$  passage.

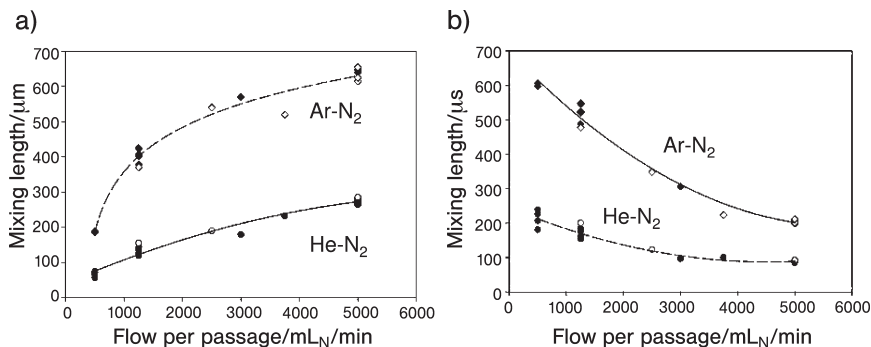


**Figure 1.106** Mixing length and mixing time for the V-type micro mixer with vertical interdigital arrangement for two gas systems (Ar-N<sub>2</sub> and He-N<sub>2</sub>) to be mixed [Pfeifer et al., Chem. Ing. Tech. 76, 5 (2004) 607].

#### Shear stress for angled injection during gas mixing

[M 39] [P 38] For angled gas-stream injection, it was detected that mixing is enhanced towards the (hypothetical) colliding point (see Figure 1.106) [40]. This is due to shear stress creating new interfaces for mixing. This leads to a discontinuity in the respective mixing degree–distance plots. For a 90° injection, the collision point was at 200 μm, the distance between the flow outlets also being 200 μm.

#### Benchmarking to standard laboratory mixing tool

[M 41] [P 35] The mixing efficiency of an interdigital micro mixer array was compared with that of mixing tees and heavily stirred vessels regarding to liquid mixing [36]. Although the comparison is more of a qualitative nature, as the flow conditions and other parameters are not equal, it gives within these limits insight into the general feasibility of using a micro mixer. Using a competitive reaction method, the micro mixer turned out to be superior to all benchmarks. The turbulent operated mixing tee was the closest reference, the same tool under laminar conditions had the worst mixing efficiency.

#### Design details – achievement of vertical lamination by 90° feed turn

[M 41] [P 35] The focusing zone of a specially interdigital micro mixer, termed ‘slit’ owing to its shape, with counter-flow and then 90° redirected feed turn, serves for flow restriction and achieves vertical lamination, if the correct geometry is chosen [36]. This is even more demanding when the focusing zone is a ring-like zone fed by multiple mixing elements instead being a single ‘slit’, which is the case for a 10-fold mixing array. It was shown that an decrease in slit width from 350 to 200 μm notably increases the mixing efficiency.

#### Design details – improving the feed channel geometry

[M 41] [P 35] The inlet flow distribution has an effect on the mixing performance in the sense that deviations from ideal feed have their influence on the gross mixing efficiency [36]. For an interdigital 10-fold mixer array, the cross-section of the inlet

channel was varied with the aim of adjusting the pressure barrier which serves for flow equilibration. A positive effect on the mixing efficiency was seen.

#### **Flow rate dependence**

[M 41] [P 35] The mixing efficiency in the slit-shaped micro mixer is constant for a comparatively large volume flow range (0.5–3 l h<sup>-1</sup>) [36]. Only at flow rates lower than 0.5 l h<sup>-1</sup> is considerably reduced performance attained.

#### **Comparison of single-element and array devices – validity of the numbering-up concept**

[M 40] [M 41] [P 35] The performances of a single-element and array micro mixer devices of interdigital feed type were compared [36]. Comparable mixing efficiencies were found, the single device being slightly better, as expected. The array mixer allows one to perform good mixing at high throughput which the single device cannot reach.

#### **Impact of lamellae width on the mixing performance**

[M 40] [M 41] [P 35] For interdigital micro mixers, the widths of the feed channel and correspondingly of the lamellae width were varied [36]. The reactive mixing characterization approach used, based on competing reactions, was able to reflect the expected increase in mixing efficiency through faster diffusion. For both single-element and array micro mixer devices improved mixing was detected on reducing the channel width from 40 to 25 μm.

#### **Luciferin/luciferase reaction to monitor multi-lamellae formation/interdigital structures for biochemical applications**

[No mixer specified here; see [128]] [no protocol] Interdigital flow configurations having a triangular focusing zone were part of an integrated biochemical system, the so-called Micro Work Bench [128]. A planar feed architecture with two rows of nozzles gave an alternate feed arrangement. An interdigital element with two outer lamellae from one fluid and one inner lamella of the other feed was realized and a respective 'numbered-up' element. As test reaction, the bioluminescence of the enzymatic reaction of firefly luciferase with ATP solution was employed, resulting in a change of fluorescence intensity, which marks the flow pattern. The thus derived patterns only roughly resembled the expected multi-lamellae flow patterns, probably for reasons of insufficient flow distribution. The fluorescence intensity decreased, indicating some mixing effect, but not to zero owing to the formation of thick in addition to thin lamellae.

#### **Interplay reaction kinetics and multi-lamination – a generic analysis**

[No details on mixer] [no protocol] Recently, the interplay between reaction kinetics and multi-lamination has been theoretically analyzed for the first time [129]. Selected types of reactions, based on different scenarios of the elemental main, side and consecutive reactions, were defined which are common in organic synthesis. For these reactions simple, but nonetheless valuable, kinetic equations were assumed. For the multi-lamination mixing also selected scenarios were taken, including small

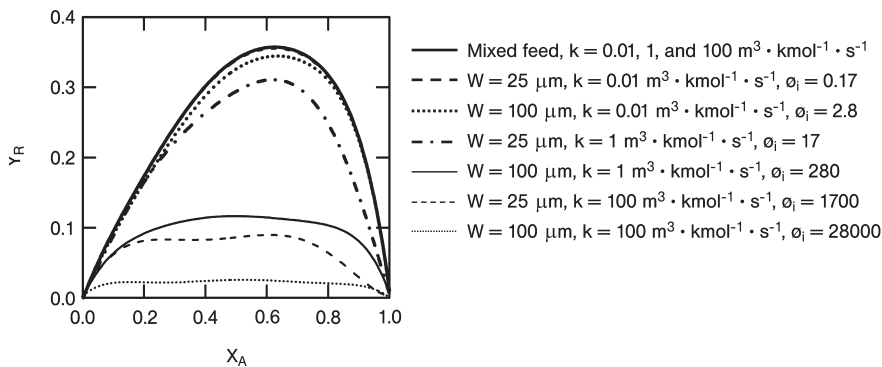


**Figure 1.107** Relation between yield of a product R and conversion of a reactant A for different rate constants and lamination widths for one selected scenario of elemental reaction (two reactants A + B form R, while B can react with R as well in a consecutive reaction to the consecutive product S). W: lamellae width; k: rate constant;  $\phi_i$ : ratio of reaction rate to diffusion rate [129] (by courtesy of Elsevier Ltd.).

lamellae widths in multi-laminated flow configurations and large lamellae widths in bi-laminated flows. Only diffusive mixing was assumed for reasons of simplicity. Then, it was calculated what might happen if such a selected reaction is undergone in such a lamellae configuration. It was found that the choice of lamellae has a strong effect on the reaction course and hence on selectivity and yield (see Figure 1.107). For some processes, thick lamellae are the preferred choice. Based on such conclusions, optimized design configurations were proposed in which part of the flow, containing mainly side products, was removed under laminar-flow conditions, leaving a purer stream with enhanced main product share. Thus, an in-line separation technique was proposed for increase in product purity.

### 1.3.10

#### Interdigital Concentric Consecutive Mixing

##### Most Relevant Citations

Peer-reviewed journals: [130]; proceedings contributions: [66]; contributions within books: [82].

In the section above, it was mentioned that microstructured platelet stacks are used for interdigital multi-lamination [40, 65]. Here, the feeds are oriented parallel towards a large mixing chamber. A variation of this principle arises, when a consecutive injection (instead of parallel) of the alternate fluid feeds is made. For this purpose, it is advised to set the mixing chamber in the center of the platelet and to benefit from a homogeneous concentric injection. Thus the corresponding platelets carry a larger breakout in their interior and smaller conduits for fluid feed in their outer region. Separation platelets (with breakout) and gaskets have to be inserted between the fluid carrying platelets in order to achieve separation between the two feed fluids. The fluid carrying platelets for the two feeds can be different in shape [66] or rely on the same design [130]. The concept of consecutive injection is

in particular amenable to an internal numbering-up, since stacking of thin plates on guide pins is very facile way to create hundreds (or thousands, on request) of alternate feeds.

The large diameter of the breakout and the high flow rates typically applied suggest strongly that mixing is performed under turbulent conditions [130]; final evidence in favor has not been given so far. Experimental findings on the mixing quality, however, again strongly support this assumption (see *Mixing quality vs. pressure*). At low flow rates, initial simulations, relying only on a coarse grid, hint that a circle segment fluid distribution is achieved, rather than achieving the more finely dispersed onion skin-like pattern.

#### 1.3.10.1 Mixer 47 [M 47]: Interdigital Consecutive Micro Mixer, StarLam300

This interdigital concentric consecutive microstructured mixer is composed of a housing with a cylindrical recess in which a platelet stack is inserted (see Figure 1.108) [130]. The device can be operated up to 100 bar and at a temperature of 600 °C.

The platelets contain a star-like breakout (see Figure 1.109), giving the device name of the series, StarLam [130]. From six ports the fluids are guided to the platelet center; a breakout of smaller diameter in the second type of plate (non-feed carrying) actually defines the whole flow conduit. Twelve holes are placed on a circular arc next to the platelet boundary.

Mounting of the device is facilitated, since the assembly of the many platelets to a stack is achieved by open accessible guide pins, where the platelets are threaded and thereby become pre-oriented; demounting is done in the same way (see Figure 1.110) [130]. The thread platelet stack can be uncompressed along the guide pins and thus facile cleaning is achieved. Another means to encounter fouling is



**Figure 1.108** Interdigital concentric consecutive microstructured mixers have the potential for use as chemical production tools, as evidenced by their comparatively large outer dimensions and owing to an internal numbering-up of the microstructured platelets. Left, front: StarLam300; right, back: StarLam3000 [130].

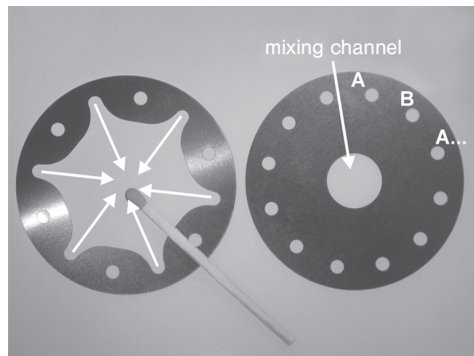


**Figure 1.109** Platelet with star-shaped breakout for fluid carriage into the mixing chamber and feed conduits (left) and separation platelet with conduits for feed distribution to the platelets (right) [130].

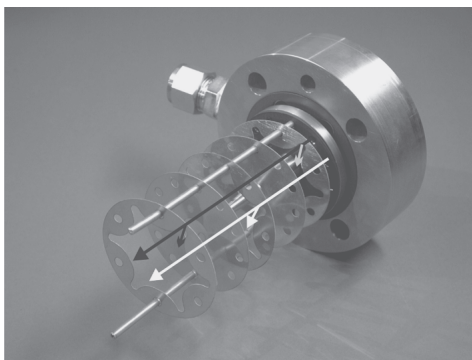


**Figure 1.110** Uncompressed stack of five platelets mounted on two guide pins and arrows indicating the fluid distribution [130].

initially to diminish it by variable adaptation of the micro spaces, i.e. choosing platelets of thicknesses ranging from 50 to 250  $\mu\text{m}$ .

The housing was made using conventional milling, turning and drilling [130]. The two platelets were realized by laser cutting with a YAG laser at 1064 nm, which allows the manufacture of all stainless steels and alloys including those customary in trade, including Hastelloy, titanium and tantalum. The design is amenable to punching or wet-chemical etching.

Mixer type	Interdigital concentric consecutive micro mixer StarLam300	Number of platelets required for forming a stack	2
Housing and platelet material	Stainless steel	Platelet material	1.4571/X 6 CrNiMo Ti 17 12 2/ASTM 316 Ti
Housing dimensions (without connectors)	$\phi 40 \text{ mm} \times 65 \text{ mm}$	Number of platelets	$2 \times 65$
Fluidic connections	Swagelok	Platelet thickness	100 $\mu\text{m}$
Mixer platelet stack dimensions	$\phi 22 \text{ mm} \times \text{max. } 17 \text{ mm}$	Seals material	Graphite; Viton; Chemraz

### 1.3.10.2 Mixer 48 [M 48]: Interdigital Consecutive Micro Mixer, StarLam3000

The StarLam3000 is the large-capacity version of its smaller counterpart, the StarLam300. The construction and fabrication of the StarLam3000 are identical with those of the StarLam300 (see [M 47]), only the design specifications vary (see below).

Mixer type	Interdigital concentric consecutive micro mixer StarLam3000	Number of platelets required for forming a stack	2
Housing and platelet material	Stainless steel	Platelet material	1.4571/X 6 CrNiMo Ti 17 12 2/ASTM 316 Ti
Housing dimensions (without connectors)	$\phi$ 100 mm $\times$ 150 mm	Number of platelets	$2 \times 113$
Fluidic connections	Swagelok	Platelet thickness	250 $\mu$ m
Mixer platelet stack dimensions	$\phi$ 56 mm $\times$ max. 57 mm	Seals material	Graphite; Viton; Chemraz

#### 1.3.10.2 Mixing Characterization Protocols/Simulation

[P 44] Pumping for determination of the highest flow rates and pressure drops was realized using a normal water conduit (28 mm copper pipe with 1 inch ball valve), a water meter customary in trade (metering precision up to 5000 l h<sup>-1</sup>) and a stopwatch [130]. The pressure drops were determined using a simple analog pressure gage (scale up to 4 bar).

[P 45] For mixing characterization, three different types of commercial membrane pumps were used depending on the capacity regime (high, thousands of l h<sup>-1</sup>; medium, hundreds of l h<sup>-1</sup>; tens of l h<sup>-1</sup>).

An original protocol for mixing characterization using the competitive iodate/iodide reaction (Dushman reaction) is given in [36]. Especially for mixing at long residence times, the mixing results are superposed by a post-reaction which thus falsifies to an extent the overall result. Meanwhile, an optimized protocol using a borate buffer has been described, yielding a stable, alkaline mixture without post reaction [79]. An aqueous solution containing 0.0319 mol l<sup>-1</sup> potassium iodide, 0.00635 mol l<sup>-1</sup> potassium iodate, 0.0909 mol l<sup>-1</sup> sodium hydroxide and 0.0909 mol l<sup>-1</sup> boric acid needs to be mixed with 0.015 mol l<sup>-1</sup> sulfuric acid [79].

#### 1.3.10.3 Typical Results

##### Maximum flow rate

[M 47] [M 48] [P 44] The current maximum flow rate of a small-scale interdigital concentric mixer (StarLam300) is 1000 l h<sup>-1</sup> at about 3 bar pressure drop [130]. For the large-scale counterpart (StarLam3000) even 3000 l h<sup>-1</sup> at only 0.7 bar is determined. Extrapolating the flow rate-pressure relationship further to 10 bar yields a flow rate of nearly 2000 l h<sup>-1</sup> for the StarLam300 and nearly 10 000 l h<sup>-1</sup> for the

StarLam3000, i.e.  $10 \text{ m}^3 \text{ h}^{-1}$ . An older StarLam version is reported to achieve about  $300 \text{ l h}^{-1}$  at 8 or 12 bar, depending on specification.

This approaches the performance of conventional static mixers, closing the gap between this smallest class of industrially used apparatus and micro mixers for analytical purposes [130]. Thus, a toolbox of microstructured mixers is available for the whole range of flow rates. This box comprises interdigital multi-laminating with a few  $\text{ml h}^{-1}$  capacity and split-and-recombine micro mixers (caterpillar type) up to  $100 \text{ l h}^{-1}$  as well as interdigital concentric microstructured mixers (StarLam type) series achieving 300, 1000 and up to  $3000 \text{ l h}^{-1}$ , dependent on the respective sub-version.

#### Maximum quality vs. flow rate

[M 47] [M 48] [P 45] Two interdigital concentric microstructured mixers of small and large scale (StarLam type) were compared for their mixing efficiency [130]. The efficiency was determined by a competitive reaction approach and is inversely proportional to a measured UV absorption signal, i.e. the extinction, relating to one reaction product, iodine. The small StarLam300 reaches extinctions as low as 0.1 at maximum flow rate, which is considered to correlate with a good mixing efficiency. The best value known for laboratory micro mixers (still smaller and lower throughput) is 0.01 [22]. The mixing performance of an older small-scale StarLam version even comes very close to this best performance of 0.01, which equals that of the caterpillar mixer at high flow rate.

The large-scale interdigital concentric microstructured mixer (StarLam3000) gives a mixing efficiency which is average, equivalent to an extinction of 0.55 (see Figure 1.111) [130]. The highest flow rate applied in these mixing-efficiency measurements did by far not correspond to the maximum possible flow rate of the StarLam3000, since for reasons of sufficient chemical stability only medium-capacity pumps could be chosen; the maximum flow rate, however, was determined using water only. Thus, it makes sense to extrapolate the mixing efficiency of StarLam3000 further to still higher flow rates. Performing this up to  $1000 \text{ l h}^{-1}$ , a similar good performance of the large version to that for its small-scale counterpart (StarLam300) is obtained.

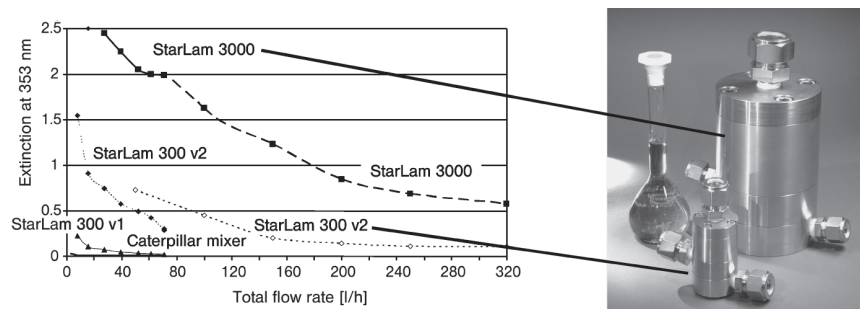


**Figure 1.111** Flow rate dependence of the Dushman mixing quality of the interdigital concentric consecutive microstructured mixers of the StarLam series and other micro mixers taken for benchmarking [130].

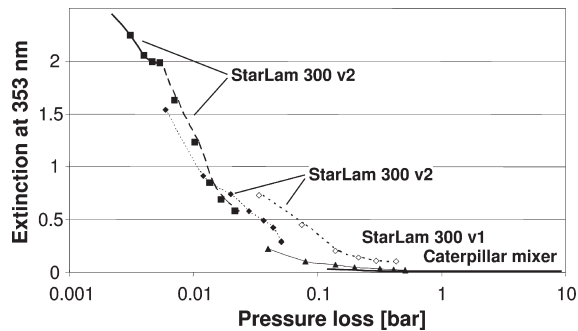


**Figure 1.112** Pressure-drop dependence of the Dushman mixing quality of the interdigital concentric consecutive microstructured mixers of the StarLam series and other micro mixers taken for benchmarking [130].

#### Mixing quality vs. pressure

[M 47] [M 48] [P 45] If the Dushman mixing efficiency of different microstructured mixers is plotted versus the pressure drop, all data sets orient on one curve (see Figure 1.112) [130]. This means that all these devices have the same decreasing relationship of pressure drop with respect to mixing efficiency, which is typical for turbulent operated static mixers. This demonstrates that achieving respectively high flow rates for each device is a prerequisite for good mixing performance. This is further evidence for the toolbox mixer concept, built from grouped devices, mentioned above.

#### Mixing quality vs. normalized flow

[M 47] [M 48] [P 45] To obtain a more general view, the flow rate can be normalized as the ratio of measured to maximum flow rate [130]. An analysis of the so-determined mixing qualities allows one to judge which percentage range of flow rates gives good mixing quality, if a threshold value for the latter is defined. The current measurements of StarLam300 and StarLam3000, which are only available up to 35% normalized flow at present owing to pumping limits, show that there is continuity when considering the percentage flows. This is further corroborated when considering the small-scale predecessor version of StarLam300. Already at 7% normalized flow rate, good mixing efficiency is achieved.

#### 1.3.11

##### Cyclone Laminating Mixing

##### Most Relevant Citations

Proceedings contributions: [109, 131, 132].

Cyclone mixers give a rotational flow field [109]. The corresponding formation of vortex patterns is another way of laminating and focusing streams. It is hoped that by folding of the vortices, thinning of the lamellae can be achieved, with an increase of residence time in the mixer [131]. A full rotation should halve the lamellae width. Hence the optimization parameter may be to have as many rotations as possible.

#### 1.3.11.1 Mixer 49 [M 49]: Cyclone Laminating Micro Mixer, Tangential Injection (I)

This cyclone mixer comprises a spherical mixing chamber with 16 equispaced nozzles which introduce the feeds tangentially at high ( $\text{m s}^{-1}$ ) fluid velocity [109] (see also [132]).

Microstructuring was effected by dry reactive ion etching (DRIE) [109, 132]. Two microstructured wafers were sandwiched between two powder-blasted wafers with through-holes and feed-rings.

Mixer type	Cyclone laminating micro mixer, tangential injection	Cover material	Pyrex
Mixer material	Silicon		

More information on the geometry was not given in [109, 132].

#### 1.3.11.2 Mixer 50 [M 50]: Cyclone Laminating Micro Mixer, Tangential Injection (II)

This cyclone mixer comprises a cylindrical mixing chamber with many nozzles, arranged on the circular arc of the chamber (see Figure 1.113) [131]. At the center of the floor of the chamber an outlet hole collects the multi-laminated streams.

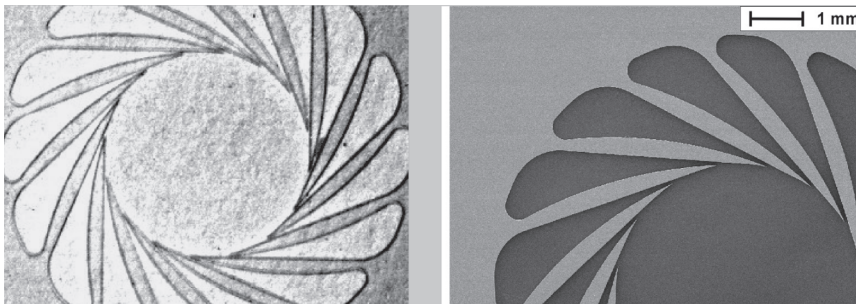


**Figure 1.113** Cyclone mixer design with tangential inlets only.

Left: photograph of a glass platelet carrying a cylindrical mixing chamber surrounded by tangential inlets.

Right: SEM image showing a detail of the same platelet [131] (source IMM).

A steel version with small mixing chamber depth and a glass version with a deeper chamber were realized. In the glass version, the nozzle feeds are located at the top of the mixing chamber, mainly for fabrication reasons, which has an extended depth. The nozzles perform fluid injection at a small angle, in the direction of the intended tangential flow. The nozzles are flat channel-type structures with strongly decreasing width so that the fluid passes through a tiny opening into the cylindrical mixing chamber.

(a) Microstructuring was effected by the LIGA process in the case of the steel version to yield a metal replica containing the cyclone-flow element [131]. This microstructured plate was inserted as an inlay in a recess of a steel housing consisting of two parts which were connected by pressure fitting using seals. The housing also contained fluid connectors.

Mixer type	Cyclone laminating micro mixer, tangential injection	Mixing chamber diameter	5 mm
Mixer material	Metal (inlay); stainless steel (housing)	Mixing chamber depth	150 $\mu\text{m}$
Nozzle width	40 $\mu\text{m}$	Outlet channel diameter	500 $\mu\text{m}$
Nozzle number	16		

(b) For the glass version, photoetching of glass and subsequent thermal bonding were applied [131]. The plate architecture was complex, i.e. as many as seven plates were needed to achieve the overall flow guidance. The thus-formed glass stack was inserted in a steel or aluminum frame with fluid connectors.

Mixer type	Cyclone laminating micro mixer, tangential injection	Mixing chamber diameter	5 mm
Mixer material	Glass	Mixing chamber depth	1150 $\mu\text{m}$
Nozzle width	40 $\mu\text{m}$	Outlet channel diameter	500 $\mu\text{m}$
Nozzle number	16	Number of micro-structured plates	7

#### 1.3.11.3 Mixer 51 [M 51]: Cyclone Laminating Micro Mixer, Cross-flow Injection

This cyclone mixer has a similar fluidic arrangement as [M 50] and was similarly fabricated, but performs the nozzle feed differently [131]. Alternating arranged vertical and tangential inlets are used, instead of having only tangential ones. Thereby, it is intended to collide jets at roughly a 90° angle in order to achieve fragmentation of the jets to smaller bodies for improved mixing. This mixer was mainly designed for multi-phase operation, in particular for gas/liquid contacting. Owing to the large space requirements of such feeding architecture, the number of nozzles is less than for [M 50]. Eleven plates were needed for the overall fluid architecture. A specially version for slurry operation was also made.

## (a) Standard version

Mixer type	Cyclone laminating micro mixer, cross-flow injection	Mixing chamber diameter	5 mm
Mixer material	Glass	Mixing chamber depth	1150 $\mu\text{m}$
Nozzle width, liquid and gas side	50 $\mu\text{m}$ , 30 $\mu\text{m}$	Outlet channel diameter	500 $\mu\text{m}$
Nozzle number	2 $\times$ 8	Number of micro-structured plates	7

## (b) Specially version for slurry operation

Mixer type	Cyclone laminating micro mixer, cross-flow injection	Mixing chamber diameter	10 mm
Mixer material	Glass	Mixing chamber depth	1150 $\mu\text{m}$
Nozzle width, liquid and gas side	50 and 150 $\mu\text{m}$ (two sets), 30 $\mu\text{m}$	Outlet channel diameter	500 $\mu\text{m}$
Nozzle number	2 $\times$ 8	Number of micro-structured plates	11

## 1.3.11.4 Mixing Characterization Protocols/Simulation

[P 46] Mixing speed was studied by finite element modeling tools [109].

Deionized water and 0.1 mM fluorescein solution were contacted in a dilution-type experiment (1 bar injection pressure) [109].

## 1.3.11.5 Typical Results

**Extension of rotational flow field in mixer outlet**

[M 49] [P 46] The extension of the rotational flow field in the mixer outlet was visualized (see Figure 1.114) (inlet speed 10  $\text{m s}^{-1}$ ;  $Re_{\text{max}}$  200; 10 bar) [109].

**Impact of mixer geometry on total rotation**

[M 49] [P 46] The total rotation was given as a function of the dimensionless geometric parameter ratio, namely the chamber diameter to nozzle width and the chamber diameter to height ratios, at various heights of injection [109]. The total rotation is notably dependent on the height of injection. Fluid volumes entering at half-height undergo the largest rotation. The mixing chamber geometry has a much smaller influence, albeit minimizing the width and optimal diameter to height ratios slightly improve the rotation.

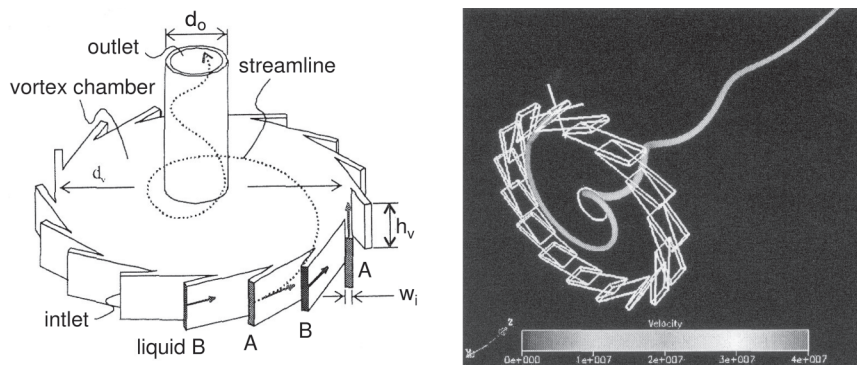


**Figure 1.114** Schematic of the cyclone mixer design (left) and streamline indicating the rotational flow field in the cyclone micro mixer [109] (by courtesy of Kluwer Academic Publishers).

#### Vortex flow patterns

[M 49] [P 46] The formation of vortex flow patterns was confirmed both by simulation and experimentally [109] (see also [132]). While the simulation suggests spirally wound fluid flow, the first experiment yields only a direct straight flow into the center outlet. However, this difference might be merely due to the fact that very initial results are presented in [109].

[M 50] [P 39] At low total flow rates, star-shaped profiles, i.e. the streams go straight from the nozzles to the center outlet hole, are visible, which indicates reasonable flow distribution (see Figure 1.115) [131]. The top image reveals a larger dark-colored fraction than the transparent one. Since large-area mixing is not likely for the short residence times in the chamber, this indicates that the fluid compartments are folded towards the optical observation axis. The top image then sums up optical information from different fluid layers, giving rise to an integral color. At higher flow rates, the streams take a more tangential direction, now folding the layers in the vertical direction which gives the typical vortex structure. At still higher flow rates, images of nearly homogeneous color texture are obtained, which again is seen to be due to layer folding and not to mixing (for reasons of the short residence time).

The images of the experimental patterns resemble with fairly large detail simulated flow images [131]. For example, fine structures such as edged bending at the inlet are found on both types of images. In the experiment, however, the image is not totally symmetrical. About one-quarter of the top view of the chamber has nearly homogeneous color, which is likely due to flow maldistribution, i.e. one fluid is fed here at some higher flow rate and occupies a much larger space.

[M 51] [P 39] For sole liquid flows, this cyclone mixer also reveals vortex-type flow patterns [131]. By increasing the volume flow, the extent of spiral winding of the liquid layers increases as in the observations made for the tangential-flow device previously (see Figure 1.115). Correspondingly, at Reynolds numbers of a few hundred, hydrodynamic focusing of liquid lamellae sets in, by which time the lamellae width becomes considerably reduced. The homogeneous texture of the

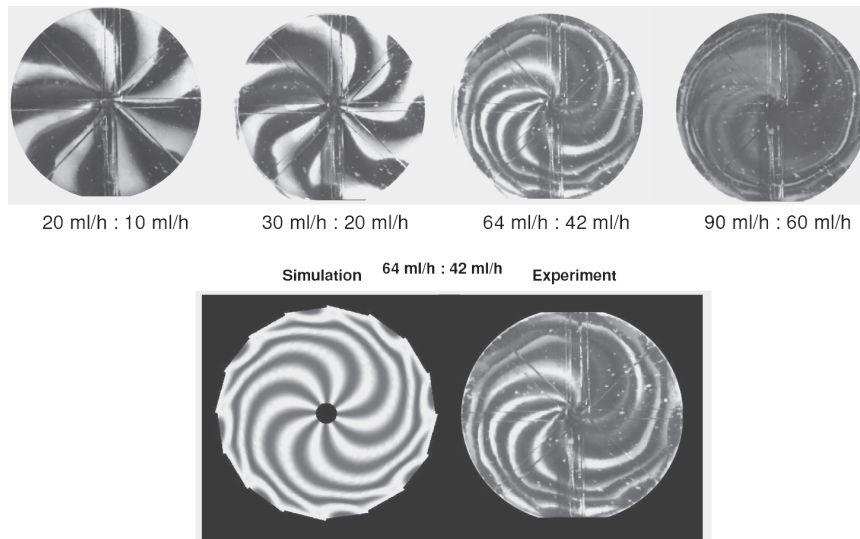


**Figure 1.115** Top: photographs of vortex-flow pattern formation at various flow rates when contacting water and dyed water (acid blue) solutions in the tangential-flow cyclone micro mixer. Bottom: comparison of the experimentally derived image of one vortex pattern with the predicted image by CFD simulation [131] (source IMM).

liquid flow in the chamber suggests a high degree of mixing; however, simulations predict that this is due to tilting of the lamellae.

Similar vortex patterns were also found for gas/liquid flows [131], which is outside the scope of this book, however.

### 1.3.12

#### Concentric Capillary-in-capillary and Capillary-in-tube Mixing

##### Most Relevant Citations

Peer-reviewed journals: [133] (see also [134]).

Capillary-in-capillary mixers use simple base structures, namely capillaries, for fluid feed and as mixing chambers [133, 134]). The very simple idea is to insert a smaller capillary into a larger one under strict control of the distance of these two objects. Albeit the capillaries themselves then may have macro dimensions, micro-space conditions may be achieved by proper adjustment of their relative diameters and, in addition, by adjustment of the following mixing chamber, i.e. thereby creating thin fluid compartments. These compartments can be two circles of an arc of similar diameter, if a cylindrical flow obstacle is placed in the larger capillary in the mixing section and the two fluids need to be passed through the free distance between the obstacle and the large capillary's wall [133, 134]. If this is not the case, one fluid forms an inner cylindrical stream surrounded by the outer shell of the other fluid, provided that laminar conditions pertain.

Capillary-in-capillary mixers were used for electrospray ionization mass spectrometry (ESI-MS), which allows one to perform on-line kinetic studies for a wide range of applications in chemistry, bioorganic chemistry, isotope exchange experiments and enzymology, just to name a few [133]. ESI-MS is a method alternative to the traditionally employed quench-flow techniques with off-line analysis.

#### 1.3.12.1 Mixer 52 [M 52]: Capillary-in-capillary Micro Mixer

A laboratory-built continuous-flow mixing set-up was constructed around a mixer made from two concentric capillaries. The capillary of larger diameter was placed in a three-way union; a sleeve was inserted at one end of the union to allow insertion of the smaller capillary. The inner capillary was closed by a rapid curing, self-priming polymer glue. Upstream a notch is cut into the side of the inner capillary so that the respective fluid has a conduit to contact the other. Both fluids have to flow along the passage until the glue plug end with very narrow diameter, by which fast completion of mixing is achieved. Then, the mixed flow was directly introduced into an analytical instrument, which was here a mass spectrometer [133].

Two syringe pumps fed the mixer, the inner capillary directly from behind, the outer capillary being fed by the third port of the three-way union, in a vertical direction to the other feed [133]. A Delron block was then positioned at the end of the outer capillary, providing a connection to a mass spectrometer.

The mixing volume of the capillary-in-capillary mixer is adjustable and can be controlled automatically, i.e. it is not necessary to have a set of various capillaries and to exchange them to match the single conditions of each new experiment [133].

Mixer type	Capillary-in-capillary micro mixer	Distance notch–glue plug, i.e. mixing length	2 mm
Inner and outer diameters of large capillary	182 $\mu\text{m}$ , 356 $\mu\text{m}$	Mixing volume and dead (mixing) time	2 nl, 8 ms
Length of outer capillary	13 cm	Glue material	Self-priming polyimide
Inner and outer diameters of small capillary	100 $\mu\text{m}$ , 167 $\mu\text{m}$	Sleeve material	Flexon
Distance between outer and inner capillaries, i.e. mixing width	8 $\mu\text{m}$		

#### 1.3.12.2 Mixer 53 [M 53]: Capillary-in-tube Micro Mixer

This double-pipe mixer contained as connection module a sort of T-piece as an outer shell to connect and fix three outer capillaries for two inlet flows and one outlet flow [134]. One tube of relatively large diameter was passed through two openings of the T-frame, so that the tube end was at the level of the end of the

T-frame. The tube end was glued to seal it and injection into the tube was made from the side through the third opening of the T-frame. In the center of the tube a small-diameter capillary was inserted; the second fluid was fed through this flow conduit. Since this small capillary had a shorter length in the outlet section than the large tube, the respective fluids were contacted from this point.

The double-pipe mixer was designed and so far only used for contacting and reacting immiscible fluids [134]. The respective flow-pattern maps were derived and annular and slug flows as well as complete spread of the inner-tube fluid were identified as distinct regimes. Since in this chapter only miscible liquids are concerned, no protocol and no results are given for the mixer below. However, the device is mentioned, since it could in principle be used also for mixing miscible fluids.

Mixer type	Capillary-in-tube micro mixer	Inner diameter of large tube	3000 $\mu\text{m}$
Tube material	Glass	Inner and outer diameters of small capillary	1588 $\mu\text{m}$ , 307/607/878 $\mu\text{m}$

#### 1.3.12.3 Mixing Characterization Protocols/Simulation

[P 47] The capillary-in-capillary mixer was especially developed for millisecond time-resolved studies by ESI-MS. Since this ranges involves an application and characterization of the mixer itself was not performed, for further information on the experimental details the reader is referred to [133].

#### 1.3.12.4 Typical Results

##### Application to ESI-MS analysis

[M 52] [P 47] The capillary-in-capillary mixer proved functionality for millisecond time-resolved studies by ESI-MS [133]. The experiments were performed in two modes of operation: in a 'spectral mode' with recording of entire mass spectra and in a 'kinetic mode' where the intensity of selected ion signals can be monitored as a function of the average reaction time. This enabled new means of resolving kinetic data, i.e. to measure reliably first-order rate constants up to at least  $100 \text{ s}^{-1}$ . This performance is four times better than for reported ESI-MS experiments.

By control experiments with a standard commercial stopped-flow instrument, it was checked that true kinetic information was derived, i.e. that there are no mixing effects any more, which limit the applicability of the device [133].

#### 1.3.13

##### Droplet Separation-layer Mixing

##### Most Relevant Citations

Peer-reviewed journals: [39, 135, 136]; proceedings contributions: [53, 137]; chapter in encyclopedia: [138]. See also [139] for a conceptual and fabrication study of a micro dosage device generating two droplets from different sources which can be merged.

Separation-layer micro mixers are specially tools for mixing solutions which react fast or tend to foul otherwise [39, 53, 135–138]. The most prominent example of such processes is probably the generation of particles by immediate precipitation, as e.g. for calcium carbonate formation. Separation-layer mixers thus overcome the limits of normal micro mixers, which tend to clog under such conditions.

Separation-layer mixers comprise a specially interdigital feed which inserts either a miscible or immiscible layer between the solutions to be mixed, i.e. a multi-layer feed with a three-layer periodicity is generated [39, 53, 135–138]. In the case of miscible solutions, the separation layer constitutes most often the solvent itself. By this measure, mixing is 'postponed' to a further stage of process equipment or at least not initiated in close vicinity of the interdigital feed. Accordingly, the solutions to be mixed are fed in a fairly defined, dispersed state to a later stage of processing, but not as a mixed state on a molecular level. It is common laboratory experience that other types of miniaturized process equipment such as tube reactors/heat exchangers do not suffer from precipitation to the same extent as mixers with their tiny nozzles do.

Two groups of separation-layer mixers were described, one having a regular interdigital feed in a planar structure and the other having a concentric interdigital feed [39, 53, 135–138]. The planar structures create multi-lamination patterns, with every third layer being the separation layer. The fluid-compartment architecture of the concentric devices composed of an inner stream is surrounded by several rings of an arc.

The separation-layer technique benefits from the unique feature of micro mixers, such as to operate in a laminar flow regime [135]. By the absence of convective recirculation patterns, at least close to the inlet, the separation layer remains as a barrier between the solution to be mixed, as long as it is not passed by molecules owing to diffusive transport.

The concentric and planar feeds can be operated in two modes, allowing either drop- or stream-like injection of liquids in mixing chambers attached or in any other processing device such as a reaction tube [53]. Drop-like injection can be used to create segmented flows, either gas/liquid and immiscible liquid/liquid. Apart from performing multi-phase reactions, such segmented flows may be used to achieve plug-flow operation with one reacting and one inert segment. This combines effective recirculation patterns for good mixing and defined setting of residence time. Again, among other uses, this may be particularly beneficial for precipitations.

Alternatively to mixing of the precipitating reactants in a droplet, these may be injected via two separate nozzles in a micro chamber where reaction takes place and possibly further downstream transport is initiated. Although such devices have not been published to the best of our knowledge, a conceptual and fabrication study of a micro dosage device gives a very schematic idea of how such configurations may look and how they may be realized. Here, configurations are proposed with two nozzles generating two droplets from different sources which merge in a chamber below [139].

### 1.3.13.1 Mixer 54 [M 54]: Concentric Separation-layer Interdigital Micro Mixer

The concentric separation-layer micro mixer is constructed as an assembly of stacked plates for feed supply with three tubes, performing lamination for mixing, set into one another (see Figure 1.116) [39, 53, 136–138] (see also [135]). The tubes are inserted into a frit. The three feed lines are each connected to a tube. In this way, a tri-layered concentric fluidic system is achieved. Besides mixing three solutions, a major application for the device is to separate the two fluids to be mixed by a separation layer, usually being the solvent of the two solutions. This is to delay the mixing process in order to avoid unwanted fouling problems at the mixer outlet. This is particularly valuable for spontaneous precipitation reactions which are the main field of application of the mixer.

The steel plates are made by milling and the PEEK tubes by turning and milling [39].

Mixer type	Concentric separation-layer interdigital micro mixer	Tube inner diameters	1.5 mm, 2.5 mm, 3.4 mm
Tube material	PEEK	Tube outer diameters	2.0 mm, 3.0 mm, 4.0 mm
Housing material	Stainless steel	Tube lengths	28.50 mm, 21.75 mm, 15.00 mm
Device outer dimensions: length, width, thickness	41 mm, 41 mm, 24 mm	Fluid layer thickness (from interior to outside)	1.5 mm, 200 $\mu\text{m}$ , 200 $\mu\text{m}$



**Figure 1.116** Schematic of the construction of the concentric separation-layer micro mixer and magnified concentric fluid layer arrangement when leaving the mixer [53] (source IMM).

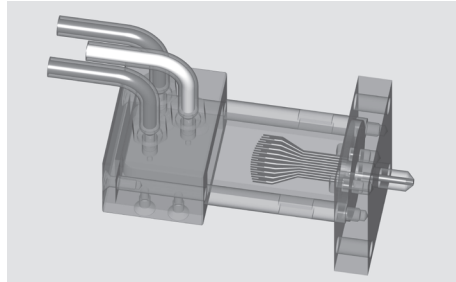


**Figure 1.117** Schematic of the construction of the stacked separation-layer micro mixer [53] (source IMM).

### 1.3.13.2 Mixer 55 [M 55]: Planar Separation-layer Interdigital Micro Mixer

The planar separation layer mixer is constructed as an assembly of stacked plates held in a frame which comprises the fluid connectors (see Figure 1.117) [39, 53, 136–138] (see also [135]). The interdigital feed structure is virtually the same as for normal interdigital micro mixers (see Section 1.3.9) with the exception that, owing to the feed of three fluids, three reservoirs and three multi-channel feeds in three plates are needed. Such interdigital feeding structure generates alternately arranged lamellae of the three liquids. The mixing chamber is rectangular from the feed inlet until close to the outlet and then becomes tapered to fit better to the round fluid adapters normally used.

The glass plates were manufactured by photoetching of a specially glass and were irreversibly bonded by a thermal soldering process [39].

Mixer type	Planar separation-layer interdigital micro mixer	Feed channel width, depth	60 $\mu\text{m}$ , 500 $\mu\text{m}$
Tube material	Glass	Fin width	50 $\mu\text{m}$
Frame material	Stainless steel, aluminum	Fluid layer thickness	110 $\mu\text{m}$
Device outer dimensions: length, width, thickness	80 mm, 41 mm, 41 mm	Mixing chamber width, depth, length	10 mm, 500 $\mu\text{m}$ , 20 mm

### 1.3.13.3 Mixing Characterization Protocols/Simulation

[P 48] Flow patterns may be visualized simply by photographic imaging using light reflection, if precipitates are generated during the mixing process [39]. This was performed for droplets generated at a concentric separation-layer micro mixer. The calcium carbonate reaction may be used as a fast precipitation following immediately the mixing process.

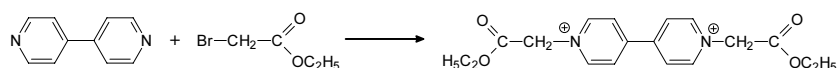
[P 49] CFD simulations were made for monitoring the flow patterns within a droplet which is generated at a concentric separation-layer micro mixer [39]. Diffusion–convection equations of two user scalars have to be solved in addition to the corresponding equation for the volume fraction of the fluids within a multi-phase CFD simulation.

The computation of free surface flows was done by means of volume tracking and relies on the solution of an advection equation for an additional scalar field with simultaneous solution of the Navier–Stokes equation [135]. Surface tension is of major importance owing to the large surface-to-volume ratio of the small droplets. CFX4.4 software was applied. The so-called ‘surface-sharpening’ algorithm was applied, which ensures global mass conservation of the phases. The calculation of mixing is done by solving an additional convection–diffusion equation for species concentration. As for many other studies, numerical diffusion can provide a non-physical mechanism which adds to the real mixing. High-order discretization schemes are employed to suppress the numerical diffusion. For discretization of the convective transport terms a higher order upwind scheme with a flux limiter was used. The mesh cell number had to be limited to 50 000 owing to constraints of present workstations.

[P 50] The fouling and plugging sensitivity was tested under real-case conditions [53]. Three test reactions were used to test the fouling sensitivity, namely the quaternization of an amine, the forced precipitation of calcium carbonate and amide formation of an acid chloride (see below). In most cases, high concentrations of the reactant solutions were used in the range  $10^{-2}$ – $1 \text{ mol l}^{-1}$ , which commonly are applied in laboratory research and chemical production. It was proved that these reactions cannot be carried out using standard micro mixers, such as the IMM interdigital micro mixers. In the last two cases, plugging within a few seconds or less occurs, naturally depending on the experimental protocol applied.

The separation-layer micro mixer was mounted about 2 cm above a funnel-shaped glass element which was connected to a glass tubular reactor, not being cooled [53]. The end of the tube was set about 2 cm above a glass beaker collecting the solutions. All experiments were made using the micro mixer and the mixer–tubular reactor set-up only.

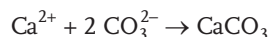
#### Quaternization of 4,4'-bipyridyl with ethyl bromoacetate



This reaction results in the precipitation of nearly the entire amount of the product if apolar, non-protic solvents are chosen [53]. This particle formation, however, needs a certain induction time, dependent on solvent and temperature.

Layers of 4,4'-bipyridyl ( $0.3 \text{ mol l}^{-1}$  in dichloromethane) and ethyl bromoacetate ( $0.3 \text{ mol l}^{-1}$  in dichloromethane) and a separation layer of dichloromethane are fitted into each other by means of the concentric separation mixer [53]. The reaction temperature is  $22 \text{ }^\circ\text{C}$ . The reaction solution is inserted as droplets or a continuous stream either directly or via the tubular reactor in the beaker. The precipitate solution yielded is passed through a frit and the remaining solid is washed with dichloromethane and dried at elevated temperature and weighed. The quaternized product is characterized by NMR spectroscopy.

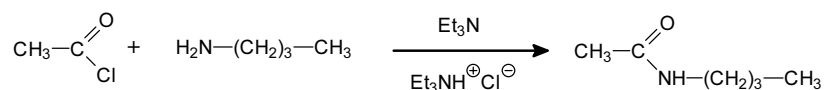
For further details of the experiments see, [53] or [72].

**Formation of calcium carbonate**

The formation of calcium carbonate is an inorganic reaction which also results in immediate precipitation [53].

Layers of calcium nitrate (40 mmol l<sup>-1</sup> in water; CaNO<sub>3</sub> · 4 H<sub>2</sub>O), potassium carbonate (40 mmol l<sup>-1</sup> in water) and a separation layer of water are fitted into each other by means of the concentric separation mixer [53]. The reaction temperature is 22 °C. The reaction solution forms droplets in a dodecane reservoir and inserted as such a segmented flow in the tubular reactor [137, 138].

For further details of the experiments, see [53] or [72].

**Amide formation from acetyl chloride and *n*-butylamine**

This reaction results more or less immediately after contact of the two reactant solutions with precipitation [53]. The reaction time is of the order of a few tens of milliseconds, if mixing is adequate.

Layers of acetyl chloride (0.79 mol l<sup>-1</sup>) in tetrahydrofuran (THF), *n*-butylamine (0.80 mol l<sup>-1</sup>) and triethylamine (0.80 mol l<sup>-1</sup>) in THF, and a separation layer of THF are fitted into each other by means of the concentric separation-layer mixer [53]. The reaction temperature is 22 °C. The reaction solution is inserted as droplets or a continuous stream either directly or via the tubular reactor in a beaker containing water. With rigorous stirring, hydrolysis of the acid chloride and hence stopping of the reaction are achieved. The phases are separated and the aqueous phase is extracted with THF. The combined THF phases are dried over Na<sub>2</sub>SO<sub>4</sub>. After filtration, the THF solvent is evaporated at 25 mbar. The remaining amide product is characterized by FTIR spectroscopy.

In a second experiment, higher concentrations were applied: acetyl chloride (0.198 mol l<sup>-1</sup>), *n*-butylamine (0.200 mol l<sup>-1</sup>) and triethylamine (0.200 mol l<sup>-1</sup>) [53].

**1.3.13.4 Typical Results****Flow patterns in concentrically multi-layered droplet mixers**

[M 54] [P 48] Separation-layer micro mixers with concentric multi-layered outlets can be operated in a droplet-forming mode [53]. If fast precipitating solutions are contacted in this way with a solvent layer for initial separation, the part of the droplet close to the tube outlets remains transparent, which demonstrates that a tri-layered system still exists with the two reacting solutions not being intermixed, as evidenced by calcium carbonate formation in aqueous solutions as described in [39, 136]. At the droplet end cap the layers collide and circulation flow sets in. As a result, mixing is achieved and precipitation occurs. The circulation patterns are visualized by the particle trajectories.

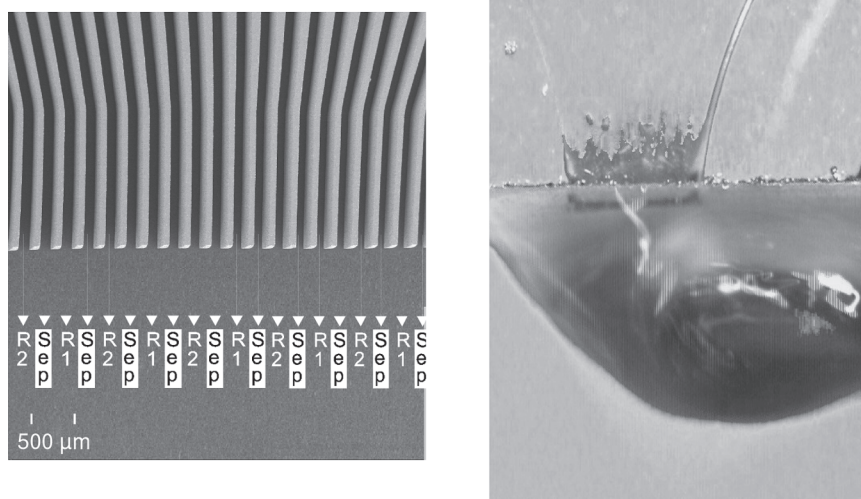


**Figure 1.118** SEM Micrograph of the planar interdigital separation-layer micro mixer (left). The multi-lamination pattern is indicated. R1, R2 and Sep refer to reactant layer 1, reactant layer 2 and separation layer, respectively. Photograph of iron and rhodanide layers each separated by a water layer flowing through the glass separation mixer (right). The multi-laminated flow in the mixing chamber is nearly transparent, hence no mixing occurred. Close to the outlet and more intense in the droplet attached discoloration due to mixing and subsequent generation of the reaction product is visible ([53]; source IMM).

#### Flow patterns in planar multi-layered stream mixers

[M 55] [P 40] Separation-layer micro mixers with planar multi-layered outlets are usually operated in continuous streaming mode. When using the iron–rhodanide reactive approach, no color formation occurs for most of the mixing chamber, which indirectly proves that nearly ideal multi-lamination flow patterns were formed [53, 136] (see Figure 1.118). This also demonstrates that no recirculation patterns such as for the concentric device arise. Hence mixing can be much better controlled and the ‘postponing effect’ is more defined than with concentric layer mixer. On the otherhand, fouling still can occur in the planar device, as the fluids are encased in a miniature mixing chamber, whereas the droplets of the concentric mixer are only exposed to a fluidic environment (no walls).

Only at the end of the mixing chamber is the formation of the colored product iron rhodanide visible (see Figure 1.118) [53]. A droplet formed at the outlet (for low volume flow rates) demonstrates even better the delay with regard to mixing.

#### Simulated equivalent diameters of droplets

[M 54] [P 49] A validation of the volume-tracking method, applied for droplet simulation, was performed by comparing the simulated equivalent diameters of droplets with data derived from analytical correlations [135]. Assuming a nozzle diameter of 1 mm and taking water and dodecane as dispersing and continuous

liquids, respectively, the analytical correlations yield values of 3.7–4.1 mm for the droplet diameter. The CFD simulations predict droplet diameters of 3.6 and 3.8 mm for flows of 10 and 40 mm s<sup>-1</sup> ( $Re = 10$  and 40), respectively.

Hence reasonable agreement of the CFD simulations and analytical correlation is achieved, demonstrating that the latter can be applied for droplet simulation studies [135].

#### Two-fluid droplet generation and mixing – close contact

[M 54] [P 49] The formation of a droplet from two aqueous solutions and the respective mixing was simulated [135] (see Figure 1.120). The inner circular liquid has 400 μm diameter and is initially separated by 100 μm from the outer annular fluid, being 150 μm thin. A series of snapshots, the concentrations given in grayscale, show the interfacial development, i.e. the flow pattern within the droplet (the diffusivity of the liquid molecules was set to zero).

A large toroidal eddy evolves and a strong upward flow in the center of the droplet is observed [135]. A more detailed image is provided by the velocity distribution and reveals that actually two toroidal eddies exist, a small one below and a large one above the stagnant interface between the upwards and downwards flows (see Figure 1.119). The mixing cannot be judged precisely owing to the numerical diffusion; however, good mixing may be assumed, especially in the droplet cap, on observing the interfacial stretching.

Two mechanisms were proposed for the strong upward and downward flows [135]. The first was based on interplay of the liquid–liquid and solid–liquid surface tensions and the gravitational and inertia forces. The second is correlated with the neck formation, the droplet break-up and the retossing of the fluid.

At the inlet the flow is almost linear and a vertical interface between the two fluids exists [135]. For this reason, fouling of the inlet is predicted and this agrees with the experimental findings.

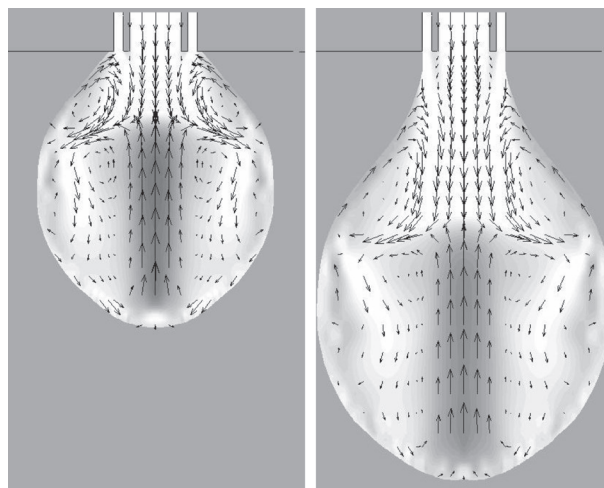


**Figure 1.119** Velocity distributions for  $t = 0.289$  and 0.6 s. For better visualization the vertical velocity component is encoded with gray tones: dark gray (white) corresponds to the maximum upward (downward) flow velocity [135].

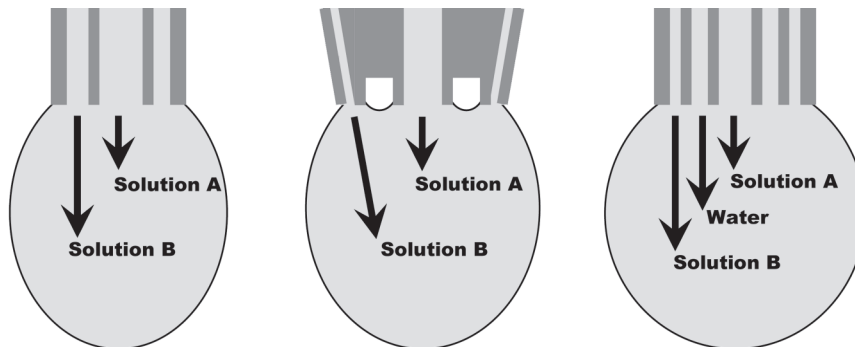


**Figure 1.120** Schematic design of the various mixing nozzles analyzed: two-fluid droplet close contact (left); two-fluid droplet separated by annulus (middle); three-fluid droplet with separation layer (right) [135].

#### Two-fluid droplet generation and mixing – fluids separated by annulus

[M 54] [P 49] Since the results mentioned above indicate that the low configuration with two closely positioned liquids is prone to fouling, simulations with a new configuration were made, placing an annulus between the two liquids [135] (see Figure 1.120). The contact of the two-fluid mixture with the nozzle walls is minimized, i.e. the wall is wetted by one fluid only. Thus, fouling should be reduced compared with the configuration with both liquids in close contact. However, the whirls are less, i.e. mixing is expected to be less.

#### Three-fluid droplet generation and mixing – separation layer

[M 54] [P 49] Simulations predict an irrotational flow pattern close to the inlet on inserting a separation-layer liquid between the two liquids to be mixed (see Figure 1.121; see also Figure 1.120). [135] (see Figure 1.121; see also [136]). Thus, this concept may be adequate to prevent fouling by keeping precipitation zones away from the tiny mixer structures. The color encoded fluid distributions suggest a low degree of mixing, which, however, is uncertain, as numerical diffusion affected most settings of the simulations.

The relative velocity distributions for the initial droplet formation exhibit a strong upward flow with toroidal eddies [135] (see also [136]). When approaching the droplet pinch-off, however, the eddies mostly disappear and only adjacent up- and downward flows are found.

Experimental findings corroborate qualitatively the predictions of the simulations [135] (see also [136]). Photographs were made with a transmitted light microscope for solutions giving a white precipitate of calcium carbonate. The precipitate scatters the light and can be detected with high resolution already with low quantities formed. In order to observe fine streaks of the precipitates (and not clouds covering most of the droplet volume), the relative flow of the separation-layer liquid was set high and the photographs were taken at an early stage of the droplet formation. Close to the inlet only a transparent solution was found, indicating absence of mixing here which is compatible with an irrotational flow pattern. At the droplet cap, a two-times folded



**Figure 1.121** Distributions of one reacting solution, the separation-layer solution and another reacting solution in black, gray and white, respectively, at time steps (from left to right)  $t = 0.03, 0.20, 0.27$  and  $0.30$  s (top). All inlet velocities were  $100 \text{ mm s}^{-1}$ . The dimensions of the separation-layer mixer are specified in [135]. The velocity distributions are given as well (bottom). Left:  $t = 0.07$  s; right:  $t = 0.76$  s. Further specifications are given in [135].

eddy is found at each side of the droplet, which proves that mixing occurred. The eddies rotate, however, in the opposite direction, as predicted by the simulations. This may be due to small misalignments of the streams in the experiment breaking the perfect rotational symmetry which is assumed in the simulations.

A further experimental proof relies on the fact that stable operation with precipitating solutions can be maintained over periods of 8 h [135].

#### **Robustness of the planar separation-layer mixer concept**

[M 54] [M 55] [P 40] Preliminary findings indicate that the mixing chamber walls of the planar separation-layer micro mixer may have a negative impact on fouling, particularly during the start-up phase and after pumping fluctuations [53]. This was not observed for the concentric mixer which does not rely on a mixing chamber; the only wall present is the mixer surface.

### Robustness of the concentric separation-layer mixer concept

[M 54] [P 50] For the concentric separation-layer mixer detailed investigations on the robustness of the reactor concept were undertaken [53]. The operation time until plugging was monitored for three well-known fast-precipitating reactions from inorganic and organic chemistry.

For the quaternization of 4,4'-bipyridyl with ethyl bromoacetate, stable operation for at least 2 h, sometimes ranging up to 8 h, was achieved [53]. The yield amounted to 75%. This yield is in the same order as for laboratory-batch operation.

For the formation of calcium carbonate, stable operation for 8 h could be achieved [53].

For amide formation from acetyl chloride and *n*-butylamine, stable operation of at least 1 h could be achieved [53]. Particularly advantageous was the setting of the flow rates to 5 : 250 : 5 ml h<sup>-1</sup>, which could be operated for 3 h. The yields achieved were between 87 and 100%. The lower yields were obtained at high total flow rates.

### Parametric studies on the impact of total flow rate, relative flow rates and concentration on the flow pattern within droplets

[M 54] [P 50] High-resolution images of the droplets at the concentric separation-layer micro mixer display details on their flow patterns when using a reactive precipitation approach. The images were taken just before rupture, i.e. refer to the most advanced mixing state during droplet formation. Thereafter, the droplets fall owing to gravity and are mixed by recirculation owing to the droplet rotation [53].

The images show a transparent and turbid portion within the droplet, indicating the absence and presence of precipitated particulates (see Figure 1.122) [53].

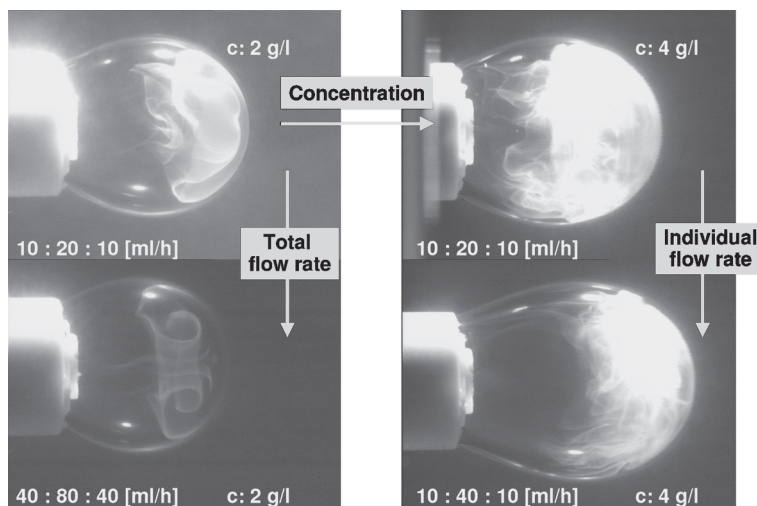


**Figure 1.122** Photographs documenting the extent and location of calcium carbonate precipitation in droplets generated by the concentric separation layer mixer. The photos were rotated by 90° to allow a better comparison ([53]; source IMM).

On increasing the concentration of the precipitating solution from 2 to 4 g l<sup>-1</sup>, the portion of the transparent section at the inlet is enlarged relative to the turbid portion containing the precipitated particulates in the bubble cap [53]. In particular, no particle strings entangling both portions are visible any longer.

On increasing the relative flow rate from 10 : 20 : 10 ml h<sup>-1</sup> to 10 : 40 : 10 ml h<sup>-1</sup> at 4 g l<sup>-1</sup>, the portion of the transparent section at the inlet is enlarged relative to the turbid portion containing the precipitated particulates in the bubble cap [53]. In particular, no particle strings entangling both portions are visible any longer.

On increasing the total flow rate from 10 : 20 : 10 ml h<sup>-1</sup> four-fold, the frequency of droplet formation is enhanced [53]. Accordingly, the residence time before rupture is reduced. This is evident by the lower degree of precipitation due to less mixing. These thin, streamline-like precipitation lines give an idea of the underlying flow patterns which are wound at the bubble cap owing to the interplay of up and down streams.

[M 54] [P 48] CFD simulations for the flow in the separation-layer micro mixer predict a stable, almost irrotational flow pattern in the inlet region, which is in line with the experimental findings of a transparent region mentioned above [39]. This pattern is maintained until the droplet end cap. Changes only occur when the droplet breaks up and falls, inducing rotational flow.

#### **Fouling prevention under fast precipitating conditions**

[M 54] [P 48] The ability of the separation-layer concept to prevent fouling even under severe conditions was demonstrated for two fast precipitating reactions, bisquaternization of 4,4'-bipyridyl and amide formation from acetyl chloride [39]. Stable operation for a few hours, and in selected cases longer, was achieved.

#### 1.3.14

#### **Split-and-recombine Mixing**

##### **Most Relevant Citations**

Peer-reviewed journals: [7, 43]; proceedings contributions: [125, 126, 140–142]; patents: [143, 144].

Split-and-recombine (SAR) micro mixers use channel splitting and recombination [7, 43, 125, 126, 140–142]. Thereby, an originally bi-laminated flow is first divided into two sets of two lamellae, each of which is guided separately in branches of the channel. During this flow passage, the cross-sections of the streams are changed in such a way that their combination yields the original cross-section. This is done repeatedly, typically 5–10 times, until 2<sup>n</sup> lamellae are achieved (*n* being the number of SAR cycles). In this way, a flow system with channel/two-channel elements as repeat unit is created. The SAR devices differ in the exact design of these repeat units which, e.g., may be of fork-like design.

For the first step, the lamellae division, a splitting plane, basically acting like a knife, can be useful [7, 140], not only for precise cutting but also for avoiding friction forces to deform the lamellae. SAR mixers were described with [7, 140] and without a splitting plane [43, 125, 126, 141, 142].

SAR mixing can also be achieved by in-channel structures [7]. The splitting here is achieved by spatially separated flow guidance of split lamellae within the channel. Elevating and descending structures can serve this purpose [7].

SAR mixing in the truest sense is only possible for very low Reynolds numbers, typically  $< 100$  [7]. At other regimes, secondary flow superposes the SAR patterns. In terms of mixing, this may even be beneficial as a faster mixing time results. However, the typical SAR flow patterns cannot be identified by flow monitoring, so that, e.g., the design cannot be optimized by these simple means.

#### 1.3.14.1 Mixer 56 [M 56]: Möbius-type Split-and-recombine Micro Mixer

The design of this SAR device was oriented on the so-called Möbius band, which is a twisted structure (see Figure 1.123) [141]. Two horizontal fluid layers are separated in the center. Thereafter, both double layers are turned by  $90^\circ$  in the same direction so that two vertically laminated systems are achieved. Then, the layers are joined to give a four-lamellae system.

The actual system consisted of two parallel rows with 10 SAR elements each [141]. The channels underwent a linear change of the width and depth to turn and reshape the flow. The mixer was an element that was intended to be integrated in a system comprising a mixing unit, reaction channel and an optical detector with crossed cylindrical lenses and optical fibers.

Microfabrication was done by means of excimer laser ablation in a polymer substrate [141]. This substrate was covered by a thin polymer sheet by thermal bonding under compression.

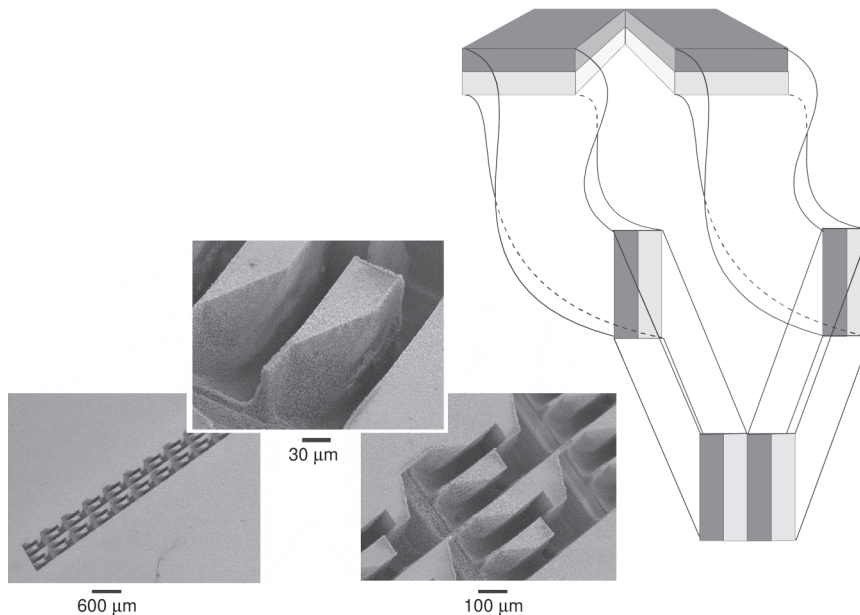


**Figure 1.123** Schematic of the SAR process in a Möbius-type SAR micro mixer [141] (by courtesy of Kluwer Academic Publishers).

Mixer type	Möbius-type SAR micro mixer	Top layer thickness	250 $\mu\text{m}$
Mixer material	Polycarbonate	Channel width	275 $\mu\text{m}$
Plate thickness	1 mm	SAR element length	500 $\mu\text{m}$
Top plate material	PMMA		

#### 1.3.14.2 Mixer 57 [M 57]: Möbius-type Split-and-recombine Micro Mixer with Fins

Another Möbius-type mixer is described in [142]. Again, a two-fold  $90^\circ$  rotation is said to be the basic principle, doubling the number of layers for laminar flow. After the first rotation, the laminated fluids are split and thereafter recombined, restoring the original geometry.

A channel with a series of diagonal fins performs the first  $90^\circ$  turn [142]. Then, the channel is split symmetrically into two channels, each having the same series of diagonal fins. Thereafter, the two channels are recombined by a junction being mirror-imaged to the first split. The original channel structure is restored. From here, the SAR step can be repeated multiple times. Experimentally it was found that seven fins are adequate for performing a correct  $90^\circ$  turn.

The microstructure was realized by a dry-film photoresist technique and based on established techniques from printed circuit board technology [142]. Dry resists are available as thin films, e.g. of thickness 50 or 100  $\mu\text{m}$ . The resist films are encased in other polymer materials which are later removed. The resist films can be deposited on various base materials such as silicon or polymers giving mechanical stability. Lamination is carried out with a roller laminator. Then, exposure is made and spray development without any solvents follows. The process steps can be repeated at multi-laminated structures. Closed structures can be made in this way. Finally, the resist is cured.

Mixer type	Möbius-type SAR micro mixer with fins	Fin width, depth	50 $\mu\text{m}$ , 200 $\mu\text{m}$
Mixer material	VACREL®	Internal mixer volume	6.5 $\mu\text{l}$
Plate material	PC-board glass-reinforced base material FR4 with 35 $\mu\text{m}$ Cu layer	Fin number (per rotation)	7
Plate thickness	1.6 mm	Number of mixing stages	4
Channel width, depth	600 $\mu\text{m}$ , 200 $\mu\text{m}$		

#### 1.3.14.3 Mixer 58 [M 58]: Fork-element Split-and-recombine Micro Mixer

The design of this mixer is based on a series of fork-shaped elements (see Figure 1.124) [43, 144]. Initially, two parallel feed channels are placed so that one

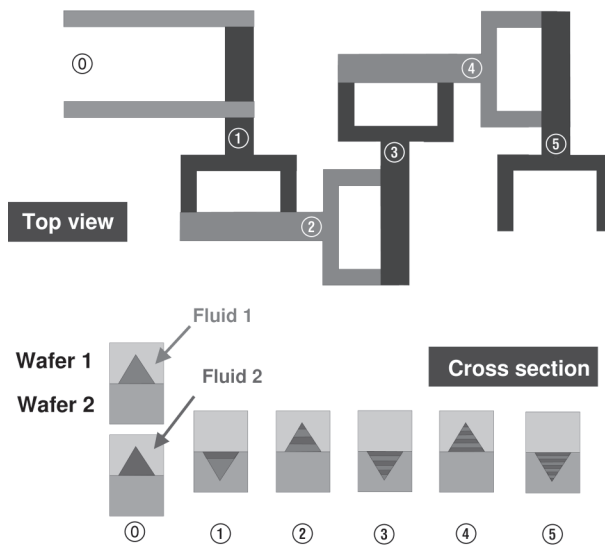


**Figure 1.124** Schematic of the SAR process using a series of fork-like elements [43] (by courtesy of IOP Publishing Ltd.).

channel is attached to the end of a fork element. The other is close to the T-junction of the fork. Thereby, the fluid layers are superposed. For reasons of simplicity, a lateral bi-laminated system is supposed. The flow is then guided through the fork like an inverse tee so that splitting into two sub-streams is achieved. The two end channels of the fork are attached to the next fork in the same way as for the first two channels. Each fork is turned by  $90^\circ$  in an anti-clockwise manner. By this repeated splitting process, the interface between the fluids is enhanced so that mixing should be promoted. For laminar flow, it is expected to have a multi-layered fluid after several SAR passages in the ideal case. The channels were of triangular shape owing to the fabrication technique chosen (see below).

Wet-chemical etching with KOH solutions was used for microfabrication [43]. The structures were etched until the natural etch stop was reached. Bonding at  $400^\circ\text{C}$  was carried out after an oxygen plasma treatment of the silicon wafer. Stainless-steel tubes were inserted in openings generated by sawing. These tubes led into transparent polymer tubing. An epoxy resin served for closing open parts in the whole system. A micropump was operated at a constant flow rate of  $10\ \mu\text{l h}^{-1}$ . The homogeneity of the fluid at the mixer outlet was investigated by using an optical microscope.

Mixer type	Fork-element SAR micro mixer	Number of mixing elements	5, 10, 15, 20
Mixer material	Silicon	Channel widths at surface	$150\ \mu\text{m}$ , $200\ \mu\text{m}$
Cross-sectional area	$1600\ \mu\text{m}^2$	SAR element length, width	$720\ \mu\text{m}$ , $500\ \mu\text{m}$

#### 1.3.14.4 Mixer 59 [M 59]: Stack Split-and-recombine Micro Mixer

This SAR device, named a stack mixer, is composed of two plates which both contain microstructures [125, 126]. By face-to-face positioning of these microstructures, a micro channel network yielding the SAR path is formed.

The two inlets feed an initial, rectangular channel, thus generating the two fluids forming adjacent lamellae with a vertical boundary (see Figure 1.125) [125, 126]. The lamellae are split horizontally by forming two sub-channels out of the inlet channel. The new channels have half the initial channel depth at same channel width. These channels are set then on the same level, at the plate interface, but still separated. Then the channels approach to each other until they merge. Thereafter, the channel width is halved and the depth doubled, restoring the initial channel geometry. This process can be repeated many times; actually five elements were placed in series in the device realized.

The actual device consists of two parallel rows of five mixing elements each [125, 126]. The lateral displacement and recombination of the sub-channels are done via  $90^\circ$  angles. In contrast, the variation of channel depth and width is done in a continuous fashion, yielding a curved horizontal and vertical structure. In particular, the curved floor structure is demanding, since a real 3-D and not just a multi-level microfabrication process is needed.

The mixer was integrated in a system composed of a four-plate device consisting of a top plate with fluid connectors, the stack mixer, a reaction channel and an optical detector using fiber optics [126]. The optical detector using fibers and cylindrical lenses to guide and focus the light and was made by LIGA for reasons of high demands on structural precision to avoid losses of light.

Microfabrication was achieved by the so-called laser-LIGA process [126] based on the replication of a master made by pulsed excimer laser ablation [125, 126]. Then, electroforming and injection molding processes followed to result finally in a replicated polymer structure identical with the master, but being amenable to mass production [126]. The plates were joined by thermal compression by heating slightly above the glass transition temperature and applying gentle pressure.

No details of the geometry specifications are given in [125, 126]. The tabulated specifications were taken from SEM images in [126].

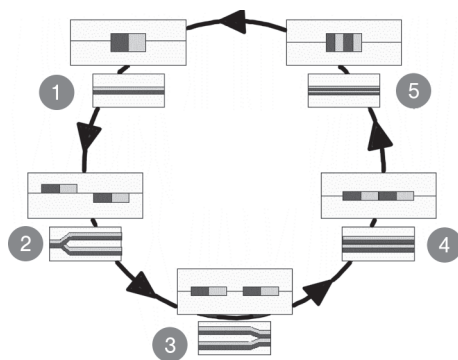


Figure 1.125 Schematic of the splitting and recombination process [125].

Mixer type	Stack SAR micro mixer	Number of parallel rows	2
Mixer material	PMMA, polycarbonate	Initial and halved channel width	120 $\mu\text{m}$ , 60 $\mu\text{m}$
Number of mixing elements	5	Mixing element length	600 $\mu\text{m}$

No characterization is provided in [125].

#### 1.3.14.5 Mixer 60 [M60]: Up-down Curved Split-and-recombine Micro Mixer

This eight-step SAR mixer was proposed with a split of one channel into two and a subsequent recombination per element, termed caterpillar mixer [7]. Since the channel is split along the horizontal axis, vertical changes of the split channels for recombination have to be undertaken. In addition, a change of the cross-section of the merged geometry has to be made to restore the original channel geometry. The vertical displacement of the split channels is achieved by smooth up and down steps, yielding a continuously curved flow structure (not step-like).

The fluidic network is formed by the assembly of two identically microstructured plates [7]. The horizontal splitting layer is inserted between the two plates as well as seals. A steel housing serves for compression and provides the fluidic connections.

The mixer plates were fabricated out of a transparent material to allow for optical inspection of the mixing process [7]. The plates were structured by milling. The unruffled surface of the channel was evident by optical and SEM inspection, revealing a continuous change of brightness. The horizontal splitting layer was realized from a thin sheet by means of pulsed sublimation cutting using an Nd:YAG laser. The graphite gaskets were made by pulsed laser cutting.

As a predecessor device, a caterpillar mixer with step-like internal structure was fabricated; without horizontal splitting layer and no separation of the streams [66].

Mixer type	Up-down curved SAR micro mixer	Splitting layer material	Stainless steel
Mixer material	PMMA	Splitting layer thickness	100 $\mu\text{m}$
Number of SAR steps	8	Gasket material	Graphite
Channel width, depth, total length (all 8 steps)	2 mm, 4 mm, 96 mm		

The same mixing geometry scaled by a factor of 0.5 was realized in stainless steel [7].

#### 1.3.14.6 Mixer 61 [M 61]: Multiple-collisions Split-and-recombine Micro Mixer

This SAR mixer, based on multiple collisions of one stream, was described by industry in a patent [143]. The same company has established the first production

plant with microstructured devices which was described in the literature, the devices being microstructured mixers [145].

One stream is split into two curved sub-streams which simply merge and then instantly split again [143]. The mixing is performed by several crosses in a row which are connected, with two channels for inlet and two for outlet. This process is repeated many times. Typical dimensions are not given and the fabrication is also not specified. Since no testing is reported, which is not surprising for an industrial proprietary method, no further information on this mixer is given below.

#### 1.3.14.7 Mixer 62 [M 62]: Separation-plate Split-and-recombine Micro Mixer

This micro mixer extends the SAR concepts mentioned above, the sequential lamination being actively supported by the use of a separation plate for flow splitting (see Figure 1.126) [140]. As a result of the splitting, two sub-channels are formed, initially at the same height level within the device. Then, one of these sub-channels undergoes a downward movement in a lower level of the device. The two flow channels are so sandwiched, the first carrying the two fluids separate from each other. At certain locations there are conduits within the sandwich to achieve flow recombination on one of the levels of the sandwich. This procedure is repeated many times.

Channel structures are etched on two plates which are later positioned face-to-face to give the overall fluid structure [140]. In the region where the channels overlap, they are separated by the separation plate defined by an etch stop layer. The channel covered by this structured plate was generated by underetching in the <100> direction through slits in the plate. The micro mixer is assembled from a silicon and a glass wafer connected by anodic bonding.

Mixer type	Separation-plate SAR micro mixer	Width of channels for inlet branches	150 $\mu\text{m}$
Mixer material	Silicon/glass	Separation-plate thickness	5 $\mu\text{m}$
Maximum channel width	300 $\mu\text{m}$	Slit width	15 $\mu\text{m}$
Channel depth	30 $\mu\text{m}$		

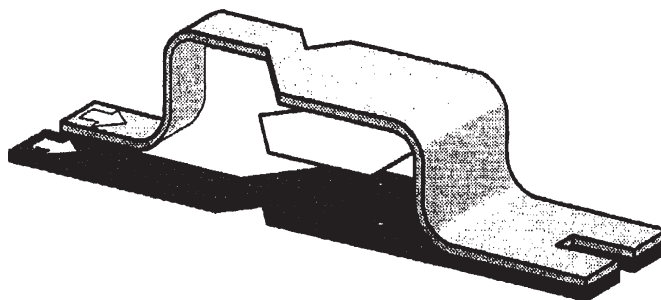


**Figure 1.126**  
Schematic of a SAR mixing concept using a separation plate [140] (by courtesy of IEEE).

#### 1.3.14.8 Mixing Characterization Protocols/Simulation

[P 51] The reduction of a solution with potassium permanganate in alkaline ethanol was used as a test reaction [141]. The course of this reaction can be simply followed by visual observation of the color changes. The reactant solution is purple, the intermediate manganate is green and the final product, manganese dioxide, is yellow to brown. One drawback relates to the precipitation of the product, which needs a cleaning step with sulfuric acid for dissolution.

[P 52] A double-syringe pump was used for liquid feed [142]. An iodine–starch solution was mixed with a photographic fixer solution in a ratio of 1 : 3.5. Thereby, the intense blue color changed to pale blue. The mixing process was followed by means of a stereo microscope.

[P 53] Mixing to the following four fluid systems was investigated [43]: (a) aqueous solutions of hydrochloric acid (1 M) and methyl orange; (b) water and air; (c) oil and air; (d) water and oil.

[P 54] The mixing experiments were performed at relatively low  $Re$ . For this purpose, 85% glycerol–water solutions were used, with dynamic viscosity and density of about 100 mPas and  $1.2 \text{ kg l}^{-1}$ , respectively [7]. Total flow rates in the range  $0.2 \text{ l h}^{-1}$  ( $Re = 0.22$ ) and  $2 \text{ l h}^{-1}$  ( $Re = 2.2$ ) were applied. For the given dimensions, CFD simulation showed that for  $Re$  above about 15, corresponding to a total flow rate of  $13.5 \text{ l h}^{-1}$ , secondary flow induced by inertial forces had a notable effect. Thus the applied flow rates were well below the critical value and pronounced secondary flow effects were not observed.

The combination of two complementary flow-pattern imaging approaches allows for reliable experimental quantization of the mixing quality [7]. First, mixing of a transparent and a dyed sub-stream is optically inspected by means of transmitted light microscopy. Second, the use of two transparent sub-streams of yellowish iron ion ( $\text{Fe}^{3+}$ ) and transparent rhodanide ( $\text{SCN}^-$ ) solutions which form a deep colored complex after mixing allows one to identify those regions where the first method mistakenly suggests good mixing due to layered lamellae configurations.

For initial simulations, a structured grid comprising 220 000 hexahedral cells was used [7]. Using the commercial solver CFX4 the Navier–Stokes equation was solved and simultaneously a convection equation for a user scalar describing a non-diffusive tracer. To minimize the discretization error, the tracer was solely used for lamellae visualization and hence the diffusivity was set to zero. A higher order differencing scheme (QUICK) was used for discretization and the SIMPLEC algorithm was applied for pressure–velocity coupling. Liquid properties of water were chosen.

[P 55] For details of the simulation approach see [140].

Flow visualization experiments were made using a pH-indicator reaction between phenol red and an acidic solution resulting in a color change. Images were recorded by a light microscope [140].

#### 1.3.14.9 Typical Results

##### Theoretical analysis of mixing via symmetric and asymmetric multi-lamination

[M 62] [P 55] The mixer design was based on a detailed theoretical analysis of flow and diffusion phenomena in the laminar regime for idealized channel geometry [140]. The time evolution of so-called asymmetric and symmetric concentration profiles was first compared for stationary conditions, i.e. without any flow.

In the symmetric case, three inner layers B–A–B of equal thickness are surrounded by two layers A of half thickness, yielding an overall layer sequence A–B–A–B–A [140]. In the asymmetric case, all layers A and B have equal thickness, but the outer layers belong to two different fluids. Thus, the sequence refers to A–B–A–B. The time required to achieve a homogeneous concentration profile, i.e. the mixing time, is much longer for the asymmetric lamination.

In addition, dynamic studies were performed including moving fluids. Generally, similar results were obtained [140]. Different from the stationary case, the width of the inner lamellae is decreased relative to the outer layers owing to the parabolic flow profile.

##### Completion of mixing

[M 57] [P 52] For a Möbius-type four-stage SAR mixer complete mixing was achieved at flow rates up to  $285 \mu\text{l min}^{-1}$  [142].

##### Relationship of residence time to reaction species for a consecutive reaction

[M 56] [P 51] In a laminar, diffusive mixing system, residence time relates to the course of mixing. Therefore, flow rates were varied when using a Möbius-type SAR mixer to vary the residence time and hence the product spectra of a consecutive reaction [141]. Reactant, intermediate and final product were all colored so that the mixing and reaction course could be directly followed by visual observation. The reduction of permanganate finally to manganese dioxide was investigated.

At fast flow rates, no color change was observed in the SAR mixer [141]. At lower flow rates, the formation of the green manganate was evident. At still lower flow rates, the brown manganese dioxide was observed. The exact flow rates were not specified.

The example shows that by control of the residence time the yield of a consecutive product can be maximized and that intermediates may be isolated at high concentration, if parameter settings are optimal [141].

##### Separation-plate SAR: visual observation

[M 62] [P 55] The mixing process was observed by flow visualization using light microscopy. A pH reaction between phenol red and an acid yielded a color change [140]. Thereby, it was possible to resolve zones with incomplete mixing in the neighborhood of the contacting zone, in particular those referring to the uneven lamination caused by the slits. A homogeneous mixture was formed in the outlet channel. Complete mixing in the whole cross-section of the outlet channel was obtained in 100–300 ms. The flow range applied was  $0.01\text{--}0.1 \mu\text{l s}^{-1}$ , which corresponds to a highly viscous flow with a Reynolds number  $< 1$ . The mixing times measured were not dependent on the flow rates.

**Fork SAR: miscible liquids – visual observation**

[M 58] [P 53] The mixing process was investigated by a pH-driven color reaction [43]. A complete change of the color was detected at the mixer outlet, i.e. mixing was assumed to be complete. This was found for SAR mixers with five and 20 mixing elements, hence a low number of mixing steps seems to be sufficient.

**Fork SAR: gas–water contacting – visual observation**

[M 58] [P 53] Air and water were contacted in a five-step fork-like micro mixer [43]. Bubbles of 200–500  $\mu\text{m}$  size resulted. The mixing in 10 mixing elements resulted in even smaller bubbles below 100  $\mu\text{m}$ . Coalescence led to the formation of larger bubbles within a few minutes.

**Fork SAR: gas–oil contacting – visual observation**

[M 58] [P 53] Oil and water were contacted in a five-step fork-like micro mixer [43]. Bubbles down to 100  $\mu\text{m}$  in size resulted, giving the whole fluid system a nearly white optical appearance. The foams were more stable than the water-based foams. About 1 h was needed until all bubbles were removed from the oil phase. When using a 20-element mixer, the oil-based foams were stable for 2–3 days.

**Fork SAR: oil–water contacting – visual observation**

[M 58] [P 53] Oil and water were contacted in a five-step fork-like micro mixer [43]. Small water droplets were achieved in this way, which soon gave a segmented oil and water flow. When using a 15-step fork-like micro mixer, smaller droplets resulted giving an opaque system of emulsion nature. The separation into two separate phases took 3–4 days.

**Increase in interfacial stretching for split–recombine mixing – lyapunov exponent**

[M 60] [P 54] In the framework of chaotic convection, the mixing performance is commonly characterized by interfacial stretching:

$$\lambda(t) = \lim_{L_0 \rightarrow 0} \frac{L(t)}{L_0} \quad (1.5)$$

where  $L_0$  and  $L(t)$  denote the characteristic dimensions of the interfacial area at  $t = 0$  and at finite time  $t$ , respectively [7]. In the case of a 2-D incompressible flow, the diffusive mass transport, which determines the mixing performance, depends quadratically on the interfacial stretching  $\lambda$ . Chaotic flows ensure particularly efficient mixing since they imply an exponential increase of stretching over time.

Accordingly, the finite-time Lyapunov exponent  $\sigma$  may be defined via

$$\lambda(t) \approx e^{\sigma t} \quad (1.6)$$

Although the repeated application of the SAR principle leads to a highly regular lamellae pattern, it also exhibits an exponential increase in interfacial area [7]. The corresponding stretching factor is given by

$$\lambda(t) = (2^n - 1) \approx 2^{u t/l} \quad (1.7)$$

where  $n$ ,  $u$  and  $l$  denote the number of SAR steps, the mean velocity and the length of one SAR unit, respectively [7]. According to above-mentioned equation, the SAR mixer has a finite-time Lyapunov exponent of  $\sigma = \ln 2(u/l)$ . Thus, even in the case of a highly regular flow pattern a positive finite time Lyapunov exponent can be achieved – a characteristic feature of chaotic advection. Whereas chaotic advection generally induces regions of regular flows and poor mixing besides regions of high chaoticity where mixing predominantly occurs here, in the case of an ideal SAR multi-lamination, spatial homogeneous mixing is obtained.

Since the final lamella dimension does not depend solely on the channel width, but also on the number of SAR steps, thorough mixing can be achieved under moderate pressure drops [7]. A linear total pressure drop  $\Delta p = n p_0$ , where  $p_0$  denotes the pressure drop of one SAR step, leads to an exponential decrease in the lamella dimension  $L_n = L_0/2^n$ .

#### Simulation of cross-sectional flow patterns without splitting plane and for non-separated SAR flows

[M 60] [P 54] SAR flow splitting can be performed using split channels or done in-line in one channel. Concerning the quality of flow splitting in the latter case, CFD simulations were performed on the example of a so-called caterpillar micro mixer [7].

For  $Re \approx 1$ , the SAR principle is imperfectly realized when aiming at separating the flow in-line in one channel (without splitting of the channel structure itself) [7]. Owing to internal friction, the horizontal splitting taking place in the first half of the geometry does not preserve the initial lamination (see Figure 1.127). This leads to an S-shaped lamellae configuration at the center of the geometry. A similar problem occurs in the recombination step (lower row in Figure 1.127). Again, owing to the internal friction the lamellae configuration is changed, ending up with a more pronounced S-shaped structure rather than a multi-lamellae configuration.

In the case of high  $Re$ , the situation is different. Inertial forces induce a secondary flow which causes strong tilting and entanglement of the lamellae and, hence, a considerable increase in interfacial area is achieved [7].



**Figure 1.127** Cross-sections taken from a CFD simulation for  $Re = 1$ , displaying the lamellae reshaping in a SAR caterpillar mixer. The initial configuration is shown in the small cross-section at upper left. The other cross-sections in the upper row show the splitting at  $x = 0.6$  and  $1.2$  mm. The cross-sections in the lower row show recombination at  $x = 1.8$  and  $2.4$  mm at the end of the first cell [7] (by courtesy of RSC).

### Simulation of cross-sectional flow patterns with splitting plane and for separated SAR flows

[M 60] [P 54] The impact of having truly separated flows was shown by CFD simulations [7]. An essential part of the flow splitting, besides having split channels which recombine later, is a splitting plane which cuts the flow like a knife. These design aspects are central parts of an optimized SAR caterpillar mixer.

Cross-sectional views for such a design depicting the lamellae configurations for  $Re = 3.45$  were determined (see Figure 1.128) [7]. According to the CFD simulation results, an almost perfect lamellae configuration is reached after passing one SAR step. The same holds true if a series of three SAR steps is simulated. Thus, by consequent implementation of the above design rules, a vertically aligned multi-lamination pattern is achieved.

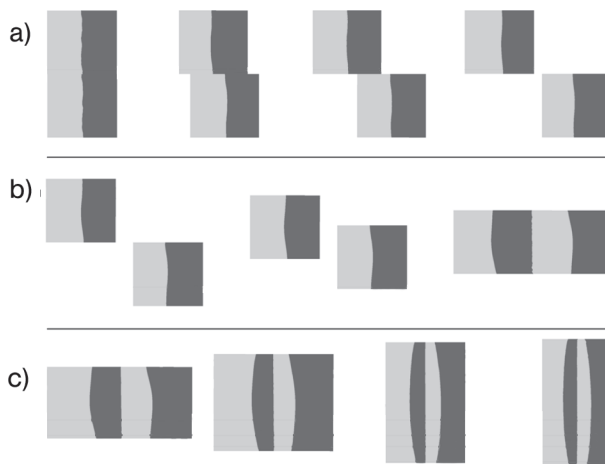


**Figure 1.128** Cross-sectional views of lamellae configurations within a SAR step for  $Re = 3.45$ . (a) Splitting; (b) rearrangement of sub-streams and recombination; (c) reshaping [7] (by courtesy of RSC).

For increased flow rates, however, the CFD simulations show more and more deviations from an ideal SAR multi-lamination pattern [7]. Since inertial forces come into play, a secondary flow pattern is superposed on the SAR velocity profile of the creeping flow regime. Streamlines seeded at the initial lamellae interface in top view for various Reynolds numbers. The lamellae pattern right at the outlet for the same set of Reynolds numbers were also given. Further simulations showed that for  $Re$  above  $\sim 15$  the center lamellae are thinned out until they detach from the top and bottom walls for  $Re \approx 30$  (see center image of Figure 1.128).

### Description of inertia forces which distort SAR flows – the Dean number

[M 60] [P 54] An analysis of the role of secondary flows which distort the SAR flows owing to inertia forces was carried out by simulations [7]. This analysis was based on using the Dean number as a measure of how to achieve ideal SAR flows, following

some assumptions. The lower the Dean number, the more ideal should be the SAR flow.

It comes out that large channel widths and heights imply low Dean numbers [7]. From this argument, the SAR mixer should be realized in macroscopic dimensions. On the other hand, in order to achieve fast mixing by diffusion, the dimension of final lamellae should be of the order of microns and a compact mixer format implies a moderate number of SAR steps, of the order of 10. Hence, an inlet width of a few millimeters is appropriate; the precise value, however, depends on the requirements of the particular process of the mixing application. Concerning the channel height, it is suggested that one should also have a large dimension in order to achieve high volume flows under low Dean numbers. However, depending on the fluid properties of the lamellae, instabilities may develop under certain conditions. The susceptibility of the lamellae to instabilities decreases with smaller channel dimensions. Again, a channel height of a few millimeters is a reasonable compromise.

#### Flow pattern analysis – dilution-type imaging

[M 60] [P 54] Dilution-type flow pattern analysis was performed for a caterpillar SAR mixer (see Figure 1.129) [7]. At a total flow rate of  $0.2 \text{ l h}^{-1}$ , highly regular lamellae patterns are observed up to the eighth SAR step. According to the low Reynolds number of 0.22, secondary flow effects are suppressed and homogeneous mixing is to be expected.

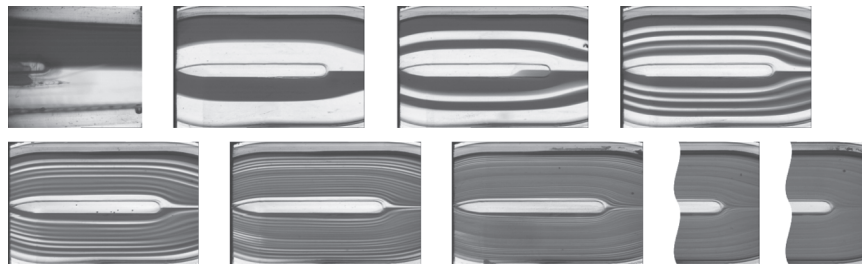


**Figure 1.129** Optical inspection of multi-lamination in the SAR mixer. The dyed (blue-colored water) and transparent lamellae of an 85% glycerol–water solution are shown in dark and light gray, respectively. The applied total volume flow rate of  $0.2 \text{ l h}^{-1}$  corresponds to  $Re = 0.22$  [7] (by courtesy of RSC).

#### Flow pattern analysis – reaction-type imaging

[M 60] [P 54] In addition to the dilution-type imaging, the flow patterns in the SAR caterpillar mixer were also analyzed by using the iron–rhodanide reaction, a reactive approach (see Figure 1.130) [7]. At a total flow rate of  $0.2 \text{ l h}^{-1}$ , the two almost transparent solutions give in the first SAR step the formation of the brown iron–rhodanide complex at the fluid interface. The increasing numbers of lamellae become evident from the increasing number of dark-colored interfaces. By mixing via diffusion, a uniform distribution of the brown iron–rhodanide complex is derived in the last mixing step. Mixing seems to be completed after eight mixing steps.

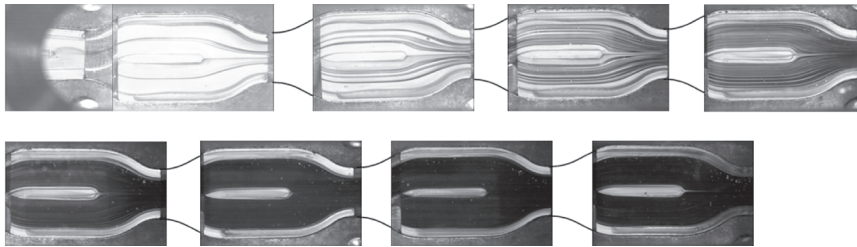


**Figure 1.130** Optical inspection of mixing in the SAR mixer. The applied total volume flow rate of  $0.2 \text{ l h}^{-1}$  is the same as for the experiment shown in Figure 1.129. Starting from a bi-lamination of yellowish iron ion ( $\text{Fe}^{3+}$ ) and transparent rhodanide ( $\text{SCN}^-$ ) solutions, homogeneous mixing is achieved in the eighth mixing step, indicated by the deep brown color of the iron–rhodanide complex formed [7] (by courtesy of RSC).

#### Flow pattern analysis – comparison between simulation and experiment

[M 60] [P 54] Good agreement between simulated and experimental flow patterns was found [7]. A simulated streamline pattern for  $Re = 0.22$  was superimposed on a photograph image of the flow pattern for the first SAR step. Besides the global SAR performance, both findings indicate a certain curvature of the lamella interface, owing to the increasing width of the dark colored interface after half of the flow element passage.

#### Analysis of performance loss due to non-ideal geometries caused by fabrication needs

[M 62] [P 55] Fluid dynamic simulations revealed the influence of cross-flow through the slits in the separation plate which were introduced only for reasons of microfabrication, i.e. underetching the plate to connect in- and outlet micro channels [140]. It could be shown that the present design suffered from the problem that about 30% of the total flow was fed through the slits, leading to uneven lamination. Further analysis demonstrated that this effect is reduced either using thinner slits, i.e. increasing the pressure loss, or combining several mixing elements in one cascade.

#### 1.3.15

##### Rotation-and-break-up Mixing

##### Most Relevant Citations

Peer-reviewed journals: [146].

A number of micro mixers use secondary or rotational flows, which are, e.g., created by in-channel flow structures, to stretch and fold fluids. The mixing approach here superposes the rotation by a break-up step, which basically is a splitting step [146]. This was done based on the analysis of elementary mixing steps and their corresponding transfer to low Reynolds number mixing.

### 1.3.15.1 Mixer 63 [M 63]: Rotation-and-break-up Micro Mixer (I)

This device has serial in-channel mixing elements composed of convex and concave units [146]. The mixer was made in two versions with short units (200  $\mu\text{m}$ ) and long segments (400  $\mu\text{m}$ ).

Microstructuring was effected using a replica molding method [146]. A negative photoresist (SU-8) was spin-coated as a thin film on a silicon wafer and a pattern was generated using a photo chrome mask. A prepolymer was spin-coated on to this structure, cured and separated from the master. In this way, a positive structure was yielded in PDMS. Two such positive structures with different designs were bonded by a self-align method using methanol after oxygen plasma treatment.

Mixer type	Rotation-and-break-up micro mixer	Channel width, depth, length	100 $\mu\text{m}$ , 50 $\mu\text{m}$ , 4 mm
Mixer material	PDMS	Length of in-channel units	200 $\mu\text{m}$ or 400 $\mu\text{m}$

### 1.3.15.2 Mixer 64 [M 64]: Rotation-and-break-up Micro Mixer (II)

This device has similar structures to [M 63], but provides a more complex texture of their units (see Figure 1.131) [146]. Five mixing units are placed laterally within the channel instead of only one in the case of [M 63]. The next row of five units is

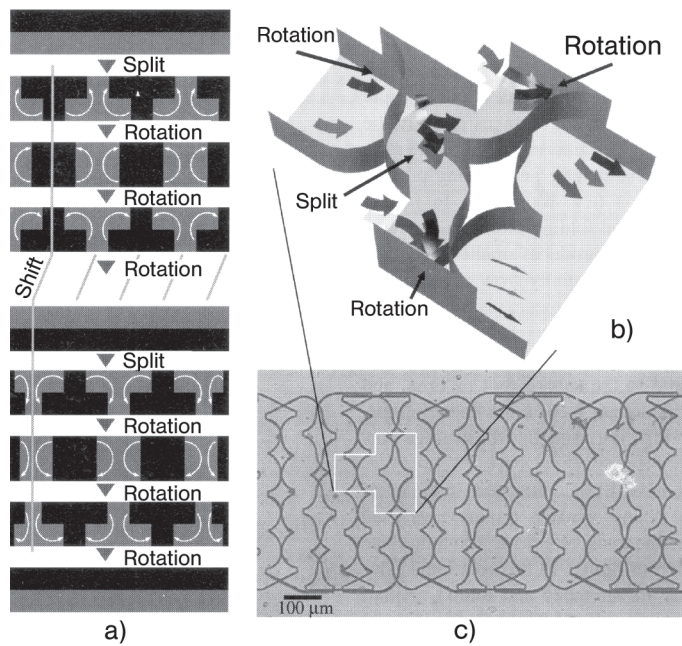


**Figure 1.131** Mixer for flow rotation and break-up. (a) Cross-sectional images of the micro channel during one mixing cycle; (b) schematic of the flow treatment involving splitting (break-up), rotation and merging steps; (c) optical micrograph of the mixer [146] (by courtesy of IOP Publishing Ltd.).

displaced by half the lateral extension of the mixing units. In this way, a complex flow pattern is yielded which performs a splitting (break-up) action and leads to rotation of such split flows.

Fabrication of the device was performed as described for [M 63].

#### 1.3.15.3 Mixing Characterization Protocols/Simulation

[P 56] Mixing was analyzed by fluorescence flow visualization using a confocal scanning microscope [146]. Water and aqueous solutions (0.02 w.-%) were mixed using syringe pumps at flow rates of 3, 30 and 150  $\mu\text{l min}^{-1}$ .

The standard deviation of the fluorescence mixing intensity was taken as a measure for judging mixing efficiency [146]. The intensity of the pixels was monitored and corrected by using flat and dark field images. All data processes were conducted using a commercial image data processor. The Sobel edge algorithm was applied.

Simulation was done using the CFD-ACE+ program considering the geometry of the element with the two convex and concave units [146]. By applying periodic boundary conditions, designs with repeated mixing steps could be modeled. Particle traces were generated by integrating numerically through the discrete velocity field using an adaptive Runge–Kutta scheme.

#### 1.3.15.4 Typical Results

##### CFD imaging of the flow rotation

[M 63] [P 56] Rotation of the flow is given both at high and low Reynolds numbers, as shown by CFD simulations (see Figure 1.132) [146]. The distortion of the interfaces is more pronounced at higher Reynolds number. When analyzing the wrapping of the interface, it becomes evident that striations were observed only for high Reynolds number flow. For low Reynolds number flow, only the position of the flow changed and the interface was not distorted, since no convective acceleration was given.

##### Experimental imaging of the flow rotation

[M 63] [P 56] The experimental findings are in accordance to the predictions made by the CFD simulations (see *CFD Imaging of the Flow Rotation*) [146]. Mixing is much better at high (50) than at low (1) Reynolds number for the reasons given above.

A mixer with short units gives better mixing performance than a mixer with long unit [146].

##### Experimental imaging of the flow rotation with break-up

[M 64] [P 56] The addition of a break-up step in addition to the flow rotation gives positive moments for mixing (see Figure 1.133) [146]. This leads to an increase in the interfacial area by stretching and folding and producing striations. At low  $Re$ , fluids were broken up and small fragments of blobs were generated. Besides the increase in interfacial area, steep concentration gradients were generated, which speed up diffusion.

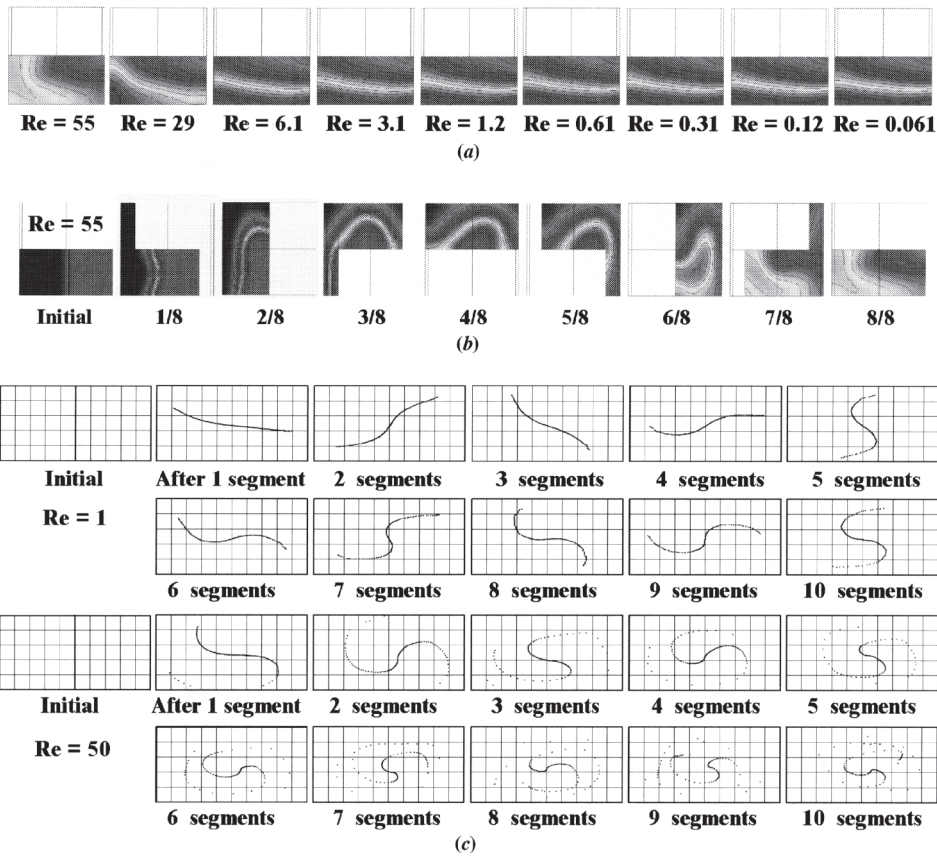


**Figure 1.132** (a) Concentration differences and imaging the distortion of the interface between two fluids for different  $Re$ . At low  $Re$ , the interface is not much deformed. (b) Wrapping of the interface between two fluids. Striations are only given at high  $Re$ . At low  $Re$ , only the position of the fluids was changed. (c) Consecutive development of the interface when passing the fluid through the mixer segments [146] (by courtesy of IOP Publishing Ltd.).

#### Reduction of mixing lengths by fluid break-up

[M 64] [P 56] More than 70% mixing is achieved for a mixing length of only 4 mm for  $Re = 1, 10$  and 50 when using rotation and break-up [146]. In contrast, for pure diffusion complete mixing is given after 1, 10 and 50 m for the same  $Re$ . Accordingly, the rotation and break-up have a considerable impact.

#### Optimal Reynolds number

[M 64] [P 56] There is an optimal  $Re$  for a mixer which is based on flow rotation and break-up [146]. For the design given here, stretching/folding, break-up and diffusion occur at  $Re = 10$ , yielding the most efficient mixing for the cases studied. At  $Re = 1$ , stretching and folding hardly occur, and only break-up and diffusion are found. At  $Re = 50$ , stretching and folding and also break-up are relevant; owing to the high flow velocity, diffusion is not completed.

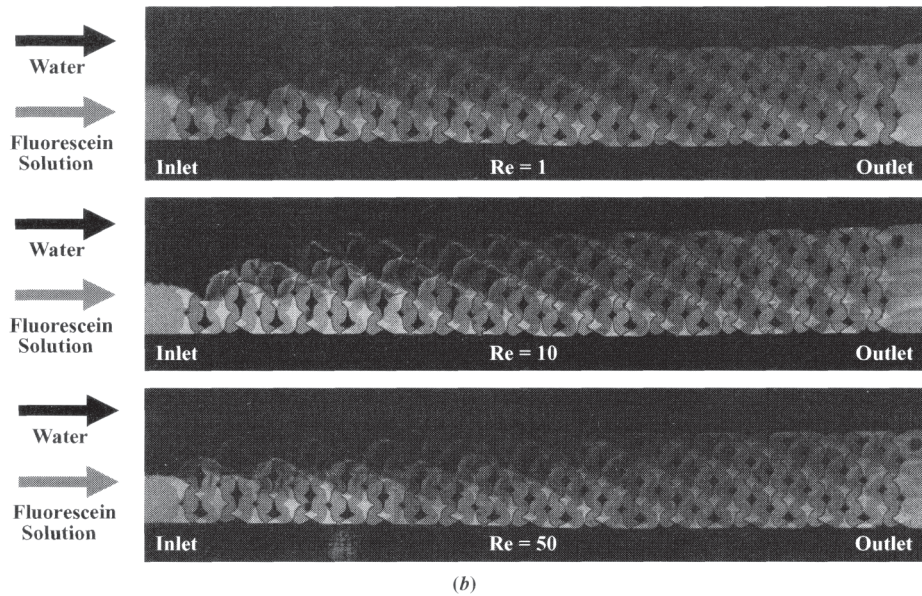
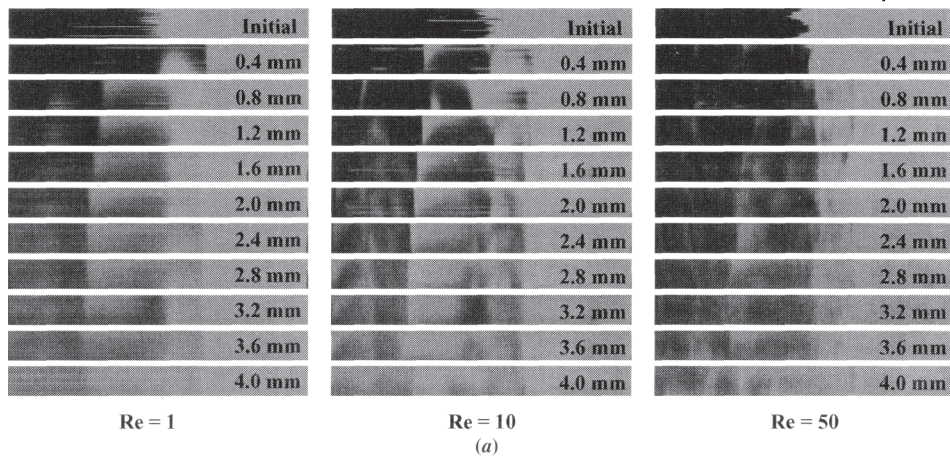


**Figure 1.133** Fluorescence micrographs obtained in a mixer using flow rotation and break-up. (a) Cross-sectional images showing the break-up which produces the smaller fragments of blobs. Thereby, the interfacial area is increased and large concentration gradients are provided. (b) Top of the mixer, clearly showing the propagation of one fluid into the other [146] (by courtesy of IOP Publishing Ltd.).

## 1.3.16

**Micro-plume Injection Mixing****Most Relevant Citations**

Proceedings contributions: [51, 147] (see also [148]).

By feed of a fluid through a nozzle array, which is a plate with many tiny holes, so-called micro-plume injection into a micro channel can be achieved [51, 147]. Typically, the micro channel's floor is perforated in a section in this way and a closed-channel fraction follows for completion of mixing. Large specific interfaces can in principle be achieved depending on the nozzle diameter. This mixing concept benefits from conceptual simplicity and fits well to existing MEMS techniques. Furthermore, it consumes less footprint area and therefore does not create much dead space, which is one of the prime requirements during  $\mu$ TAS developments.

It stands to reason that plumes are only formed under certain hydrodynamic conditions, e.g. ratios of flow rates of the liquids. Otherwise, simple bi-lamination with comparatively low specific interface may occur. In addition, a flow maldistribution within the array may occur for certain conditions, i.e. most flow passes the first row of nozzles at the expense of the residual holes. So far, there is, to the best of our knowledge, no detailed report on modeling these aspects or an experimental proof where indeed plume fluid structures are visualized; only gross characterization of the mixing was given (see below).

A micro-plume injection mixer as described above was also part of a microfluidic system composed of a mixer with an array of nozzles as through-holes, stirring part and reactor with integrated heater [148]. The main reason for choosing this mixing concept was to achieve integration into a simple straight channel overall structure with minimal dead space. The holes (10  $\mu\text{m}$  in diameter with 30–100  $\mu\text{m}$  depth) were fabricated in macroporous silicon by electrochemical etching. The system was intended for use in biochemical analysis; no details on specific applications or testing were given in the reference.

**1.3.16.1 Mixer 65 [M 65]: Micro-plume Injection Micro Mixer**

The central part of this device is a square mixing chamber which contains a sieve bottom through which a multitude of fluid bulbs, 'micro plumes', are injected into a main stream (see Figure 1.133) [51, 147]. The idea is to enlarge the fluid interface and to speed up diffuse mixing. The fluid of the main stream is fed through one channel which enters at half chamber width and leaves on the opposite chamber side again through a channel at half chamber width. The second fluid is fed through a channel oriented at 90° relative to the other feed channel and also leads to the chamber at half width. This channel is on a lower level than the other feed and the outlet channels and leads to a reservoir beneath the mixing chamber.

Bulk micromachining was applied for structuring a silicon wafer [51]. The sieve and the mixing chamber as through-structures were obtained by etching from both sides. The wafer was covered from both sides with Pyrex glass by anodic bonding. A light-reflecting silicon layer of the same size was deposited on the Pyrex plate by

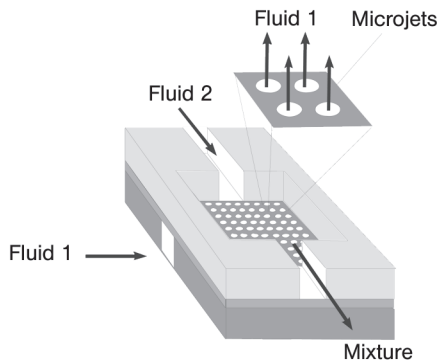


**Figure 1.134** Schematic of the micro-plume injection mixer design (newly drawn following [51]).

thin-film technology and structured by reactive ion etching. Inlet and outlet ports were drilled into the top glass wafer.

Mixer type	Micro-plume injection mixer	Hole depth of the sieve	10–30 $\mu\text{m}$
Mixer material	Silicon	Distance between the holes of the sieve	100 $\mu\text{m}$
Top plate material	Pyrex	Number of holes in the sieve	400
Hole diameter of the sieve	10–30 $\mu\text{m}$	Mixing chamber dimensions	$2.2 \times 2 \times 0.33 \text{ mm}$

#### 1.3.16.2 Mixing Characterization Protocols/Simulation

[P 57] A fluorescent dye was injected through the sieve of the micro-plume injection mixer [51]. The changes in fluorescence intensity thereafter in the mixing chamber were monitored by using a fluorescence microscope.

In addition, visible absorption measurements using an optical-fiber setup were performed directly in the mixing chamber [51]. The optical path and hence the signal intensity could be substantially increased by passing the light through the long axis of the mixing chamber using multiple reflections between the mixer bottom plate and the thin-film coated layer. By  $90^\circ$  reflection at the beginning and end of the optical reflection zone, the signal is introduced and passed via fibers, respectively.

#### 1.3.16.3 Typical Results

##### Numerical analysis of mixing time

[M 65] [P 57] By numerical analysis of the diffusion process, it was shown that the multiple injection of the micro-plumes leads to notable speed-up of mixing compared with a single-point injection, as expected [51]. The latter corresponds in a wider sense to a mixing tee flow configuration. Mixing is therefore improved for all flow rates; the best results are given at higher flow rates. These simulation results were taken as input for the design of the mixer.

**Top-view fluorescence mixing detection**

[M 65] [P 57] The fluorescence measurements proved complete mixing within a few seconds [51].

**In-line visible mixing detection**

[M 65] [P 57] Visible absorption measurements proved complete mixing at a flow rate of about  $1 \mu\text{l s}^{-1}$  [51].

## 1.3.17

**Slug Injection Mixing****Most Relevant Citations**

Proceedings contributions: [149].

**1.3.17.1 Mixer 66 [M 66]: Segmented-flow Micro Mixer**

In this device, two liquids are injected using minute conventional valves with two injectors into a mixing channel arranged as a serpentine structure [149]. The switching rate of the valves is 1 Hz.

Fabrication is effected by precision milling of PMMA laminates which are sealed by diffusion bonding [149].

Mixer type	Segmented flow micro mixer	Mixer internal volume	10 $\mu\text{l}$
Material	PMMA	Injector width, depth	100 $\mu\text{m}$ , 30 $\mu\text{m}$
Channel width, depth, length	1000 $\mu\text{m}$ , 200 $\mu\text{m}$ , 100 mm	Total size of the chip	5 cm $\times$ 4 cm $\times$ 0.5 cm

**1.3.17.2 Mixing Characterization Protocols/Simulation**

[P 58] Dilution-type mixing was accomplished with blue and yellow solutions which were image-processed and then yielded black and white colors, the mixture being gray [149].

Pressure-driven operation was used for fluid feed [149].

**1.3.17.3 Typical Results****Mode of flow injection – impact on mixing**

[M 66] [P 58] When two flow injectors were constantly open, the two flows injected into a micro channel formed a bi-laminated pattern [149]. For alternative injection, equal alternate slugs, i.e. a segmented flow, were found. Upon flow transport, mixing by diffusion occurs and the color of the plugs is ‘smeared’. The mixing was claimed to be rapid; however, no time scale is given in the reference. A concentration profile over an arbitrary channel length gives an idea of how the course of mixing develops.

## 1.3.18

**Secondary Flow Mixing in Zig-zag Micro Channels****Most Relevant Citations**

Peer-reviewed journals: [59]; proceedings contributions: [150, 151].

The continuous change of flow direction in zig-zag channels can induce secondary flow patterns at sufficiently high  $Re$ , which besides diffusion can act as a mixing mechanism. By means of recirculation patterns, material is transported transverse to the flow direction and improves the mixing.

**1.3.18.1 Mixer 67 [M 67]: Y-type Micro Mixer with Zig-zag or Straight Channel**

All mixers described in this sub-section have a micromachined Y-type contactor (90° angle between the two feed channels) attached to a micro channel where mixing occurs (see Figure 1.135) [59].

Mixer type	Y-type micro mixer with a zig-zag or straight channel	Zig-zag channels (periodic step 1, 2, 4, 8): effective length	2828 $\mu\text{m}$
Mixer material	PET	Reference case A (straight channel): width, length	141 $\mu\text{m}$ , 2000 $\mu\text{m}$
Periodic step	0, 100, 200, 300, 400, $\infty$ $\mu\text{m}$	Reference case B (straight channel): width, length	100 $\mu\text{m}$ , 2828 $\mu\text{m}$
Ratio of periodic step to channel width (meandering ratio)	0, 1, 2, 4, 8, $\infty$	Reference case C (straight channel): width, length	100 $\mu\text{m}$ , 2000 $\mu\text{m}$
Zig-zag channels (periodic step 1, 2, 4, 8): width, length	100 $\mu\text{m}$ , 2000 $\mu\text{m}$		

The first group of devices has a long zig-zag micro channel attached, with 90° angles for each fluid turn [59]. Four devices differing in the periodic step were made, with equal width and linear length of the micro channel (see Figure 1.136). To classify these mixers, the ratio of the periodic step to the channel width was introduced. In the following, this will be termed the meandering ratio. As reference

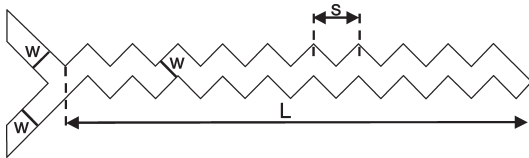


**Figure 1.135** Characteristic dimensions of a microfluidic mixing element with Y-type contactor attached to a zig-zag channel:  $w$ , width of the micro channel;  $s$ , linear length of the periodic step;  $L$ , linear length of the zig-zag micro channel [59] (by courtesy of ACS).

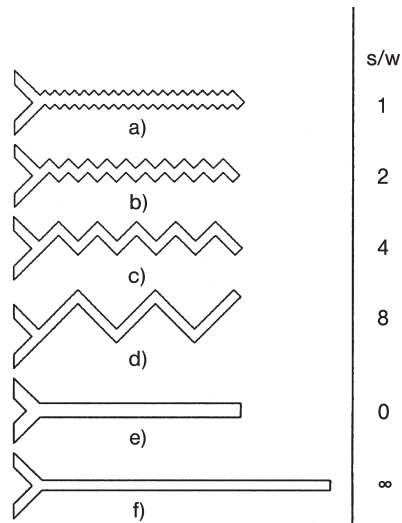


**Figure 1.136** Microfluidic mixing elements with Y-type contactor attached to a zig-zag channel having different geometries in the meandering section. (a)  $s/w = 1$ ; (b)  $s/w = 2$ ; (c)  $s/w = 4$ ; (d)  $s/w = 8$ ; (e)  $s/w \rightarrow 0$ ; and (f)  $s/w \rightarrow \infty$  [59] (by courtesy of ACS).

cases, three straight channel devices were made, representing the asymptotic cases with the periodic step approaching zero or infinite (see Figure 1.136). Accordingly, the linear length of these two devices changes.

The micro devices were fabricated from a polyethylene terephthalate (PET) substrate using 193 nm ArF excimer laser ablation [59]. Microstructures produced in this way were thermally sealed by a lamination machine.

### 1.3.18.2 Mixer 68 [M 68]: T-type Micro Mixer with Zig-zag or Straight Channel

Two sets of bend and straight channels were designed, with different hydraulic diameter, thus called ‘micro’ and ‘mini’ [151]. All contained a T-type contactor at the beginning.

(a) The ‘mini’ channels were made by traditional precision engineering machining [151].

Mixer type	T-type micro mixer with a zig-zag or straight channel; ‘mini’	Length between two bends (for zig-zag mixer only)	1 $\mu\text{m}$
Mixer material	Acrylic plastic	Bend length to hydraulic diameter	2.5 (zig-zag), 250 (straight)
Micro channel width, depth, length	300 $\mu\text{m}$ , 600 $\mu\text{m}$ , 100 mm	Number of bends	80

(b) The ‘micro’ channels were fabricated by silicon micro machining [151]. A glass cover was bonded to allow visual observation.

Mixer type	T-type micro mixer with a zig-zag or straight channel; ‘micro’	Length between two bends (for zig-zag mixer only)	2.5 $\mu\text{m}$
Mixer material	Silicon/glass	Bend length to hydraulic diameter	57 (zig-zag), 114 (straight)
Micro channel width, depth, length	180 $\mu\text{m}$ , 25 $\mu\text{m}$ , 25 mm (zig-zag) or 5 mm (straight)	Number of bends	10

#### 1.3.18.3 Mixing Characterization Protocols/Simulation

[P 59] Mixing was simulated based on a model considering the laminar mixing of species along a 2-D section of a micro channel [59]. The following assumptions were made: the flow profile is constant along the depth axis; variations in concentration do not modify the viscosity and density of the fluid; and the channel walls are smooth; the wall surface tension forces are neglected. The momentum and mass transport equations are solved in two steps, as described in detail in [59]. For the hydrodynamic calculations, a parabolic Poiseuille profile is assumed at both inlet boundaries. The fluid velocity is fixed to 0 along the wall boundaries (no slip conditions), and a free condition is assumed at the outlet boundary.

As mixing efficiency, the ratio between minimal and maximal concentrations at the outlet cross-section is defined [59].

[P 60] The observation of the flow patterns was performed using a microscope with a video camera [151]. Flow feed was achieved by hydrostatic pressure. A pH-indicator reaction with bromothymol blue and sodium hydroxide solution was applied, resulting in a dark blue color. Experiments were performed at flow rates of 50, 900 and 4000  $\mu\text{l min}^{-1}$  for the ‘mini’ channels and 60 and 6000  $\mu\text{l min}^{-1}$  for the ‘micro’ channels.

#### 1.3.18.4 Typical Results

##### Mixing efficiency as a function of the meandering ratio

[M 67] [P 59] The mixing efficiency was calculated as a function of the ratio of periodic step to channel width, i.e. of the degree of meandering of the channel, having discrete values of 1, 2, 4, and 8 [59]. For low  $Re$  of 0.26 (fluid velocity:  $1.3 \cdot 10^{-3} \text{ m s}^{-1}$ ) a monotonic increase in the mixing efficiency with increasing geometric ratio was found, from 65 to 84% (see Figure 1.137). For  $Re$  of the order of 1000 times higher (267; fluid velocity:  $1.3 \text{ m s}^{-1}$ ), a more pronounced increase up to a maximum at a geometric ratio of 4 was found, from then slightly decreasing up to a ratio of 8. The maximum efficiency was near 99%; it was still about 88% at a ratio of 8.

For reference case A (largest width), a low mixing efficiency of 29% is found, as expected [59]. On decreasing this parameter from 141 to 100  $\mu\text{m}$  (reference case B),

consequently the mixing efficiency increases to 72%. A further increase in mixing length to the value of the effective length (2828  $\mu\text{m}$ ; reference case C) even further increases the mixing efficiency to 86%.

The results show that zig-zag channels may have superior mixing performance to geometrically straight channels [59]. This increase in performance is gained, however, only at large  $Re$  and large ratios of periodic step to width (i.e. moderate meandering).

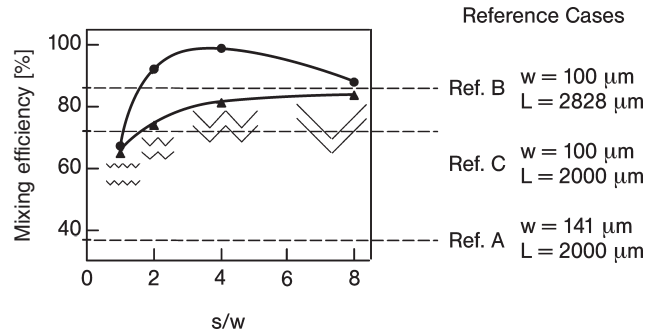


**Figure 1.137** Mixing efficiency versus the meandering ratio  $s/w$  at  $Pe = 2600$  and at two different  $Re$  for a set of zig-zag and straight-channel micro mixers.  $Re = 0.26$  (triangles);  $Re = 267$  (circles) [59];  $w$  = channel width,  $L$  = channel length (by courtesy of ACS).

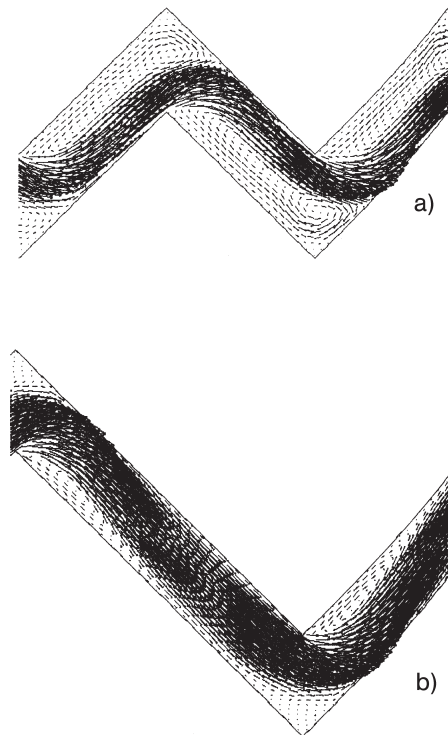


**Figure 1.138** Flow patterns in two zig-zag micro mixers at  $Re = 267$ , given as velocity vectors. (a)  $s = 400 \mu\text{m}$ ; (b)  $s = 800 \mu\text{m}$  [59] (by courtesy of ACS).

#### Hydrodynamics at different meandering ratios

[M 67] [P 59] Fluid dynamic simulations show that the mixing efficiency is influenced by recirculation patterns which are exhibited in the corners of the zig-zag channels, i.e. at the 90° fluidic turns (see Figure 1.138) [59]. Recirculations induce a transversal component of the velocity and thus transport material from the interface to the walls. At a meandering ratio of 4, this pattern is fully developed and expands into the entire arm of the channel after each angle. At a ratio of 8, recirculation is fixed to the corner only. In this view, it is understandable that for the latter flow geometry lower mixing efficiency (88%) is found than for the meandering ratio 4 case (near 99%).

#### Mixing efficiency as a function of the Reynolds number

[M 67] [P 59] At a constant Peclet number of 2600, the mixing efficiency was calculated for different  $Re$  in the range 0.26–267 [59]. Up to  $Re = 80$ , the mixing efficiency stays almost constant at 81% (see Figure 1.139). Here, only diffusion causes mixing. For  $Re > 80$ , a pronounced increase in mixing efficiency takes places, which is due to the induction of flow circulation patterns (see *Hydrodynamics at different meandering ratios*).

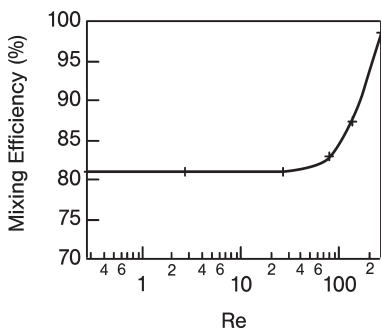


Figure 1.139 Mixing efficiency versus  $Re$  number for one zig-zag micro mixer, with  $s = 400 \mu\text{m}$ , at  $Pe = 2600$  [59] (by courtesy of ACS).

#### Maximum velocity development in zig-zag channels

[M 67] [P 59] The ratio of the maximum velocity in a zig-zag channel normalized by the maximum velocity in a straight channel was calculated as a function of the number of zig-zag turns for various meandering ratios [59]. Up to about six turns, this ratio increases as a consequence of developing more recirculation zones which restrict the flow path for the ‘non-circulated’ flow and thus increases the corresponding maximum velocity.

When the outlet maximum velocity (after eight turns) at a meandering ratio of 4 is plotted versus  $Re$ , a curve similar to the dependence of the mixing efficiency on  $Re$  is yielded [59]. At  $Re \approx 80$ , the outlet maximum velocity increases considerably, whereas at low  $Re$  it remains nearly constant.

#### Mixing efficiency at various diffusion constants

[M 67] [P 59] The mixing efficiency was calculated for various diffusion constants, ranging from  $2 \cdot 10^{-7}$  to  $10 \cdot 10^{-7} \text{ m}^2 \text{ s}^{-1}$  [59]. A meandering ratio of 4 was assumed

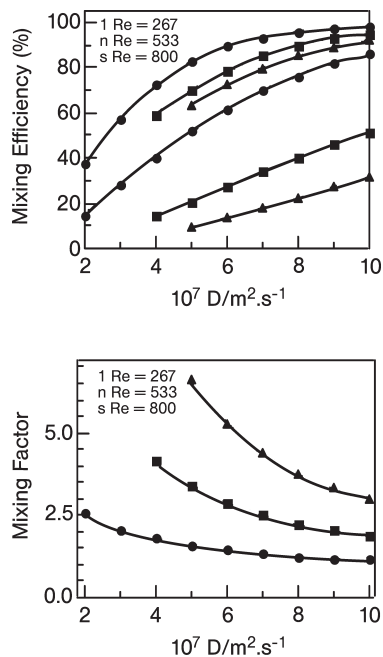


**Figure 1.140** Mixing efficiency versus diffusion constant for one zig-zag micro mixer (lines) with  $s = 400 \mu\text{m}$  and one straight-channel micro mixer (dashed lines), reference case B, at three different  $Re$  values (top). Mixing factor, the ratio between the mixing efficiency of comparable zig-zag and straight-channel micro mixers, versus diffusion constant (bottom) [59] (by courtesy of ACS).

for the zig-zag channel and three  $Re$  values were taken into account, 267, 533 and 800. For comparison, the same analysis was performed with a straight channel of comparable dimensions, again at the same  $Re$  values. As expected, the efficiency increases in all cases with larger diffusion constants (see Figure 1.140). The performance of the zig-zag channel at all three  $Re$  values is better than the best performance of the straight channel. Also as to be expected, the difference between the mixing efficiencies at the three  $Re$  values is remarkable in the linear case. This is simply due to the respective differences of residence times and diffusion widths. Concerning the zig-zag case, the relative differences between the same curves are much smaller, which is due to the compensating effect of recirculation.

A mixing factor was introduced, defined as the ratio of the mixing efficiency of the zig-zag and the straight channels under otherwise equal conditions [59]. The mixing factor decreases with increasing diffusion constant, showing that the zig-zag channels are most effective for solutes with low diffusion constant. It is also confirmed that the largest differences, up to a value of about 6.5, are given for operation at high  $Re$  (800). Here, the relative contribution of recirculation patterns to mixing is the highest.

#### Experimental mixing efficiency as a function of the flow rate

[M 67] [P 59] The mixing efficiency was derived experimentally in a device with a meandering ratio of 8, i.e. a periodic step of  $800 \mu\text{m}$  [59]. The channels were  $100 \mu\text{m}$  wide and  $48 \mu\text{m}$  deep with a linear distance of  $2000 \mu\text{m}$ . An aqueous buffer solution and a buffer solution with fluorescein were contacted; the fluorescence intensity was measured at the end of the channel. Owing to the known problems of biasing

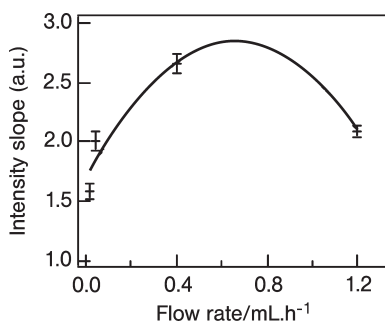


**Figure 1.141** Slope of the fluorescence intensity versus flow rate for one zig-zag micro mixer with  $s = 800 \mu\text{m}$  and  $w = 100 \mu\text{m}$ . The slope is proportional to the mixing efficiency. In a dilution-type experiment, an aqueous fluorescein solution is mixed with an aqueous solution [59] (by courtesy of ACS).

for such dilution experiments, i.e. to an overestimation of mixing efficiency as a result of limited resolution, the mixing efficiency was estimated from the slope of the intensity curves, rather than taking these values directly (see Figure 1.141).

The analysis of the slope of the intensity as a function of the flow rate (from 0.04 to 1.2 ml h<sup>-1</sup>) is qualitatively in accordance with the theoretical predictions from the mixing-efficiency calculations [59]. The slope is highest at the lowest flow rate, owing to the large residence time. It decreases when the flow rate is increased, but increases again above a certain critical flow rate. The corresponding increase in mixing efficiency is caused by recirculation flows, as is known from the calculations and the hydrodynamic studies discussed above (see *Mixing efficiency as a function of the meandering ratio* and *hydrodynamics at different meandering ratios*). The respective critical  $Re$  is 7; this, however, differs considerably, by an order of magnitude, from the theoretical  $Re$  of 80, derived from the calculations. The origin of this difference is not clear. It is speculated that it may be caused by non-smooth surface profiles of the micro channels due to re-deposition processes of material during the excimer laser manufacturing. Such attached particles are flow obstacles and also contribute to mixing.

#### Comparison with straight/zig-zag channels

[M 68] [P 60] At a very early stage of worldwide activities in the field of mixing with micro mixers, an experimental comparison was made between the mixing performance of straight and zig-zag channels [151]. The investigations covered mini and micro channels.

The ‘mini’ channels had a width of 300  $\mu\text{m}$  and a depth of 600  $\mu\text{m}$  and 80 curves were placed on a passage of 100 mm, yielding a length from bend to bend of 1 mm [151]. The curved channels showed very different behavior depending on the flow rate and correspondingly the Reynolds number. At  $Re = 1.85$  and a flow rate of 50  $\mu\text{l min}^{-1}$ , mixing was similar to that of a straight channel of the same total length. Bi-laminated patterns were visible and a weakly developed mixing was found close to the interface. The zig-zag structure had no impact, acting only as a dead zone.

At  $Re = 33$  and a flow rate of 900  $\mu\text{l min}^{-1}$ , the flow pattern changed to secondary flow with recirculation [151]. The mixing was completed at the end of the channel, as found by visual inspection. This was much further improved at  $Re = 148$  and a flow rate of 4000  $\mu\text{l min}^{-1}$ ; here complete mixing was achieved after a passage of

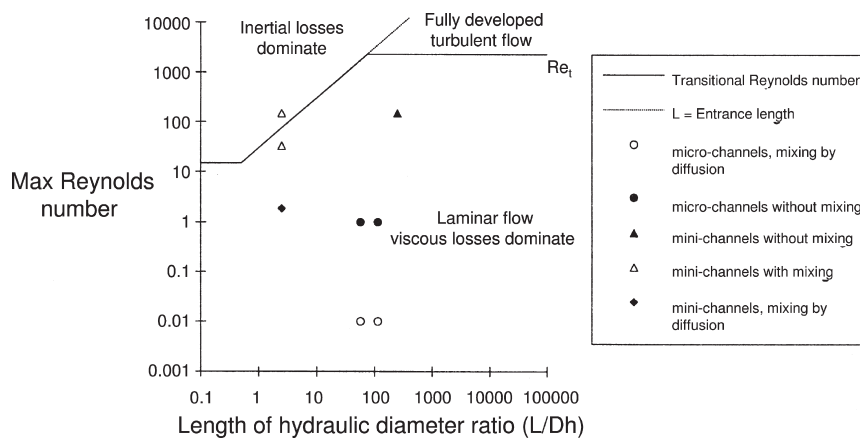


**Figure 1.142** A kind of flow-pattern map for zig-zag micro mixers of various dimensions correlating their Reynolds numbers with their hydrodynamic regimes as a function of their ratio of bend length to hydraulic diameter [151] (by courtesy of Kluwer Academic Publishers).

about one-third of the channel length. For the same conditions, no observable mixing was found for a straight channel of the same length.

The bended 'micro' channels had a width of 180  $\mu\text{m}$  and a depth of 25  $\mu\text{m}$  and a reduced length (25 mm) compared with the 'mini' channels [151]. The flow in such channels was characterized at two very low  $Re$  (1.0 and 0.1) and compared with the flow in straight channels under some hydrodynamic conditions. In all four cases, undisturbed laminar flow was found. Mixing was only detectable at  $Re = 0.1$  owing to diffusion mixing at a much prolonged residence time. At  $Re = 1$ , no mixing could be detected.

Based on these experiments, a kind of flow-pattern map was proposed describing a region of laminar flow where viscous losses dominate, an intermediate region with secondary flow where inertial losses dominate (albeit still not turbulent) and a region of fully developed turbulent flow (see Figure 1.142) [151]. The transitional Reynolds number from the pure laminar to the secondary-flow regime increases with the ratio of bend length to hydraulic diameter.

#### Comparison with straight/column-filled channels – use in micellar electrokinetic chromatography

[No details on mixer] [no protocol] By means of fluorescence imaging (buffer and fluorescein solutions), the flow patterns in the following microstructured elements are derived: in a straight channel, a straight channel with a row of rectangular columns in the center, and a zig-zag channel with 90° turns only [150]. For details on the mixers, see the original literature. The most homogeneous color texture was given for the zig-zag channel. The straight channel gave a bi-laminated flow; a similar finding was made for the column-row mixer, where the columns actually act more as a separation wall than to induce secondary flow and to improve mixing.

The zig-zag mixer was then used as a pre-column reactor to derivatize biogenic amines such as histamine and tyramine with *o*-phthalaldehyde and to detect the corresponding products with micellar electrokinetic chromatography [150]. A separation of four amines, histamine, tyramine, putrescine and tryptamine, was demonstrated in that way.

### 1.3.19

#### Mixing by Helical Flows in Curved and Meander Micro Channels

##### Most Relevant Citations

Peer-reviewed journals: [47, 152, 153]; proceedings contributions: [49].

The generation of secondary 'helical' flows in suitably curved channels, known as Dean vortices, is not an entirely new fluidic phenomenon discovered at the micro scale; actually it was found already also for wound tubings of conventional diameter (see a summary in [152]). In-depth studies concerning Dean vortices in curved channels were made in the framework of various applications such as filtration, heat exchange, friction and mixing.

When guiding fluids through curved channels, the maximum in the velocity profile is displaced towards the outer channel wall and Dean vortices form (as reported, e.g., in [152]). The latter are typically characterized by two counter-rotating vortices above and below the symmetry plane of the channel coinciding with its plane of curvature. Fluid is transported outwards in this plane by means of centrifugal forces. By recirculation, back transport along the channel walls is induced.

A Dean number of  $\sim 140$  is a kind of threshold value [47, 152]. For lower values, two counter-rotating vortices are found, whereas for higher values, two additional counter rotating vortices appear which are close to the center of the outer channel wall. Means to achieve this are changes in the flow velocity, the hydraulic diameter and the radius of curvature.

Not only can simple helical flows be induced, but also chaotic flow patterns of alternating helical flows can be achieved [152]. For the latter purpose, a switch between two flow patterns has to be achieved by either consecutively changing the geometry parameters (hydraulic diameter or radius of curvature) or altering the Reynolds number such that the Dean number changes via its threshold value. Accordingly, improved mixing can be achieved by periodic alterations of flow patterns in simple curved channels, laid within planar geometry. The corresponding type of micro mixer can be based on an alternative change of curvature, i.e. a meander design [152].

Helical flows are not only found for 2-D mixer designs. In analogy with findings for macro-scale alternating helical coils, microstructured 3-D designs were proposed [49, 153]. For reasons of limitations of today's micro fabrication, not real helices were made, but easier to fabricate structures such as complex micro channels based of L-shaped elements arranged in a 3-D fashion.

##### 1.3.19.1 Mixer 69 [M 69]: Curved Channel Micro Mixer

This refers to a generic design of a curved channel as given in [152] (see Figure 1.143).

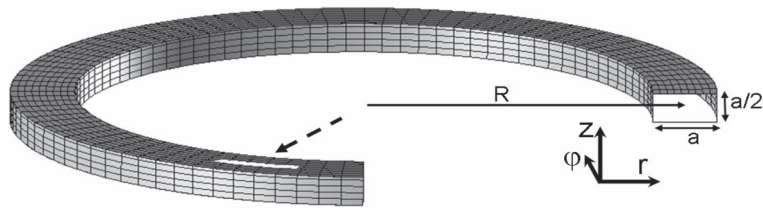


**Figure 1.143** Model geometry of the curved square channel used for simulating helical flows. Only half the geometry is shown due to reflection symmetry;  $a$  and  $R$  denote the channel dimension and the radius of curvature, respectively [152].

Mixer type	Curved channel micro mixer	Channel width	200 $\mu\text{m}$
Mixer material	Not realized, simulation work only	Radius of curvature	1 mm

#### 1.3.19.2 Mixer 70 [M 70]: Meander Channel Micro Mixer

Here, micro mixers with a repeatedly curved, i.e. meander, design are considered [152].

*Version (a)*. This refers to a generic design of a meander channel as given in [152] (see Figure 1.144).

Mixer type	Meander channel micro mixer	Channel width	200 $\mu\text{m}$
Mixer material	Not realized, simulation work only	Radius of curvature	1 mm

*Version (b)*. This design of meander mixer was actually realized. It refers to a structure with a large number of mixing elements which was micro-machined by precision milling in a plastic material [47]. Irreversible sealing of the channel was accomplished by insertion of a thin PMMA foil via solvent bonding.

Mixer type	Meander channel micro mixer	Number of mixing elements	20
Mixer material	PMMA	Thickness of PMMA foil for sealing	100 $\mu\text{m}$
Channel width, depth	1 mm, 1 mm	Inlet connectors	Plastic tubing of about 1.4 mm inner diameter
Channel length	322 mm	Outlet connector	1/8 inch steel tube connector

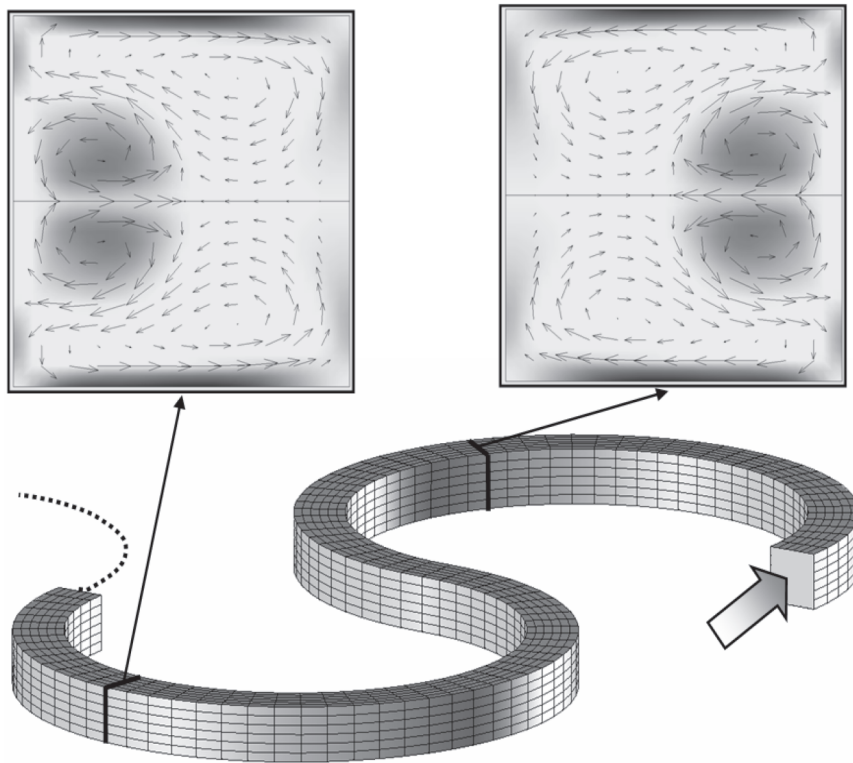


**Figure 1.144** Top, cross-sectional view of secondary flows taken in flow direction; bottom, sketch of a meander channel build up from circular segments [152].

#### 1.3.19.3 Mixer 71 [M 71]: 3-D L-shaped Serpentine Micro Mixer

A tortured, 3-D flow serpentine path was achieved by complex connection of various L-shaped microstructured elements [49, 153]. Such a structure is a miniature analog of alternating macro-scale helical coils that are known to give chaotic flows. Basically, the flow exposes multiple  $90^\circ$  turns instead of being guided along bend structures. The fluids are introduced via a T-structure.

The L-shaped structures can simply be made by conventional silicon micro machining. The microstructured wafer was covered by a glass slip using a thin layer of a silicone adhesive [153].

Mixer type	3-D L-shaped serpentine micro mixer	Long and short axis of L-element	700 $\mu\text{m}$ , 400 $\mu\text{m}$
Mixer material	Silicon/glass	Channel width, depth	300 $\mu\text{m}$ (at the surface), 150 $\mu\text{m}$

#### 1.3.19.4 Mixing Characterization Protocols/Simulation

[P 61] The numerical simulations were based on the solution of the incompressible Navier–Stokes equation and a convection–diffusion equation for a concentration field by means of the finite-volume method [152]. The Einstein convention of summation over repeated indices was used. For pressure–velocity coupling, the SIMPLEC algorithm and for discretization of the species concentration equation the QUICK differencing scheme were applied. ‘Hybrid’ and the ‘central’ differencing schemes referred to velocities and pressure, respectively (commercial flow solvers CFX4 and CFX5).

Because numerical errors due to discretization of a convective term introduce an additional, unphysical diffusion mechanism, termed numerical diffusion (ND), the diffusion coefficient  $D$  was set to zero [152]. The resulting concentration fields nonetheless are indicative of the distribution of a solute within the micro channel volume. In this way, convective patterns can be derived for the redistribution of the liquid transverse to the flow direction. Accordingly, the stretching, tilting and thinning of liquid lamellae can be followed.

[P 62] A Lagrangian particle tracking technique, i.e. the computation of trajectories of massless tracer particles, which allows the computation of interfacial stretching factors, was coupled to CFD simulation [47]. Some calculations concerning the residence time distribution were also performed. A constant, uniform velocity and pressure were applied at the inlet and outlet, respectively. The existence of a fully developed flow without any noticeable effect of the inlet and outlet boundaries was assured by inspection of the computed flow fields obtained in the third mixer segment for all Reynolds numbers under study.

A two-step procedure was used for numerical computation of the mixing performance [47]. First, the velocity and pressure fields were derived by solving the Navier–Stokes equations and the equation of mass conservation for an incompressible fluid. In a second step, trajectories of mass less particles were computed by streamline integration of the velocity field.

The commercial flow solver CFX4, relying on the finite volume method (FVM), was applied to solve the velocity field [47]. The SIMPLEC algorithm and the QUICK differencing scheme were used for pressure–velocity coupling and for discretization of the velocity fields, respectively. For an accelerated convergence the algebraic multi-grid (AMG) iterative method was applied.

Two strategies of particle tracking were used. As a first strategy, tracers were distributed along the ‘interface’ of the two fluids (virtual, since miscible) for computation of interfacial stretching factors [47]. Then an iterative method for computing interfacial stretching was established.

In a second approach, the paths of a large number of tracers, which were distributed uniformly over a certain volume element, were followed [47]. The time at which the tracers penetrate out of the element was taken. By such an iterative procedure the residence-time distribution was determined.

[P 63] A reactive-type flow visualization method was used for quantification of mixing [47] (citing a protocol described in detail in [20] and given in [P 40]). Colorless solutions of iron(III) nitrate and sodium rhodanide form a colored compound,

Fe(III) rhodanide. The local concentration of the colored compound is determined photometrically from the digitized images of the flow inside the channel.

Two continuously working double-action syringe pumps were used for liquid pumping [47]. The pulsations of the step motors were damped by a 20 ml gas ballast. Overall flow rates ranged from 200 to 2000 ml h<sup>-1</sup>. The corresponding Dean numbers tested ranged from 35 to 351. Digital video equipment with planar illumination from a fluorescence light source from below was used for flow monitoring.

It can be seen that even if the residence time for the  $K = 141$  flow is about a factor of 4 smaller than for  $K = 35$  at the same position, mixing proceeded to a higher degree for the larger Dean number, as is clearly visible especially when comparing the images recorded at position 2.

The Lambert–Beer law was applied for the determination of the mixing performance, the local concentration  $c$  being measured by photometry via the relation

$$\ln \frac{\Phi_0}{\Phi} = \varepsilon c l \quad (1.8)$$

where  $\Phi$  ( $\Phi_0$ ) denotes the photometric brightness obtained from the digitized images with finite (zero) rhodanide concentration,  $\varepsilon$  is the extinction coefficient,  $c$  is the Fe(SCN)<sub>3</sub> concentration in the dye solution and  $l$  is the layer thickness.

[P 64] Phenolphthalein in ethanol and sodium hydroxide in ethanol were contacted in the serpentine mixer [153]. Microscopy observations were used for qualitative judging of mixing. Cross-sectional imaging was obtained by focusing of the microscope on the vertical segments of the channel. Apart from this qualitative analysis, quantitative information was derived by normalized average red dye intensity analysis from the microscope images.

### 1.3.19.5 Typical Results

#### Flow patterns of helical flow, depicted by velocity vectors

[M 70a] [P 62] Computational flow simulation of the secondary flow, depicted by velocity vectors, was performed for Dean numbers of 10 and 100 [47]. The helical flow is weak for the smaller Dean number. The center of rotation is located close to the midpoint of the patch. For a Dean number of 100, a notable increase in the relative strength of the helical flow is observed: the center of the vortex is shifted towards the outer channel wall.

At a still higher Dean number of 200, the flow pattern changes considerably (see Figure 1.145) [47]. An additional counter-rotating vortex appears is found, yielding a 4-vortex flow pattern. The new vortex is located close to the outer channel wall. On following the flow-pattern evolution along the flow path the four-vortex pattern, it is observed that it is well developed already at an early stage.

#### Species concentration and velocity fields along the flow passage at Dean numbers above and below the threshold value

[M 69] [P 61] For a curved channel design, species concentration and velocity fields of the secondary flow were given (see Figure 1.146) [152]. These fields each were

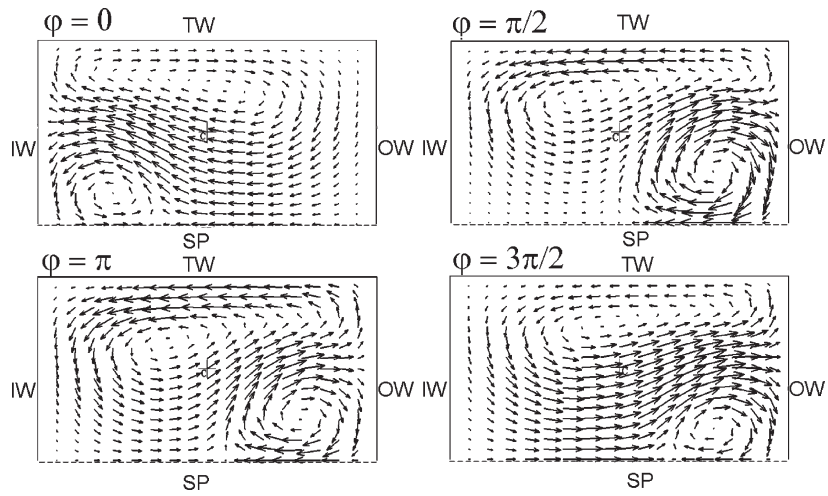


Figure 1.145 Evolution of the four-vortex helical flow in a mixing element for  $K = 200$  [47].

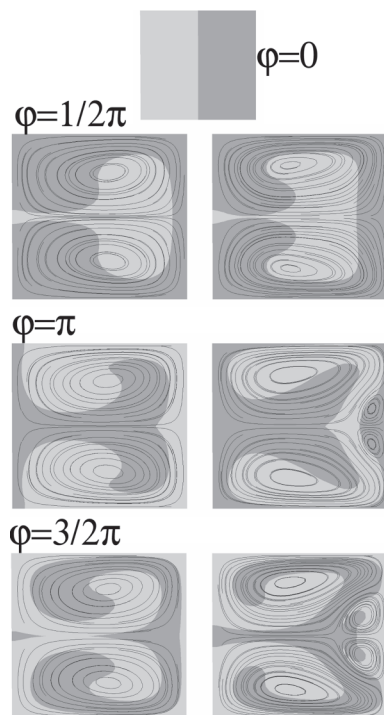


Figure 1.146 Species concentration (encoded in gray) given for cross-sections at the inlet, outlet and two intermediate positions for two Dean numbers,  $K = 150$  (left) and  $300$  (right). The initial condition is shown on the left, i.e. two lamellae. Additionally, the velocity fields of the secondary flow are shown [152].

determined at various channel cross-sections, at the inlet, outlet and at two intermediate positions. Two Dean numbers,  $K = 150$  and  $450$ , were considered. Starting from two initial lamellae, it was found that the velocity profiles were at the beginning qualitatively identical, thus giving similar concentration distributions. Already at an early stage in the flow passage, an additional pair of counter-rotating vortices develop for  $K = 450$ . These vortices are found close to the center of the outer channel wall. In this way, one lamella is incompletely displaced, leaving a certain fraction. At a later stage in the flow passage, a well developed, steady velocity profile with four vortices is achieved.

#### Vorticity of helical flows

[M 69] [P 61] In a curved channel, helical flows can be produced with four vortices, composed of two times two types, a small and large one (see Figure 1.147) [152]. The total vorticity of the small vortices was integrated over the relevant part of the cross-section. It is found that these vortices start to develop at Dean numbers around 200. The strongest increase in the vorticity is observed at Dean numbers between 300 and 400.

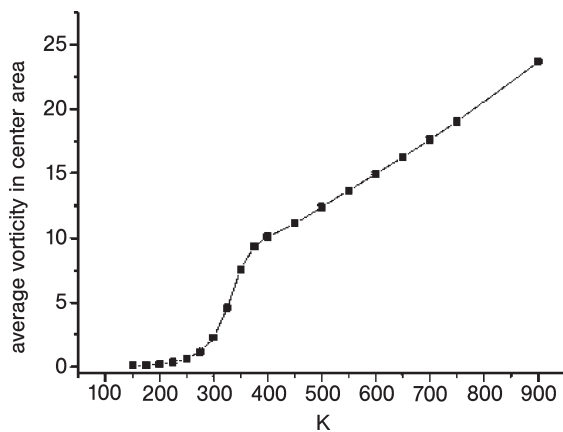
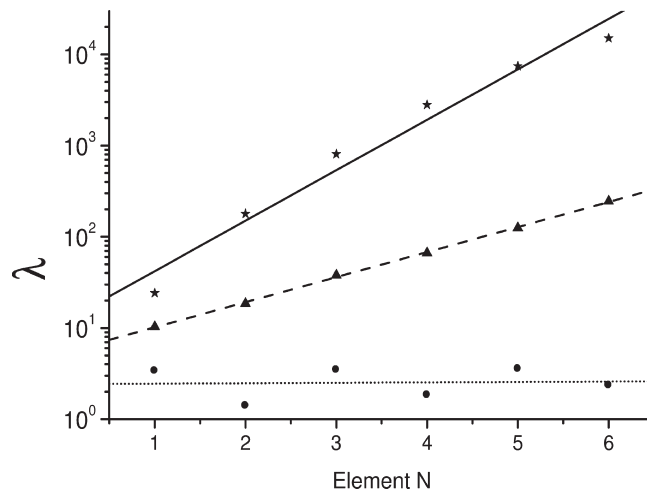


Figure 1.147 Total secondary vorticity as function of the Dean number [152].

#### Interface stretching

[M 70a] [P 62] As an initial situation, the fluid interface is set as a vertical straight line across the inlet [47]. An iterative method was employed for interface tracking owing to the high interfacial stretching. In this way, the seeding density was adjusted to eliminate interface self-crossing during particle tracking and to improve the accuracy of interface stretching calculations. The tracer numbers referring to Dean numbers  $K = 10$ ,  $100$  and  $200$  were about  $3000$ ,  $10000$  and  $56000$ , respectively.

As interface stretching factor, the interface length at a certain position divided by the initial interface length is defined [47]. Such stretching factors were given as a function of the number of segments of a meander mixer (see Figure 1.148). At a Dean number  $K = 10$  nearly no stretching takes places. In contrast, exponential



**Figure 1.148** Interface stretching factor vs. element number for different Dean numbers: (●)  $K = 10$ ; (▲)  $K = 100$ ; (★)  $K = 200$  [47].

growth of the interface is observed for  $K = 100$  and  $200$ . A positive Lyapunov exponent is given, confirming chaotic mixing at large Dean numbers.

The flow pattern switch at  $K = 100$  differs from that at  $K = 200$  [47]. In the first case, the center of rotation of the two Dean vortices changes when the sign of curvature is altered, similar to the situation reported in [154]. At the higher Dean number, a four-vortex pattern of pronounced asymmetry is given; a meandering flow has here a significant impact on the resulting change of the flow pattern.

At  $K = 10$ , the helical flow is nearly symmetric and a meandering flow has hardly any impact on the interface stretching; actually the initial flow situation is restored at certain positions (see Figure 1.149) [47]. At  $K = 100$ , an asymmetric two-vortex system experiences interfacial stretching similar to the 'blinking-vortex' flow pattern reported in [154]. At  $K = 200$ , the appearance of the two new vortices leads to even more substantial changes of the superposed flow pattern, giving large increases in interfaces. Later investigations confirmed that a four-vortex vortices system is yielded already at  $K = 150$ .

#### Residence time distribution

[M 70a] [P 62] Simulated residence time distributions (RTDs) were obtained for  $K = 200$  at various positions for a meander mixer and compared with RTDs simulated for Poiseuille and for plug flow in a straight square channel with the same cross-sectional dimension (see Figure 1.150) [47]. The RTDs in the meander mixer come close to those given by plug flow, but are much narrower than those of Poiseuille flow. The RTD in the meander mixer is the better, the more downstream the flow is investigated. This is due to the homogenization of the flow by chaotic flow patterns.

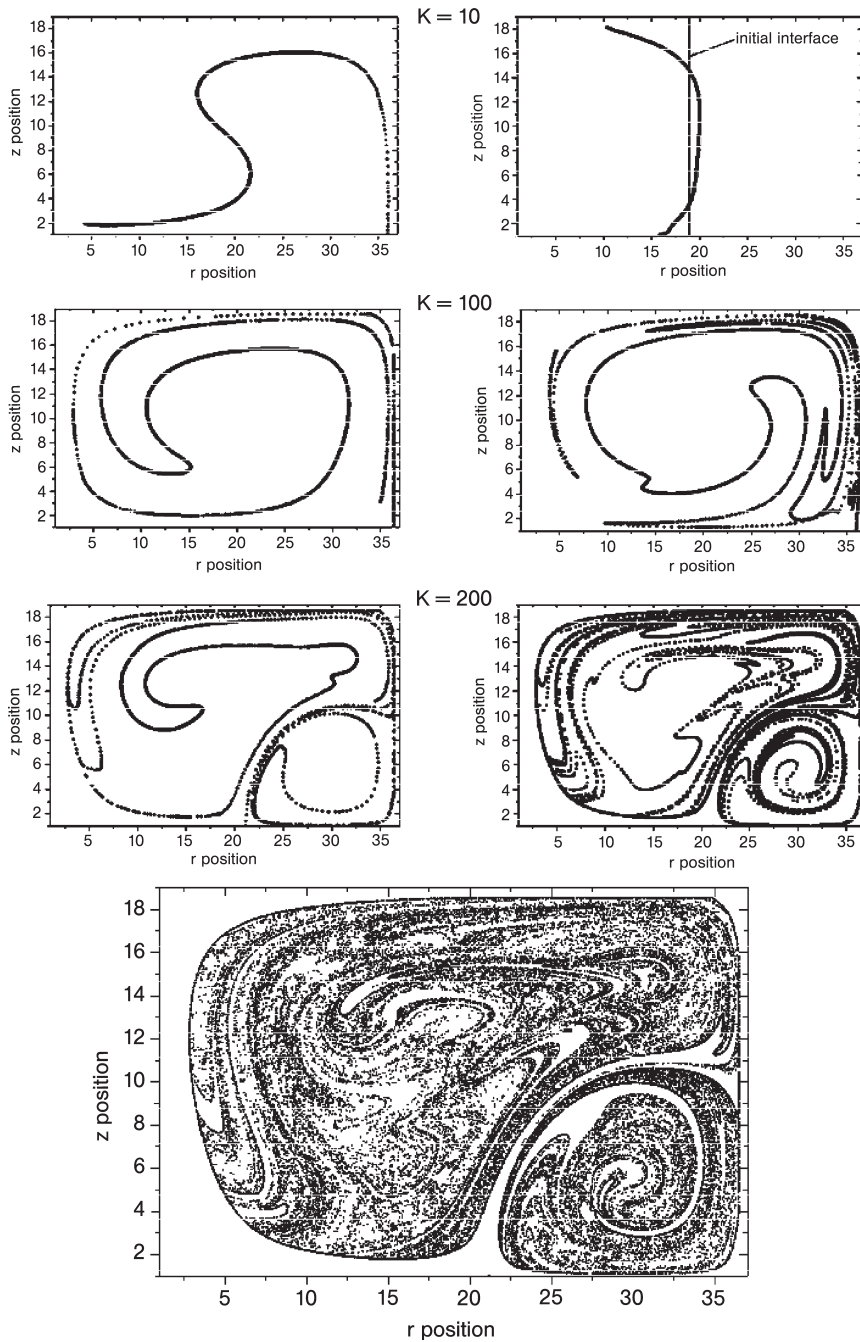


**Figure 1.149** Interface shapes obtained from particle tracking for  $K = 10$  (upper row),  $K = 100$  (middle row) and  $K = 200$  (lower row). The left column shows the shapes after the first mixing element and the right column those after the second mixing element. The last image at the bottom refers to the shape after the sixth mixing element at  $K = 200$  [47].

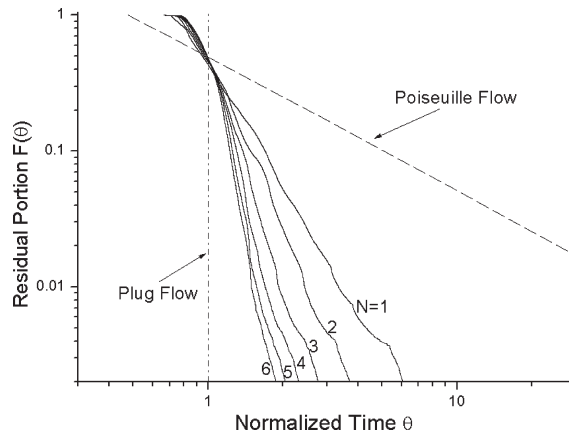


Figure 1.150 Residual portion of particles remaining in the meander mixer for  $K = 200$  [47].

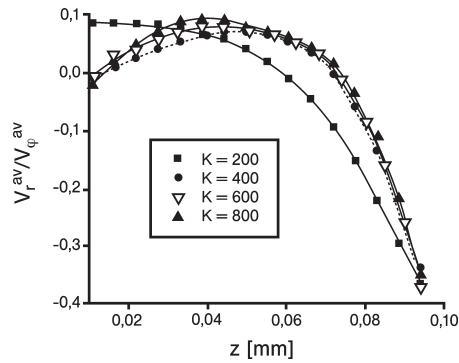


Figure 1.151 Relative transverse velocities averaged over a certain zone for Dean numbers between  $K = 200$  and  $800$  [152].

#### Benchmarking of helical flow strength in curved and bas-relieved channels

[M 70a] [P 61] The strength of the helical flow in curved channels was compared with that in bas-relief structured micro channels, considering the averaged relative transverse velocity for a series of Dean numbers (see Figure 1.151) [152]. The curve yielded at  $K = 200$  is distinctively different from those obtained at  $K = 400, 600$  and  $800$ , which equal each other. This is due to the different flow patterns; at low Dean numbers only one pair of vortices is given, whereas two pairs of vortices develop at larger Dean numbers, yielding curves with an intermediate maximum of the relative transverse velocity.

The relative transverse velocity of the curved channel corresponds well with data published for bas-relief structured channels [152]. Hence, also the very simple design of a curved channel can lead to efficient mixing.

#### Periodic switching of helical flow in curved channels – chaotic advection

[M 70a] [P 61] It is known that stirring and chaotic mixing can be achieved by an unsteady potential flow [154]. This can also be utilized for helical flows in curved

channels [152]. For this purpose, the geometric parameters need to be repeatedly changed to alter the Dean number. In this way, a periodic switch between the flow regimes above and below a threshold value of the Dean number, i.e. between two and four counter-rotating vortices, is achieved.

Hence alternating flows can also be achieved by repetitive induction of entrance flow effects [152]. This relies to a constant re-direction of flows from one curved channel into another.

The sum of both effects, the flow-pattern switch and the entrance flow effects, is achieved when the sign of curvature is simply altered [152]. The respective design is that of a meander channel. At large Dean numbers, chaotic flow can be induced in this way, as evidenced by cross-sectional views of different segments of the meander channel.

#### Qualitative judgement of mixing – visual inspection

[M 70b] [P 63] At a Dean number  $K = 141$ , video images show improved color formation for reactive imaging in the meander micro mixer as compared with  $K = 35$ , which proves more advanced mixing (see Figure 1.152) [47]. This is particularly remarkable, since at the higher Dean number the residence time for the flow is about a factor of 4 shorter than for the  $K = 35$  at the same position. Thus, the theoretically predicted higher vorticity (see *Vorticity of helical flows* and *Interface stretching*) indeed results in experimentally confirmed better mixing.

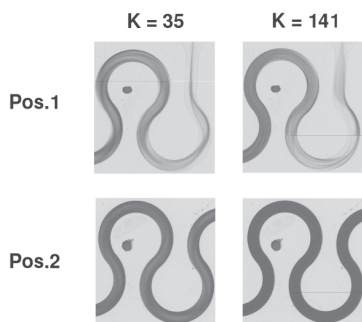


**Figure 1.152** Micro photographs of the mixing patterns in the meander micro mixer for different Dean numbers and positions [47].

#### Quantitative judgement of mixing – reactive imaging analyzed by photometry

[M 70b] [P 63] Photometric concentration profiles were obtained for mixing of 50 mM reactant solutions at 25 °C and  $K = 246$  in a meander micro mixer close to the inlet (see Figure 1.153) [47]. At the start of the mixing process only one lamella is visible, corresponding to about 10 mM reaction product. Further downstream, the next profiles provide a multitude of lamellae, which represent between 2 and 24 mM product. At still further positions in the meander channel, more homogeneous flow patterns are yielded and the product content is increased to between 15 and 28 mM. Finally, the concentration increases to values close to 50 mM which indicates complete mixing.

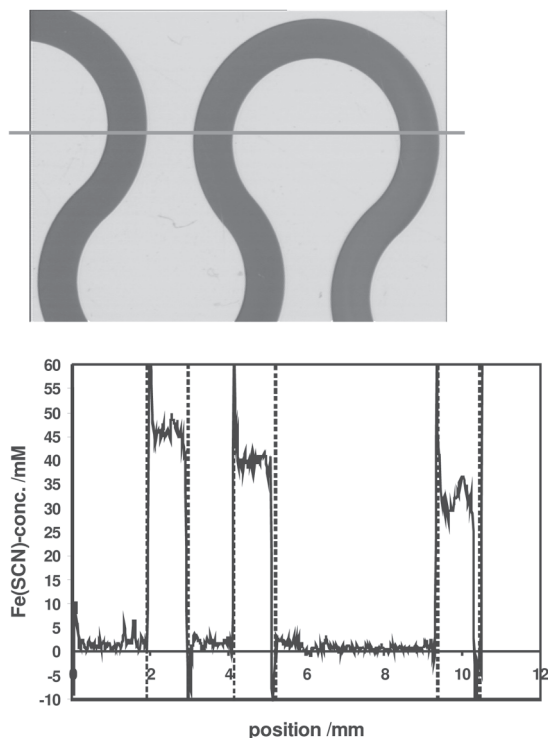


**Figure 1.153** Top: micro photograph of the flow patterns obtained from the mixing and reaction taken close to the inlet of the mixer. The horizontal line denotes the cut over which the concentration was determined. Bottom: resulting photometric concentration profile. The dashed lines enclose the channel regions [47].

#### Mixing time – reactive imaging analyzed by photometry

[M 70b] [P 63] The relationship between mixing time and Dean number was determined using a meander micro mixer and a reactive-imaging approach [47]. For Dean numbers ranging from  $K = 105$  to 141, the mixing time is considerably reduced. This correlates with the predicted changes in flow patterns by simulation (see *Vorticity of helical flows* and *Interface stretching*). The relative strength of the helical flow, as compared with the mean flow velocity, increases with  $K$ . In addition, the ‘blinking vortex’ principle becomes more and more effective, because the centers of the vortices are continuously shifted towards the outer channel wall. As a result of both effects, chaotic advection arises.

The results obtained on mixing time also give experimental evidence for the existence of a threshold value around  $K = 140$ , which is associated with a change in vorticity [47]. At this point, the helical flow pattern switches from a two- to the four-vortex fluid system. Besides qualitatively confirming such a threshold value, the experiments are also in very good quantitative accord with the value predicted by the simulations.

Above  $K = 141$ , a steady but comparatively small reduction in mixing time was measured [47]. This confirms that the four-vortex pattern is relatively stable for Dean numbers above the threshold value. The increase in interfacial stretching obviously is now more compensated by the reduction in residence time, as for the cases reported above.

In this regime at  $K = 141$ , mixing times below 50 ms are reached [47]. For the geometry chosen, a Dean number of 140 corresponds to a Reynolds number of about 313. Hence the critical transition for meander (Dean) micro mixers is almost an order of magnitude smaller than the critical Reynolds number for the laminar-to-turbulent transition in straight channels. Hence meander micro mixers can achieve fast mixing in a regime where mass transfer in straight channels is usually slow and dominated by diffusion. Considering their ease of fabrication, meander micro mixers can be considered a simple, but efficient means and design.

#### Flow patterns in L-shaped micro mixer

[M 71] [P 64] Flow cross-sectional images were taken in the 3-D L-shaped micro mixer using a reactive approach to characterize mixing [153]. Initially, a bi-laminated system is observed, then the interface becomes more and more stretched and elongated, and finally the streams intertwine deeply and mixing results from this enlarging of specific interface.

#### Concentration monitoring in L-shaped micro mixer

[M 71] [P 64] A sort of concentration monitoring was achieved for the 3-D L-shaped micro mixer giving a quantitative analysis of the mixing [153]. A normalized average intensity clearly shows the speeding up of mixing at higher  $Re$ . At  $Re = 70$ , mixing is complete within 20 ms.

#### Mixing and bacteria capture in L-shaped micro mixer

[M 71] [details of protocol in [49]] L- and C-shaped serpentine PDMS micro mixers use chaotic advection [49]. Numerical results regarding the degree of mixing at different flow rates and at different locations were determined. The degree of mixing actually increased with increasing flow rate ( $0.05\text{--}0.4\text{ ml min}^{-1}$ ), despite the reduction of the residence, more than compensated by increasing secondary-flow mixing. This is corroborated by experimental findings, showing superior performance at high Reynold number.

A biological application, bacteria capture by mixing of blood/bacteria samples with magnetic beads, was carried out in the L-shaped micro mixer [49]. A high capture efficiency of 99% was obtained at a short time of 0.15 s. The blood cells and bacteria remained intact after the mixing process, evidencing the low shear strain field of the flow.

### 1.3.20

#### Distributive Mixing with Traditional Static Mixer Designs

##### Most Relevant Citations

Peer-reviewed journals: [2].

A straightforward idea is to ‘shrink’ the designs of conventional static mixers, i.e. to keep the geometry exactly by simply decreasing all dimensions with the same reduction factor [2]. The static mixers are basically pipes with in-line elements which serve as flow obstacles. They thus perform distributive mixing, e.g. splitting, rearranging and recombining or stretching and folding of the flow. The miniaturized versions are expected to induce a comparable action. This looks at first sight similar to the split-and-recombine (SAR) mixers. However, the distributive mixing described here results in much more complex flow patterns, not comparable to the lamellae patterns obtained at low Reynolds number of SAR devices. At high Reynolds numbers, both mixing approaches may behave similarly, but this is not known in detail at present.

#### 1.3.20.1 Mixer 72 [M 72]: Intersecting Elements Microstructured Mixer

This mixer resembles conventionally widely used Sulzer™ and Koch™ static mixers which have an intersecting design, a series of rigid elements. A similar miniaturized design with four in-line mixing elements was realized [2]. Each mixing element is made by multiple bars placed at  $\pm 45^\circ$  to yield intersecting channels. The mixing elements result from their predecessor by reflection and a  $90^\circ$  rotation.

The CAD design generated the geometry by performing Boolean operations on simple volumic primitives [2]. The microstructure was realized by microstereolithography. This technique is based on a layer-by-layer light-induced polymerization of a liquid resin, a pre-polymerized solution. Actually, about 1800 layers of  $5 \mu\text{m}$  thickness were superimposed in this way (5 h manufacturing time).

Mixer type	Intersecting elements micro mixer	Mixing element: width (tube diameter), length	1200 $\mu\text{m}$ , 1200 $\mu\text{m}$
Mixer material	Polymer	Number of bars	24
Number of mixing elements	4	Angle of bars	$\pm 45^\circ$

#### 1.3.20.2 Mixer 73 [M 73]: Helical Elements Micro Mixer

This mixer resembles the conventionally widely used Kenics™ static mixer having a short-helix design with alternately arranged right- and left-handed elements. The fluid is stretched and folded. A similar miniaturized design with six in-line mixing elements was realized [2]. Each helix element is aligned at  $90^\circ$  from the previous one and has a twist angle of  $90^\circ$ . Right- and left-handed elements are alternately arranged within the tube.

Mixer type	Helical micro mixer	Number of mixing elements	6
Mixer material	Polymer	Mixing element: width (tube diameter), length	1200 $\mu\text{m}$ , 900 $\mu\text{m}$

### 1.3.20.3 Mixing Characterization Protocols/Simulation

[P 65] Pumping was achieved by pressuring water with nitrogen [2]. The pressure was measured with a pressure gauge. The flow rate was determined gravimetrically. Degassed, dionized, filtered water was used as fluid. Before the experiments, the mixers were primed to remove resting air bubbles.

Qualitative, numerical simulations were performed with the commercial tool FLUENT-5 to evaluate mixing efficiency [2]. The simulations were oriented on concepts employed for conventional 3-D static mixing. The micro-mixer geometries were laid out using the GAMBIT predecessor as well as the meshing of surfaces and volumes and the specification of boundary conditions. Entrance and exit sections were also simulated.

### 1.3.20.4 Typical Results

#### Volume flow–pressure drop relation

[M 72] [M 73] [P 65] A linear dependence of the pressure drop on the volume flow rate was observed both for the intersecting and the helical microstructured mixers (see Figure 1.154) [2]. The pressure drop of the helical device is lower than that of the intersecting mixer. A flow rate of about  $1 \text{ l h}^{-1}$  was found for the helical mixer at a pressure of about 150 mbar, whereas the intersecting mixer gives  $0.75 \text{ l h}^{-1}$  at about 250 mbar.

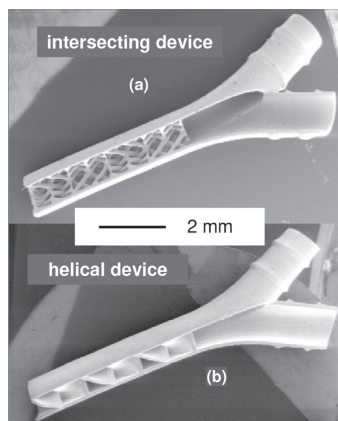


**Figure 1.154** Cut view of micro mixers manufactured by microstereolithography.

(a) Intersecting channel device;  
(b) helical-element device [2] (by courtesy of RSC).

#### Cross-sectional velocity profiles

[M 72] [M 73] [P 65] The analysis of cross-sectional velocity profiles (water as fluid;  $Re = 12$ ) shows that the intersecting structures have intricate gradient fields near the bars of the internals, while the helical device displays entrance and exit effects over more than one-quarter of the flow field (see [155] e.g. for fluid flow through macroscopic helical static elements) [2].

#### Mixing efficiency

[M 72] [M 73] [P 65] When judging mixing efficiency by particle trajectories (water as fluid;  $Re = 12$ ), it is evident that the intersecting device performs manifold splitting

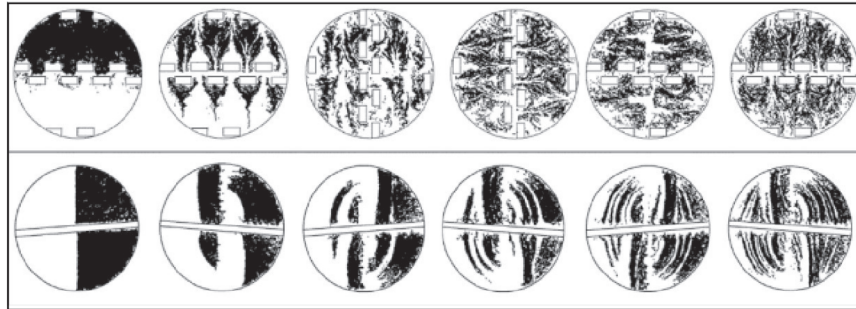


**Figure 1.155** Particle-tracking imaging aiming at visualization of the mixing process ( $Re = 12$ ). The location of 65 000 particles is given at various locations at the beginning of the structured in-line elements. Top, intersecting mixer; bottom, helical mixer [2] (by courtesy of RSC).

and recombining of the flow, yielding a fine-dispersed system at the end, i.e. achieving a good mixing efficiency (see Figure 1.155). In contrast, flow stretching and folding are found for the helical device, resulting in a coarsely textured fluid, which means less efficient mixing.

### 1.3.21

#### Passive Chaotic Mixing by Posing Grooves to Viscous Flows

##### Most Relevant Citations

Peer-reviewed journals: [44, 45, 152, 156, 157]; micro fabrication: [118]; proceedings contributions: [142, 158].

Grooves oriented at an oblique angle on the ground level of a micro channel are known to induce transverse flows by using a steady axial pressure gradient [44]. These grooves pose an anisotropic resistance to viscous flows, mainly in the orthogonal direction. In this way, an axial pressure gradient is built up and generates a mean transverse component of the flow. The flow originates at the floor structures and circulates back across the top of the channel, giving helical streamlines for the full flow.

The functioning of grooves was proven under pressure-driven [44] and electro-osmotic flow [156] conditions and both cases are described below.

##### 1.3.21.1 Mixer 74 [M 74]: Non-grooved Channel – Reference Case

As a reference case, this straight channel design without any grooves was taken [44]. In the following, one typical set of design specifications is given.

Mixer type	Non-grooved micro channel	Channel width, depth	200 $\mu\text{m}$ , 70 $\mu\text{m}$
Mixer material	Polydimethylsiloxane		

### 1.3.21.2 Mixer 75 [M 75]: Oblique, Straight-grooved Micro Mixer (I)

The main feature of this class of mixers is patterned grooves on the floor of the micro channel [44]. In the simplest version, the array of grooves presents a repeating, periodic sequence of the base structure. In the following, one typical set of design specifications is given.

Microfabrication was done by means of photolithography using an SU-8 photoresist [44]. In a two-step procedure first the negatively shaped channel structure was established and thereafter the groove pattern was generated. Molds of these structures were made in PDMS, yielding the positive structure. Sealing was achieved by exposure of the PDMS structure to a plasma for 1 min and subsequent coverage with a glass cover slip.

Mixer type	Oblique, straight-grooved mixer	Channel width, depth	200 $\mu\text{m}$ , 70 $\mu\text{m}$
Mixer material	Polydimethylsiloxane	Angle of groove tilting	45°
Ratio groove structure height to channel depth	0.2		

### 1.3.21.3 Mixer 76 [M 76]: Oblique, Asymmetrically Grooved Micro Mixer – Staggered Herringbone Mixer (SHM)

In this more advanced version of the patterned grooved mixer, more complex patterns are created which have a repeated sequence of mirror-imaged sub-arrays, typically consisting of bendt grooves (see Figure 1.156) [44]. These are known to create a sequence of rotational and extensional local flows, i.e. the shape of the grooves is varied as a function of the channel length. A prominent design of this class is the staggered herringbone mixer (SHM). Here, the positions of the centers of rotation and of the up and down wellings (local extensional flow) of the transverse flow are exchanged. In the following, one typical set of design specifications is given.

Microfabrication was effected in the same way as described for the [M 75] device [44].

Mixer type	Oblique, asymmetrically-grooved mixer: staggered herringbone mixer (SHM)	Channel width, depth	200 $\mu\text{m}$ , 77 $\mu\text{m}$
Mixer material	Polydimethylsiloxane	Angle of groove tilting	45°
Ratio groove structure height to channel depth	0.23		

The fabrication of staggered herringbone structures was also achieved by a high-brightness diode-pumped Nd:YAG laser direct write method [118]. A PDMS

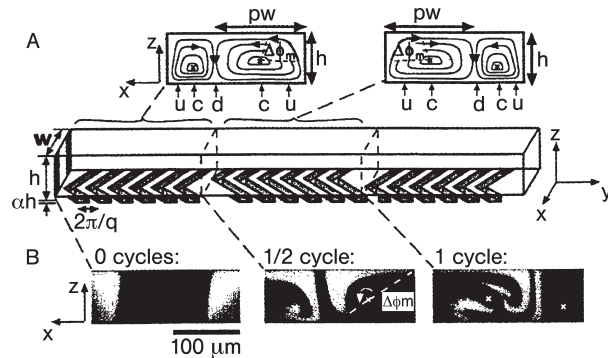


**Figure 1.156** (A) Design of the staggered herringbone micro mixer, displaying one-and-a-half cycle of the floor structures (SHM). Streamlines are also given. For details of the symbols used, which describe the rotational and extensional flow, see [44]. (B) Confocal micrographs of vertical cross-sections of the channel given in (A) [44] (by courtesy of AAAS).

structure was realized in one step and tested for mixing function by fluorescence imaging. The method provides rapid prototyping of master structures and is said to have high flexibility.

#### 1.3.21.4 Mixer 77 [M 77]: Oblique, Straight-grooved Micro Mixer (II)

This device contains in a T-type micro channel oblique, straight grooves, termed slanted wells in the original publication (see Figure 1.156) [156]. The grooves have the same purpose as given for the devices discussed below, namely to induce lateral transport to promote mixing.

The T-shape was imprinted into a polymer substrate yielding a trapezoid cross-sectional shape [156]. By excimer laser fabrication, a series of slanted wells beginning close to the T-junction were made. This microstructure was then sealed by a polymer cover.

Mixer type	Oblique, straight-grooved mixer	Channel width at top and bottom, depth	72 $\mu\text{m}$ , 28 $\mu\text{m}$ , 31 $\mu\text{m}$
Mixer material	Polycarbonate	Number of grooves	4
Cover material	Polyethylene terephthalate glycol	Cross-sectional groove width	14 $\mu\text{m}$
Inlet and outlet (mixing) channel width	511 $\mu\text{m}$ , 100 $\mu\text{m}$	Spacing between the grooves	15.2 $\mu\text{m}$

#### 1.3.21.5 Mixer 78 [M 78]: Diagonal-grooved Micro Mixer

A mixer, which is part of a sensor system, has diagonal grooves on the channel bottom [142]. This creates a lateral flow enlarging the interfacial area. No indication is given whether this measure causes the flow to become chaotic.

Mixer type	Diagonal grooved mixer	Plate thickness	1.6 mm
Mixer material	VACREL®	Channel width at top and bottom, depth	600 µm, 100 µm, 170 mm
Plate material	PC-board glass-reinforced base material FR4 with 35 µm Cu layer	Groove width, depth	200 µm, 50 µm

#### 1.3.21.6 Mixing Characterization Protocols/Simulation

[P 66] Equal streams of 1 mM solutions of fluorescein-labeled polymer (polyethylenimine, molecular weight 500 000) in water–glycerol mixtures (0 and 80% glycerol) and a clear solution were injected into the channel [44]. The flow was achieved by compressed air at constant pressure. Imaging was achieved by applying a confocal fluorescence microscope.

[P 67] Simulations were made following experiments made previously [156]. Therein 0.11 mM Rhodamine B solutions in 20 mM carbonate buffer were mixed with the same carbonate buffer. For the buffer solution, the physical properties of water were approximated. For Rhodamine B, a diffusion coefficient of  $2.8 \cdot 10^{-6} \text{ cm}^2 \text{ s}^{-1}$  was taken. Electroosmotic flow was applied for liquid transport. For all of the walls in the domain the electroosmotic (EO) mobility was set to  $3.4 \cdot 10^{-4} \text{ cm}^2 \text{ V}^{-1} \text{ s}^{-1}$ , which corresponds to a zeta potential ( $\zeta$ ) of  $-44.1 \text{ mV}$ . The electric field in the outlet channel was  $1160 \text{ V cm}^{-1}$ . The Reynolds number was 0.22. The electric field strength was set low in order to decrease diffusive (pre-)mixing prior to the groove structure.

A 3-D model geometry was generated using the CFD-ACE+ v6.6 software package [156]. Both steady-state and transient mixing simulations were undertaken, the latter describing the mixing of plugs. As plug size  $100 \text{ µm}$  was assumed, being initially located  $50 \text{ µm}$  before the series of grooves. The plug mixing was investigated for a straight channel, without a T-junction so as to avoid the band broadening which would have occurred for such a flow configuration. Further details of the plug experiments are given in [156].

[P 68] A double-syringe pump was used for liquid feed [142]. An iodine–starch solution was mixed with a photographic fixer solution at a ratio of 1 : 3.5. Thereby, the intense blue color changed to a pale blue. The mixing process was followed by means of a stereo microscope.

#### 1.3.21.7 Typical Results

##### Completion of mixing

[M 78] [P 68] For a diagonal-groove mixer, complete mixing was observed by reactive-type imaging for flow rates up to  $1.3 \text{ µl min}^{-1}$  [142]. For comparison, complete mixing is given for a channel without grooves only up to  $0.12 \text{ µl min}^{-1}$ . Hence the diagonal grooves allow for a 10-fold increase in flow rate at similar mixing performance.

**Impact of Reynolds number on flow**

[M 75] [M 76] [P 66] For grooves of small extension relative to the channel diameter, it was found that a variation of  $Re$  (in the range  $Re < 1$ ) does not change the form of the flow, i.e. the shape of the trajectories [44]. Even at  $Re < 100$  the form of the flow is qualitatively maintained.

**Modeling the relationship between groove geometry and flow form**

[M 75] [M 76] [P 66] Experimentally found dependences of the average rate of rotation on the geometry of the grooves can be described by a simple model [44].

**Groove asymmetry**

[M 75] [M 76] [P 66] Symmetrical grooves produce non-chaotic flows; at the optimized asymmetrical groove geometry most of the cross-sectional area is filled with chaotic flow [44].

**Groove depth**

[M 77] [P 67] Lateral transport is enhanced on increasing the groove depth at constant channel depth, as evidenced using a four-groove structure angled at  $45^\circ$  (fluid transport given by electroosmotic field) [156]. For groove depths exceeding  $50\ \mu\text{m}$  (at a channel depth of  $50\ \mu\text{m}$ ), no additional impact is given, however; the mixing effect is constant from hereon.

This behavior can be correlated with the magnitude of the  $z$ -component of the electric field,  $E_z$  (see Figure 1.157) [156]. This increases with groove depth and is spatially maximal at the ends of the slanted grooves.

**Groove angle**

[M 77] [P 67] The angle of the grooves, relative to the channel long axis, was varied from  $15^\circ$  to  $90^\circ$  for a four-grooved structure (fluid transport given by electroosmotic field;  $50\ \mu\text{m}$  deep grooves) [156]. The concentration profiles yielded by exposing the flow to  $90^\circ$  perpendicular grooves show no effect of lateral mixing, as expected. The bi-laminated pattern remains nearly undisturbed. For all other angled grooves, lateral mass transport is evident. The smaller the angle, the larger is the effect. This is explained by electric-potential plots as a function of the relevant structural dimensions. As the groove angle decreases, the difference in potential between the grooves' ends increases. This leads to a larger electric field and to enhanced electroosmotic flow.

The disadvantage of small-angled grooves, however, is that they consume a much larger footprint area so that for practical solutions a compromise between lateral-mixing capacity and area of the mixing element may have to be made [156].

**Fluid folding vs. fluid stretching**

[M 77] [P 67] For groove angles as small as  $15^\circ$ , fluid folding, finally leading to recirculation patterns, is observed, whereas at larger angles only fluid stretching occurs (see Figure 1.158 and *Groove angle*, above) [156].

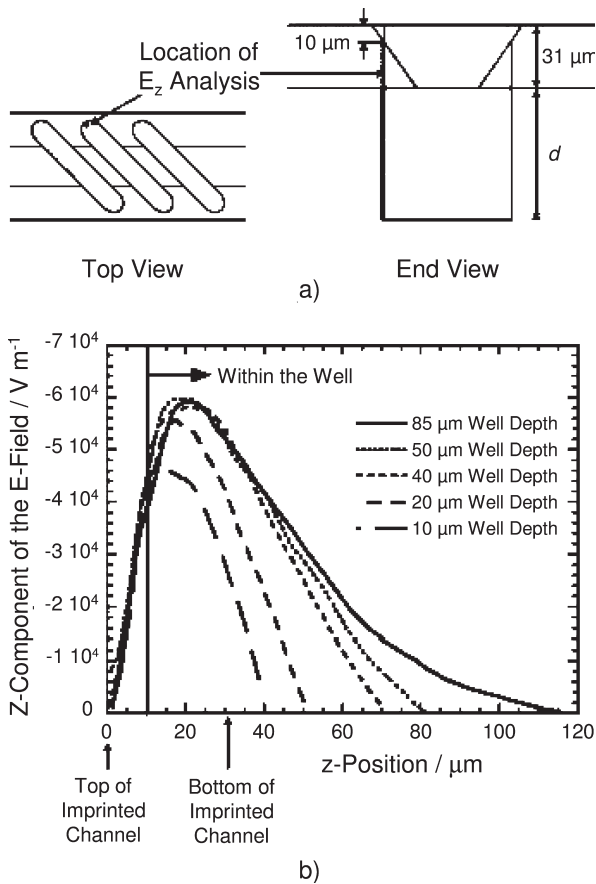


**Figure 1.157** Analysis of the magnitude of the z-component of the electric field  $E_z$ . (a) Depiction of the location of the analysis; (b)  $E_z$  as a function of the depth of the grooves for various absolute groove depths [156] (by courtesy of RSC).

#### Wall EO mobility variation

[M 77] [P 67] The wall EO mobility is dependent on the manufacturing process of the grooves [156]. It is known, for example, that laser ablated surfaces have larger EO mobility than imprinted surfaces. For different ratios of the groove-(laser ablated)-to-channel-(imprinted) mobilities, their effect on the concentration profiles was investigated. Only at ratios of about 3.0 is enhanced lateral transport observed, evident from the presence of fluid folding and recirculation instead of fluid stretching only (groove angle,  $45^\circ$ ; groove depth,  $50 \mu\text{m}$ ). Such high ratios are above the experimental data obtained for the naked surfaces so far; hence surface modifications will be needed (e.g. deposition of polyelectrolyte multi-layers) to increase the ratio further. If this is done, the ratio of the groove-to-channel mobilities will be a second means of increasing lateral transport and hence chaotic mixing under the action of an electroosmotic field, in addition to the variation of the groove angle (see *Groove angle*, above).

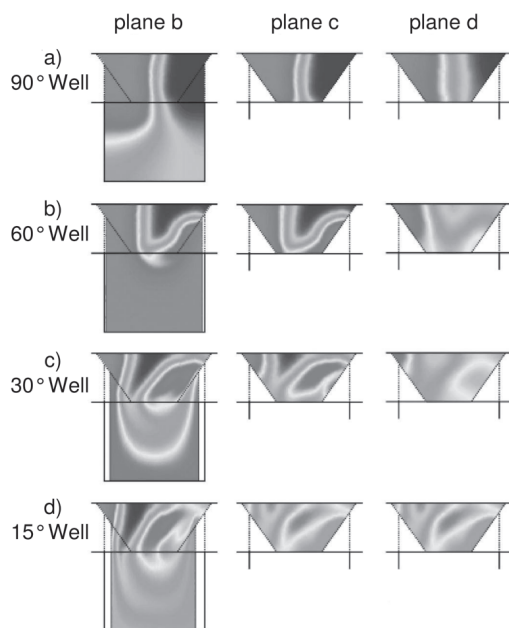


**Figure 1.158** Concentration profiles of Rhodamine B imaged on various planes of the four-grooved channels for different groove angles at a constant groove depth of  $50\ \mu\text{m}$  [156] (by courtesy of RSC).

#### Transient mixing of plugs

[M 77] [P 67] When mixing plugs, it is desired to have fast mixing similar to steady flows; however, in addition, the axial dispersion should be minimized, since the corresponding increase in plug length should be kept minimal [156].

As to be expected, the axial dispersion is larger at increased groove depth, because the grooves somehow act like dead zones and the residence time within the grooves is longer (groove angle:  $15^\circ$ ) [156]. Too shallow grooves give rise to insufficient lateral mixing.

Concentration profiles as a function of time, similar to time–age residence time plots, give quantitative information on the degree of axial dispersion (see Figure 1.159) (groove angle,  $15^\circ$ ; groove depth,  $20\ \mu\text{m}$ ) [156]. This was done for ratios of the groove-to-channel mobilities of 1 and 2. The axial dispersion in both cases is low, as a comparison of the curves obtained by guiding flow through grooved channels and a blank channel (without groove internals) reveals. The residence-time plots of the grooved structures are only to a small extent broader ( $< 10\%$ ) as compared with the undisturbed flow. The axial broadening of the flow at a ratio of the groove-to-channel mobilities of 2 is lower, which is explained by the larger lateral flux. It was confirmed by concentration plots that for both grooved-channel structures mixing is effective; the standard deviation of the concentration across the channel is reduced by 72%.

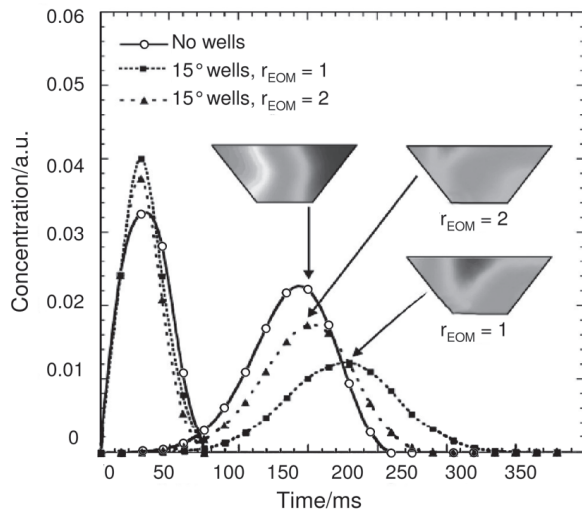


**Figure 1.159** Concentration profiles of an injected plug of Rhodamine B traveling over a four-groove structure in a micro channel at two different groove-to-channel mobilities  $r_{EOM}$  and for an unstructured channel as reference case. This plot describes the axial broadening of the pulse signal. In addition, cross-sectional concentration profiles are given to analyze the corresponding impact on mixing [156] (by courtesy of RSC).

#### Twisting flow

[M 75] [P 66] 3-D twisting flow is found for a mixer design with an array of multiple obliquely oriented, straight grooves [44].

#### Benchmarking of non-grooved, oblique grooved and staggered herringbone designs

[M 74] [M 75] [M 76] [P 66] Confocal fluorescence imaging of the cross-sections of the flow in the micro channel were used for judging the mixing quality. For a simple channel without any grooves, almost no mixing is detected (see Figure 1.160) [44]. For the mixer design with an array of multiple obliquely oriented, straight grooves incomplete mixing is found, even after a 30 mm flow passage. The staggered herringbone mixer gives good mixing, even at high  $Pe$  ( $9 \cdot 10^5$ ). The fluorescence images show an increase of fluidic filaments, i.e. of specific interfaces, the more cycles are passed.

#### Quantified mixing efficiency

[M 75] [M 76] [P 66] The standard deviation of the fluorescence intensity of cross-sectional flow images was taken as a measure of the mixing efficiency (see Figure 1.160) [44]. The SHM mixer performs well over a large range of  $Pe$ . The mixing length required for 90% mixing increases by less than a factor of 3 from the lowest to the highest  $Pe$ . The straight-grooved mixer and the non-grooved channel have much reduced performance.

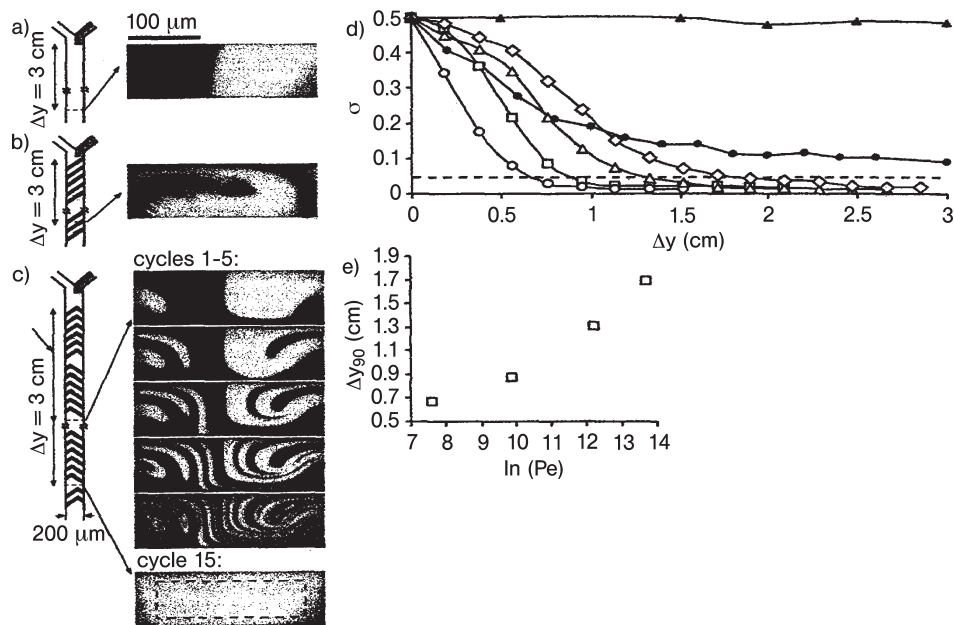


**Figure 1.160** (A) Confocal micrograph of the vertical cross-section of the channel for a non-grooved channel. (B) Same type of image for the oblique, straight-groove design. (C) Same type of images for the oblique, asymmetric groove design (staggered herringbone mixer, SHM). (D) Standard deviation, a measure of mixing efficiency, versus mixing length for various  $Pe$ : SHM (open symbols), (○)  $Pe = 2 \cdot 10^3$ ; (□)  $Pe = 2 \cdot 10^4$ ; (△)  $Pe = 2 \cdot 10^5$ ; (◇)  $Pe = 9 \cdot 10^2$ ; (▲) oblique, straight-rigded channel; (●) non-grooved channel. (E) Mixing length for 90% mixing as a function of  $Pe$ . For further details of this figure, see [44] (by courtesy of AAAS).

#### Impact of Peclet number

[M 76] [P 66] The mixing length for the staggered herringbone mixer increases linearly with  $\ln(Pe)$  (see Figure 1.160) [44].

#### Mixing lengths for a real-case example

[M 74] [M 76] [P 66] The mixing length for different micro channels was calculated for the mixing of a protein solution in aqueous buffer (molecular weight  $10^5$ ; diffusion constant  $10^{-6} \text{ cm}^2 \text{ s}^{-1}$ ; velocity  $1 \text{ cm s}^{-1}$ ) [44]. For  $Pe = 10^4$ , a simple, non-grooved channel requires 100 cm for mixing completion, whereas 1 cm is sufficient for the SHM. If the velocity is increased by a factor of 10 ( $Pe = 10^4$ ), the mixing length of the SHM device amounts to 1.5 cm. A non-grooved channel will need 10 m for the same mixing task.

#### Axial dispersion

[M 74] [M 76] [P 66] Axial dispersion, an important parameter, e.g., in pressure-driven flows in liquid chromatography, is significantly reduced for the SHM-type

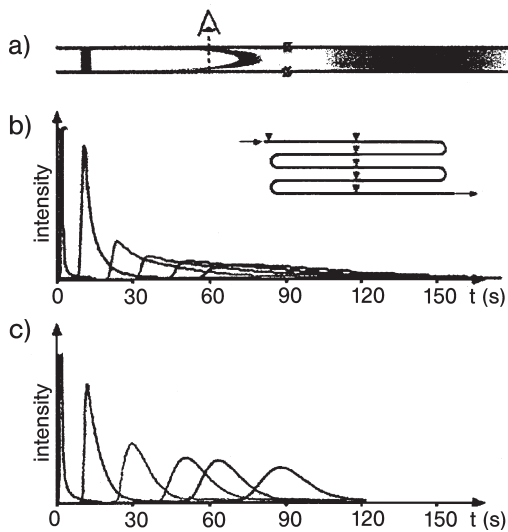


**Figure 1.161** Axial dispersion with and without SHM. (a) Schematic showing the dispersion of a plug in Poiseuille flow. (b) Unstirred Poiseuille flow in a non-grooved channel (depth,  $70\ \mu\text{m}$ ; width,  $200\ \mu\text{m}$ ;  $Pe \approx 10^4$ ). (c) Stirred Poiseuille flow in a staggered herringbone mixer (SHM) of the same design [44] (by courtesy of AAAS).

mixing as compared with non-grooved flows (see Figure 1.161) [44]. In addition, the dispersion curves for the non-grooved flow are notably asymmetric, which is due to a low-dispersed central flow and a highly dispersed flow close to the walls caused by shear forces. In contrast, the flow in the SHM device is initially asymmetric, but becomes symmetrical the more groove arrays are passed.

**Simulation of helical flows for channel with oblique ridges – relative transverse velocity** [M 74] [M 76] [P 66] The flow of a channel with a structured bottom wall with dimensions corresponding to the oblique-ridge structured channel examined experimentally [44, 45] was simulated. For the twisted, helical flow, the ratio of the average velocities in the  $y$ - and  $x$ -directions was calculated as function of the vertical position in the channel ( $z$ -coordinate). The relative transverse velocity exhibits an almost linear increase inside the grooves, a steep increase above the grooves, changes sign and flattens from about half the channel height to the top wall, there approaching a maximum. The maximum value of 0.052 yielded by the simulation is in good accord with the experimental result of 0.06 [44, 45].

**Simulation of helical flows for channel with oblique ridges – relative structure height** [M 76] [P 66] The relative structure height was varied from 0.01 to 0.76 [44]. The corresponding maximum relative transverse velocities calculated, i.e. the boundary values at the top, correspond well to the experimental values of  $\alpha$ . Also, good agreement between the numerical results and an analytical approximation was achieved.

### **Simulation of helical flows for channel with oblique ridges – single- and double-sided structured channels**

[M 76] [P 66] The relative transverse velocities of single- and double-sided structured channels were compared, each having oblique ridges [44]. For the double-sided structured channel, a symmetric curve with a point of reflection was obtained, as expected. Both curves almost coincide except for the regions close to the top of the channel. Owing to the correlation of the absolute transverse velocity and the increase in the interfacial area, an improved mixing performance when using double-sided structured channels can be predicted compared with solely single-sided channels.

This is also evident when considering the convective entanglement of two initially vertical liquid lamellae. For the double-sided structured channel, a considerable increase in the lamellae entanglement and an enlarged interfacial surface area are observed.

### **Simulation of helical flows for channel with oblique ridges – Reynolds number flow regime**

[M 76] [P 66] The relative transverse velocity depends only vaguely on the Reynolds number for oblique ridged channels [44]. This is surprising at first sight, since the absolute transverse velocity within the oblique ridges is considerably enhanced in this way.

### **Investigations on band broadening and mixing**

[No details on the mixer] [no protocol] The mixing of a fluorescent dye with a transparent solution was performed in a mixer with alternate arranged oblique ridges to obtain data on band broadening and mixing [158]. The ridges were manufactured by excimer-laser ablation in a polymer. Fluorescence intensity profiles were thus derived and compared with results obtained for an equivalent channel structure without the ridges and with theoretically derived perfect mixing. The measured profiles were close to the perfect mixing and very different from those obtained without ridge mixing, which resembled bi-laminated structures. Hence, the results are in line with the findings reported above.

#### 1.3.22

### **Chaotic Mixing by Twisted Surfaces**

#### **Most Relevant Citations**

Peer-reviewed journals: [46].

Chaotic particle motion can occur for two-dimensional velocity fields which are time dependent and for three-dimensional velocity fields [46]. For induction of such complex fields, one option is to guide the flow close to structured surfaces, e.g. placed on a channel's bottom, starting from a T-type flow inlet configurations.

#### **1.3.22.1 Mixer 79 [M 79]: Twisted Surface Micro Mixer**

Four T-type mixer designs were investigated which differ in the type of structuring of the mixing channel of the T-structure (see Figure 1.162) [46]. As a reference

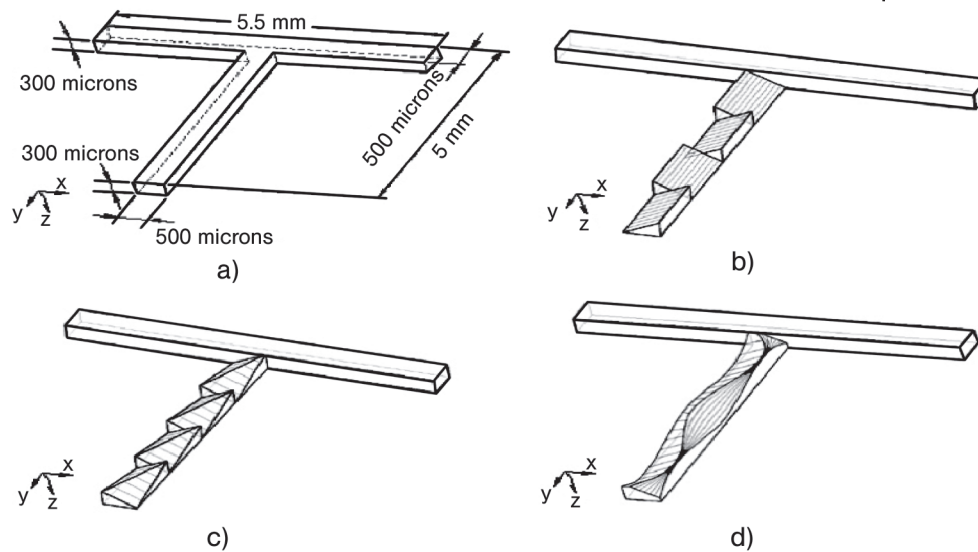


**Figure 1.162** Design of four T-type mixers, three of them containing twisted microstructured internals [46] (by courtesy of RSC).

case, a channel without any internals was used. Three mixer designs with twisted internals were developed, with inclined, oblique and wave-like structures on the channel's surface. The idea is that by interaction with the flow, chaotic regimes are induced passively. For this reason, the structures are arranged in an alternately periodic manner so that the flow repeatedly sways around the structures.

Mixer type	Twisted surface micro mixer	Feed channel width, depth, length	300 $\mu\text{m}$ , 500 $\mu\text{m}$ , 5.5 mm (whole T with two feeds)
Mixer material	Simulation study only Polymers such as PMMA and PDMS may be suitable	Mixing channel width, depth, length	300 $\mu\text{m}$ , 500 $\mu\text{m}$ , 5 mm

#### 1.3.22.2 Mixing Characterization Protocols/Simulation

[P 69] Gas mixing by diffusion and convection was investigated. Simulations were performed by CFD-ACE software on a personal computer [46]. The finite-element method and three-dimensional unstructured grids were used for solving the governing equations, which are the continuity equation, momentum conservation (Navier–Stokes) equations and species convection–diffusion equation. Laminar flow and adiabatic conditions were assumed. The SIMPLEC method was adopted for pressure–velocity coupling. The total number of elements ranged from 9000 to 16 000 depending on the complexity of the internal structure investigated.

### 1.3.22.3 Typical Results

#### Mixing mechanism – diffusion vs. convection

[M 79] [P 69] By calculation of the Peclet number ( $Pe$ ), the ratio of mass transport by convection relative to diffusion was analyzed [46]. For the range of velocities investigated ( $0.5\text{--}2.5\text{ m s}^{-1}$ ),  $Pe$  values  $> 2$  were found, which is indicative of the dominance of convection for all simulations carried out that are described below. For instance,  $Pe = 6.75$  is obtained for a velocity of  $0.5\text{ m s}^{-1}$ .

#### T-type mixing without internals – impact of velocity

[M 79] [P 69] Mass contour fraction plots within the T-type mixer design for oxygen mixing at different inlet velocities were calculated [46]. At an inlet velocity of  $0.5\text{ m s}^{-1}$ , mixing is completed after about two-thirds of the flow passage. Only a low degree of mixing, and virtually bi-laminated streams, are found for an inlet velocity of  $2.5\text{ m s}^{-1}$ .

#### T-type mixing with internals – mass contour fractions

[M 79] [P 69] Mass contour fraction plots were simulated for gas mixing in three T-type mixer designs with internals (four sub-sections) at an inlet velocity of  $2.0\text{ m s}^{-1}$  [46]. It turned out that the inclined design gave the best results.

A mixing length of 5.64 mm for 99% mixing was found for the inclined mixer, whereas a length of 7.90 mm was required for an unstructured channel [46]. Hence a positive effect for enhancing mixing is given, albeit the absolute magnitude is not very large, being of the order of 30%.

This is in line with tracks of the fluid flow giving the sway of the flow [46]. The largest amplitude is given for the inclined mixer, hence ‘disturbing’ to the largest extent the flow which is expected to result in improved mixing.

#### Mixing with the inclined mixer with various sub-sections – mass contour fractions

[M 79] [P 69] Mass contour fraction plots were simulated for gas mixing in the inclined T-type mixer design with various numbers of sub-sections (2–12) at an inlet velocity of  $2.0\text{ m s}^{-1}$  and at a fixed mixing channel length of 4.5 mm [46]. A plot of the mixing length (for 99% mixing) as a function of the number of sub-sections exhibits a minimum-type dependence (see Table 1.7). The fastest mixing

**Table 1.7** Calculated mixing lengths for the inclined mixer with different numbers of sub-sections (at an inlet velocity of  $2.0\text{ m s}^{-1}$ ) [46].

<i>Number of sub-sections at fixed length of 4.5 mm</i>	<i>Length per section (mm)</i>	<i>Mixing length (mm)</i>
2	2.2500	6.44
4	1.1250	5.62
6	0.7500	5.46
8	0.5625	5.64
10	0.4500	5.71
12	0.3750	6.26

is obtained for 6 sub-sections. The difference in mixing lengths between the best and the worst structures amounts to about 15%. For more than six sub-sections, the structures obviously stand too close to have an impact on the flow, i.e. the structuring does not result in swaying any longer.

### 1.3.23

#### Chaotic Mixing by Barrier and Groove Integration

##### Most Relevant Citations

Peer-reviewed journals: [3, 58].

The ‘chaos screw’ is a mixing device developed for chaotic mixing for polymer extrusion processes [58]. The channel for the molten polymer is defined by the interstice between the extruder shell and the screw root, two adjacent flights, and a barrel wall, similar to a flight, but of smaller height. The device has macroscopic dimensions and operates at  $Re \ll 1$ . The barriers are so placed that barrier-free zones are followed by barrier-containing zones; the flow field consequently changes. By use of the barrier structures, a hyperbolic point is caused in the flow field. The flow field changes depending on the location along the down-channel direction in an alternating manner, creating chaotic flow.

Based on these considerations, a planar version of the ‘chaos screw’ was designed with micron-sized dimensions, the barrier embedded micro mixer [3, 58].

##### 1.3.23.1 Mixer 80 [M 80]: Barrier-embedded Micro Mixer with Slanted Grooves

In this barrier-embedded micro mixer, oblique grooves, placed at the channel's floor, and barrier structures at the channel ceiling replace the flights and barriers of the ‘chaos screw’ [58]. The placement of the structures, however, is not essential for the functions. The positions at the floor and ceilings may change without loss of performance; two-sided structures are expected to exhibit improved mixing over single-sided structures. The barriers are placed periodically so that barrier-free zones intersect.

In the no-barrier zone, the cross-sectional flow field helical flow is induced by the grooves and shows non-linear rotation with only one elliptic point [58]. In the barrier zone, a spatially periodic perturbation on the helical flow is imposed and thereby two co-rotating flows form, characterized by a hyperbolic point and two elliptic points. By periodic change of the two flow fields, a chaotic flow can be generated.

This passive chaotic mixing concept is achieved with only minor modification of the flow channel, i.e. placement of only small obstacles, so that a low pressure loss for a given mixing task is expected [58].

The flow field of the barrier-embedded micro mixer has one hyperbolic point which considerably increases the specific interfacial fluid area, leading to rapid mixing by stretching and folding [58]. This is different to the staggered herringbone micro mixer with oblique grooves changing alternately the angle of tilting. Here, counter-rotating flows having one parabolic point with a lesser degree of interfacial area gain.

The mixer is composed of two plates. Two SU-8 masters were fabricated by conventional photolithography: one for the bottom channel with the slanted grooves by two-step photolithography and the other for the top with the barrier structures by one-step photolithography [58]. The photolithographic processes can be made simpler when both grooves and barriers are put on the bottom plate. To prevent irreversible bonding of the PDMS replicas, having plasma-oxygen treated surfaces, before proper alignment, methanol was used as a surfactant.

Mixer type	Barrier-embedded micro mixer with slanted grooves	Groove tilt angle	45°
Mixer material	Polydimethylsiloxane	Mixing channel width, depth, length	240 μm, 60 μm, 21 mm
Groove depth, length	100 μm, 9 μm	Barrier width, height	30 μm, 40 μm

For comparison, a simply slanted grooved micro channel (without barriers) and a T-shaped channel (without grooves and barriers) were fabricated using the same technologies, but with fewer steps for the photolithography [58].

#### 1.3.23.2 Mixer 81 [M 81]: Barrier-embedded Micro Mixer with Helical Elements

This barrier-embedded micro mixer was made with helical static elements, resembling the internals of a Kenics mixer, and barrier structures at the channel ceiling [3].

Fluid flow through macroscopic helical static elements (see, e.g., [4, 64] for static mixers) has been well studied by many groups (see, e.g., [155]). In previous studies miniaturized helical elements (without barriers) were realized [2]. Here, their mixing performance was inferior to that with intersecting static elements, resembling Sulzer packings. However, the latter reduced considerably the throughput by high-pressure drop. Hence, it was envisaged to develop a mixer with helical static mixing elements with good mixing efficiency and reasonable throughput. For this reason, the helical elements were equipped with barriers.

Mixer type	Barrier-embedded micro mixer with helical elements	Number of helical elements	6
Mixer material	Photopolymer resin SL-5410	Number of barriers per helical element	2
Total number of layers for the stereolithography	272	Mixing channel diameter, length	1 mm, 9.4 mm
Layer thickness mixer part	40 μm	Barrier thickness, height, length	100 μm, 150 μm, 413 μm
Helical element thickness, length	100 μm, ~1.64 mm	Cross-section of square inlets	1000 μm × 1000 μm

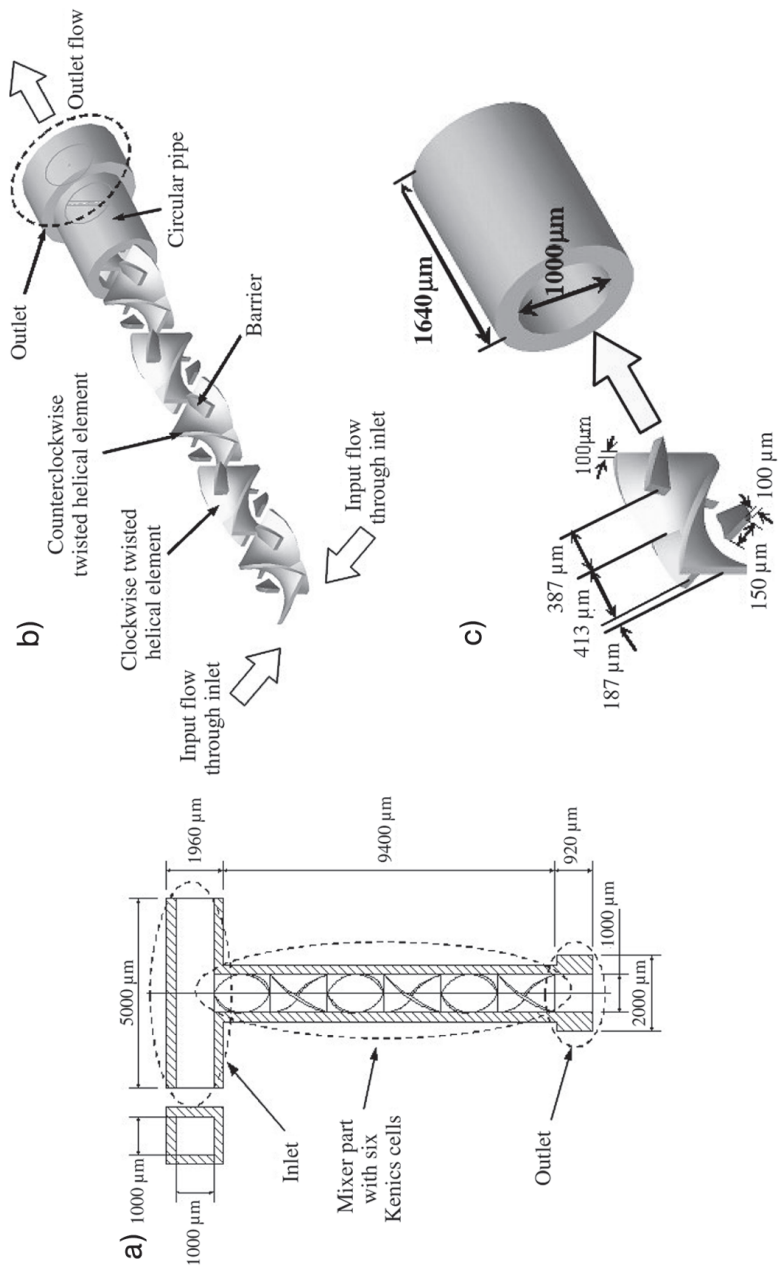


**Figure 1.163** Schematics of (a) the top view of the Kenics micro mixer with detailed dimensions, (b) the 3-D view of the barrier-embedded micro mixer and (c) the 3-D view of one mixing element with detailed dimensions [3] (by courtesy of IOP Publishing Ltd.).

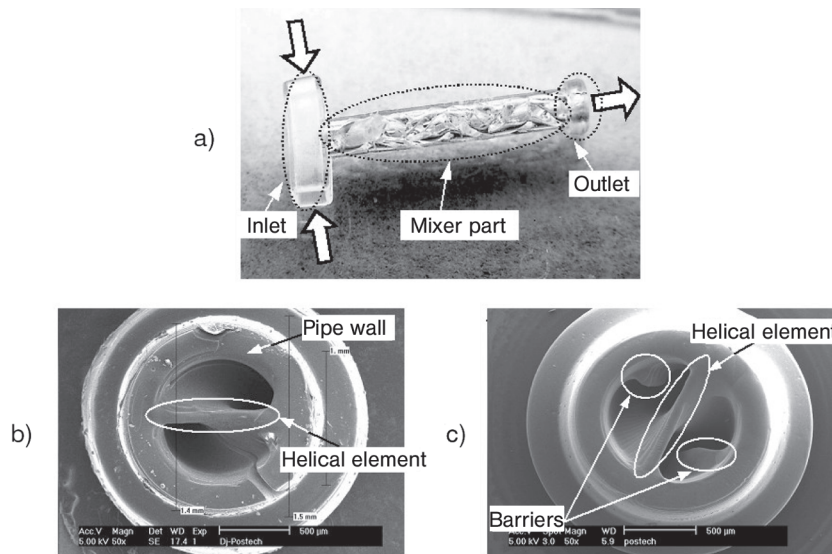


**Figure 1.164** (a) Complete view of the barrier-embedded helical micro mixer; (b) Kenics cell with a helical element only; (c) Kenics cell with a helical element and two barriers [3] (by courtesy of IOP Publishing Ltd.).

The static elements were internals of a circular T-pipe. The mixer realized had Kenics cells with helical elements twisted by  $180^\circ$ , giving a fully 3-D structure (see Figure 1.163) [3]. Two barriers were placed on the wall of the pipe. Counterclockwise- and clockwise-rotated helical elements were alternately arranged. Four barriers were introduced in the pipe wall in each Kenics cell. For comparison, pipes with only helical elements (no barriers) and empty pipes (no internals) were also fabricated.

Microfabrication was achieved by micro-stereolithography using a CW  $\text{Ar}^+$  laser (see Figure 1.164) [3].

#### 1.3.23.3 Mixing Characterization Protocols/Simulation

[P 70] The mixing performance along the channel length was characterized by a pH-indicator reaction using phenolphthalein ( $0.31 \text{ mol l}^{-1}$ ) and NaOH ( $0.33 \text{ mol l}^{-1}$ ) in 99% ethanol solution [58]. Images were taken using a stereoscopic microscope and a graphic grabber system. A white lamp served as illumination system.

As a second imaging approach, confocal laser scanning microscopy was applied to monitor the cross-sectional mixing of Rhodamine B solutions (99% ethanol) and pure 99% ethanol [58]. Laser scanning over the entire cross-sectional area was performed and at various locations along the channel.

#### 1.3.23.4 Typical Results

##### Reaction imaging of mixing along the channel passage

[M 80] [P 70] The mixing performance of three mixing devices was characterized by a pH-indicator reaction using phenolphthalein: a T-channel, slanted grooved

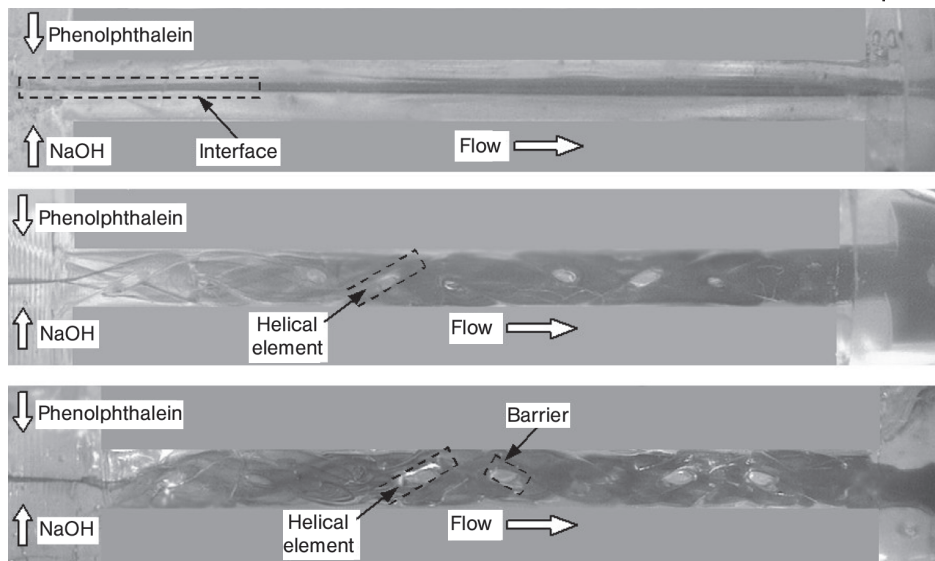


**Figure 1.165** Images of the color formation as measure for mixing using a reactive visualization approach. (a) Circular pipe; (b) helical micro mixer; (c) barrier-embedded helical micro mixer [3] (by courtesy of IOP Publishing Ltd.).

and barrier-embedded micro mixer [58]. The color formation of the indicator was imaged at three locations, referring to the start of contacting the solutions, the center of the mixing channel and its end.

The T-shaped mixer yields color formation only at the interface of the bi-laminated flow which becomes clearly visible at about half the channel length [58]. The other two mixers show already at the beginning of the channel notable mixing, which then results in a fairly homogeneous color after half of the channel passage (which does not necessarily mean approaching 100% mixing). From direct visual observation, albeit not evident in the images, it is stated that the barrier-embedded micro mixer has a deeper color formation than the slanted grooved one, i.e. potentially may have a higher degree of mixing.

[M 81] [P 70] A microscopy-image analysis of the color formation due to a reactive approach reveals that the micro mixer with helical elements and barriers gives a better performance than the micro mixer with helical elements but without barriers and a reference pipe structure without either helical elements or barriers (see Figure 1.167) [3]. The pipe gives the expected profile with two colorless fluid compartments on top and at bottom, separated by a colored interface. This is indicative of the absence of any swirling, secondary flow.

#### Quantification of the degree of mixing

[M 80] [P 70] The intensity of the color in the channel was monitored for quantitative analysis of the degree of mixing [58]. Images were taken over 11 regions and a normalized intensity was derived.

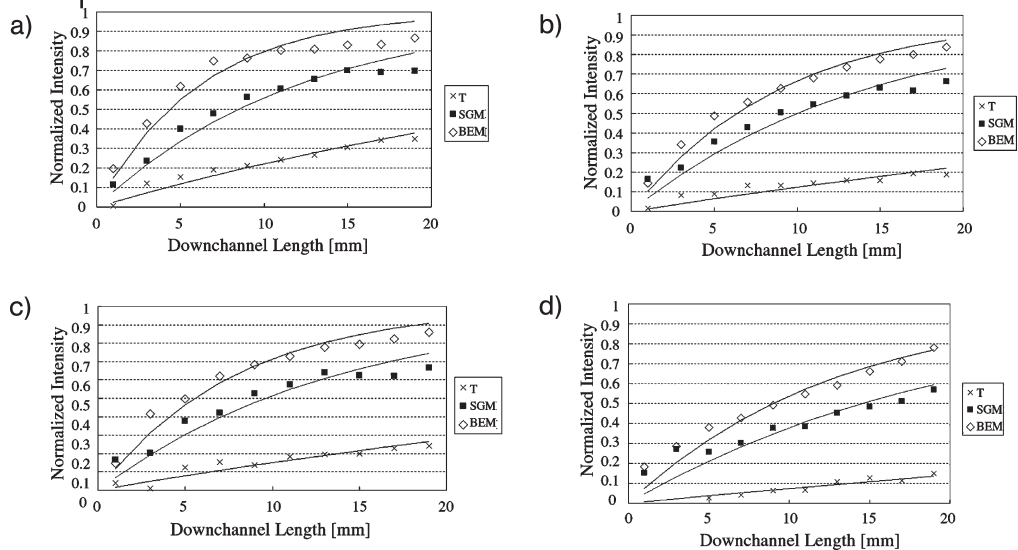


**Figure 1.166** Normalized average intensity changes along the down-channel direction of three micro-mixer devices with barrier-embedded, slanted grooved and T-channel structures at (a)  $Re = 0.228$ , (b)  $0.457$ , (c)  $0.685$  and (d)  $2.28$  [58] (by courtesy of IOP Publishing Ltd.).

A plot of the normalized intensity versus the down-channel length clearly shows that the mixing efficiencies of the devices have the following sequence: barrier embedded mixer > slanted grooved mixer >> T-channel mixer (see Figure 1.166) [58]. When operating at larger Reynolds numbers (up to 2.28), the residence time is decreased, since operation is done at constant length. Hence, the measured mixing performances are lower compared with the initial experiment at  $Re = 0.228$ . The relative degree of mixing performance is lower for the T-channel mixer than for the other two grooved mixers. In the latter case, the helical flow circulation is intensified at higher  $Re$ , partly compensating the effect of the reduction of the residence time.

[M 81] [P 70] A plot of the normalized intensity versus the down-channel length clearly shows that the mixing efficiencies of the devices have the following sequence: barrier-embedded helical mixer > helical mixer >> pipe mixer (see also Figure 1.165) [3]. The relative degree of mixing performance is lower for the pipe mixer than for the other two helical mixers. This is most evident for the three plots with  $Re \geq 13.96$ .

#### Cost for enhancing mixing performance by barrier structures

[M 80] [P 70] From prior experience with the ‘chaotic screw’ extruder, it was estimated that the presence of the barrier structures in the barrier-embedded mixer accounts for about a 10% reduction in flow rate as compared with the slanted grooved mixer [58]. Thus, a large mixing improvement is given at the cost of only a small reduction in flow rate.

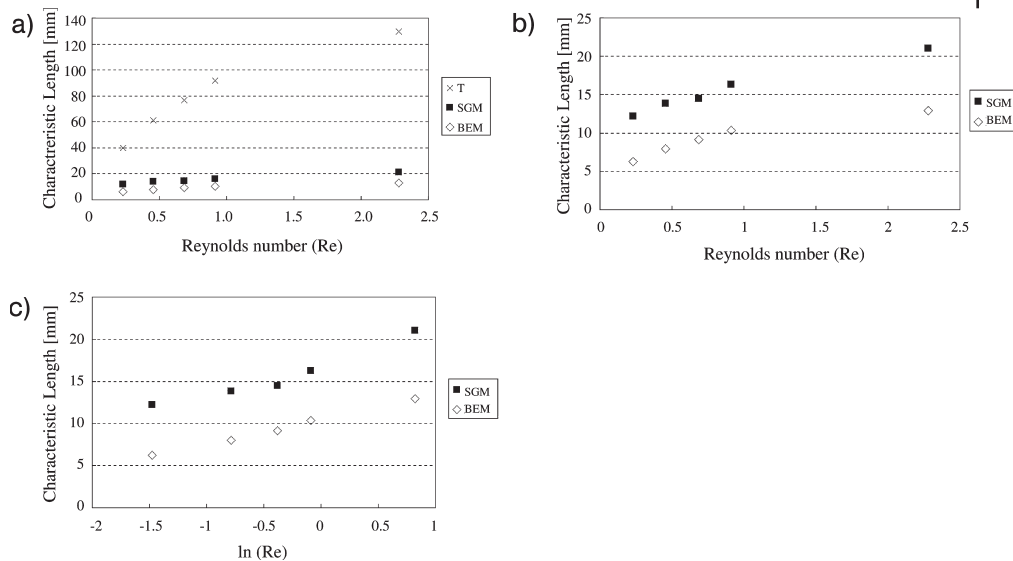


**Figure 1.167** (a) Characteristic mixing length of all three micro devices and (b) detailed view of the mixing length of the barrier embedded and slanted grooved micro mixers only, as a function of the flow regime. (c)  $\ln(Re)$  plot of the latter data set [58] (by courtesy of IOP Publishing Ltd.).

#### Characteristic mixing length

[M 80] [P 70] A characteristic mixing length was defined [58]. Such a mixing length is two times shorter for the barrier-embedded mixer than the slanted grooved mixer for the whole flow range observed (see Figure 1.167). The mixing length is about 4–10 times shorter than for the T-channel mixer. The T-device exhibits a strong increase in the mixing length with increasing  $Re$ , as this means a reduction in the residence time. The slanted grooved and barrier-embedded mixers, in contrast, exhibit only a slightly increasing mixing length for  $Re$  ranging from 0.228 to 2.28. Actually, a logarithmic increase in mixing length with  $Re$  is observed.

[M 81] [P 70] The characteristic mixing length is much shorter for the barrier-embedded helical mixer and the helical mixer than the pipe mixer [3]. The barrier-embedded helical mixer is slightly better than the helical mixer; hence, the effect of the barriers is evident, albeit not strong. The characteristic mixing length of 2–3 mm of the barrier-embedded helical mixer increases only slightly Reynolds numbers ranging from 7 to 28.

#### Cross-sectional mixing

[M 80] [P 70] Cross-sectional images of the flow patterns, gained by confocal microscopy, demonstrate the interfacial stretching and hence are indicative of mixing in the barrier-embedded mixer [58]. At the non-barrier entrance structure clearly the helical flow induced by the slanted grooves is evident. In the barrier

section, the flow rotation is further clearly improved. At the exit the image is homogeneous, which is indicative of at least large fluid segregation, if not demonstrating completion of mixing.

### 1.3.24

#### Distributive Mixing by Cross-sectional Confining and Enlargement

##### Most Relevant Citations

Proceedings contributions: [159].

The mixer discussed below is part of a ferrofluidic microsystem [159]. Ferrofluids can be used for fluid displacement by magnetic action using an external permanent magnet source. Ferrofluids are superparamagnetic liquids.

##### 1.3.24.1 Mixer 82 [M 82]: Distributive Micro Mixer with Varying Flow Restriction

Two micro mixer designs were developed, both containing confining and expanding structures for distributive mixing by interface enlargement [159]. The confining and expanding structure can be the micro channel itself, which repeatedly changes its cross-section or internals such as columns which are flow obstacles.

The first design has a slightly curved serpentine channel comprising square columns. The second design is an arrow-shaped channel [159]. Circular holes, two before and one after the mixing channel, serve as fluid reservoirs for both designs.

The mixers were fabricated by deep reactive ion etching (DRIE) into silicon [159]. The silicon structure was anodically bonded to a glass wafer.

Mixer type	Distributive micro mixer with varying flow restriction	Mixing channel width, depth, length	1000 $\mu\text{m}$ , 30 $\mu\text{m}$ , ~8 mm
Mixer material	Silicon	Feed channel width, depth	400 $\mu\text{m}$ , 30 $\mu\text{m}$
Top plate material	Glass	Reservoir diameter (fluids to be mixed)	1.5 mm
Top plate thickness	0.5 mm	Reservoir diameter (mixed fluids)	2 mm

##### 1.3.24.2 Mixing Characterization Protocols/Simulation

[P 71] For fluid transport, ferrofluid magnetic displacement by using a commercial hydrocarbon-based ferrofluid was applied [159]. This fluid is compatible with several aqueous dyed solutions. Miniature permanent magnets were used.

The mixing of dyed fluids was observed by microscopy [159].

##### 1.3.24.3 Typical Results

###### Mixing pattern observation

[M 82] [P 71] Observations on the course of mixing for two mixer designs were made by imaging the complete channel with flow-confining structures [159]. The

solutions to be mixed are moved by ferrofluid displacement using an external magnet. No details were given; only the finding of the onset of mixing was stated.

### 1.3.25

#### Time-pulsing Mixing

##### Most Relevant Citations

Peer-reviewed journals: [26]; proceedings contributions: [48].

Time pulsing can be achieved by simply varying the flow rates of the streams in two inlets of a mixer [26] or by using more intricate flow structures such as the superposition of unsteady cross-flow injection and a steady flow in a main channel [48].

By simply varying the flow rates in the inlet channels periodically with time, mixing can be enhanced, without any need for further moving parts or complex fluid architectures (see Figure 1.168) [26]. A low-frequency sinusoidal flow rate is superimposed upon a steady flow rate. For steady-state inlet velocities of  $1.0 \text{ mm s}^{-1}$ , time-dependent inlet velocities of the form  $1.0 + 7.5 \sin(5 \cdot 2 \pi t) \text{ mm s}^{-1}$  were used, where  $t$  is being the time.

Time pulsing can be characterized by the Strouhal number ( $St$ ), which is a dimensionless parameter describing the ratio of the flow characteristic time scale ( $L/V$ ) to the pulse time period ( $1/f$ ) [Eq. (1.8)] [26], where  $L$  is the hydraulic diameter,  $V$  the average velocity in the outlet channel and  $f$  the pulsing frequency. For a pulsing frequency of 5 Hz, a Strouhal number of 0.375 derives.

$$St = (fL) / V = (L/V) / (1/f) \quad (1.9)$$

Another paper describes the stretching and folding of material lines yielded by simulation and experimental imaging, induced by time-pulsing mixing via unsteady cross-flow injection in a steady-flow main channel [48].

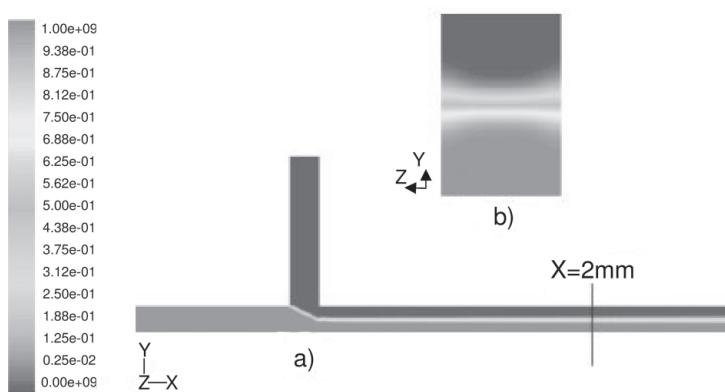


**Figure 1.168** Inlet mean velocity as a function of time in the control case (dashed line) and in the biased sinusoidal pulsing case (solid line) [26] (by courtesy of RSC).

### 1.3.25.1 Mixer 83 [M 83]: Time-pulsing Cross-flow Micro Mixer (I)

[M 83] This time-pulsing device comprises a cross-flow channel arrangement with three channel branches, specifically consisting of one main channel on to which a perpendicular channel is so attached that a smaller part of the main channel serves as inlet and the larger residual part is the mixing flow-through chamber [26]. The perpendicular channel then has the function of a second inlet. Both the inlet and outlet channels have the same size. These dimensions were assumed to be typical for many  $\mu$ TAS applications and are also thought to be amenable to mass production, e.g. by means of injection molding. Furthermore, devices made in this way can be fed by pumping, both mechanically and electrically. Both options can undergo periodic switching of the feed flows.

A numerically controlled mill fabricated trenches and through holes at the ends of the trenches in a thin, colorless, polyacrylic acid plate [26]. This thin plate was bonded to a more rigid, transparent polycarbonate base plate with UV-curing optical adhesive. The through holes in the plate were connected to holes in the base plate, thereby forming one conduit. The latter holes did not penetrate the base plate, but rather were connected to cross-type arranged borings. Thereby, fluid connections could be attached to the side of the base plate.

A glass cover slip bonded to the acrylic plate enclosed the trenches, forming in this way the micro channels [26]. (18 and 25 gage) Syringe needles were light press fitted into these cross-holes. Bonding the joints with epoxy ensured good seals and mechanical integrity.

Mixer type	Time pulsing cross-flow mixer	Channel width, depth	200 $\mu$ m, 120 $\mu$ m
Mixer material	Polyacrylic acid/glass	Channel length before, after confluence	1.25 mm, 3 mm

### 1.3.25.2 Mixer 84 [M 84]: Time-pulsing Cross-flow Micro Mixer (II)

This device consists simply of a T-type junction where two pressure-driven flows are contacted (see Figure 1.169) [48]. After a short passage, such a bi-laminated stream is exposed to injections from both sides by adjacent channels, which yields a cross-flow configuration. From there on, the injected flow passes a long main channel and finally reaches a reservoir.

The switching-on of the transverse flow leads to bending of the material line when the flow passes the intersection at the cross-flow configuration (see Figure 1.170) [48]. After switching off of the transverse flow, folding of the material line takes place owing to the parabolic flow profile. This enhances the interfacial area and speeds up mixing, in a traditional way. Moreover, chaotic flow can be achieved by multiple repetition of the transverse injection structures and hence multiple stretching and folding.

The micro mixer was fabricated from two plates by standard MEMS technology, using deep reactive ion etching (DRIE) [48]. Anodic bonding is used for sealing the plates.

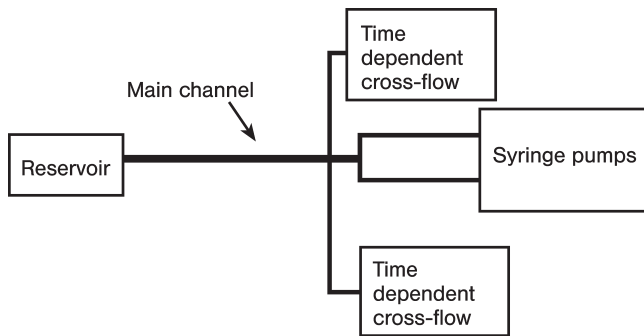


Figure 1.169 Schematic of the time pulsing cross-flow mixer [48].

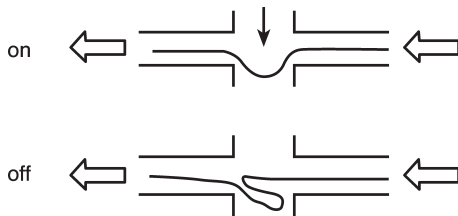


Figure 1.170 Schematic of the working principle of the mixer: stretching and folding of material lines are achieved by periodic perturbation of the main flow with adjacent flows [48] (by courtesy of Springer-Verlag).

Mixer type	Time pulsing cross-flow mixer	Top plate	Pyrex
Mixer material	Silicon		

No details on the dimensions of the mixer are given [48].

### 1.3.25.3 Mixing Characterization Protocols/Simulation

[P 72] Detailed simulations and two feasibility experiments were carried out [26].

For both the simulations and the experiments, aqueous solutions were fed at room temperature with a time-averaged mean velocity of  $1.0 \text{ mm s}^{-1}$  ( $Re = 0.3$ ) [26]. For reasons of simplicity, the same solutions were fed through both inlets for the simulations. In the experiments, a dye dissolved in water was mixed with pure water; the nature of the dye was not disclosed. Mass fractions were recorded. From this the weighted standard deviation was calculated, giving the degree of mixing when being normalized by an average value of the mass fraction (for the exact definitions see [26]).

The kinematic viscosity considered in the simulations was that of water. Here, as diffusion constant  $D$  a value of  $10^{-10} \text{ m}^2 \text{ s}^{-1}$ , a typical value for diffusion of small proteins in aqueous solutions, was taken.

The modeling considered 1.25 mm of the channel before the confluence and 3 mm of the channel after the confluence with a plane of symmetry at half the channel depth. The computational domain was discretized with structured hexahedral meshes, the size of the cells being  $10 \text{ }\mu\text{m}$  long. Diffusion was modeled.

Tests were conducted with peristaltic pumps [26]. Two signals from  $-1.2$  to  $+1.2$  V DC control the pumping from maximum reverse to maximum forward flow. The control signal comes from the center taps of potentiometers used as voltage dividers. A function generator sends a sinusoidal signal to one end of both voltage dividers and a power supply fixes the other ends of the voltage dividers to specified voltages. Mixing is observed using a standard microscope and images were taken on a color video camera.

[P 73] Syringe pumps were used for the liquid feed of the main and adjacent streams [48]. The injection flow was provided by a sinusoidal mode.

Sucrose or glycerol solutions were contacted with the same solutions containing a fluorescent tracer [48]. Both streams were fed with the same flow rate. Fluorescence microscopy was used for flow monitoring.

A two-dimensional kinematic simulation was performed, assuming Pouseuille flow in both the main and adjacent channels.

#### 1.3.25.4 Typical Results

##### Constant flow rate for both inlets

[M 83] [P 72] When contacting two feeds in the cross-flow mixers with constant inlet flow rates of  $1.0 \text{ mm s}^{-1}$ , a tri-lamellae flow pattern is generated, as expected ( $Re = 0.3$ ) [26]. Two broader outer lamellae are found separated by a thin, diffuse layer. Both lamellae remain totally unchanged, i.e. contain only the material which they originally possessed, and are thus unmixed.

At the interface a small diffusive region exists where mixing takes place. This region is broader on the top and bottom of the channel, i.e. is smallest at half channel height. This is due to the higher velocity in the center of the channel, reducing the residence time.

The overall degree of mixing for the whole channel is therefore low, being limited to only 12% [26]

##### Increase in constant flow rate for both inlets

[M 83] [P 72] On increasing the constant inlet flow rate from  $1.0$  to  $8.5 \text{ mm s}^{-1}$  (from  $Re = 0.3$  to  $2.55$ ), a tri-lamellae flow pattern is again generated [26]. Mixing here is even decreased compared with the  $1.0 \text{ mm s}^{-1}$  case, since residence time is reduced and only diffusion takes place. The degree of mixing is 8% in absolute terms, hence is 34% less than in the  $1.0 \text{ mm s}^{-1}$  case.

The flow rate of  $8.5 \text{ mm s}^{-1}$  corresponds to the maximum flow rate induced by period switching of the flow [26].

##### Pulsed flow for the perpendicular inlet

[M 83] [P 72] The inlet flow rate in one feed channel was set constant at  $1.0 \text{ mm s}^{-1}$  and the flow rate of the other inlet was varied periodically in time with  $1.0 + 7.5 \sin(5 \cdot 2 \pi t) \text{ mm s}^{-1}$  [26]. The flow pattern is again of tri-lamellae type with two outer unmixed and an inner diffuse, mixed layers; however, the diffuse mixed zone is now much larger than in the constant flow case (see Figure 1.171 and *Constant flow rate for both inlets*).

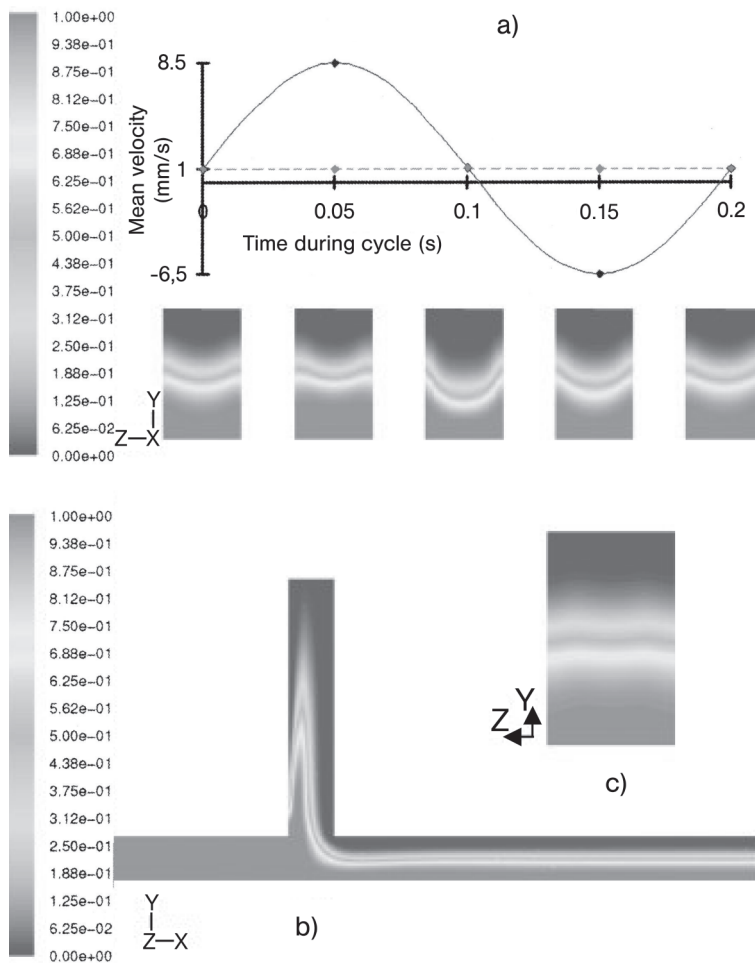


**Figure 1.171** Numerical simulation results obtained with a pulsed flow from the perpendicular inlet. (a) Mean velocity as a function of time in the inlet (dashed line) and in the perpendicular inlet (solid line). Contour levels of the mass fraction of one liquid in the YZ-plane cross-section taken 0.25 mm downstream of the confluence at various times marked on the previous curves are also given. (b) Contour levels of the mass fraction of one liquid in the XY-plane at half the channel depth at the first time in the cycle shown in (a). The channels in (b) are clipped short in the X-direction for more compact stacking. (c) Contour levels of the mass fraction of one liquid in the YZ-plane cross-section taken 2 mm downstream of the confluence at the first time shown in (a) [26] (by courtesy of RSC).

As a consequence of the time pulsing of one inlet flow rate, one of the feed lamellae and the diffuse zone penetrate also the inlet region of the other fluid, i.e. generating a tri-lamellae peak here. The diffuse interface is now no longer symmetric with regard to the channel width (as for constant flows), but is curved and changes with time. Thereby, material transport is done, the diffuse zone becomes broader

and mixing is enhanced. The degree of mixing is now 22%, being 79% larger than for constant flows. As expected, the degree of curvature of the interface is largest near the point of confluence, e.g. as images taken at 0.25 mm evidence, and becomes small downstream. At a 2.0 mm distance from the point of confluence, nearly no time-dependent behavior can be observed any longer.

If twice the amplitude is taken, the degree is unchanged at 22% [26]. If the standard pulsing is done in a channel half as deep, the degree of mixing is again nearly unchanged, 21%.

#### Variation of amplitude of time pulsing

[M 83] [P 72] If the amplitude for time pulsing is doubled, the degree of mixing remains unchanged, being 22% in both cases [26]. The increase in amplitude amounts to a maximum flow rate of  $17.0 \text{ mm s}^{-1}$  instead of  $8.5 \text{ mm s}^{-1}$  used formerly.

#### Variation of channel depth

[M 83] [P 72] If the channel depth is halved at otherwise the same time pulsing conditions, the degree of mixing remains nearly unchanged, being 22 and 21% for full-channel and half-channel depth, respectively [26].

#### Pulsed flow from both inlets in-phase

[M 83] [P 72] When pulsing both inlet flow rates in-phase, the degree of mixing is only 19%, being 13% lower than for one-inlet-flow pulsing (see *Pulsed flow for the perpendicular inlet*) [26]. The two fluids are basically flowing side-by-side, albeit moved forwards and backwards. The interface is not stretched extensively by this action.

#### Pulsed flow from both inlets with 90° phase difference

[M 83] [P 72] When pulsing both inlet flow rates with a phase difference of 90° (amplitude and frequency being the same), the degree of mixing is notably increased to 59%, being more than doubled as compared with one-inlet-flow pulsing (see Figure 1.172 and *Pulsed flow for the perpendicular inlet*) [26]. One inlet flow is operated with  $1.0 + 7.5 \sin(5 \cdot 2 \pi t) \text{ mm s}^{-1}$  and the other with  $1.0 + 7.5 \sin(5 \cdot 2 \pi t + \pi/2) \text{ mm s}^{-1}$ .

The flow pattern is again of lamellae type with a much more pronounced degree of diffuse, mixed layers (see *Constant flow rate for both inlets*) [26]. As a consequence of the time pulsing of both inlet flow rates, both inlet streams also penetrate the other inlet region periodically. The diffuse interface is now twice folded, resulting in a mixed island deeply penetrating into the other liquid. Good mixing occurs already very close to the point of confluence and persists in the outlet channel.

#### Pulsed flow from both inlets with 180° phase difference

[M 83] [P 72] When pulsing both inlet flow rates with a phase difference of 180° (amplitude and frequency being the same), the degree of mixing is notably increased to 56%, being more than doubled compared with one-inlet-flow pulsing (see Figure 1.173 and *Pulsed flow for the perpendicular inlet*) [26]. One inlet flow is operated

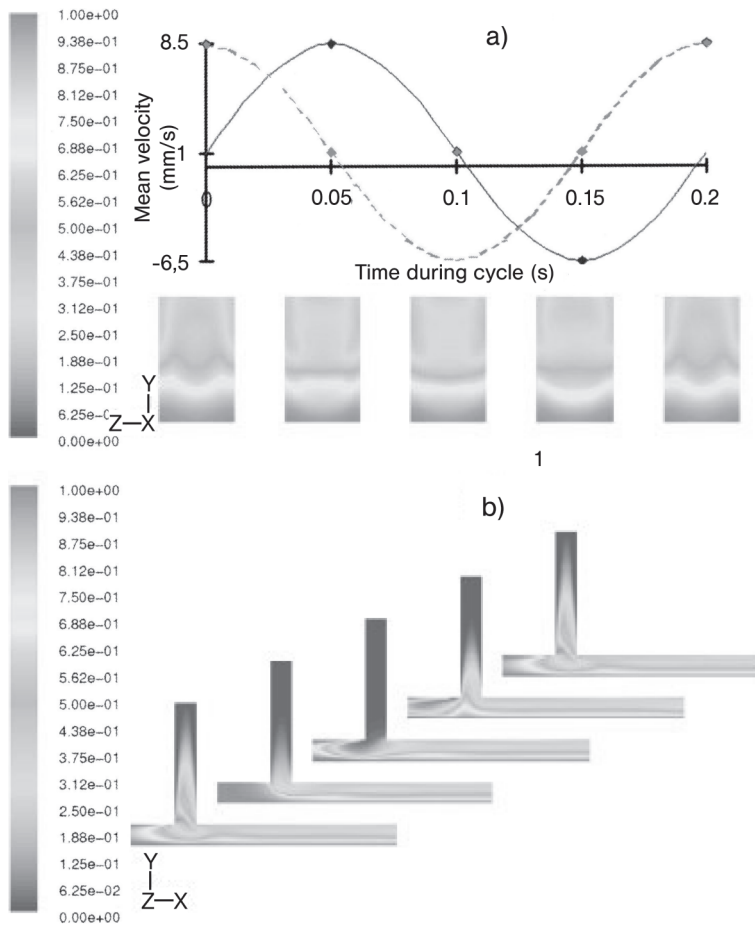


**Figure 1.172** Numerical simulation results obtained with a pulsed flow from both inlets, one flow being at  $90^\circ$  phase difference to the other. (a) Mean velocity as a function of time in the inlet (dashed line) and in the perpendicular inlet (solid line). Contour levels of the mass fraction of one liquid in the YZ-plane cross-section taken 0.25 mm downstream of the confluence at various times marked on the previous curves are also given. (b) Contour levels of the mass fraction of one liquid in the XY-plane at half the channel depth at the first time in the cycle shown in (a). The channels in (b) are clipped short in the X-direction for more compact stacking [26] (by courtesy of RSC).

with  $1.0 + 7.5 \sin(5 \cdot 2\pi t) \text{ mm s}^{-1}$  and the other with  $1.0 + 7.5 \sin(5 \cdot 2\pi t + \pi) \text{ mm s}^{-1}$ .

However, the mixing degree is not higher than for  $90^\circ$  phase pulsing, but actually slightly lower [26]. Nonetheless,  $180^\circ$  phase operation has distinct advantages. Only by this operation is a constant, time-invariant outlet flow achieved, which is important when the mixed flow has to enter a downstream microfluidic element.

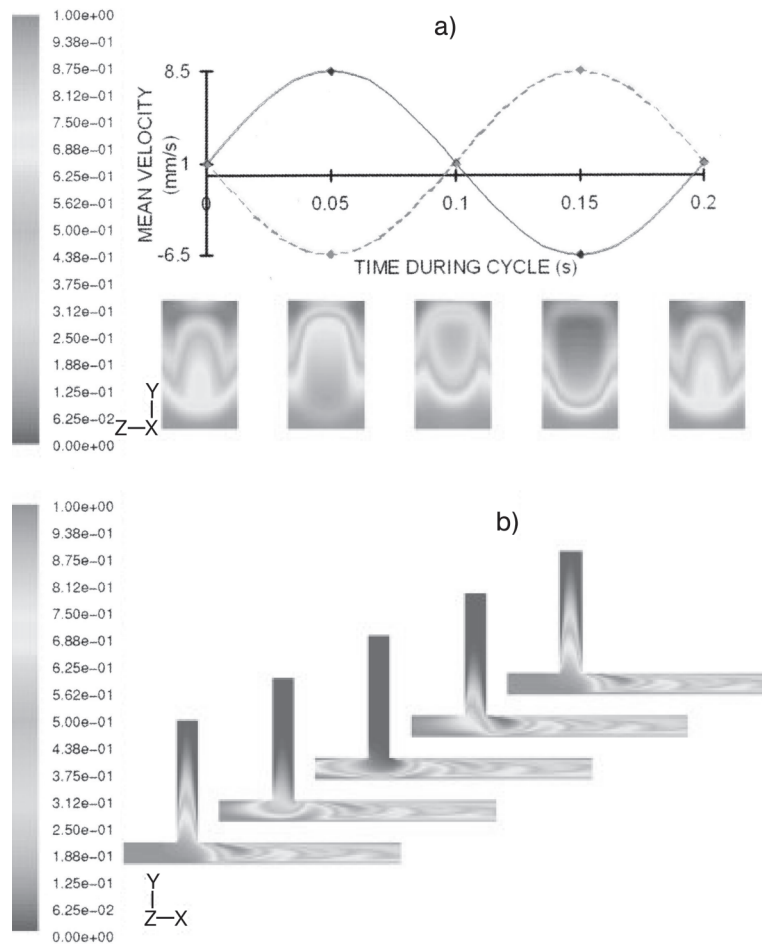


**Figure 1.173** Numerical simulation results obtained with a pulsed flow from both inlets, one flow being at  $180^\circ$  phase difference to the other. (a) Mean velocity as a function of time in the inlet (dashed line) and in the perpendicular inlet (solid line). Contour levels of the mass fraction of one liquid in the YZ-plane cross-section taken 0.25 mm downstream of the confluence at various times marked on the previous curves are also given. (b) Contour levels of the mass fraction of one liquid in the XY-plane at half the channel depth at the first time in the cycle shown in (a). The channels in (b) are clipped short in the X-direction for more compact stacking [26] (by courtesy of RSC).

Here, one does not desire variation of the flow rate, as this may affect the performance of this and further microfluidic elements downstream. The individual flow rates are time dependent; owing to their interrelationship the sum is a constant over time.

The flow pattern is no longer of lamellae type (see *Constant flow rate for both inlets*), but rather consists of alternate puffs of the two liquids [26]. Each puff has

the form of a hairpin-like structure, since it travels at the velocity of the flow, which depends on the distance from the center of the channel. In this way, hairpins become more elongated the more they travel downstream. The hairpins slowly dissipate as they travel downstream owing to diffusion. The diffuse interface is now significantly folded; the composition of the mixed island, however, varies with time, having a greater content of the one or the other liquid in a periodic manner.

#### **Pulsed flow from both inlets with irrational ratio of frequencies**

[M 83] [P 72] When pulsing both inlet flow rates with an irrational ratio of frequencies, a lesser degree of mixing of only 52% compared with the 90° phase time pulsing with the same frequency is obtained (mixing degree 56%) [26]. The different pulsing frequencies are sometimes undesirably close in phase, leading to reduced mixing. In a closed system (not a flow-through system), time pulsing at different frequencies may lead to a different situation, giving rise to improved results.

#### **Comparison experiment with numerical simulation results**

[M 83] [P 72] For constant flows at both inlets, the same lamellae-type flow pattern is found [26]. For time pulsing with 180° phase difference, the experimental image also roughly resembles the computer simulation. To have a realistic image made by the latter, several images taken at various depths of the channel were overlaid, since the experimental image consists of optical data gathered along the optical path which is parallel to the channel depth. In particular, the penetration of one liquid into the other is evident.

#### **Simulation of the bending of material lines**

[M 84] [P 73] Simulation were undertaken to reveal the impact of the perturbation amplitude on the material line folding [48]. At small amplitude, only weak oscillations are observed. With increasing perturbation, the oscillation amplitude becomes larger. At still larger amplitude, chaotic behavior is observed, correlated with multiple folding. An extremely convoluted periodic flow pattern is formed downstream, promoting mixing.

Intricate periodically bendt patterns result downstream in the main channel [48].

#### **Determination of the degree of chaoticity**

[M 84] [P 73] The degree of chaos was determined by calculating the Lyapunov exponent, a measure for material line stretching [48]. Within the parametric limits of the simulation study made, the highest Lyapunov exponent was 0.1. On adding a further adjacent channel, this parameter can be increased to 0.4.

#### **Experimental flow visualization**

[M 84] [P 73] The intricate periodically bendt patterns downstream in the main channel, predicted by the simulation, are confirmed by experimental flow visualization (see Figure 1.174) [48]. This is supported by the parabolic velocity profile along the channel, promoting convolute interface structures. The profiles flatten downstream.

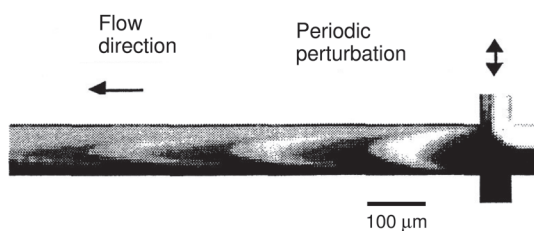


**Figure 1.174** Experimental image of the intricate, periodic flow patterns generated by the oscillating injection via adjacent channels into a main stream [48] (by courtesy of Springer-Verlag).

### 1.3.26

#### **Bimodal Intersecting Channel Mixing**

##### **Most Relevant Citations**

Peer-reviewed journals: [160, 161].

Capillary electrochromatography column (CEC) operation in the sub-15 nl volume range demands mixers that have an order of degree smaller internal volumes, i.e. a few hundred picoliters or less. The internal volumes of today's micro mixers are typically in the range of a few hundred nanoliters, and hence are not suitable. Therefore, a new mixing concept was developed that was oriented on regular packed-bed mixing (see Figure 1.175) [160]. Here, the goal is to achieve transverse mixing along the flow path of fluids flowing around the obstacles. Highly regular micro-machined packed beds can also be realized; however, it still seems problematic to achieve sufficient transverse mass transfer. This is particularly due to heterogeneities in the flow path of existing packed beds. An improvement in this situation was seen in promoting convection streams by so-called trans-channel coupling, which means the deliberate formation of voids in the packed bed which are due to convective transport besides the diffusive transport that occurs in the interstices of the packed bed's objects. These voids are naturally not located linearly downstream (as otherwise all the flow will take this option), but should meander along the residual packed-bed volume. In this way, a main stream is split repeatedly into smaller side streams, which after passage merge again with the main stream.

The bimodal intersecting channel micro mixer is the micromachined version of such a packed-bed-with-voids approach (see Figure 1.175) [160]. It has two types of channels, larger ones for the main convective transport and many smaller ones for decreasing the diffusion path so that efficient mixing can take place (see Figure 1.176). Liquid transport generally is achieved by electroosmotic flow (EOF) action. In the course of the flow, many repeated sequences of flow splitting and recombination are given. The mixer has two domains with micro channels of very different hydraulic diameter, thus being *bimodal*, which *intersect* and of different mixing mechanism; some regions are dominated by EOF transport and diffusive mixing (large channels), others are ruled by convective transport (small channels).

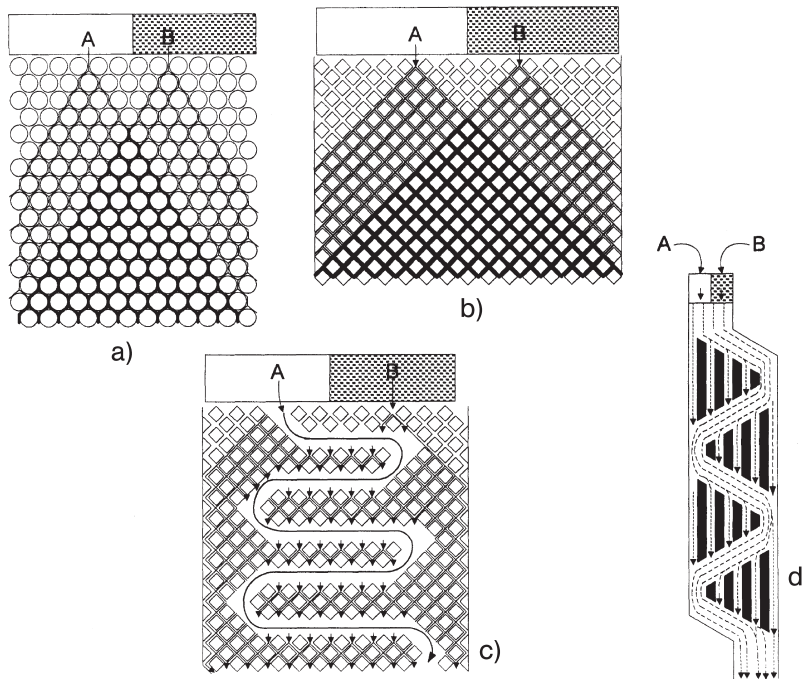


**Figure 1.175** (a) 2-D image of a packed bed composed of densely packed spherical particles. Two confluent liquid streams (A and B) are injected at distant points on top of the packed bed and move statistically downwards. At a certain point they merge and mixing takes place by diffusion at constantly recreated and renewed interfaces. (b) A similar flow arrangement with square bed objects; however, this time a micromachined packed bed is shown. (c) Artificial new structure of a packed bed where some objects of the packed bed have been removed. Now, flow conduits exist which are intended to promote lateral mixing. (d) Bimodal intersecting channel micro mixer, which is a micromachined design resembling the idea depicted in (C) [160] (by courtesy of ACS).

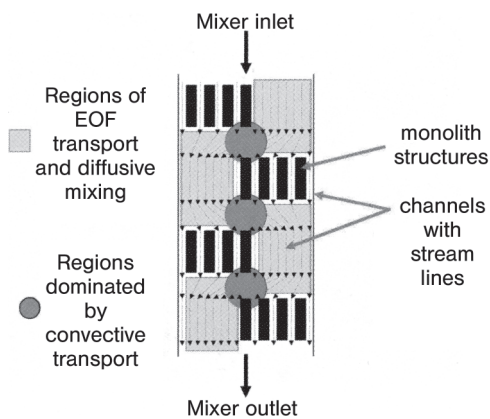


**Figure 1.176** A suggestion as to how the flow might develop in the bimodal intersecting channel micro mixer. Distinct zones with small and large channels serve to promote mixing by diffusive and convective transport, respectively [160] (by courtesy of ACS).

### 1.3.26.1 Mixer 85 [M 85]: Bimodal Intersecting Channel Micro Mixer

This micro device contains one zig-zag-like main micro channel. In the direction of the flow, four smaller channels intersect this main flow path [160]. These smaller channels have all the same width, but differ in length. The two confluent streams enter the micro mixer in parallel fashion.

The micro mixer was made by standard photolithographic and etching methods on an ultra-flat quartz substrate [160]. The microstructure created in this way was shielded by a cover plate by thermal bonding. This cover plate contained access holes for fluid supply and withdrawal. Internal surfaces of the chip were activated to have a high density of silanol groups needed for the EOF transport.

Mixer type	Bimodal intersecting channel micro mixer	Large micro channel: 27 $\mu\text{m}$ , 10 $\mu\text{m}$ width, depth
Mixer material	Quartz	Small micro channel: 5 $\mu\text{m}$ , 10 $\mu\text{m}$ width, depth
Flatness of quartz substrate	< 3 $\mu\text{m}$ across the whole wafer surface	Total volume of the mixer ~100 pl
Whole mixer structure: width, length, depth	100 $\mu\text{m}$ , 200 $\mu\text{m}$ , 10 $\mu\text{m}$	

### 1.3.26.2 Mixing Characterization Protocols/Simulation

[P 74] The liquids were moved by electroosmotic flow using a computer-controlled power supply [160]. Analog voltages were generated by an analog power output card. The voltage output was set by a laboratory-written LabVIEW program. The flow rate was set to 0.25  $\text{mm s}^{-1}$ .

Mixing was characterized by an optical microscope with an epifluorescence attachment [160]. A  $10^{-4}$  M fluorescein solution in sodium phosphate buffer (10 mM, pH 7, with trace of methanol) was applied. A filter cube was used for fitting the excitation and emission characteristics, allowing selective passages of the radiation. A CCD digital camera collected real-time fluorescence images.

For simulation, a 3-D random walk algorithm was developed to study diffusion-controlled mixing phenomena [160]. Several assumptions were made, i.e. only EOF carries out fluid transport, only neutral and point-like analytes are present and the transport in each dimension is fully independent. An elastic collision mechanism was applied for molecule-wall collisions. The analyte was introduced as a stream of 200 molecules  $\text{ms}^{-1}$ .

[P 75] A static enzyme assay experiment was carried out using a stopped-flow method [161]. This is commonly used for monitoring reaction kinetics.  $\beta$ -Galactosidase was used as model enzyme to convert the substrate fluorescein mono- $\beta$ -D-galactopyranoside (FMG) via hydrolysis into fluorescein. As buffer solution 10 mM potassium phosphate at pH 7.2 with 1 mM ascorbic acid was used to minimize photobleaching. The enzymatic reaction is accompanied by a change in fluorescence intensity which can be monitored with a microscope.

### 1.3.26.3 Typical Results

#### Studies on diffusive mixing in a channel without the micro mixer

[M 85]/[P 74] In order to demonstrate the need for a micro mixer, theoretical studies were undertaken to show how slow diffusion in a simple micro channel is, under the flow parameters applied for the micro mixer and in a channel of dimensions similar to those for the purposes envisaged [160]. The information was given as a 2-D plot on the spatial evolution of concentration within the micro channel along the flow axis. Although both fast and slow diffusion constants ( $10^{-6}$  and  $10^{-8}$   $\text{cm}^2 \text{s}^{-1}$ ) were assumed, in no case was complete mixing found for a flow passage of 1 mm. These theoretical findings were confirmed by control experiments with bi-laminated channel flows, demonstrating that even after a 3 mm flow passage (100 and 20  $\mu\text{m}$  channel width and depth, respectively) mixing is not completed, as expected for diffusion in such dimensions.

It was further calculated how long micro channel have to be to ensure complete mixing [160]. It was found that depending on the diffusion constant assumed this can take several millimeters of flow passage. A mixing length of a few hundred micrometers, as desired, was only valid for a high diffusion constant of  $10^{-6}$   $\text{cm}^2 \text{s}^{-1}$  and a very short mixing channel width of 10  $\mu\text{m}$ . The latter was regarded as feasible concerning today's micromachining capabilities, but as rather impracticable. Therefore, the need for incorporating a micro mixer was demonstrated.

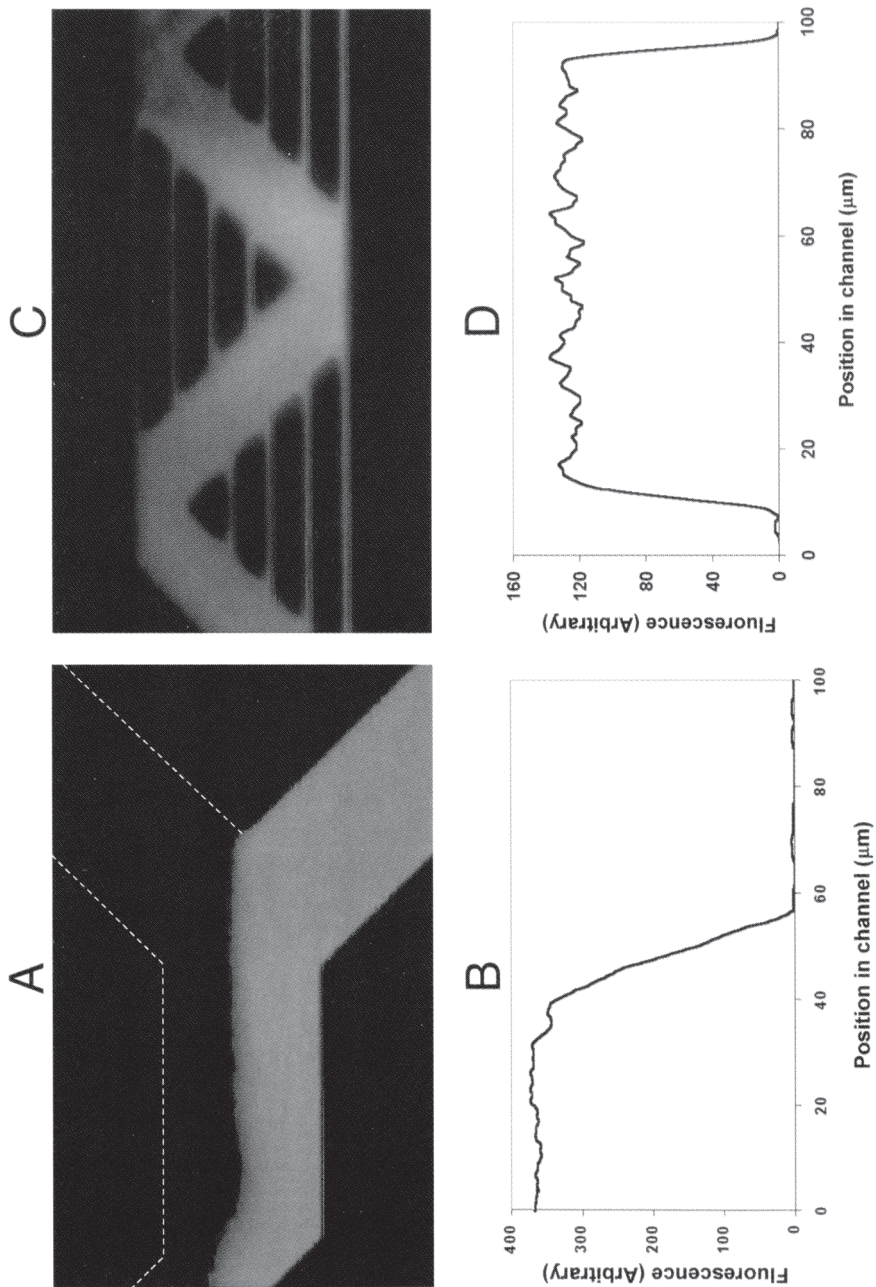
#### Microscopy images/fluorescence intensity profiles

[M 85]/[P 74] Microscopy images and fluorescence intensity profiles were recorded for bi-laminated streams (not having passed the micro mixer) and streams which leave the outlet of the micro mixer (see Figure 1.177) [160]. In the first case, two separated areas are found, divided by a thin interface. This hydrodynamic information corresponds well to the fluorescence intensity profile having two distinct zones, showing the maximum and zero concentration of the dye separated by an  $\sim 25$   $\mu\text{m}$  thin mixed interface. For a stream mixed by the micro mixer, a rather uniformly colored microscopy image and even fluorescence intensity profile were found, which indicates that complete mixing had occurred. Hence, the basic functioning of the mixer could be proven.

#### Static enzyme assay – stopped flow method

[M 85]/[P 75] In order to determine reaction kinetics by a stopped-flow method, the mixing step within a microfluidic system was improved [161]. Traditionally, an efficient external T-channel mixer is used for this purpose. Now, the bimodal intersecting channel micro mixer was integrated into the system. The mixer has the following advantages over the current state of the art:

- mixing volume is  $\leq 100$  pl
- transport time through the mixer is 0.5–1 s
- axial distance through the mixer is 400  $\mu\text{m}$
- volume of the entire channel network is  $\sim 6$  nl = consumption of enzyme solution.



the flow pattern. (C) Microscopy image of the flow at the outlet of the micro mixer. Visual inspection suggests intense mixing. (D) A fluorescence intensity profile over the cross-section of the mixer outlet flow of (C) was taken. The even profile suggests completion of mixing [160] (by courtesy of ACS).

**Figure 1.177** (A) Two solutions (fluorescein–buffer and buffer) merge in a bi-laminated configuration into a larger channel. A distinct interface is indicative of slow mixing only. (B) A fluorescence intensity profile over the cross-section of the bi-laminated flow of (A) was taken. Two discrete areas compare well with the findings of

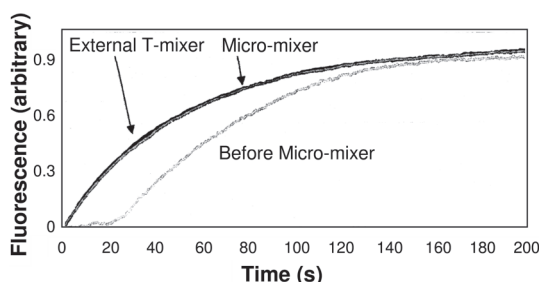


**Figure 1.178** Stopped-flow enzymatic assays when using an external T-channel micro mixer, the bimodal intersecting channel micro mixer and the flow before the micro mixer with only diffusion mixing [161] (by courtesy of ACS).

Other advantages concerning variation of the ratio of the substances to be mixed, flushing of the reaction mixture, rinsing capabilities and recycle times are also mentioned [161].

By fluorescence monitoring of the concentration profile along the channel width in a special microfluidic chip, it could be shown that mixing times may be of the order of several tens of seconds for low molecular weight molecules and of several hundred seconds for high molecular weight molecules in aqueous solutions [161]. This fits expectations from simple calculations on the rate of diffusion. Therefore, a micro mixer is required.

It could be shown that the bimodal intersecting channel micro mixer clearly improves the mixing performance. The corresponding axial concentration profile is virtually flat, i.e. mixing has led to the same concentration within the channel [161]. Without the use of the micro mixer more or less the initial concentration profile is found, i.e. a two-sectioned profile with two constant concentration values due to the bi-laminated structure.

When performing the stopped-flow enzymatic assay, the substrate fluorescein mono- $\beta$ -D-galactopyranoside (FMG) is converted via hydrolysis into fluorescein using the enzyme  $\beta$ -galactosidase (see Figure 1.178) [161]. By monitoring the accompanying change in fluorescence intensity, it was found that the corresponding yield increase for fluorescein over time is identical with that observed when using an external T-channel mixer. Since the latter is a validated and commonly used device, this means optimal functioning of the novel intersecting channel micro mixer. It was also demonstrated that processing which did not make use of this micro mixer results in a poorer performance, i.e. lower yield per unit time.

### 1.3.27

#### Micro-bead Interstices Mixing

##### Most Relevant Citations

Peer-reviewed journals: [162].

The mixing results of the bimodal intersecting mixer show that microstructured analogs of packed-bed structures can mix efficiently. Small micro channels resemble

here the interstices of the packed bed. It was therefore logical to look also at the mixing properties of small packed beds themselves. Small spherical polymer particulates, so-called micro beads, are commercially available and can be placed in a section of a micro channel forming a miniature packed bed [162].

#### 1.3.27.1 Mixer 86 [M 86]: Micro-bead Interstices Micro Mixer

A microfluidic system was made consisting of a Y-type channel structure and a packed bed of micro beads in a zone in the center of the outlet channel [162]. At the end of the micro-bead bed a weir is placed. The outlet channel then reopens to a larger flow zone which has several parallel micro channels, splitting the main flow into many sub-streams. These micro channels serve as spatially addressable detection lanes.

The device was fabricated using standard lithographic and replica molding methods [162].

Mixer type	Micro-bead interstices mixer	Width of detection lanes	50 $\mu\text{m}$
Mixer material	PDMS	Number of detection lanes	10
Inlet channel width	100 $\mu\text{m}$	Micro-bead material	Polystyrene
Outlet channel width	100 $\mu\text{m}$	Micro-bead diameter	15 $\mu\text{m}$
Depth of all channels	23 $\mu\text{m}$	Depth of weir	7–12 $\mu\text{m}$

#### 1.3.27.2 Mixing Characterization Protocols/Simulation

[P 76] The micro beads were introduced into the channel by means of hand pumping in less than 30 s [162].

Mixing was monitored by fluorescence imaging [162]. For this purpose, a 50  $\mu\text{M}$  fluorescein solution in Tris–HCl (pH 7.4) buffer and pure buffer were pumped through the two inlet channels at a flow rate of 0.5  $\mu\text{l min}^{-1}$ .

To analyze the mixing, fluorescence micrographs were taken and also a cross-sectional quantitative analysis of the mixing intensity was performed [162]. A reaction analysis with a two-step reaction was also made. Glucose in buffer was first oxidized to gluconic acid and hydrogen peroxide using the enzyme biotin-labeled glucose oxidase fixed to the micro beads, which were coated with streptavidin. As a follow-up reaction, hydrogen peroxide and amplex red reacted to give fluorescent resorufin using the enzyme horseradish peroxidase.

#### 1.3.27.3 Typical Results

##### Flow patterns without micro-bead bed

[M 86] [P 76] Flow-pattern analysis without micro beads was performed to ensure that laminar-flow properties are maintained throughout the whole microfluidic system, especially concerning the weir conduit [162]. Fluorescence images taken at the Y-contact, at the empty channel and at the parallel detection lanes prove that bi-

laminated patterns are found (one layer being fluorescent, the other not). This is indicative of laminar flow without any secondary flows. This also shows that mixing is weak in the absence of the micro-bead packing, which is to be expected, however.

A quantitative data analysis of the fluorescence intensity in the 10 detection lanes revealed strong intensity in five lanes, one weak signal in one lane and four lanes without any detectable fluorescence, which is in line with a bi-laminated pattern fed to a multi-channel architecture [162].

#### **Flow patterns with micro-bead bed**

[M 86] [P 76] The flow patterns with micro beads give a completely different fluorescence texture compared with the experiment without beads (see *Flow patterns without micro-bead bed*, above) [162]. While the initial situation is the same, i.e. a bi-laminated structure after the Y-contact, nearly homogeneous flow patterns are found starting with the micro-bead zones and in the region of the parallel detection lanes (see Figure 1.179). Besides simple visual inspection, this is corroborated by quantitative data. The fluorescence intensity in the 10 detection lanes is virtually the same.

#### **Reaction performance of the micro-bead bed**

[M 86] [P 76] The above-mentioned findings of the mixing performance of the micro-bead bed fluidic system suggest fast and complete mixing. Therefore, fast reactions should be carried out without any delay. In order to prove this, a biochemical reaction, the oxidation of glucose in buffer to gluconic acid and hydrogen peroxide, was studied [162]. In an additional micro-bead zone, fluorescent resorufin is generated by reaction of hydrogen peroxide and amplex red using the enzyme horseradish peroxidase.

Fluorescence images at the start and end of the micro-bead zone reveal that within only a short distance after entering the micro-bead bed, fluorescence is observed, whereas there is no fluorescence before [162]. A quantitative fluorescence analysis confirms this visual observation.

### 1.3.28

#### **Recycle-flow Coanda-effect Mixing Based on Taylor Dispersion**

##### **Most Relevant Citations**

Peer-reviewed journals: [163]; proceedings contributions: [55]

The use of the Coanda effect is based on the desire to have a second passive momentum to speed up mixing in addition to diffusion [55, 163]. The second momentum is based on so-called transverse dispersion produced by passive structures, which is in analogy with the Taylor convective radial dispersion ('Taylor dispersion') (see Figure 1.180 and [163] for further details). It was further desired to have a flat ('in-plane') structure and not a 3-D structure, since only the first type can be easily integrated into a  $\mu$ TAS system, typically also being flat. A further design criterion was to have a micro mixer with improved dispersion and velocity profiles.

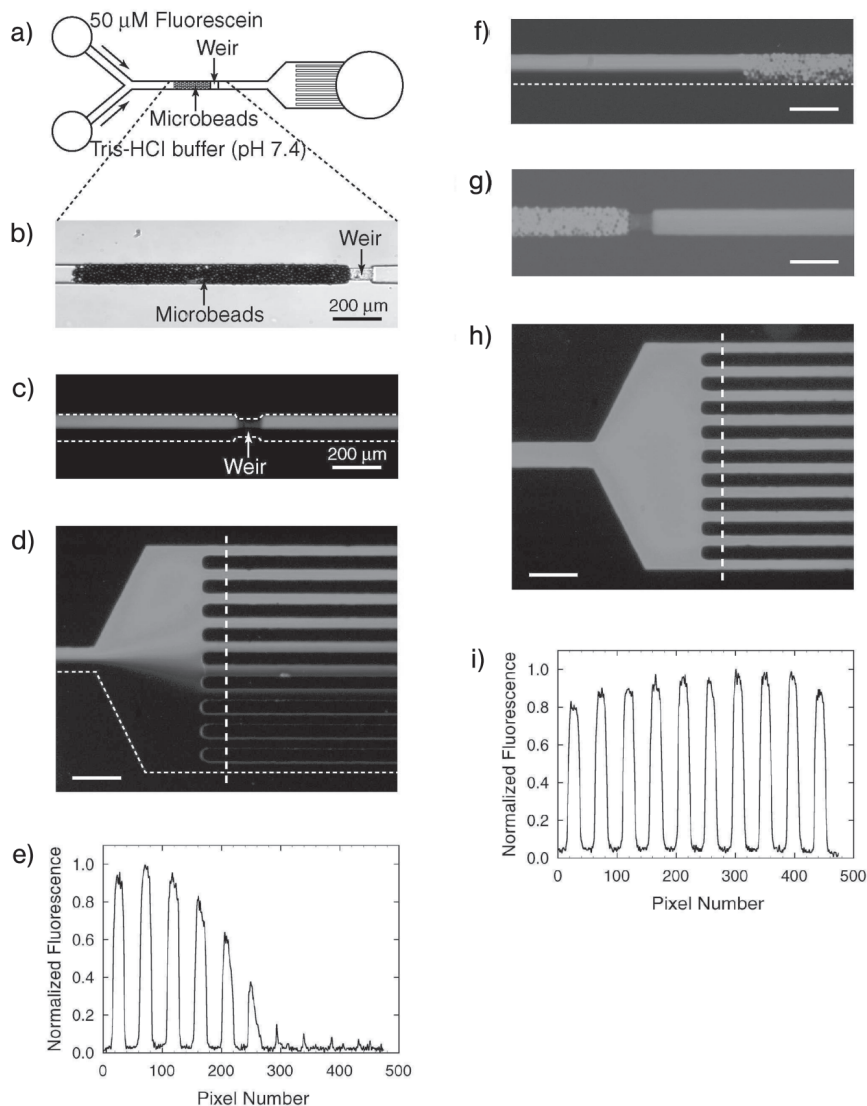


**Figure 1.179** (a) Schematic of the microfluidic device with a zone of micro beads. (b) Optical image of the micro beds packed in the micro channel. (c) Fluorescence micrograph of the weir in the channel in the absence of micro beads. (d) Fluorescence micrograph of the 10-lane detection zone in the absence of micro beads. (e) Fluorescence intensity line scans in the 10-lane detection zone in the absence of micro beads, as indicated by the dashed line in (d). (f) Fluorescence micrograph of the channel zone before the micro beads in the presence of micro beads. (g) Fluorescence micrograph of the mixed stream after leaving the micro bead zone. (h) Fluorescence micrograph of the 10-lane detection zone in the presence of micro beads. (i) Fluorescence intensity line scans in the 10-lane detection zone in the presence of micro beads, as indicated by the dashed line in (h) [162] (by courtesy of ACS).

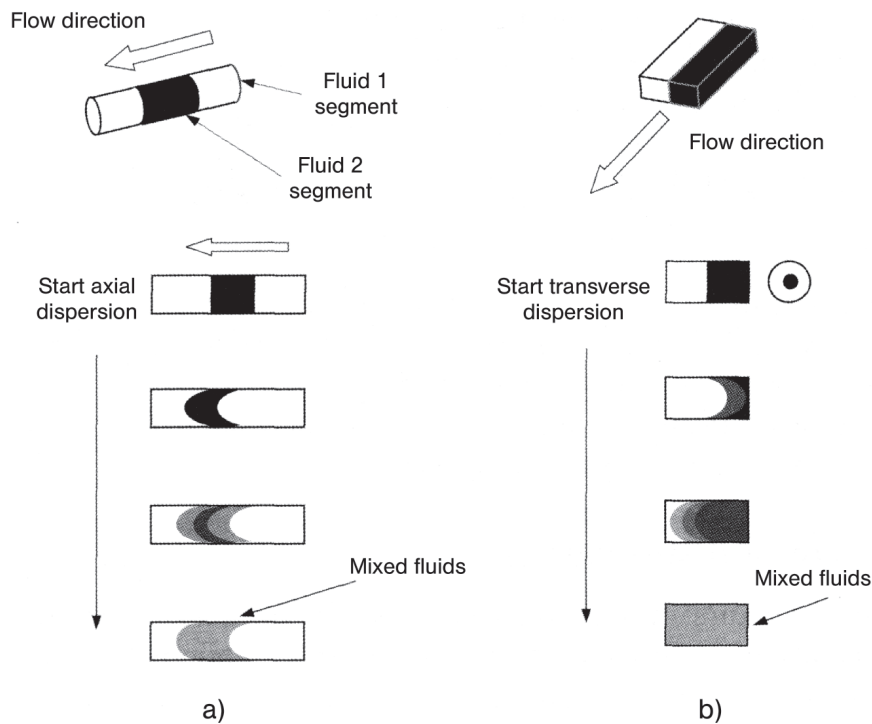


**Figure 1.180** (a) Mixing in a capillary tube by Taylor dispersion. (b) Design concept of the micro mixer using a Tesla structure to exploit the Coanda effect [163] (by courtesy of RSC).

Relying on the knowledge of flow pattern generated by the Coanda effect in-plane micro valves and micro pumps, it was envisaged to transfer this technique to a micro-mixer device [55]. In the latter case, using a Tesla structure (see [163] for geometric details), the flow is redirected and collision of streams occurs.

#### 1.3.28.1 Mixer 87 [M 87]: Coanda-effect Micro Mixer with Tesla Structures

In the Coanda-type mixer, the fluids are first bi-laminated in a T-type configuration and then pass a so-called Tesla structure (see [55] for geometric details) which comprises angled surfaces (so-called wing structure) [55]. By flowing along the latter, splitting and redirection of the flow are achieved, which leads to a kind of collision (see Figure 1.181). While one stream passes the major angled passage, the neighboring stream approaches both this major passage and a smaller secondary passage, set in a Y-type flow configuration. This stream splits into two sub-streams according to the different pressure losses of both passages. The flow of both passages is so oriented that collision results. Thus, a larger stream with predominantly one fluid collides with a smaller stream of the pure other liquid. Mixing is said to take place by turbulence.

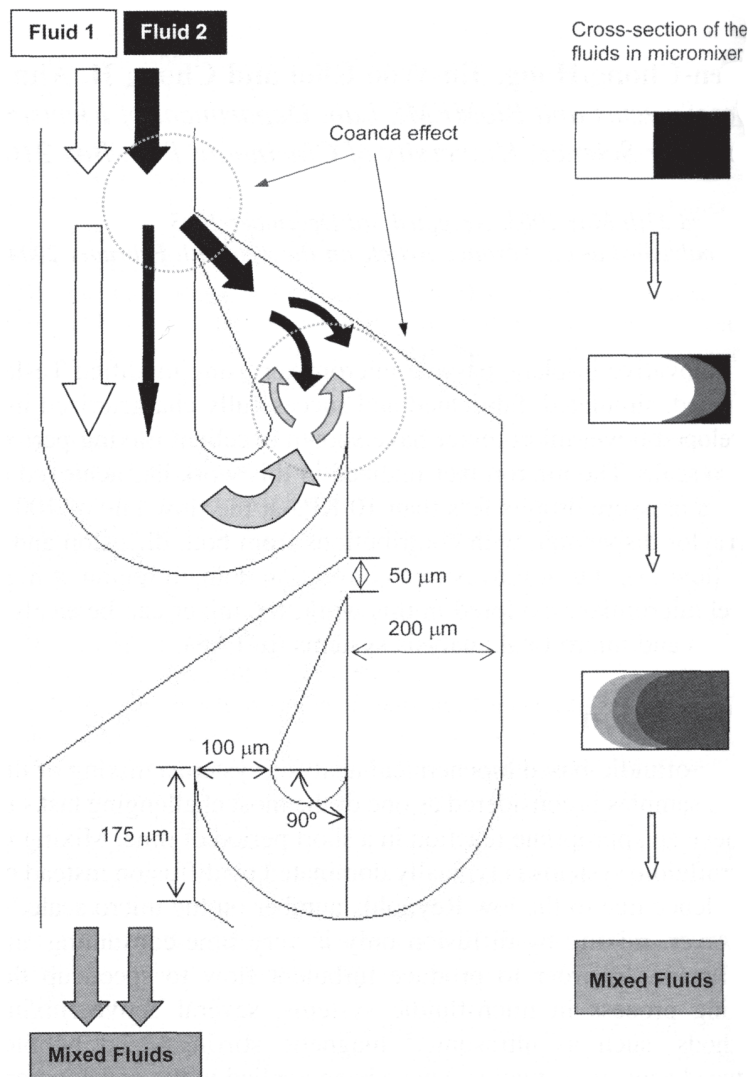
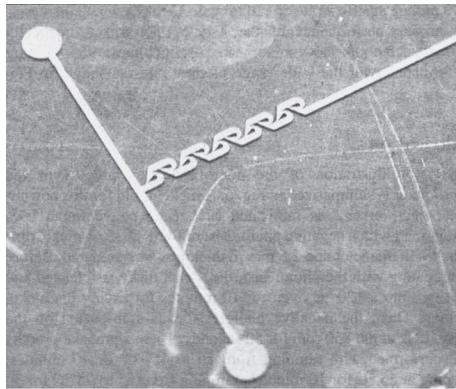


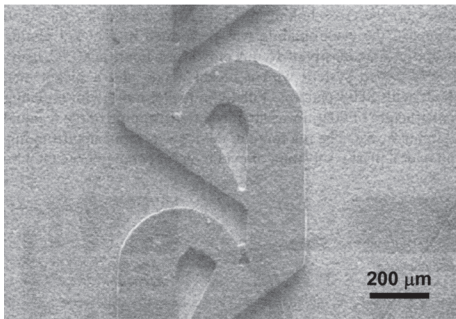
**Figure 1.181** Schematic of the action of the Coanda effect on the fluid flow, expressed by major stream directions [163] (by courtesy of RSC).

The Tesla structure is repeated many times in a row so that a sequential mixing is achieved [55, 163].

Microfabrication was achieved by UV-lithography with a negative photoresist SU-8 2035 based on a nickel plate [163]. By means of electroforming of the exposed and developed resist structure, a nickel mold was prepared (see Figure 1.182). By hot embossing, the final polymer mixer structures were prepared. Holes for fluid connectors were drilled. The microstructured substrate was joined with a blank polymer plate by thermal fusion bonding.



a)



b)

**Figure 1.182** Nickel mold for producing the Coanda micro mixer.  
 (a) Microphotograph of the whole device;  
 (b) scanning electron micrograph of the underlying Tesla flow structure [163]  
 (by courtesy of RSC).

Mixer type	Coanda-effect micro mixer with Tesla structures	Angle of turn for the main passage	90°
Mixer material	PDMS; cycloolefin copolymer (COC)	Length of the passage with combined streams before next Tesla structure	175 μm
Opening diameter of main passage, initial, final	200 μm, 100 μm	Channel depth	110 μm
Opening diameter of side passage	50 μm		

#### 1.3.28.2 Mixing Characterization Protocols/Simulation

[P 77] Simulation was done using CFD-ACE+ [55, 163]. The physical properties of water were assumed. Discretization with structured grids of 15 μm length was used. The first-order upwind scheme and conjugate gradient with preconditioning solver were applied.

[P 78] Blue and yellow deionized water streams were mixed in a dilution-type experiment using a syringe pump [55]. A CCD camera recorded the changes in color in the mixer.

[P 79] A quantitative analysis of mixing performance was made by use of pH analysis [163]. Solutions of different pH were mixed and the corresponding changes in pH were collected from four outlet ports. Then, 0.05 M potassium biphthalate buffer (pH 4, 25 °C) and 0.05 M potassium phosphate monobasic–sodium hydroxide buffer (pH 7, 25 °C) were mixed, fed by a syringe pump. The pH changes were monitored with a commercial pH sensor. A reference curve with the sensor was taken in advance.

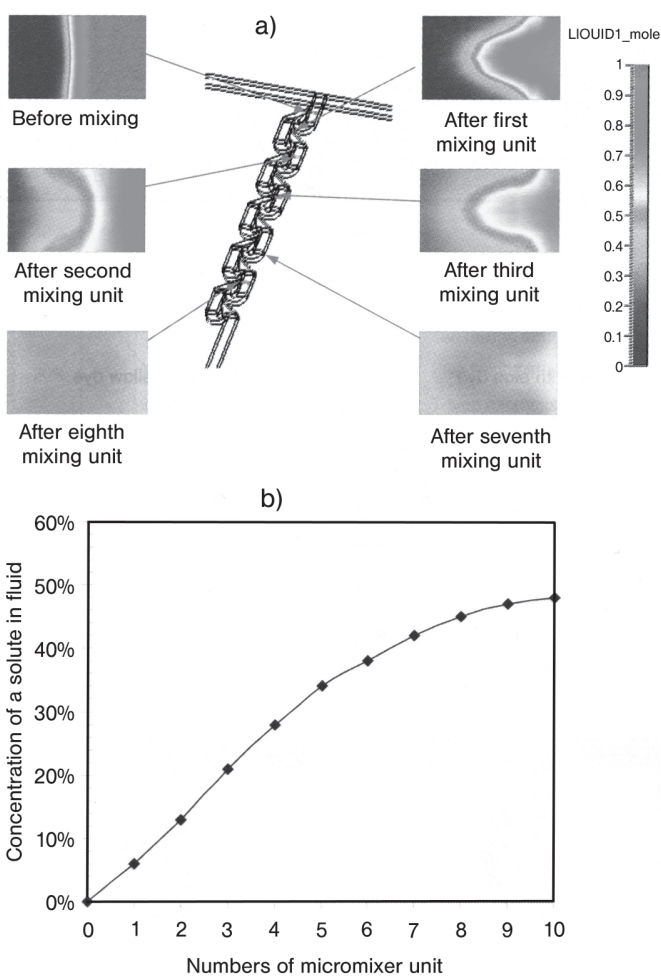


**Figure 1.183** (a) Simulation results for the Coanda micro mixer at a flow rate of  $50 \mu\text{l min}^{-1}$ . Cross-sections of the concentration patterns for various mixing units are given [163] (by courtesy of RSC). (b) Quantitative concentration development along the mixing flow path.

### 1.3.28.3 Typical Results

#### Impact of the Coanda structure on mixing

[M 87] [P 77] [P 78] Simulations show that the largest contribution to the mixing process is exerted by the Coanda structure and not by diffusion owing to the lamination beforehand. A dilution-type experiment with blue and yellow dyes reveals the formation of a central mixed zone in the initial units, as evident from the green color. Further, downstream the degree of mixing is further increased (see Figure 1.184) [55].

#### Effectiveness of transverse dispersion

[M 87] [P 77] Simulations show that, as intended, transverse dispersion is achieved at the Coanda structure and mixing is completed after passing four Tesla structures (see Figure 1.183 and 1.184) [163].

#### Comparison with mixers of other designs

[M 87] [P 77] [P 78] Three designs were compared for their mixing performance with the Coanda micro mixer, a Coanda design without wing, a T-type mixer and a ring-type mixer [55] (see also [163]). An analysis of flow patterns at  $50 \mu\text{l min}^{-1}$  by a dilution-type experiment clearly reveals the onset of mixing for the 'real' Coanda structure, whereas all three other designs do not give any visual hint of mixing.

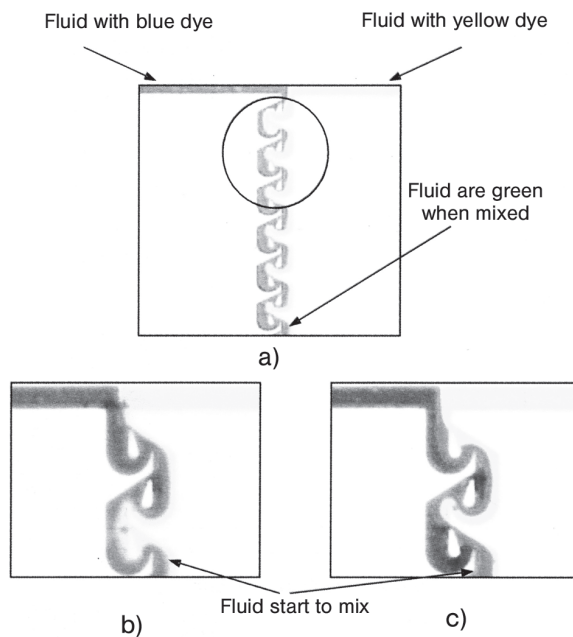


**Figure 1.184** Dilution-type experiment using blue- and yellow-colored streams for visualization of the flow patterns during mixing. (a) Flow-pattern image of the entire mixer device. (b) Flow-pattern image of the first two mixing units for  $1 \mu\text{l min}^{-1}$ . (c) Flow pattern image of the first two mixing units for  $100 \mu\text{l min}^{-1}$  [55] (by courtesy of Kluwer Academic Publishers).

In addition, simulation results predict that after only two mixing stages complete mixing is achieved [55, 163].

#### Mixing performance as a function of flow rate

[M 87][P 78] The mixing performance of the Coanda micro mixer is nearly constant over a large range of volume flows, from 1 to 100  $\mu\text{l min}^{-1}$  [55]. The small deviation from ideal is maximum at a flow rate of about 10  $\mu\text{l min}^{-1}$ . The T-type mixer instead shows a notable decrease in mixing efficiency with flow rate, simply owing to the reduction in residence time.

For a flow rate of 1  $\mu\text{l min}^{-1}$ , CCD-camera monitoring of a dilution-type experiment showed a homogeneous texture of the images, when the flow had passed five mixing elements [163]. Albeit this does not necessarily indicate completeness of mixing, it illustrates that a certain degree of dispersion was achieved.

#### Quantitative pH analysis of mixing performance as a function of flow rate

[M 87][P 79] By injection of solutions of different pH, quantitative analysis of mixing efficiency was performed (see Figure 1.185) [163]. It is found that the Coanda micro

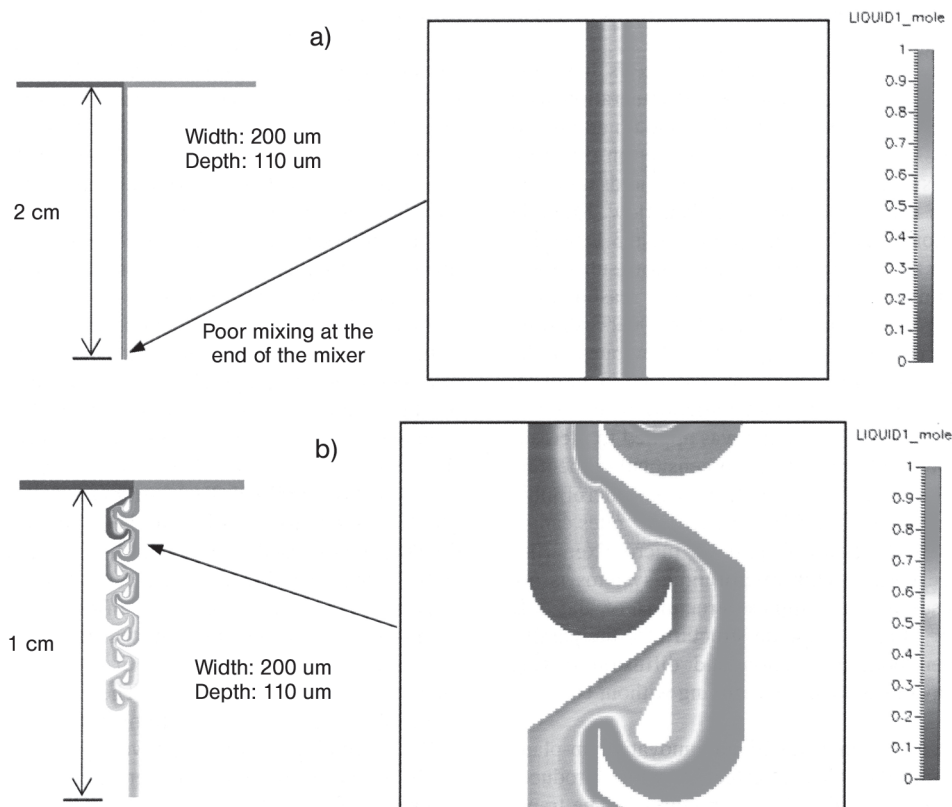


**Figure 1.185** Comparison of flow patterns for T-channel and two Coanda micro mixers, revealing the degree of mixing [163] (by courtesy of RSC).

mixer displays a nearly flat curve of mixing efficiency as a function of mixing length, whereas the T-channel mixer shows a decrease, owing to the reduction in residence time and to basing diffusion as the only mixing mechanism. The use of 10 instead of five mixing elements gives better results. Both curves are not far from the ideal behavior, which is a totally flat curve, i.e. the mixing efficiency does not change with flow rate.

[M 87][P 77] These experimental results are similar to predictions made by simulation on the same comparison [163]. The only small difference between experiment and simulation is that the real performance of the Coanda mixer is somewhat lower than the predicted one, as expected. This requires design optimization.

### 1.3.29

#### Recycle-flow Mixing Based on Eddy Formation

##### Most Relevant Citations

Peer-reviewed journals: [56].

Recycle mixers have a mixing chamber which contains, in addition to the fluid inlet and outlet, additional outlets and re-inlets which build up a recycle loop to withdraw fed fluid and to insert it back to the chamber [56]. Thus a portion of the fluid passes simply through the mixer, while another portion re-enters. The effect is not only prolongation of the residence time, but also, and this is more important, a generation of secondary flows, e.g. eddies, when the primary jet is contacted with the re-entering jets. This generates new interfaces and enhances mixing. The ratio of through and re-entering streams is governed by the pressure losses of both flow paths so that the overall mixing principle is a passive one.

Recycle reactors equipped with pumps are widely used in the chemical industry to achieve high conversion and to reduce the reactor volume for a given conversion [56].

##### 1.3.29.1 Mixer 88 [M 88]: Recycle-flow Micro Mixer

The mixing chamber of the recycle-flow mixer has an inverse V-shape with the inlet at top (at the 'V-corner') and two outlets at the branches of the 'V' (see Figure 1.186) [56]. The two outlets are recombined to one outlet. The width of the 'V'-type mixing chamber is 10 times larger than the inlet and outlet widths in order to allow the formation of secondary flows. At the branches of the 'V', two side channels for recycle flow are also placed. Via two 90° turns the flow re-enters the mixing chamber at the top part, adjacent to the inlet. Five mixing elements were connected in series to ensure complete mixing. The combined outlet of one mixing element serves as inlet for the next. Two large, square-like ports placed in line fed the series of mixing elements; the same type of port served as the device outlet behind the elements.

Conventional photolithography with a negative photoresist SU-8 on a silicon wafer was used for manufacture [56]. PDMS pre-polymer and a curing agent were mixed and poured on this master. The PDMS replica was separated and inlet and outlet holes were punched into the replica. The PDMS microstructure was bonded to glass slides by oxygen plasma treatment.

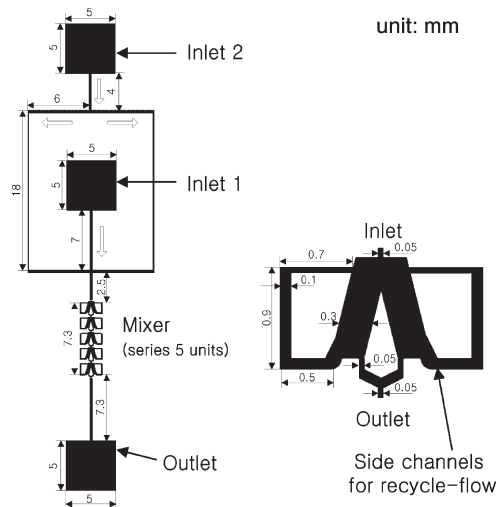


**Figure 1.186** Schematic of the recycle-flow micro mixer with five mixing elements [56] (by courtesy of Transducer Research Foundation).

Mixer type	Recycle-flow micro mixer	Outlet channel width	50 $\mu\text{m}$
Mixer material	PDMS/glass	Side channel width initial, at re-entry	100 $\mu\text{m}$ , 50 $\mu\text{m}$
Number of mixing units in series	5	Length of V-type mixing chamber and of side channel	900 $\mu\text{m}$
Total depth (for all channels)	100 $\mu\text{m}$ , 150 $\mu\text{m}$ , 200 $\mu\text{m}$	Mixing chamber inlet width, side-arm width	500 $\mu\text{m}$ , 300 $\mu\text{m}$
Inlet channel width	50 $\mu\text{m}$	Total device size	5 cm $\times$ 1.5 cm

**1.3.29.2 Mixing Characterization Protocols/Simulation**

[P 80] The simulation was carried out with CFD-ACE+ [56]. The diffusion, velocity and pressure were calculated in the user scalar module using a finite element method and three-dimensional structured grids. Quantitative analysis of mixing efficiencies was performed.

Mixing was characterized by dilution-type imaging using ink and pure water solutions [56]. As a reactive approach, color imaging was performed by a pH-indicator reaction, merging phenolphthalein solution (0.01 M in water-ethanol) and aqueous NaOH solution (0.3 M).

**1.3.29.3 Typical Results**

**Recycle flow ratio and flow pattern**

[M 88] [P 80] For an overall channel depth of 150  $\mu\text{m}$ , CFD simulations were performed as a function of flow rates and Reynolds number [56]. At low  $Re = 7$

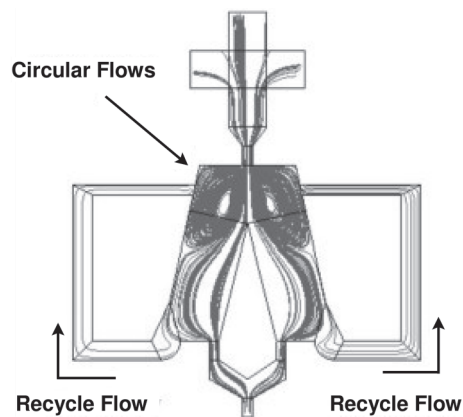


**Figure 1.187** Simulated flow pattern of the first element of the recycle-flow micro mixer ( $Re = 14$ ;  $150\ \mu\text{m}$ ) [56] (by courtesy of Transducer Research Foundation).

( $0.05\ \text{ml min}^{-1}$ ), the flow split into the recycle channel, but ran in the opposite direction, as expected. At low  $Re = 14$  ( $0.1\ \text{ml min}^{-1}$ ), the correct flow passage into the recycle loop was observed. A detailed flow pattern of such operation depicts eddy formation on both sides when the two re-entering streams collide with the primary inlet stream (see Figure 1.187). The amount of the recycle to primary inlet flow was low, amounting to 0.2%. At low  $Re = 42$  ( $0.3\ \text{ml min}^{-1}$ ), this share increased to 3%. The results were explained by the relative pressure drops of outlet and inlet streams.

#### Quantitative mixing analysis

[M 88] [P 80] The simulated mixing percentage in the recycle-flow micro mixer increased with increasing flow rate and Reynolds number ( $Re = 7\text{--}42$ ;  $0.05\text{--}0.3\ \text{ml min}^{-1}$ ) [56]. The efficiencies also increased with increasing number of mixing elements. For  $Re = 28$  and  $42$ , nearly complete mixing was achieved after passage of five mixing elements. The difference between the latter two flow regimes was only obvious for a passage of two mixing elements and then was equal.

The depth of the mixing chamber also had a notable influence [56]. A large depth of  $200\ \mu\text{m}$  gave much improved performance, while the simulated mixing percentage was nearly the same for depths of  $150$  and  $100\ \mu\text{m}$ .

#### Dilution- and reaction-type flow imaging – CFD flow simulation

[M 88] [P 80] Good agreement was found for flow patterns predicted by CFD simulation and a dilution-type experiment using ink for flow visualization ( $Re = 14$ ;  $150\ \mu\text{m}$ ) [56]. At the outlet fully mixed profiles are found for both simulation and experiment.

Similar findings were made in the reactive experiment. Since now initially only the interfaces are colored, fine details of the flow patterns can be visualized ( $Re = 14$ ;  $150\ \mu\text{m}$ ) [56]. The results confirm the existence of two eddies at the re-entering flow at the top of the mixing chamber (see Figure 1.188).

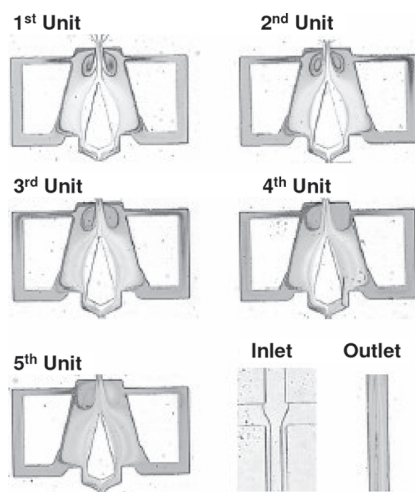


**Figure 1.188** Microscope images of the color formation due to a reactive characterization of mixing in the five mixing elements of the recycle-flow micro mixer ( $Re = 28$ ;  $150 \mu\text{m}$ ). Phenolphthalein and NaOH solutions were mixed [56] (by courtesy of Transducer Research Foundation).

### 1.3.30

#### Cantilever-valve Injection Mixing

##### Most Relevant Citations

Proceedings contributions: [33].

The combination of pumping action and mixing, as given e.g. for the mixer pumps, is sometimes used in the chemical industry. Thus, attempts at mixing in micro spaces were described which make use of flow energy, which is anyway available within miniature integrated systems. For example, micro pumps or valves create fluid motion; part of this energy can be transferred into mixing action.

##### 1.3.30.1 Mixer 89 [M 89]: Cantilever-valve Injection Micro Mixer

This micro mixer is based on using a cantilever-plate flapper valve for injection of volume into a main stream and performing mixing in a subsequent flow-through chamber (see Figure 1.189) [33]. This design is realized by sandwiching two microstructured wafers, the bottom wafer containing the valve and two ports and the upper wafer with the mixing chamber.

The operation of the mixer/valve is as follows. A sample flow passes continuously through the chamber [33]. At certain times, small reagent volumes are injected via the valve and diffusive mixing occurs. As a first guess, it is thought that the injected volume gives an underneath layer in the mixing chamber, similar to a bilayer configuration. Thereafter, the injection mode is stopped and the mixed reagent flow passes downstream to another functional element.

The relative flow rates determine the mixing ratio and pressure at reagent and sample ports [33]. Accordingly, the device is passively pressure-actuated.

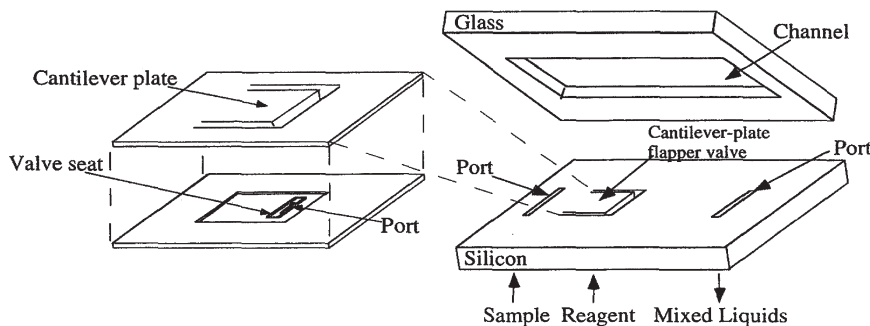


**Figure 1.189** Schematic exploded views of the cantilever-valve injection mixer [33] (by courtesy of Kluwer Academic Publishers).

Microfabrication is based on standard silicon micro machining protocols using wet-chemical etching/deep reactive ion etching and oxide protection layers [33]. On one wafer the valve seat and the ports are made in this way. This microstructured silicon wafer is fusion bonded with an SOI (silicon-on-insulator) wafer with a thin silicon overlayer forming the cantilever. After removal of the bulk silicon from this sandwich, it is joined by anodic bonding with a glass wafer, which is structured using a three-part masking scheme.

Mixer type	Cantilever-valve injection mixer	Distance fin-to-fin (underneath the cantilever), fin width	70 $\mu\text{m}$ , 5 $\mu\text{m}$
Mixing chamber material (top plate)	Glass	Distance from cantilever to fins below	2.3 $\mu\text{m}$
Valve and port material (bottom plate)	Silicon	Distance fin-to-cantilever end (underneath the cantilever)	515 $\mu\text{m}$
Cantilever width, length, thickness	800 $\mu\text{m}$ , 600 $\mu\text{m}$ , 3 $\mu\text{m}$	Flow-through mixing chamber width, depth	940 $\mu\text{m}$ , 70 $\mu\text{m}$

### 1.3.30.2 Mixing Characterization Protocols/Simulation

[P 81] The investigation is based on the dependence of the quantum yield of the fluorescent dye fluorescein on pH [33]. It is high at large pH (alkaline media) and low at small pH (acidic media). Hence a basic solution of fluorescein is mixed with an acidic solution. In this way, a fluorescence turn-off length (FTOL) is defined, which, however, is not equal to the mixing length, but may give an idea of it.

Simulations of three-component time-dependent diffusion were made based on two slightly different models using Matlab software [33]. Basically, fluid layer thicknesses are predicted, which determine diffusion distances. In this way, the  $\text{H}^+$  and  $\text{OH}^-$  concentrations are revealed which can be related back to the pH. By the known fluorescence intensity–pH relationship, the quantum yield is thus given.

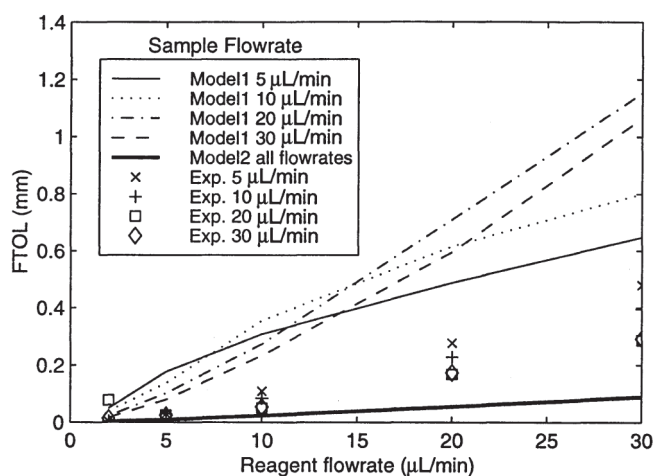


**Figure 1.190** Comparison of simulated and experimentally determined fluorescence turn-off lengths (FTOL) [33] (by courtesy of Kluwer Academic Publishers).

### 1.3.30.3 Typical Results

[M 89] [P 81] The experimental turn-off lengths for fluorescence quantum yield decay are between the two predictions based on different models (see Figure 1.190) [33]. Hence the models give a rough estimate. From these data, mixing times can be extracted.

The data also show that mixing is probably better than expected for diffusion as the only mechanism [33]. This is to be expected, since owing to shearing of the layers it is likely that secondary motion is induced. Further, the measurements show that the FTOL and the mixing length are not necessarily equal.

### 1.3.31

#### Serial Diffusion Mixer for Concentration Gradients

##### Most Relevant Citations

Peer-reviewed journals: [164].

The generation of defined concentration gradients in a flowing stream can have many practical analytical uses, e.g. for drug screening (see e.g. [164]). Continuous concentration gradients have a continuously decreasing concentration along the channel, whereas discontinuous gradients give a spontaneous change in concentration at a certain locations and have near-constant concentration in between, similar to a step-like profile. By use of specially fluidic networks, both types of concentration gradients can be realized. One solution is based on the multiple serial contacting of a main stream with side flows at certain, spatially confined locations. For a short time, typically, mixing can occur here via diffusion. Between the contact zones, the main stream flow is 'undisturbed', i.e. no material from other sources is introduced, and only concentration equilibration within the main channel is achieved.

To realize such interactions between many streams in a complex fluidic network, excellent pressure control over all inlets is required, because minute differences may result in undesired breakthroughs or even changes in the flow direction [164].

#### 1.3.31.1 Mixer 90 [M 90]: Serial-diffusion Micro Mixer for Concentration Gradients

A micro channel network is composed of four channel systems, each two representing a symmetric, mirror-imaged design (see Figure 1.191) [164]. Two channels approach each other in a Y-type configuration and come close, do not merge, but are separated by a dam-like structure, restricting the interface to a very small area. The dam structure is due to special application demands for biological cell immobilization, as the fluidic network is part of a  $\mu$ TAS chip, and is not essential for the functioning of the network to work for concentration gradient generation. After the side-to-side arrangement of the two main channels, the flow is redirected twice, yielding partly two separate channels again. Finally, the side-to-side arrange-

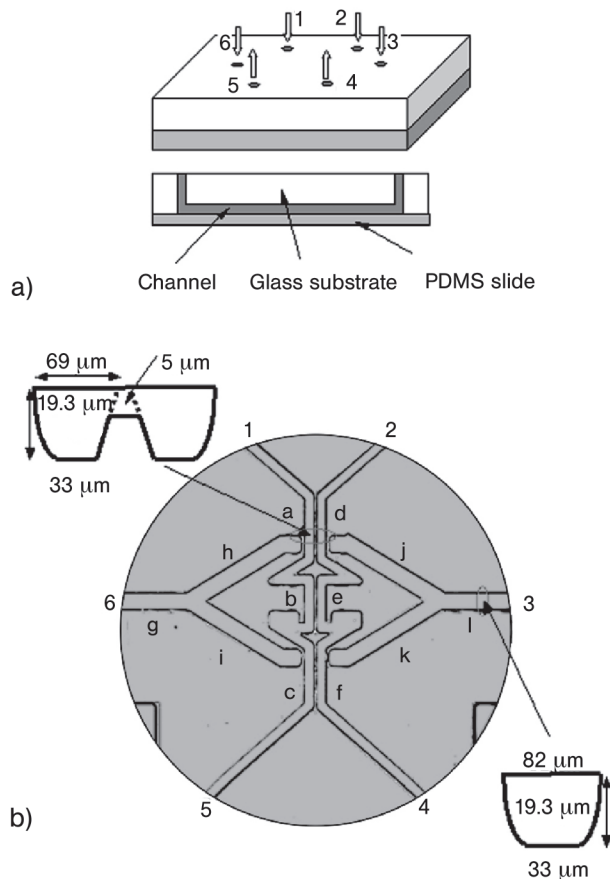


**Figure 1.191** (a) Construction of the microfluidic chip and (b) schematic of the microfluidic network for feeding analyte and buffer solutions [164] (by courtesy of RSC).

ment is given again with a dam structure and thereafter the channels are separated by an inverse-Y-type structure.

The two symmetrical side channels are arranged like a Y-configuration, which attaches at its ends two times each the main channels [164]. At these intersections, mixing takes place via diffusion.

The microfluidic structure was manufactured in glass by classical photolithography and wet-chemical HF etching methods [164]. Holes for fluid connection were drilled. A polymer membrane was prepared in-house and served as a top plate to give a glass–polymer sandwich chip. Pressure sealing was applied.

Mixer type	Serial-diffusion mixer for concentration gradients	Channel depth at dam structure	5 $\mu\text{m}$
Fluidic network material (bottom plate)	Glass	Side channel width at top and bottom of the channel, depth	82 $\mu\text{m}$ , 33 $\mu\text{m}$ , 19.3 $\mu\text{m}$
Cover material (top plate)	PDMS elastomer	Total size of the chip	5 $\times$ 4 $\times$ 0.5 cm
Main channel width at top and bottom of the channel, depth	69 $\mu\text{m}$ , 33 $\mu\text{m}$ , 19.3 $\mu\text{m}$	Inner diameter of connectors	3 mm

#### 1.3.31.2 Mixing Characterization Protocols/Simulation

[P 82] Dilution-type mixing was accomplished with the fluorescent dyes acridine orange (0.01% solution in 20 mM in TE buffer; see below) or trypan blue (prepared in 0.85% saline) contacted with buffer solution (TE buffer: 10 mmol l<sup>-1</sup> Tris–HCl, pH 7.4, 1 mmol l<sup>-1</sup> EDTA, pH 8.0) [164]. Images were taken by a laser scanning confocal microscope. Profiling data analysis was employed along detection lines.

Numerical calculations using MATHEMATICA software were made based on a theoretical model which assumes flow distribution in circular pipes under laminar conditions as described by the Bernoulli equation and applies an electrical circuit model based on Ohm's law [164].

#### 1.3.31.3 Typical Results

##### Continuous concentration gradients

[M 90] [P 82] As a symmetrical flow mode, an operation is described in which the fluorescent dye and buffer solutions are guided in the two main channels side-by-side [164]. Buffer solution is introduced from the two side channels and can mix with the main channel at the two intersections.

In this way, a discontinuous concentration gradient can be built up, as evident from the presence of three distinct concentration plateaus measured by the fluorescence intensity (see Figure 1.192) [164]. For the last mixing step, fluorescence intensity monitoring was possible along the whole flow path from the intersection point (start of mixing) until a considerable passage downstream (completion of

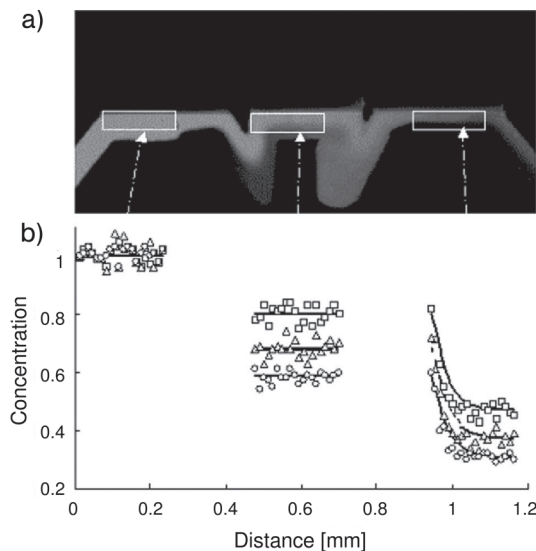


**Figure 1.192** (a) Fluorescence micrograph in the main channel of the microfluidic network. (b) Discontinuous, step-like concentration profiles generated in this way [164] (by courtesy of RSC).

mixing). Clearly, the decay of the fluorescence signal due to the increased dilution of the buffer solution within the main channel was visible. Finally, a plateau of the concentration was reached, since mixing was completed.

Numerical simulations match the experimental findings perfectly [164].

The exact shape of the concentration gradient can be controlled by adjusting the pressure of the main stream to the side stream [164]. The pressure of the buffer solution from the side has a key function here.

#### Mixing of fluorescent dyes of different molecular weight

[M 90] [P 82] As expected, the decay of intensity is not equal for the two different fluorescent dyes having different molecular masses and hence different diffusion coefficients [164]. In a sense, this indicates also that diffuse mixing is effective and is a major contribution to mixing. However, some deviations from diffusion as the only mixing mechanism seem to take place, since the theoretical models are not fully able to describe the experimental behavior. This indicates the presence of other secondary-flow mechanisms besides diffusion.

#### Asymmetric flow mode

[M 90] [P 82] As asymmetric flow mode an operation is described for which the fluorescent dye is guided in one main channel and the other main channel is left empty [164]. Buffer solution is introduced from the two side channels and can mix with the main channel at the two intersections. In this way, asymmetric pressures are generated between the symmetrical inlets.

A large concentration gradient was so established by having a mixing protocol different to the symmetrical flow mode (for details, see [164]). Simulation results basically agree with the experimental findings.

## 1.3.32

**Double T-junction Turbulent Mixing****Most Relevant Citations**

Peer-reviewed journals: [6].

Multi-laminating devices may yield millisecond liquid mixing times. However, mixing devices are needed for the sub-millisecond range, e.g. as measuring tools for studying fast consecutive reactions and processes. Such studies are, in particular, important in the field of quench-flow and stopped-flow analysis, e.g. to monitor protein folding, where a time resolution of  $< 1$  ms is required [6]. Therefore, a sudden start and stop of processes and reactions by intimate mixing has to be ensured. Moreover, the volume of the mixing chamber, which usually is fairly large for macroscopic mixing devices, has to be strongly reduced in order to minimize dead volumes and, hence, dead times.

**1.3.32.1 Mixer 91 [M 91]: Double T-junction Micro Mixer**

The mixing device comprises a micro channel system with three inlet and one outlet ports, which resembles two mixing tees connected in series (see Figure 1.193) [6]. The outlet of the first mixing tee forms one inlet of the second mixing tee, and the other inlet is fed by an external source. In the second mixing tee, another fluid is introduced and mixed with the mixture of the first two fluids.

Basically, this geometry provides a residence time channel of defined length separated by two mixing tees [6]. In the idealized case of indefinitely short mixing, this configuration would enable one immediately to start a reaction and to control the reaction time by variation of flow rate or length of flow passage before stopping the reaction by a second mixing process. In practice, a major part of the volume of the residence time channel will, even if good mixing is ensured, be demanded by mixing issues rather than by needs of reaction (as proven by the results below). As the mixing mechanism turbulent mixing was used, as this is said to result in fast mixing. For this reason, flow velocities of the liquid streams had to be used which are unusually high for microfluidic devices.

Mixer type	Double T-junction micro mixer	Sub-channel width, length	400 $\mu\text{m}$ , ~2 mm
Mixer material	Silicon	Outlet hole diameter	750 $\mu\text{m}$
Cover material	Glass	Total size of the mixing chip	10 mm $\times$ 10 mm
Number of sub-channels	6		

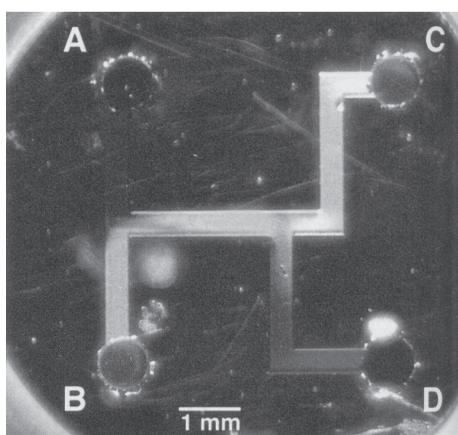
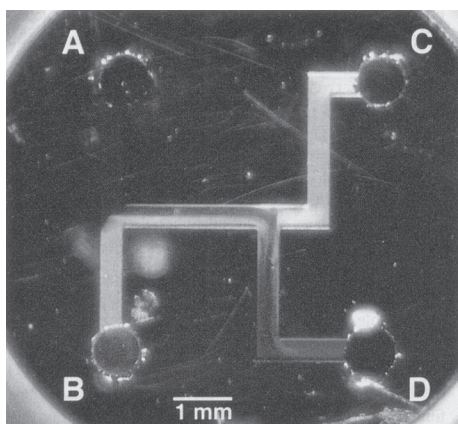


**Figure 1.193** Schematic representation of the double mixing tee-type arrangement of a micro mixer for sub-millisecond quench-flow analysis [6] (by courtesy of ACS).

The micro channel system was fabricated by standard silicon micromachining via etching of a silicon wafer with potassium hydroxide using thermal oxide as an etch mask [6]. The double mixing tee configuration consists of six micro channels. For fluid connection, an outlet hole was drilled into the silicon chip. The chip was anodically bonded to a glass slide with three inlet holes, clamped in a holder and, thereby, connected to a commercially available quench-flow instrument.

#### 1.3.32.2 Mixing Characterization Protocols/Simulation

[P 83] In feasibility experiments, the time scale of mixing was determined and compared with that of the reactions to be investigated [6]. The first and second mixing processes were followed by flow visualization using two-fold color changes of a pH indicator-containing solution. In a first step, mixing with an acid resulted in a color change. Second, the original color was re-established by subsequent addition of a base.

As a real reaction, the basic hydrolysis of phenyl chloroacetate was investigated in a kind of quench-flow analysis experiment [6].

In order to vary residence times and mixing performance, flow rates in the range 1.8–9.0 l h<sup>-1</sup> were applied, corresponding to Reynolds numbers from 1000 up to 8000 [6].

#### 1.3.32.3 Typical Results

##### Ensuring well-developed turbulence and high mixing quality

[M 91] [P 83] The mixing device was tested as a measuring tool for studying fast consecutive reactions and processes [6]. This concerned applications in quench-flow and stopped-flow analysis, where a time resolution of < 1 ms is required.

A pH-indicator reaction was used first for flow visualization. A fully developed color profile, proving high mixing quality, along the channel axis of the mixer was only observed for flow rates as high as 2.7 l h<sup>-1</sup> [6]. For smaller flow rates, e.g. 0.7 l h<sup>-1</sup>, only incomplete mixing resulted.

##### Feasibility of dual fast mixing for quench-flow analysis

[M 91] [P 83] On the basis of the above-mentioned results, a flow range of 1.8–9.0 l h<sup>-1</sup> was chosen for the investigation of the basic hydrolysis of phenyl chloroacetate as a test reaction for quench-flow analysis [6]. This reaction is sufficiently fast to follow the mixing. Chemical reaction data for the hydrolysis of phenyl chloroacetate showed a mixing dead time of 100 μs. Hence, the feasibility of initiating and quenching reactions with time intervals down to 110 μs in the micro mixer could be proven.

#### 1.3.33

##### Jet Collision Turbulent or Swirling-flow Mixing

##### Most Relevant Citations

Peer-reviewed journals: [39, 54, 136, 165, 167]; chapter in encyclopedia: [138]; proceedings contributions: [53, 137, 166]; patents: [52].

Impinging jets are one way to generate large interfaces by ‘converting’ fluids from large reservoirs into multiple small-diameter micro plumes [39, 52–54, 136, 137, 166, 167]. The various impinging jet techniques differ in the way in which they exploit such freshly generated interfaces. Impinging jets can be contacted in a mixing chamber or in free space. They may be guided into air or gas media or introduced into a liquid (which was filled from prior jets). The jets may be directed without offset [39, 136], i.e. collide, or with off-set [54], to penetrate deeply into a liquid and by flowing aside the next jet to create eddies which further enlarge the interface.

By collision of jets, in particular at high fluid velocity, mixing can be accomplished. At high velocities, turbulent mixing can be achieved [39, 52–54, 136, 137, 166, 167]. Even under laminar conditions, collision mixing may be adequate, e.g. when no other type of micro mixer may be suitable and, nevertheless, microfluidics is chosen as the processing concept [39, 136]. This is the case, e.g., when performing precipitation reactions which can be mixed using jet collision in a free-flow configuration [39, 136, 165].

Jets can be collided frontal, i.e. at a  $180^\circ$  angle [52]. Here, the energy input is maximal. The fluid can be virtually 'atomized' in this way and has to be surrounded by a mixing chamber to be re-collected. In a Y-type flow configuration, a 'softer' contact can be achieved [39, 136]. The two jets simply merge to a third one. Under unfavorable conditions, however, a separated, bi-laminated fluid system is achieved.

#### 1.3.33.1 Mixer 92 [M 92]: Frontal-collision Impinging Jet Micro Mixer, 'Microjet Reactor'

[M 92] A special frontal-collision mixer merges two high-velocity jets in a small mixing chamber which is a recess in a solid metal piece (see Figure 1.194) [52, 166]. The jets are introduced via fluid connectors from opposite sides of the chamber and need a very accurate alignment, so as not to be displaced for merging. Owing to the very high velocities, being close to or even above supersonic speed, misalignment may cause destruction of the wall material by cavitation effects. In some versions of the device, massive spheres are introduced which prevent this material damage by being hit by the fluid stream and protecting so the wall beneath.

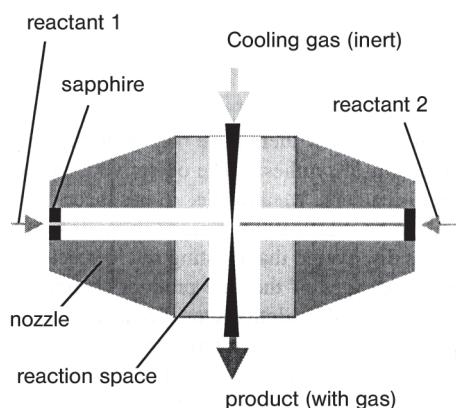


**Figure 1.194** Schematic of a commercial frontal-collision mixer [166] (by courtesy of VDE-Verlag).

After jet merging, the material is brought out by an air stream, which redirects the merged stream by  $90^\circ$  into an outlet tubing [52, 166]. This is particularly done because a major application task of the mixer is to perform precipitation reactions. In the latter case, the mixed fluid is sprayed as small droplets or particles. If the droplets still contain solvent, nanoparticles can be produced by evaporation.

No details on the geometry of the device and the fabrication were published.

#### 1.3.33.2 Mixer 93 [M 93]: Y-Type Collision Impinging Jet Micro Mixer

Impinging jet micro mixers merge two liquid jets in a Y-like configuration at a point outside the flow-guiding element [39, 136]. The latter contains the two fluid connectors on the side and two tiny outlet nozzles. The nozzles are angled in such a way that the jets merge. The impinging jet element can be inserted into a housing, e.g. serving as a mixing chamber, enabling operation under an inert gas atmosphere, and maintaining temperature control.

Impinging jet elements were constructed as a cylindrical block comprising two feed tubes which become smaller towards the outlet (see Figure 1.195) [39, 136].

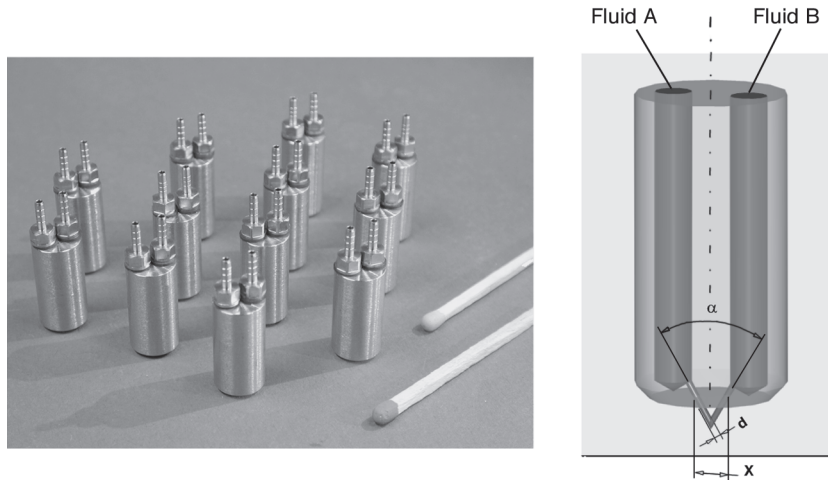


**Figure 1.195** Photograph of the impinging jet micro mixer (left) and schematic of the design of the device (right) [53] (source IMM).

Accordingly, the main characteristics of these mixers are the diameter of the outlet boring, the interspaces between the borings and the angle defined by the orientation of borings (relative to the normal) [39, 136]. For one study, nine impinging jet micro mixers were made which differ in these specifications, listed in Table 1.8.

**Table 1.8** List of parameters specifying the different impinging jet micro mixers: diameter of the outlet boring  $d$ , the interspaces between the borings  $x$  and the angle  $\alpha$  defined by the orientation of borings ([53]; source IMM).

<i>Jet mixer No.</i>	<i>Diameter of outlet boring, <math>d</math> (<math>\mu\text{m}</math>)</i>	<i>Interspaces between the borings, <math>x</math> (mm)</i>	<i>Angle <math>\alpha</math> defined by the orientation of borings (<math>^\circ</math>)</i>
1	1000	3	60
2	500	2	45
3	500	2	60
4	500	2	90
5	500	3	45
6	500	3	60
7	500	4	45
8	350	3	45
9	350	4	60

The jet mixers were made of Hastelloy and manufactured by die sinking, a special variant of the  $\mu$ -EDM technique using small cylindrical electrodes [39, 136].

### 1.3.33.3 Mixer 94 [M 94]: Impinging Jet Array Micro Mixer

Arrays with multiple oblique impinging jets are generated via 3-D channel networks which feed fluid from a reservoir via the outlet nozzles of the network into a mixing chamber (see Figures 1.196 and 1.197) [54]. Perforated plates contain such arrays.

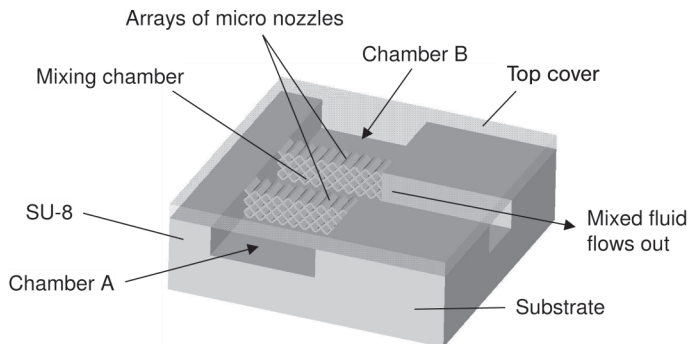


**Figure 1.196** Schematic design of the impinging-jet array micro mixer [54] (by courtesy of IOP Publishing Ltd.).

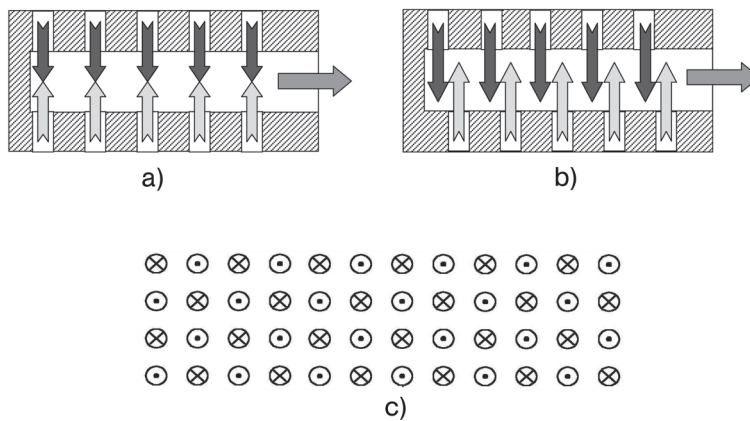


**Figure 1.197** Schematic of the flow guidance in the impinging-jet array micro mixer. (A) Without offset; (B) with offset; (C) cross-sectional view of the jet orientation under offset conditions. The two symbols denote jets which have a  $90^\circ$  and a  $-90^\circ$  direction relative to the plane of the paper [54] (by courtesy of IOP Publishing Ltd.).

These plates are inserted in a T-channel structure in a still thicker plate, directly at the T-junction at the ends of the two feed channels. In this way, a rectangular mixing chamber is formed in the outlet channel of the T-structure, having multi-nozzle arrays on both sides. The arrays can be positioned with and without offset to collide the jets directly and to let them flow aside. In the latter case, it is thought that eddies are produced at sufficiently high velocity of the jets.

The micro mixer was fabricated by UV lithography of SU-8 [54]. Two lithography masks were employed, one for the inlet and outlet channels and sidewalls and the other for making the array of micro nozzles. A non-conventional tilted lithographic method was used. A thick layer of SU-8 was exposed at  $45^\circ$  and  $-45^\circ$  as well as other angles. A special resist development technique for the small and deep nozzle structures also had to be explored.

Mixer type	Impinging-jet array micro mixer	Nozzle length	300 $\mu\text{m}$
Mixer material	SU-8 resist	Nozzle angle (relative to array front)	28°
Distance between two nozzles	1000 $\mu\text{m}$	Mixing chamber width (i.e. array distance) depth, length	210 $\mu\text{m}$ , 1000 $\mu\text{m}$ , 5000 $\mu\text{m}$
Cross-sectional area of the nozzles	70 $\times$ 70 $\mu\text{m}$		

#### 1.3.33.4 Mixing Characterization Protocols/Simulation

[P 84] A jet of acetyl chloride ( $0.197 \text{ mol l}^{-1}$ ) in THF at a flow rate of  $1000 \text{ ml l}^{-1}$  and a jet consisting of *n*-butylamine ( $0.200 \text{ mol l}^{-1}$ ) and triethylamine ( $0.200 \text{ mol l}^{-1}$ ) in THF at a flow rate of  $1000 \text{ ml h}^{-1}$  are generated by an impinging jet mixer [53]. Both jets merge in a Y-type flow configuration. The reaction temperatures are 22 °C. The reaction solution was inserted as droplets or a continuous stream either directly or via the tubular reactor in a beaker containing water. By rigorous stirring, hydrolysis of the acid chloride and hence stopping of the reaction are achieved. The phases are separated and the aqueous phase is extracted with THF. The combined THF phases are dried over  $\text{Na}_2\text{SO}_4$ . After filtration, the THF solvent is evaporated at 25 mbar. The remaining amide product is characterized by FTIR spectroscopy.

[P 85] Two set-ups comprising the above-mentioned mixer type were tested, both being micro mixer–tubular reactor configurations [53]. These set-ups differ in the type of tube used. A first set-up was equipped with a spirally wound steel tube, a geometry commonly found in chemical applications (due to savings of space). The vertically mounted tube was 3.30 m long and of 4 mm inner diameter. In contrast, the second set-up comprised a 0.75 m long straight glass tube of 0.3 mm inner diameter. Both set-ups used a laboratory-made housing in which the impinging jet mixer was inserted. The housing chamber was tapered like a funnel in order to collect the liquid mixture and to introduce it directly into the tubular reactor attached, without any wakes. Four inspection windows around the housing allowed judging of the jet formation and the extent of fouling. Feeds into the housing optionally allowed the insertion of inert or cooling/heating gas or an immiscible liquid as heat transfer medium.

[P 86] A solution with a commercial fluorescent dye (1.2 mM) and deionized water were fed by syringe pumps into the micro mixer [54]. A mercury lamp illuminated the mixing chamber. Filters were used to select between the emission light and the reflected light. A microscope with a digital camera was used for flow monitoring.

### 1.3.33.5 Typical Results

#### Robustness test for the impinging-jet mixer – fouling sensitivity during precipitations

[M 93] [P 84] Different types of flow are found for the impinging jet mixers, dependent on the flow rate (see Table 1.9 and Figure 1.198) [53]. At low flow rates, the two fluids merge immediately after leaving the outlets, wet the mixer surface and finally form droplets. At increasing flow rate, the frequency of the droplets increases and results in merging to a jet. For flow rates next to the droplet regime, the jets formed are often not stable with regard to the axial position, but rather are moving along an angle to the normal. This was termed ‘wobbly jet’, whereas a stable jet is at a standstill in the normal position. When the two initial jets join at a distance to yield a third jet, this is referred as ‘Y-type’. ‘T-type’ merging is characterized by immediate contact after leaving the outlets (similar to the droplet formation). Thereby, only one jet is generated. Increasing the flow rate further yields a broadening of the jet, first being termed ‘fan-shaped’ and thereafter ‘fanned-out’ when broadening is intense.

**Table 1.9** Types of flow for the different impinging-jet micro mixers, as defined in Table 1.8 ([53]; source IMM).

Jet mixer No.	600 ml h <sup>-1</sup>	1000 ml h <sup>-1</sup>	1400 ml h <sup>-1</sup>	1800 ml h <sup>-1</sup>	2200 ml h <sup>-1</sup>	2600 ml h <sup>-1</sup>	3000 ml h <sup>-1</sup>
1	Droplets	Droplets	Droplets	Droplets	Droplets	Stable jet, T-type	Stable jet, T-type
2	Droplets	Droplets	Wobbly jet, T-type	Wobbly jet, T-type	Stable jet, T-type	Fan-shaped jet, T-type	Fan-shaped jet, T-type
3	Droplets	Droplets	Wobbly jet, T-type	Stable jet, T-type	Stable jet, T-type	Fan-shaped jet, Y-type	Fanned-out jet, Y-type
4	Droplets	Droplets	Droplet/jet-transition	Wobbly jet, T-type	Wobbly jet, T-type	Stable jet, T-type	Fanned-out jet, T-type
5	Droplets	Wobbly jet, T-type	Stable jet, T-type	Stable jet, T-type	Stable jet, Y-type	Fan-shaped jet, Y-type	Fan-shaped jet, Y-type
6	Droplets	Wobbly jet, T-type	Stable jet, T-type	stable jet, T-type	Stable jet, T-type	Stable jet, T-type	Fan-shaped jet, Y-type
7	Droplets	Droplets	Wobbly jet, T-type	Wobbly jet, T-type	Wobbly jet, T-type	Stable jet, Y-type	stable jet, Y-type
8	Droplets	Droplets	Wobbly jet, Y-type	Stable jet, Y-type	Fan-shaped jet, Y-type	Fan-shaped jet, Y-type	Fanned-out jet, Y-type
9	Droplets	Droplet/jet-transition	Wobbly jet, T-type	– *	– *	– *	– *

\* No measurement was possible owing to a too high pressure loss using the existing equipment.

The preferred type of flow concerning the operation of fouling-sensitive reactions is the stable Y-type jet [53]. Mixing is here performed at a position distant from the mixer outlets. Since the mixer surface ideally is only wetted separately by the reactant solutions, the precipitation is kept a ‘safe’ distance from the micro channels. With regard to fouling, any operation resulting in direct merging of the streams is not

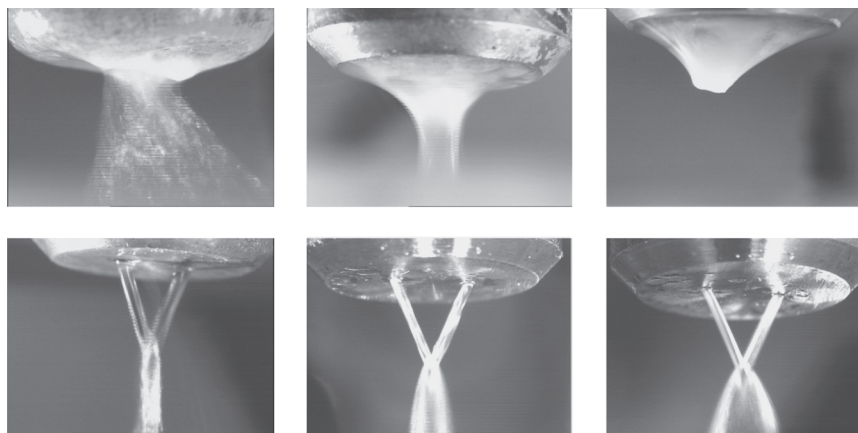


**Figure 1.198** Types of flow for different impinging jet mixers, using the acetyl chloride (THF) and *n*-butylamine/triethylamine (THF) solutions ([53]; source IMM). Top left: wobbly jet, T-type (initial flow before plugging); total flow rate  $200 \text{ ml h}^{-1}$ , mixer type 3. Top middle: stable jet, T-type (initial flow before plugging);  $2000 \text{ ml h}^{-1}$ , mixer type 6. Top right: device plugged after some minutes of T-type jet operation;  $2000 \text{ ml h}^{-1}$ , mixer type 2. Bottom left: stable jet, Y-type;  $2000 \text{ ml h}^{-1}$ , mixer type 5. Bottom middle: fan-shaped jet, Y-type;  $2000 \text{ ml h}^{-1}$ , mixer type 7. Bottom right: fanned-out jet, Y-type;  $3000 \text{ ml h}^{-1}$ , mixer type 7.

avored, since the mixed solution wets the micro channels, usually leading rapidly to plugging. The advantages of stable versus wobbly and normally thin versus fanned-out jets currently are not foreseen as clearly.

The results show that devices with tiny openings seem to give the most preferred flow patterns [53]. For instance, device 8 with openings of  $350 \mu\text{m}$  diameter has a favorably large Y-type flow regime, ranging from  $700$  to at least  $1500 \text{ ml h}^{-1}$ . The results indicate that a distance of  $3 \text{ mm}$  and an angle of  $45^\circ$  are particularly suitable for the generation of Y-type flow, as evidenced by the respective large range of flow rates of mixers 5 and 8. In contrast, at higher angles the collision point of the two jets is closer to the mixer surface, hence wetting and correspondingly T-type jets are more likely.

#### Mixing quality determined by competing reactions approach

[M 93] [P 84] A chemical method based on competitive reactions was used for the analysis of mixing quality [53]. An analysis of the mixing quality of the impinging jet mixers 1–9 (see Table 1.8) in the flow rate range from  $300$  to  $1500 \text{ ml h}^{-1}$  reveals a decrease in absorption for all curves, and an increase in mixing quality, with increasing flow rate until a constant, low level is approached (see Figure 1.199). Obviously, the penetration of the jets is intensified at high flow rates, generating larger specific interfaces for mixing.

Jet mixers 8 and 9 with the smallest openings of  $350 \mu\text{m}$  (see Table 1.8) give the best mixing, whereas mixer type 1 with  $1000 \mu\text{m}$  borings performs worst [53]. Even

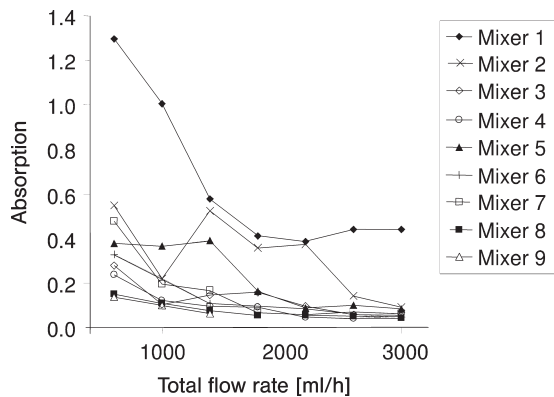


**Figure 1.199** Determination of the mixing quality of the different impinging jet micro mixers using a competing reactions approach based on measuring UV-Vis absorption ([53]; source IMM).

at the largest flow rate measured, the performance of the latter device is lower than that of most of the other mixers operated at low flow rate. Regarding the influence of the interspaces, there is no clear indication of better mixing with mixers 5 and 6 ( $x = 3$  mm) than mixers 2–4 ( $x = 2$  mm) or 7 ( $x = 4$  mm). Accordingly, mixing in Y-type flow mode is not necessarily superior to T-type mixing.

Moreover, the comparison of the mixing performance of the grouped mixers 5/6 and 8/9 allows one to judge the influence of the angle  $\alpha$  [53]. It was found that the mixing quality at  $60^\circ$  is better than that at  $45^\circ$ . This can be explained by the more frontal collision of the jets at  $60^\circ$ .

Mixers 2–4, in contrast to all other devices, do not exhibit a continuous decrease in absorption, but rather a maximum of absorption at a flow rate of about  $700\text{--}900\text{ ml h}^{-1}$  [53]. This is most prominent for mixer 2 having an angle of  $45^\circ$ . In view of the hydrodynamic investigations summarized in Table 1.9, this corresponds to the change from the droplet to the T-type wobbly jet regime. This relationship is further confirmed by the small plateau of mixing quality of mixer 7, also having this change of flow.

#### Robustness test for the impinging-jet mixer – fouling sensitivity during precipitations

[M 93] [P 84] As a test for fouling sensitivity, amide formation from acetyl chloride and *n*-butylamine was carried out using different impinging jet mixers at various total flow rates [53]. Depending on the flow pattern generated, the extent of fouling varied widely. In the case of droplet or T-type jet formation, processing suffered severely from plugging of the mixer outlets. For Y-type jets, fouling is at least significantly reduced, in some cases totally absent.

It turned out that one impinging jet mixer design (two  $350\text{ }\mu\text{m}$  openings, separated by 3 mm, and inclined to each other by  $45^\circ$ ), giving stable Y-type flows, was particularly advantageous [53].

**Fouling sensitivity during precipitations for two set-ups with different tube geometry**

[M 93] [P 85] Two set-ups with two different kinds of tubing, straight and spirally wound, were tested for their fouling sensitivity, each comprising a impinging-jet micro mixer [53]. When performing amide formation in the set-up with the spirally wound steel tube, plugging occurred after only 42 s operating time (see Table 1.10). In contrast, the set-up with the straight glass tube could be used for a much longer period, at least 20 min. This indicates only a minimal time, since the operation was deliberately stopped owing to the large amount of chemicals and solvents already consumed.

**Table 1.10** Operating times achieved with the different set-ups with various process parameters [53].

<b>Set-up</b>	<b>Dimensions</b>	<b>Experimental protocol</b>	<b>Operation time/ observations</b>
Mixer/funnel/tube linear	Mixer type 8, 0.75 m long tube with 0.3 mm i.d.	0.200 mol l <sup>-1</sup> , 2000 l h <sup>-1</sup>	20 min*, Et <sub>3</sub> NHCl lumps + gas bubbles
Mixer/funnel/tube linear	Mixer type 8, 0.75 m long tube with 0.3 mm i.d.	0.400 mol l <sup>-1</sup> , 2000 l h <sup>-1</sup>	38 min*, extensive Et <sub>3</sub> NHCl lump formation + gas bubbles
Mixer/funnel linear, tube connector bendt, tube linear	Mixer type 8, 0.30 m long bend connector with 0.3 mm i.d., 0.75 m long tube with 0.3 mm i.d.	0.400 mol l <sup>-1</sup> , 2000 l h <sup>-1</sup>	30 s, system plugged owing to extensive Et <sub>3</sub> NHCl lump formation
Mixer/funnel linear, tube spirally wound	Mixer type 8, 3.30 m long tube with 4 mm i.d.	0.200 mol l <sup>-1</sup> , 2000 l h <sup>-1</sup>	42 s, system plugged

\* The operation was stopped intentionally, i.e. much longer processing is possible.

In addition, the hydrodynamics were monitored. The main features were gas bubble formation (HCl) and particulate formation (Et<sub>3</sub>NHCl) and agglomeration, both due to the reaction. The flow in the glass tube seemed to be rather undisturbed [53]; only from time to time, bubble formation due to HCl gas evolution and passing of Et<sub>3</sub>NHCl lumps were observed. These bubbles and lumps moved with the liquid mixture and were rinsed out of the tube and hence did not behave as obstacles which could cause a breakdown of the flow.

In a further run, the reactant concentration was doubled (see Table 1.10) [53]; 0.395 mol l<sup>-1</sup> acetyl chloride in THF and 0.400 mol l<sup>-1</sup> *n*-butylamine and 0.400 mol l<sup>-1</sup> Et<sub>3</sub>N in THF were processed in the second set-up with the straight tube at a total flow rate of 2000 ml h<sup>-1</sup>. Although extensive precipitation of Et<sub>3</sub>NHCl was observed, still the respective lumps were carried out of the tube. After 38 min of operation, no plugging was observed.

When processing in a set-up with a short, curved flow element (0.3 m long bendt Teflon tube of 0.3 mm inner diameter) between the funnel and straight tubular reactor plugging occurred after only 30 s (see Table 1.10) [53]. Hence the insertion of curved flow passages is detrimental, even for only short paths.

Accordingly, the results show that a linear arrangement of the whole set-up is crucial for the avoidance of fouling [53]. Then, even highly concentrated solutions entrapping solid lumps and gas bubbles can be passed through tubes of diameter of much less than 1 mm. Thus, means of building a properly working set-up were derived to handle fast and heavily precipitating reactions, while still using micro-space operation.

#### Two arrays of oblique impinging jets in frontal collision and in offset orientation

[M 94] [P 86] By means of fluorescence imaging, it could be shown that mixing is only completed in a downstream section below the mixing chamber and the nozzle-array section [54]. This is explained by the comparatively low interfacial enlargement on direct collision.

In contrast, injection under offset conditions, where the jets slide along each other, shows completion of the mixing already in the mixing chamber within 1 s (see Figure 1.200) [54]. This is explained by the generation of eddies by guiding the jets in different velocity directions.

It was further found that the impinging-jet array mixer with narrower mixing chambers, i.e. shorter gap between the jets, give better mixing [54]. This is thought to be due to the higher possibility of complete penetration to the other side of the mixing chamber. Lastly, smaller sized and consequently more jets in total have more efficient mixing, as expected.

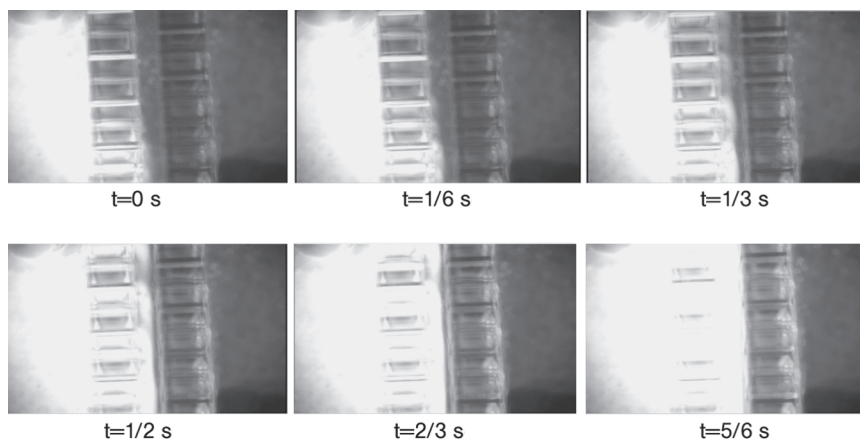


**Figure 1.200** Dilution-type fluorescence imaging for visualization of the mixing process in the impinging-jet array micro mixer under offset conditions for the arrays at various times [54] (by courtesy of IOP Publishing Ltd.).

## References

- 1 KRESTA, S. M., KREBS, R., MARTIN, T., The future of mixing research, *Chem. Eng. Technol.* **2004**, *27*, 208–214.
- 2 BERTSCH, A., HEIMGARTNER, S., COUSSEAU, P., RENAUD, P., Static micro-mixers based on large-scale industrial mixer geometry, *Lab Chip* **2001**, *1*, 56–60.
- 3 KIM, D. S., LEE, I. H., KWON, T. H., CHO, D.-W., A barrier embedded Kenics micromixer, *J. Micromech. Microeng.* **2004**, *14*, 1294–1301.
- 4 STREIFF, F. A., ROGERS, J. A., Don't overlook static mixer reactors, *Chem. Eng.* **1994**, *6*, 77–82.
- 5 OROSKAR, A. R., VANDEN BUSSCHE, K., TOWLER, G., Scale up vs numbering up – can miniaturization change the rules in chemical processing, in *Proceedings of the VDE World Microtechnologies Congress, MICRO.tec 2000* (25–27 Sept. 2000), VDE Verlag, Berlin, EXPO Hannover, **2000**, 385–392.
- 6 BÖKENKAMP, D., DESAI, A., YANG, X., TAI, Y.-C., MARZLUFF, E. M., MAYO, S. L., Microfabricated silicon mixers for submillisecond quench flow analysis, *Anal. Chem.* **1998**, *70*, 232–236.
- 7 SCHÖNFELD, F., HESSEL, V., HOFMANN, C., An optimized split-and-recombine micro mixer with uniform 'chaotic' mixing, *Lab Chip* **2004**, *4*, 65–69.
- 8 REYES, D. R., IOSSIFIDIS, D., AUROUX, P. A., MANZ, A., Micro total analysis systems: 1. Introduction, theory, and technology, *Anal. Chem.* **2002**, *74*, 2623–2636.
- 9 AUROUX, P. A., IOSSIFIDIS, D., REYES, D. R., MANZ, A., Micro total analysis systems: 2. Analytical standard operations and applications, *Anal. Chem.* **2002**, *74*, 2637–2652.
- 10 EHRNSTRÖM, R., Miniaturization and integration: challenges and breakthroughs in microfluidics, *Lab Chip* **2002**, *2*, 26N–30N.
- 11 MANZ, A., BECKER, H., *Microsystem Technology in Chemistry and Life Science*, *Topics in Current Chemistry*, Vol. 194, Springer-Verlag, Heidelberg, **1998**.
- 12 KNAPP, M. R., KOPF-SILL, A., DUBROW, R., CHOW, A., CHIEN, R.-L., CHOW, C., PARCE, J. W., Commercialized and emerging lab-on-a-chip applications, in RAMSEY, J. M., VAN DEN BERG, A. (Eds.), *Micro Total Analysis Systems*, Kluwer, Dordrecht, **2001**, 7–9.
- 13 VAN DEN BERG, A., LAMMERINK, T. S. J., Micro Total Analysis Systems: Microfluidic Aspects, Integration Concept and Applications, in MANZ, A., BECKER, H. (Eds.), *Topics in Current Chemistry*, Vol. 194, Springer Verlag, Heidelberg, **1998**, 21–49.
- 14 RAMSEY, J. M., Miniature chemical measurement systems, in WIDMER, E., VERPOORTE, E., BANARD, S. (Eds.), *Proceedings of the 2nd International Symposium on Miniaturized Total Analysis Systems, Analytical Methods and Instrumentation, Special Issue  $\mu$ TAS '96*, Basel, **1996**, 24–27.
- 15 VAN DEN BERG, A., BERGVELD, P.,  *$\mu$ -TAS: Miniaturized Total Chemical Analysis Systems*, Kluwer, Dordrecht, **1995**.
- 16 VESER, G., Experimental and theoretical investigation of H<sub>2</sub> oxidation in a high-temperature catalytic microreactor, *Chem. Eng. Sci.* **2001**, *56*, 1265–1273.
- 17 KESTENBAUM, H., LANGE DE OLIVERA, A., SCHMIDT, W., SCHÜTH, H., EHRFELD, W., GEBAUER, K., LÖWE, H., RICHTER, T., Synthesis of ethylene oxide in a catalytic microreactor system, *Stud. Surf. Sci. Catal.* **2000**, *130*, 2741–2746.
- 18 KESTENBAUM, H., LANGE DE OLIVERA, A., SCHMIDT, W., SCHÜTH, F., EHRFELD, W., GEBAUER, K., LÖWE, H., RICHTER, T., Silver-catalyzed oxidation of ethylene to ethylene oxide in a microreaction system, *Ind. Eng. Chem. Res.* **2000**, *41*, 710–719.
- 19 HAAS-SANTO, K., GÖRKE, O., SCHUBERT, K., FIEDLER, J., FUNKE, H., A microstructure reactor system for the controlled oxidation of hydrogen for possible application in space, in MATLOSZ, M., EHRFELD, W., BASELT, J. P. (Eds.), *Microreaction Technology – IMRET 5: Proc. of the 5th International Conference on Microreaction Technology*, Springer-Verlag, Berlin, **2001**, 313–320.
- 20 HESSEL, V., HARDT, S., LÖWE, H., SCHÖNFELD, F., Laminar mixing in different interdigital micromixers – Part I: Experimental characterization, *AIChE J.* **2003**, *49*, 566–577.

- 21 GRAVESEN, P., BRANJEJBERG, J., JENSEN, O. S., Microfluidics – a review, in *Proceedings of Micro Mechanics Europe, MME '93* (September 1993), Neuchatel, Switzerland, **1993**, 143–164.
- 22 YANG, Z., MATSUMOTO, S., GOTO, H., MATSUMOTO, M., MAEDA, R., Ultrasonic micromixer for microfluidic systems, *Sens. Actuators A* **2001**, *93*, 266–272.
- 23 LIU, R. H., YANG, J., PINDER, M. Z., ATHAVALE, M., GRODZINSKI, P., Bubble-induced acoustic micromixing, *Lab Chip* **2002**, *2* (3), 151–157.
- 24 LIU, R. H., LENIGK, R., DRUYOR-SANCHEZ, R. L., YANG, J., GRODZINSKI, P., Hybridization enhancement using cavitation microstreaming, *Anal. Chem.* **2003**, *75*, 1911–1917.
- 25 ODDY, M. H., SANTIAGO, J. G., MIKKELSEN, J. C., Electrokinetic instability micromixing, *Anal. Chem.* **2001**, *73*, 5822–5832.
- 26 GLASGOW, I., AUBRY, N., Enhancement of microfluidic mixing using time pulsing, *Lab Chip* **2003**, *3*, 114–120.
- 27 NIU, X., LEE, Y.-K., Efficient spatial–temporal chaotic mixing in microchannels, *J. Micromech. Microeng.* **2003**, *13*, 454–462.
- 28 QIAN, S., BAU, H. H., A chaotic electroosmotic stirrer, *Anal. Chem.* **2002**, *74*, 3616–3625.
- 29 PAIK, P., PAMULA, V. K., FAIR, R. B., Rapid droplet mixers for digital microfluidic systems, *Lab Chip* **2003**, *3*, 253–259.
- 30 WOIAS, P., HAUSER, K., YACOB-GEORGE, E., An active silicon micromixer for  $\mu$ TAS applications, in VAN DEN BERG, A., OLTUIS, W., BERGVELD, P. (Eds.), *Micro Total Analysis Systems*, Kluwer, Dordrecht, **2000**, 277–282.
- 31 WEST, J., KARAMATA, B., LILLIS, B., GLEESON, J. P., ALDERMAN, J., COLLINS, J. K., LANE, W., MATHEWSON, A., BERNEY, H., Application of magnetohydrodynamic actuation to continuous flow chemistry, *Lab Chip* **2002**, *2*, 224–230.
- 32 LU, L.-H., RYU, K. S., LIU, C., A novel microstirrer and arrays for microfluidic mixing, in RAMSEY, J. M., VAN DEN BERG, A. (Eds.), *Micro Total Analysis Systems*, Kluwer, Dordrecht, **2001**, 28–30.
- 33 VOLDMAN, J., GRAY, M. L., SCHMIDT, M. A., Liquid mixing studies with an integrated mixer/valve, in HARRISON, J., VAN DEN BERG, A. (Eds.), *Micro Total Analysis Systems*, Kluwer, Dordrecht, **1998**, 181–184.
- 34 BRANJEJBERG, J., LARSEN, U. D., BLANKENSTEIN, G., Fast mixing by parallel multilayer lamination, in WIDMER, E., VERPOORTE, E., BANARD, S. (Eds.), *Proceedings of the 2nd International Symposium on Miniaturized Total Analysis Systems, Analytical Methods and Instrumentation, Special Issue  $\mu$ TAS '96*, Basel, **1996**, 228–230.
- 35 FLOYD, T. M., LOSEY, M. W., FIREBAUGH, S. L., JENSEN, K. F., SCHMIDT, M. A., Novel liquid phase microreactors for safe production of hazardous specially chemicals, in EHRFELD, W. (Ed.), *Microreaction Technology: 3rd International Conference on Microreaction Technology, Proc. of IMRET 3*, Springer-Verlag, Berlin, **2000**, 171–180.
- 36 EHRFELD, W., GOLBIG, K., HESSEL, V., LÖWE, H., RICHTER, T., Characterization of mixing in micromixers by a test reaction: single mixing units and mixer arrays, *Ind. Eng. Chem. Res.* **1999**, *38*, 1075–1082.
- 37 HARDT, S., SCHÖNFELD, F., Laminar mixing in different interdigital micromixers – Part 2: Numerical simulations, *AIChE J.* **2003**, *49*, 578–584.
- 38 DRESE, K., Optimization of interdigital micromixers via analytical modeling – exemplified with the SuperFocus mixer, *Chem. Eng. J.* **2004**, *101*, 403–407.
- 39 LÖB, P., DRESE, K. S., HESSEL, V., HARDT, S., HOFMANN, C., LÖWE, H., SCHENK, R., SCHÖNFELD, F., WERNER, B., Steering of liquid mixing speed in interdigital micromixers – from very fast to deliberately slow mixing, *Chem. Eng. Technol.* **2003**, *27*, 340–345.
- 40 ZECH, T., HÖNICKE, D., FICHTNER, M., SCHUBERT, K., Superior performance of static micromixers, in *Proceedings of the 4th International Conference on Microreaction Technology, IMRET 4* (5–9 March 2000), AIChE Topical Conf. Proc., Atlanta, GA, **2000**, 390–399.
- 41 EHLERS, S., ELGETI, K., MENZEL, T., WIESSMEIER, G., Mixing in the offstream of a microchannel system, *Chem. Eng. Proc.* **2000**, *39*, 291–298.

- 42 BESSOTH, F. G., DEMELLOW, A. J., MANZ, A., Microstructure for efficient continuous flow mixing, *Anal. Commun.* **1999**, 36, 213–215.
- 43 SCHWESINGER, N., FRANK, T., WURMUS, H., A modular microfluidic system with an integrated micromixer, *J. Micromech. Microeng.* **1996**, 6, 99–102.
- 44 STROOCK, A. D., DERTINGER, S. K. W., AJDARI, A., MEZIC, I., STONE, H. A., WHITESIDES, G. M., Chaotic mixing in microchannels, *Science* **2002**, 295, 647–651.
- 45 STROOCK, A. D., DERTINGER, S. K. W., WHITESIDES, G. M., AJDARI, A., Patterning flows using grooved surfaces, *Anal. Chem.* **2002**, 74, 5306–5312.
- 46 JEN, C.-P., WU, C.-Y., LIN, Y.-C., WU, C. Y., Design and simulation of the micromixer with chaotic advection in twisted microchannels, *Lab Chip* **2003**, 3, 73–76.
- 47 JIANG, F., DRESE, K. S., HARDT, S., KÜPPER, M., SCHÖNFELD, F., Helical flows and chaotic mixing in curved micro channels, *AIChE J.* **2004**, 50 (9), 2297–2305.
- 48 LEE, Y.-K., DEVAL, J., HO, C. M., TABELING, P., Chaotic mixing in electrokinetically and pressure driven micro flows, in MATLOSZ, M., EHRFELD, W., BASELT, J. P. (Eds.), *Microreaction Technology – IMRET 5: Proc. of the 5th International Conference on Microreaction Technology*, Springer-Verlag, Berlin, **2001**, 185–191.
- 49 LIU, R. H., WARD, M., BONNANO, J., GANSER, D., ATHAVALE, M., GRODZINSKI, P., Plastic on-line chaotic micromixer for biological applications, in RAMSEY, J. M., VAN DEN BERG, A. (Eds.), *Micro Total Analysis Systems*, Kluwer, Dordrecht, **2001**, 163–164.
- 50 SOLOMON, T. N., MEZIC, I., Uniform resonant chaotic mixing in fluid flows, *Nature* **2003**, 425, 376–380.
- 51 MIYAKE, R., LAMMERINK, T. S. J., ELWENPOEK, M., FLUITMAN, J. H. J., Micromixer with fast diffusion, in *Proceedings of the IEEE-MEMS '93* (Feb. 1993), Fort Lauderdale, FL, **1993**, 248–253.
- 52 PENTH, B., *Method and device for carrying out chemical and physical processes*, WO 00/61275, **1999**.
- 53 WERNER, B., DONNET, M., HESSEL, V., HOFMANN, C., JONGEN, N., LÖWE, H., SCHENK, R., ZIOGAS, A., Specially suited micromixers for process involving strong fouling, in *Proceedings of the 6th International Conference on Microreaction Technology, IMRET 6* (11–14 March 2002), AIChE Pub. No. 164, New Orleans, **2002**, 168–183.
- 54 YANG, R., WILLIAMS, J. D., WANG, W., A rapid micro-mixer/reactor based on arrays of spatially impinging micro-jets, *J. Micromech. Microeng.* **2004**, 14, 1345–1351.
- 55 HONG, C.-C., CHOI, J.-W., AHN, C. H., A novel in-plane passive micromixer using coanda effect, in RAMSEY, J. M., VAN DEN BERG, A. (Eds.), *Micro Total Analysis Systems*, Kluwer, Dordrecht, **2001**, 31–33.
- 56 JEON, M. K., KIM, J.-H., YOON, H. J., NOH, J., KIM, S. H., YOON, E., PARK, H. G., WOO, S. I., Design and characterization of a passive recycle-micromixer, in *Proceedings of the 7th International Conference on Micro Total Analysis Systems* (5–9 Sept. 2003), Squaw Valley, CA, **2003**, 109–112.
- 57 GOBBY, D., ANGELI, P., GAVRIILIDIS, A., Mixing characteristics of T-type microfluidic mixers, *J. Micromech. Microeng.* **2001**, 11, 126–132.
- 58 KIM, D. S., LEE, S. W., KWON, T. H., LEE, S. S., A barrier embedded chaotic micromixer, *J. Micromech. Microeng.* **2004**, 14, 798–805.
- 59 MENGEAUD, V., JOSSEAND, J., GIRAULT, H. H., Mixing processes in a zigzag microchannel: finite element simulations and optical study, *Anal. Chem.* **2002**, 74, 4279–4286.
- 60 HARDT, S., DRESE, K. S., HESSEL, V., SCHÖNFELD, F., Passive micro mixers for applications in the micro reactor and  $\mu$ TAS field, in *Proceedings of the 2nd International Conference on Microchannels and Minichannels* (17–19 June 2004), Rochester, NY, **2005**, in print.
- 61 HESSEL, V., LÖWE, H., Micro mixers – a review on passive and active mixing principles, *Chem. Eng. Sci.* **2005**, in print.
- 62 HESSEL, V., LÖWE, H., Mixing principles of micro mixers – passive and active mixing, in WANG, Y., HOLLADAY, J. (Eds.), *Microreactor Technology and Process Intensification, Microreactor Technology and Process Intensification Symposium of the 226th ACS National Meeting* (7–11 Sep. 2003), New York, **2005**, in print.

- 63 JENSEN, K. F., Smaller, faster chemistry, *Nature* **1998**, 393, 735–736.
- 64 BAYER, T., HIMMLER, K., HESSEL, V., Don't be baffled by static mixers, *Chem. Eng.* **2003**, 5, 2–9.
- 65 SCHUBERT, K., BRANDNER, J., FICHTNER, M., LINDER, G., SCHYGULLA, U., WENKA, A., Microstructure devices for applications in thermal and chemical process engineering, *Microscale Thermal Eng.* **2001**, 5, 17–39.
- 66 LÖWE, H., EHRELD, W., HESSEL, V., RICHTER, T., SCHIEWE, J., Micromixing technology, in *Proceedings of the 4th International Conference on Microreaction Technology, IMRET 4* (5–9 March 2000), AIChE Topical Conf. Proc., Atlanta, GA, **2000**, 31–47.
- 67 KOCH, M., CHATELAIN, D., EVANS, A. G. R., BRUNNSCHWEILER, A., Two simple micromixers based on silicon, *J. Micromech. Microeng.* **1998**, 8, 123–126.
- 68 WONG, S. H., WARD, M. C. L., WHARTON, C. W., Micro T-mixer as a rapid mixing micromixer, *Sens. Actuators B* **2004**, 100, 359–379.
- 69 KAWAZUMI, H., TASHIRO, A., OGINO, K., MAEDA, H., Observation of fluidic behavior in a polymethylmethacrylate-fabricated microchannel by a simple spectroscopic analysis, *Lab Chip* **2002**, 2, 8–10.
- 70 GREINER, K. B., DESHPANDE, M., GILBERT, J. R., Design analysis and 3D measurement of diffusive broadening in a Y-mixer, in VAN DEN BERG, A., OLTHUIS, W., BERGVELD, P. (Eds.), *Micro Total Analysis Systems*, Kluwer, Dordrecht, **2000**, 87–90.
- 71 WONG, S. H., BRYANT, P., WARD, M., WHARTON, C., Investigation of mixing in a cross-shaped micromixer with static mixing elements for reaction kinetics studies, *Sens. Actuators B* **2003**, 95, 414–424.
- 72 HESSEL, V., HARDT, S., LÖWE, H., *Chemical Micro Process Engineering – Fundamentals, Modeling and Reactions*, Wiley-VCH, Weinheim, **2004**.
- 73 SKELTON, V., GREENWAY, G. M., HASWELL, S. J., STYRING, P., MORGAN, D. O., WARRINGTON, B. H., WONG, S., Micro reaction technology: synthetic chemical optimization methodology of Wittig synthesis enabling a semi-automated micro reactor for combinatorial screening, in *Proceedings of the 4th International Conference on Microreaction Technology, IMRET 4* (5–9 March 2000), AIChE Topical Conf. Proc., Atlanta, GA, **2000**, 78–88.
- 74 BOURNE, J. R., CRIVELLI, E., RYS, P., 289. Chemical selectivities by mass diffusion. V. Mixing-disguised azo coupling reactions, *Helv. Chim. Acta* **1977**, 60, 2944–2956.
- 75 BOURNE, J. R., KUT, O. M., LENZNER, J., MAIRE, H., An improved reaction system to investigate micromixing in high-intensity mixers, *Ind. Chem. Res.* **1992**, 31, 949–958.
- 76 BOURNE, J. R., KUT, O. M., LENZNER, J., MAIRE, H., Kinetics of the diazo coupling between 1-naphthol and diazotized sulfanilic acid, *Ind. Chem. Res.* **1990**, 29, 1761–1765.
- 77 ROESSLER, A., RYS, P., Selektivität mischungsmaskierter Reaktionen: Wenn die Rührgeschwindigkeit die Produktverteilung bestimmt, *Chemie in unserer Zeit* **2001**, 35, 314–322.
- 78 VILLERMAUX, J., FALK, L., FOURNIER, M.-C., DETREZ, C., Use of parallel competing reactions to characterize micromixing efficiency, *AIChE Sym. Ser.* **1991**, 88, 286, 6.
- 79 PANIC, S., LOEBBECKE, S., TUERCKE, T., ANTES, J., BOSKOVIC, D., Experimental approaches to a better understanding of mixing performance of microfluidic devices, *Chem. Eng. J.* **2004**, 101, 409–419.
- 80 LOEBBECKE, C. S., SCHWEIKERT, W., TUERCKE, T., ANTES, J., MARIOTH, E., KRAUSE, H., Applications of FTIR microscopy for process monitoring in silicon microreactors, in *Proceedings of the VDE World Microtechnologies Congress, MICROtec 2000* (25–27 Sept. 2000), VDE Verlag, Berlin, EXPO Hannover, **2000**, 789–791.
- 81 LOEBBECKE, S., ANTES, J., TUERCKE, T., BOSKOVICH, D., SCHWEIKERT, W., MARIOTH, E., SCHNUEHER, F., KRAUSE, H. H., Black box microreactor? Possibilities for a better control and understanding of microreaction processes by applying suitable analytics, in *Proceedings of the 6th International Conference on Microreaction Technology*,

- IMRET 6 (11–14 March 2002), AIChE Pub. No. 164, New Orleans, **2002**, 37–38.
- 82 EHRFELD, W., HESSEL, V., LÖWE, H., *Microreactors*, Wiley-VCH, Weinheim **2000**.
- 83 JÄHNISCH, K., HESSEL, V., LÖWE, H., BAERNS, M., Chemistry in Microstructured Reactors, *Angew. Chem. Int. Ed.* **2004**, *43*, 406–446.
- 84 HESSEL, V., LÖWE, H., Micro chemical engineering: components – plant concepts – user acceptance: Part I, *Chem. Eng. Technol.* **2003**, *26*, 13–24.
- 85 PENNEMANN, H., WATTS, P., HASWELL, S., HESSEL, V., LÖWE, H., Application of micro reactors: benchmarking for analytical applications and lab-scale synthesis, *Org. Proc. Res. Dev.* **2004**, *4*, 422–439.
- 86 JENSEN, K. F., Microreaction engineering – is small better? *Chem. Eng. Sci.* **2001**, *56*, 293–303.
- 87 FLETCHER, P. D. I., HASWELL, S. J., POMBO-VILLAR, E., WARRINGTON, B. H., WATTS, P., WONG, S. Y. F., ZHANG, X., Micro reactors: principle and applications in organic synthesis, *Tetrahedron* **2002**, *58*, 4735–4757.
- 88 HASWELL, S. T., WATTS, P., Green chemistry: synthesis in micro reactors, *Green Chem.* **2003**, *5*, 240–249.
- 89 GAVRIILIDIS, A., ANGELI, P., CAO, E., YEONG, K. K., WAN, Y. S. S., Technology and application of microengineered reactors, *Trans. IChemE* **2002**, *80/A*, 3–30.
- 90 DE MELLO, A., WOOTTON, R., But what is it good for? Applications of microreactor technology for the fine chemical industry, *Lab Chip* **2002**, *2*, 7N–13N.
- 91 EL MOCTAR, A. O., AUBRY, N., BATTON, J., Electro-hydrodynamic micro-fluidic mixer, *Lab Chip* **2003**, *3*, 273–280.
- 92 LEE, C.-Y., LEE, G.-B., FU, L.-M., LEE, K.-H., YANG, R.-J., Electrokinetically driven active micro-mixers utilizing zeta potential variation induced by field effect, *J. Micromech. Microeng.* **2004**, *14*, 1390–1398.
- 93 ODDY, M. H., SANTIAGO, J. G., C., M. J., Electrokinetic instability micromixer, in RAMSEY, J. M., VAN DEN BERG, A. (Eds.), *Micro Total Analysis Systems*, Kluwer, Dordrecht, **2001**, 34–36.
- 94 CHOI, J.-W., HONG, C.-C., AHN, C. H., An electrokinetic active mixer, in RAMSEY, J. M., VAN DEN BERG, A. (Eds.), *Micro Total Analysis Systems*, Kluwer, Dordrecht, **2001**, 621–622.
- 95 WILSON, C. F., WALLACE, M. I., MORISHIMA, K., SIMPSON, G. J., ZARE, R. N., Coupled Electrorotation of Polymer Microspheres for Microfluidic Sensing and Mixing, *Anal. Chem.* **2004**, *74*, 5099–5104.
- 96 BAU, H. H., ZHONG, J., YI, M., A minute magneto hydro dynamic (MHD) mixer, *Sens. Actuators B* **2001**, *79*, 207–215.
- 97 PAIK, P., PAMULA, V. K., POLLACK, M. G., FAIR, R. B., Electrowetting-based droplet mixers for microfluidic systems, *Lab Chip* **2003**, *1*, 28–32.
- 98 POLLACK, M. G., SHEDEROV, A. D., FAIR, R. B., Electrowetting-based actuation for integrated microfluidics, *Lab Chip* **2002**, *2*, 96–101.
- 99 SCHWARTZ, J. A., VYKOUAL, J. V., GASCOYNE, R. C., Droplet-based chemistry on a programmable microchip, *Lab Chip* **2004**, *4*, 11–17.
- 100 TANIGUCHI, T., TORII, T., HIGUCHI, T., Chemical reactions in microdroplets by electrostatic manipulation of droplets in liquid media, *Lab Chip* **2002**, *2*, 19–23.
- 101 TORII, T., TANIGUCHI, T., TORII, N., HIGUCHI, T., Chemical reaction in microdroplets, in *Proceedings of the 6th International Conference on Microreaction Technology, IMRET 6 (11–14 March 2002)*, AIChE Pub. No. 164, New Orleans, **2002**, 192–201.
- 102 GAU, H., HERMINGHAUS, S., LENZ, P., LIPOWSKY, R., Liquid morphologies on structured surfaces: from microchannels to microchips, *Science* **1999**, *283*, 46–49.
- 103 YANG, Z., GOTO, H., MATSUMOTO, M., YADA, T., Micro mixer incorporated with piezoelectrically driven valveless micro-pump, in HARRISON, J., VAN DEN BERG, A. (Eds.), *Micro Total Analysis Systems*, Kluwer, Dordrecht, **1998**, 177–180.
- 104 ZŁOKARNIK, M., JUDAT, H., *Rührtechnik – Theorie und Praxis*, Springer-Verlag, Berlin, **1999**.
- 105 TATTERSON, G. B., *Scaleup and Design of Industrial Mixing Processes*, McGraw-Hill, New York, **1994**.
- 106 SCHMIDT, K., EHRLICH, R., ELLINGER, T., McCASKILL, J. S., A microflow reactor with components for mixing, separation and detection for biochemical experi-

- ments, in EHRFELD, W., RINARD, I. H., WEGENG, R. S. (Eds.), *Process Miniaturization: 2nd International Conference on Microreaction Technology, IMRET 2, Topical Conf. Preprints, AIChE*, New Orleans, 1998, 125–126.
- 107 SCHMIDT, K., McCASKILL, J. S., *Schaltbarer dynamischer Mikromischer mit minimalem Totvolumen*, DE 19728520, IMB Institut für Molekulare Biotechnologie e.V. Jena, 1997.
- 108 WALZEL, P., LANGER, G., New dynamic micro mixer for viscous fluids, in *Proceedings of the 27th International Exhibition-Congress on Chemical Engineering, Environmental Protection and Biotechnology, AIChE (19–24 May 2003)*, DECHEMA, Frankfurt, 2003, 21.
- 109 BÖHM, S., GREINER, K., SCHLAUTMANN, S., DE VRIES, S., VAN DEN BERG, A., A rapid vortex micromixer for studying high-speed chemical reactions, in RAMSEY, J. M., VAN DEN BERG, A. (Eds.), *Micro Total Analysis Systems*, Kluwer, Dordrecht, 2001, 25–27.
- 110 HINSMANN, P., FRANK, J., SVASEK, P., HARASEK, M., LENDL, B., Design, simulation and application of a new micro-mixing device for time resolved infrared spectroscopy of chemical reactions in solution, *Lab Chip* 2001, 1, 16–21.
- 111 SEIDEL, R. U., SIM, D. Y., MENZ, W., ESASHI, M., A capillary force filled auto-mixing device, in EHRFELD, W. (Ed.), *Microreaction Technology: 3rd International Conference on Microreaction Technology, Proc. of IMRET 3*, Springer-Verlag, Berlin, 2000, 506–513.
- 112 KNIGHT, J. B., VISHWANATH, A., BRODY, J. P., AUSTIN, R. H., Hydrodynamic focusing on a silicon chip: mixing nanoliters in microseconds, *Phys. Rev. Lett.* 1998, 80 (17), 3863–3866.
- 113 BAKAJIN, O., CARISON, R., CHOU, C. F., CHAN, S. S., GABEL, C., KNIGHT, J., COX, T., AUSTIN, R. H., Sizing, fractionating and mixing of biological objects via microfabricated devices, in HARRISON, J., VAN DEN BERG, A. (Eds.), *Micro Total Analysis Systems*, Kluwer, Dordrecht, 1998, 193–198.
- 114 VEENSTRA, T. T., LAMMERINK, T. S. J., ELWENSPOEK, M. C., VAN DEN BERG, A., Characterization method for a new diffusion mixer applicable in micro flow injection analysis systems, *J. Micromech. Microeng.* 1998, 9, 199–202.
- 115 VEENSTRA, T. T., LAMMERINK, T. S. J., VAN DEN BERG, A., ELWENSPOEK, M. C., A mixer based on diffusion-mixing designed for the MAFIAS-Project, in *Proceedings of the Sensor Technology in the Netherlands: State of the Art (2 March 1998)*, Enschede, Netherlands, 1998, 263–267.
- 116 VEENSTRA, T. T., LAMMERINK, T. S. J., VAN DEN BERG, A., ELWENSPOEK, M. C., Characterization method for a new diffusion mixer applicable in micro flow injection analysis systems, in *Proceedings of the Micromechanics Europe (MNE) (3 June 1999)*, Ulvik, Norway, 1999, 186–189.
- 117 DERTINGER, S. K. W., CHIU, D. T., JEON, N. L., WHITESIDES, G. M., Generation of gradients having complex shapes using microfluidic networks, *Anal. Chem.* 2001, 73, 1240–1246.
- 118 LIM, D., KAMOTANI, Y., CHO, B., MAZUMDER, J., TAKAYAMA, S., Fabrication of microfluidic mixers and artificial vasculatures using a high-brightness diode-pumped Nd:YAG laser direct write method, *Lab Chip* 2003, 3, 318–323.
- 119 KAKUTA, M., HINSMAN, P., MANZ, A., LENDL, B., Time-resolved Fourier transform infrared spectrometry using a microfabricated continuous flow mixer: application to protein conformation study using the example of ubiquitin, *Lab Chip* 2003, 3, 82–85.
- 120 JACKMAN, R. J., FLOYD, T. M., GHODSSI, R., SCHMIDT, M. A., JENSEN, K. F., Integrated microchemical reactors fabricated by both conventional and unconventional techniques, in *Proceedings of the 4th International Conference on Microreaction Technology, IMRET 4 (5–9 March 2000)*, AIChE Topical Conf. Proc., Atlanta, GA, 2000, 62–70.
- 121 HESSEL, V., DIETRICH, T., FREITAG, A., HARDT, S., HOFMANN, C., LÖWE, H., PENNEMANN, H., ZIOGAS, A., Fast mixing in interdigital micromixers achieved by means of extreme focusing, in *Proceedings of the 6th International Conference on Microreaction Technology, IMRET 6 (11–14 March 2002)*, AIChE Pub. No. 164, New Orleans, 2002, 297–305.

- 122 SCHUBERT, K., BIER, W., LINDER, G., SEIDEL, G., MENZEL, T., KOGLIN, B., PREISIGKE, H.-J., *Method and device for performing chemical reactions with the aid of microstructure mixing*, WO 95/30476, Bayer, 1994.
- 123 SCHUBERT, K., BIER, W., LINDER, G., SEIDEL, D., MENZEL, T., KOGLIN, B., PREISIGKE, H.-J., HERRMANN, E., *Verfahren und Vorrichtung zur Durchführung chemischer Reaktionen mittels Mikrostruktur-Mischung*, EP 0758981, Bayer, 1994.
- 124 HERWECK, T., HARDT, S., HESSEL, V., LÖWE, H., HOFMANN, C., WEISE, F., DIETRICH, T., FREITAG, A., Visualization of flow patterns and chemical synthesis in transparent micromixers, in MATLOSZ, M., EHRFELD, W., BASELT, J. P. (Eds.), *Microreaction Technology – IMRET 5: Proc. of the 5th International Conference on Microreaction Technology*, Springer-Verlag, Berlin, 2001, 215–229.
- 125 HESSEL, V., EHRFELD, W., MÖBIUS, H., RICHTER, T., RUSSOW, K., Potentials and realization of micro reactors, in *Proceedings of the International Symposium on Microsystems, Intelligent Materials and Robots* (27–29 Sept. 1995), Sendai, Japan, 1995, 45–48.
- 126 MÖBIUS, H., EHRFELD, W., HESSEL, V., RICHTER, T., Sensor controlled processes in chemical microreactors, in *Proceedings of the 8th Int. Conf on Solid-State Sensors and Actuators, Transducers '95 -Euroensors IX* (25–29 June 1995), Stockholm, 1995, 775–778.
- 127 LÖB, P., PENNEMANN, H., HESSEL, V., g/l-Dispersions in interdigital micromixers with different mixing chamber geometries, *Chem. Eng. J.* 2004, 101, 75–85.
- 128 FUJII, T., HOSOKAWA, K., SHOJI, S., YOTSOMOTO, A., NOJIMA, T., ENDO, I., Development of a microfabricated biochemical workbench – improving the mixing efficiency, in HARRISON, J., VAN DEN BERG, A. (Eds.), *Micro Total Analysis Systems*, Kluwer, Dordrecht, 1998, 173–176.
- 129 AOKI, N., HASEBE, S., MAE, K., Mixing in microreactors: effectiveness of lamination segments as a form of feed on product distribution for multiple reactions, *Chem. Eng. J.* 2004, 101, 323–331.
- 130 WERNER, B., HESSEL, V., LÖB, P., Mischer mit mikrostrukturierten Folien für chemische Produktionsaufgaben, *Chem. Ing. Tech.* 2004, 76, 567–574.
- 131 HARDT, S., DIETRICH, T., FREITAG, A., HESSEL, V., LÖWE, H., HOFMANN, C., OROSKAR, A., SCHÖNFELD, F., VANDEN BUSSCHE, K., Radial and tangential injection of liquid/liquid and gas/liquid streams and focusing thereof in a special cyclone mixer, in *Proceedings of the 6th International Conference on Microreaction Technology, IMRET 6* (11–14 March 2002), AIChE Pub. No. 164, New Orleans, 2002, 329–344.
- 132 VAN DEN BERG, A., Integrated micro- and nanofluidics: silicon revisited, in RAMSEY, J. M., VAN DEN BERG, A. (Eds.), *Micro Total Analysis Systems*, Kluwer, Dordrecht, 2001, 207–209.
- 133 WILSON, D. J., KONERMANN, L., A capillary mixer with adjustable reaction chamber volume for millisecond time-resolved studies by electrospray mass spectrometry, *Anal. Chem.* 2003, 75, 6408–6414.
- 134 TAGAKI, M., MAKI, T., MIYAHARA, M., MAE, K., Production of titania nanoparticles by using a new microreactor assembled with same axle dual pipe, *Chem. Eng. J.* 2004, 101, 269–276.
- 135 SCHÖNFELD, F., RENSINK, D., Simulation of droplet generation by mixing nozzles, *Chem. Eng. Technol.* 2003, 26, 585–591.
- 136 SCHENK, R., HESSEL, V., WERNER, B., ZIOGAS, A., HOFMANN, C., DONNET, M., JONGEN, N., Micromixers as a tool for powder production, *Chem. Eng. Trans.* 2002, 1, 909–914.
- 137 SCHENK, R., DONNET, M., HESSEL, V., HOFMANN, C., JONGEN, N., LÖWE, H., Suitability of various types of micromixers for the forced precipitation of calcium carbonate, in MATLOSZ, M., EHRFELD, W., BASELT, J. P. (Eds.), *Microreaction Technology – IMRET 5: Proc. of the 5th International Conference on Microreaction Technology*, Springer-Verlag, Berlin, 2001, 489–498.
- 138 SCHENK, R., HESSEL, V., JONGEN, N., BUSCAGLIA, V., GUILLEMET-FRITSCH, S., JONES, A. G., Nanopowders produced using microreactors, in *Encyclopedia of Nanoscience and Nanotechnology*, Vol. 7, 2004, 287–296.

- 139 ADAMSCHIK, M., SCHMID, P., MAIER, C., HINZ, M., SELIGER, S., HOFER, E. P., KOHN, E., Micro dosage controlled micro reactor based on CVD-diamond, in *Proceedings of the 4th International Conference on Microreaction Technology, IMRET 4* (5–9 March 2000), AIChE Topical Conf. Proc., Atlanta, GA, **2000**, 114–120.
- 140 BRANEJBERG, J., GRAVESEN, P., KROG, J. P., NIELSEN, C. R., Fast mixing by lamination, in *Proceedings of IEEE-MEMS '96* (12–15 Feb. 1996), San Diego, CA, **1996**, 441–446.
- 141 MENSINGER, H., RICHTER, T., HESSEL, V., DÖPPER, J., EHRFELD, W., Microreactor with integrated static mixer and analysis system, in VAN DEN BERG, A., BERGFELD, P. (Eds.), *Micro Total Analysis Systems*, Kluwer, Dordrecht, **1995**, 237–243.
- 142 SVASEK, P., JOBST, G., URBAN, G., SVASEK, E., Dry film resist based fluid handling components for  $\mu$ TAS, in WIDMER, H. M., VERPOORTE, E., BARNARD, S. (Eds.), *Proceedings of the 2nd International Symposium on Miniaturized Total Analysis Systems, Analytical Methods & Instrumentation, Special Issue  $\mu$ TAS '96*, Basel, **1996**, 78–80.
- 143 KOOP, U., SCHMELZ, M., BEIRAU, A., *Mikromischer*, DE 19746583, Merck, **1997**.
- 144 SCHWESINGER, N., FRANK, T., *Device for mixing small quantities of liquids*, DE 96911955, Merck, **1995**.
- 145 KRUMMRADT, H., KOPP, U., STOLDT, J., Experiences with the use of microreactors in organic synthesis, in EHRFELD, W. (Ed.), *Microreaction Technology: 3rd International Conference on Microreaction Technology, Proc. of IMRET 3*, Springer-Verlag, Berlin, **2000**, 181–186.
- 146 PARK, S.-J., KIM, J. K., PARK, J., CHUNG, S., CHUNG, C., CHANG, J. K., Rapid three-dimensional passive rotation micromixer using the breakup process, *J. Micromech. Microeng.* **2004**, *14*, 6–14.
- 147 FLUITMAN, J. H., VAN DEN BERG, A., LAMMERICK, T. S., Micromechanical components for  $\mu$ TAS, in VAN DEN BERG, A., BERGFELD, P. (Eds.), *Micro Total Analysis Systems*, Kluwer, Dordrecht, **1995**, 73–83.
- 148 YOTSUMOTO, A., NAMAKURA, R., SHOJI, S., WADA, T., Fabrication of an integrated mixing/reaction micro flow cell for  $\mu$ TAS, in HARRISON, J., VAN DEN BERG, A. (Eds.), *Micro Total Analysis Systems*, Kluwer, Dordrecht, **1998**, 185–188.
- 149 TRACEY, M. C., COX, T. I., DAVIS, J. B., Microfluidic mixer employing temporally interleaved liquid slugs and parabolic flow, in RAMSEY, J. M., VAN DEN BERG, A. (Eds.), *Micro Total Analysis Systems*, Kluwer, Dordrecht, **2001**, 141–141.
- 150 RO, K. W., LIM, K., HAHN, J. H., PDMS Microchip for precolumn reaction and micellar electrokinetic chromatography of biogenic amines, in RAMSEY, J. M., VAN DEN BERG, A. (Eds.), *Micro Total Analysis Systems*, Kluwer, Dordrecht, **2001**, 651–662.
- 151 BRANEJBERG, J., FABIUS, B., GRAVESEN, B., Application of miniature analyzers: from microfluidic components to  $\mu$ TAS, in VAN DEN BERG, A., BERGFELD, P. (Eds.), *Micro Total Analysis Systems*, Kluwer, Dordrecht, **1995**, 141–151.
- 152 SCHÖNFELD, F., HARDT, S., Simulation of helical flows in microchannels, *AIChE J.* **2004**, *50*, 771–778.
- 153 LIU, R. H., YANG, J., LENIGK, R., BONANNO, J., GRODZINSKI, P., Self-contained, fully integrated biochip for sample preparation, polymerase chain reaction amplification, and DNA microarray detection, *Anal. Chem.* **2004**, *76*, 1824–1831.
- 154 AREF, H., Stirring by chaotic advection, *J. Fluid Mech.* **1984**, *143*, 1–21.
- 155 UJHIDY, A., NEMETH, J., SZEPVÖLGYI, J., Fluid flow in tubes with helical elements, *Chem. Eng. Proc.* **2003**, *42*, 1–7.
- 156 JOHNSON, T. J., LOCASIO, L. E., Characterization and optimization of slanted well designs for microfluidic mixing under electroosmotic flow, *Lab Chip* **2002**, *2*, 135–140.
- 157 AUBIN, J., FLETCHER, D. F., BERTRAND, J., XUERE, C., Characterization of the mixing quality in micromixers, *Chem. Eng. Technol.* **2003**, *26*, 1262–1270.
- 158 JOHNSON, T. J., ROSS, D., GAITAN, M., LOCASIO, L. E., Laser modification of channels to reduce band broadening or to increase mixing, in RAMSEY, J. M., VAN DEN BERG, A. (Eds.), *Micro Total Analysis Systems*, Kluwer, Dordrecht, **2001**, 603–604.

- 159 PEREZ-CASTILLEJOS, R., ESTEVE, J., ACERO, M. C., PLAZA, J. A., Ferrofluidics for disposable microfluidic systems, in RAMSEY, J. M., VAN DEN BERG, A. (Eds.), *Micro Total Analysis Systems*, Kluwer, Dordrecht, **2001**, 492–494.
- 160 HE, B., BURKE, J., ZHANG, X., ZHANG, R., REGNIER, F. E., A picoliter-volume mixer for microfluidic analytical systems, *Anal. Chem.* **2001**, *73*, 1942–1947.
- 161 BURKE, B. J., REGNIER, F. E., Stopped-flow enzyme assays on a chip using a microfabricated mixer, *Anal. Chem.* **2003**, *75*, 1786–1791.
- 162 SEONG, G. H., CROOKS, R. M., Efficient mixing and reactions with microfluidic channels using microbead-supported catalysts, *J. Am. Chem. Soc.* **2002**, *124*, 13360–13361.
- 163 HONG, C.-C., CHOI, J.-W., AHN, C. H., A novel in-plane passive microfluidic mixer with modified Tesla structures, *Lab Chip* **2004**, *4*, 109–113.
- 164 YANG, M., YANG, J., LI, C.-W., ZHAO, J., Generation of concentration gradient by controlled flow distribution and diffusive mixing in a microfluidic chip, *Lab Chip* **2002**, *2*, 158–163.
- 165 DONNET, M., BOWEN, P., JONGEN, N., LEMAITRE, J., HOFMANN, H., SCHREINER, A., JONES, A. G., SCHENK, R., HOFMANN, C., Successful scale-up from millilitre batch optimization to a small scale continuous production using the segmented flow tubular reactor: example of calcium carbonate precipitation, *Chem. Eng. Trans.* **2002**, *1*, 1353–1358.
- 166 PENTH, B., New non-clogging micro-reactor for chemical processing and nano materials, in *Proceedings of the Micro.tec 2000, VDE World Microtechnologies Congress Expo 2000 (25–27 Sept. 2000)*, VDE Verlag, Berlin, **2000**, 401–405.
- 167 SCHÖNFELD, F., RENSINK, D., Simulation of droplet generating by mixing nozzles, *Chem. Eng. Technol.* **2003**, *26* (5), 585–591.